Characterisation of two clinical mutations of Xanthine Oxidoreductase related to Hyperuricaemia

A dissertation presented to the Faculty of Medicine and Surgery in part fulfilment of the requirements for the degree of Master of Science in Biochemistry at the University of Malta

Supervisor: Prof. Thérèse Hunter B.Sc.(Hons.)(N.Y.),M.Sc.(N.Y.),Ph.D.(Cran.)

Co-Supervisor: Dr Brandon Charles Seychell B.Sc. (Hons)(Melit), Ph.D.(Melit)

Elena Ilia

2025

L-Università ta' Malta

University of Malta Library – Electronic Thesis & Dissertations (ETD) Repository

The copyright of this thesis/dissertation belongs to the author. The author's rights in respect of this work are as defined by the Copyright Act (Chapter 415) of the Laws of Malta or as modified by any successive legislation.

Users may access this full-text thesis/dissertation and can make use of the information contained in accordance with the Copyright Act provided that the author must be properly acknowledged. Further distribution or reproduction in any format is prohibited without the prior permission of the copyright holder.

FACULTY/INSTITUTE/CENTRE/SCHOOL Faculty of Medicine and Surgery

DECLARATIONS BY POSTGRADUATE STUDENTS

(a) Authenticity of Dissertation

I hereby declare that I am the legitimate author of this Dissertation and that it is my original work.

No portion of this work has been submitted in support of an application for another degree or qualification of this or any other university or institution of higher education.

I hold the University of Malta harmless against any third party claims with regard to copyright violation, breach of confidentiality, defamation and any other third party right infringement.

(b) Research Code of Practice and Ethics Review Procedures

I declare that I have abided by the University's Research Ethics Review Procedures. Research Ethics & Data Protection form code MED-2024-00446.

As a Master's student, as per Regulation 77 of the General Regulations for University Postgraduate Awards 2021, I accept that should my dissertation be awarded a Grade A, it will be made publicly available on the University of Malta Institutional Repository.

ACKNOWLEDGMENTS

This project was carried out at the Laboratory of Biochemistry and Protein Science at the University of Malta.

Firstly, I would like to express my deepest gratitude to my supervisor, Professor Thérèse Hunter, for her continuous guidance, patience, and encouragement throughout this journey. Her dedication, insightful advice, and belief in my abilities gave me the confidence to grow both academically and personally. I am truly grateful for the time and care she invested in me and my work.

I am also sincerely thankful to my co-supervisor, Dr. Brandon Charles Seychell, for his invaluable support and understanding throughout the duration of this project. His approachability and calm reassurance made even the most challenging moments feel manageable. I am especially thankful for his patience, encouragement, and willingness to listen, which provided both guidance and confidence during times of uncertainty. His thoughtful feedback and steady support were invaluable.

I would also like to thank Professor Gary J. Hunter for his guidance and support, which were greatly appreciated throughout this academic journey. My heartfelt thanks go to Dr. Marita Vella, Ms. Abigail Dalli, and Ms. Sephora Galea for their willingness to help at every step. In moments of doubt, exhaustion, and frustration, they stood by me, believed in me, and reminded me of my own resilience. Their support, shared knowledge, and genuine kindness created an environment where I felt supported and understood. The sense of teamwork and friendship within the lab made even the most demanding days more manageable and rewarding.

Finally, my deepest and most personal gratitude goes to my family, especially my dad, my mom, and my sisters. Their unconditional love, constant encouragement, and unwavering belief in me have been my greatest source of strength throughout this journey. They supported me through every challenge, celebrated every small success, and stood by me during moments when the path felt overwhelming. Their sacrifices, patience, and endless reassurance carried me though times of self-doubt and exhaustion. This thesis is not only the result of my own efforts, but also a reflection of their love, support, and faith in me. I could not have reached this milestone without them.

Abstract

Xanthine oxidoreductase (XOR) is a molybdoflavin enzyme and a homodimer with a mass of 290 kDa. In mammals, XOR exists in two interconvertible forms: Xanthine Dehydrogenase (XDH) and Xanthine Oxidase (XO). XOR catalyses the final steps of purine catabolism, converting hypoxanthine to xanthine and subsequently to uric acid. These two reactions can generate reactive oxygen species (ROS), specifically hydrogen peroxide and superoxide anion radicals. XOR has been associated with various health conditions, including hyperuricemia, oxidative stress, and hypertension. ROS generated by XOR contribute to endothelial dysfunction, with increased ROS levels reacting with nitric oxide (NO) to form peroxynitrite radicals, exacerbating hypertension. Different variants have also been linked with increased XOR activity as well as higher risk of diseases, such as hyperuricemia and hypertension. In this project, the hXOR wildtype (WT) and two known clinical variants identified in a Maltese study by the MAMI study, I646V and I703V, as well as a novel double mutant (I646V-I703V) also identified in the Maltese population, were characterised. Apart from the clinical variants, the I646A mutation was also constructed to characterise to assess the effect of the substitution of a large non-polar branched amino acid such as isoleucine with a smaller one. The aim of this project was to determine the effect these amino acid changes have on the hXOR protein.

Transformed TP1000 *E.coli* cells harbouring either the pTrc-HisXOR WT or the variants were grown under aerobic conditions without and with heat shock. Purification was performed using immobilised metal affinity chromatography. The purified proteins were characterised using SDS-PAGE, Native-PAGE, Blue-Native gel, and Dynamic Light Scattering (DLS) for size and oligomeric state. The enzymatic activity was evaluated using the uric acid spectrophotometric assay and the Nitro Blue Tetrazolium (NBT) assay. Secondary structure, thermal stability (melting temperature), and amyloid fibril formation were assessed using circular dichroism, DLS, and the Thioflavin T (ThT) assay, respectively. The amyloidogenic potential was further investigated using the ZipperDB server.

All variants exhibited significantly higher enzymatic activities compared to the WT hXOR sample, with the I646A variant showing the highest activity (9-fold greater than WT). Analysis of DLS data confirmed that the native proteins of all mutants predominantly occur in the active native dimer conformation. Conversely, the WT hXOR exhibited the lowest activity and formed the largest oligomeric structures. The WT hXOR

formed amyloid fibrils in the ThT assay, supported by the identification of amyloidogenic stretches using ZipperDB. Most variants did not show fibrillization, specifically I703V, I646A, I646V+HS, I646V-I703V+HS, and I646A+HS. The substitution of Ile646 with Valine or Alanine (I646V, I646A) significantly reduced the amyloidogenic propensity while increased substantially the enzymatic activity. I646V-I703V+HS also exhibited high enzymatic activity and displayed no fibril formation. These findings show that while WT hXOR activity is dampened by fibril formation, the clinical variants remain hyperactive and stable. This high activity of hXOR may result in significant ROS production and hyperuricemia potentially leading to various health conditions, such as hypertension.

Keywords: Hypertension; Uric acid; Nitric Oxide; Reactive Oxygen Species; Variants; Amyloid fibrils; Xanthine Oxidoreductase

TABLE OF CONTENTS

LIST OF TABLES

LIST OF FIGURES

LIST OF ABBREVIATIONS

The following abbreviations have been used within this dissertation:

ACE	angiotensin-converting enzyme
ARB	angiotensin receptor blockers
AO	Aldehyde Oxidase
ATP	Adenosine Triphosphate
APS	Ammonium persulphate
Arg	Arginine
BCA	Bicinchoninic acid
BP	Blood pressure
bXOR	bovine Xanthine Oxidoreductase
CCB	Calcium Channel blockers
CD	Circular Dichroism
cPMP	cyclopyranoperin monophosphate
Cryo EM	Cryo Electron Microscopy
Cys	Cysteine
Da	Daltons
DLS	Dynamic Light Scattering
DMSO	Dimethyl sulphoxide
DTT	1,4-dithiothreitol
EDTA	Ethylenediaminetetraacetic acid
EPR	Electron paramagnetic resonance spectroscopy
FAD	Flavin adenine dinucleotide
Fe-S	Iron-sulphur
FT	Flow through
GAG	Glycosaminoglycan
Gln	Glutamine
H_2O_2	Hydrogen peroxide
HS	Heat shock
HSP	Heat shock proteins
hXOR	Human xanthine oxidoreductase
IM	Imidazole

IMAC	Immobilised metal affinity chromatography
IPTG	Isopropyl-β-D-thiogalactopyranoside
KCl	Potassium chloride
Lys	Lysine
Moco	Molybdenum cofactor
MPT	Molybdopterin
mRNA	messenger RNA
NaCl	Sodium chloride
NAD+	Oxidised nicotinamide adenine dinucleotide
NADH	Reduced nicotinamide adenine dinucleotide
NADPH	Reduced nicotinamide adenine dinucleotide phosphate
NBT	Nitro blue tetrazolium
NO	Nitric Oxide
O_2	Oxygen
O_2^-	Superoxide
OD_{600}	Optical density
$ONOO^-$	Peroxynitrite radicals
PAGE	Polyacrylamide gel electrophoresis
PBS	Phosphate buffered saline
PCR	Polymerase Chain Reaction
PEG	Polyethylene glycol
PMSF	Phenylmethylsulfonyl fluoride
RAS	Renin-Angiotensin System
RNS	Reactive Nitrogen species
ROS	Reactive Oxygen species
PSI	Rounds per square inch
rpm	Revolution per minute
S	Sulphur
SDS	Sodium dodecyl sulphate
SNP	Single nucleotide polymorphism
SUA	Serum uric acid
TCEP	Tris(2-carboxyethyl) phosphine
TEM	Transmission Electron Microscopy
TEMED	Tetramethyl ethylenediamine

ThT	Thioflavin T
TLS	Tumour Lysis Syndrome
TM	Melting temperature
WT	Wildtype
XDH	Xanthine Dehydrogenase
XO	Xanthine Oxidase
XOR	Xanthine Oxidoreductase

Chapter 1 Literature Review

According to the World Health Organization (WHO), high blood pressure affects 1.28 billion people aged 30-79 years globally and is a leading risk factor for cardiovascular disease and kidney failure (World Health Organisation, 2023). Hypertension is often referred to as the 'silent killer' because it typically shows no early symptoms while being the most significant risk factor for heart disease, including myocardial infarction, heart failure, and stroke (Fatima & Mahmood, 2021; Sawicka et al., 2011). Even though, hypertension is a fairly common disorder, it is not easy to prevent and treat it, since only a small portion of adults diagnosed with high blood pressure are able to achieve an adequate blood pressure (Cuevas et al., 2019). The development of hypertension involves mainly genetic factors and this might be the reason that only about 50% of treated individuals manage to control their blood pressure levels since genetic variations may affect the efficacy of antihypertensive medications (Cuevas et al., 2019; Rysz et al., 2020; Sawicka et al., 2011).

1.1. Hypertension

Hypertension is characterised by a rise in systolic blood pressure and/ or diastolic blood pressure (BP) (World Health Organisation, 2023). BP is expressed as the ratio of the systolic BP, which is the pressure that the blood exerts on the arterial walls when the heart contracts and the diastolic BP, which is the pressure when heart relaxes. One is diagnosed with hypertension with a systolic blood pressure of 140 mmHg or higher and a diastolic pressure of 90 mmHg or higher (Sawicka et al., 2011; Gabb, 2020).

1.1.1. Stages of Hypertension

Although the cut-off point which defines hypertension is 140/90 mmHg using standard clinic methods of measurements, such a blood pressure can be considered as grade 1 hypertension. Meanwhile, grade 2 hypertension is considered when the systolic blood pressure is between 160-179 mmHg or diastolic blood pressure between 100-109 mmHg. Grade 3 hypertension is considered when systolic blood pressure is above 180 mmHg or diastolic blood pressure above 110 mmHg (Gabb, 2020; Sawicka et al., 2011).

1.1.2. Types of Hypertension

There are two types of hypertension, specifically the primary and the secondary. Primary hypertension, also known as essential hypertension or idiopathic, is the most common, affecting 90-95% of hypertensive individuals (Sawicka et al., 2011; Carretero & Oparil, 2000). Its development is multifactorial and complex, involving genetic factors and environmental influences such as obesity, smoking, salt sensitivity, and alcohol consumption (Carretero & Oparil, 2000; Sawicka et al., 2011; Carey et al., 2018). While increased salt intake and obesity alone may not be sufficient to elevate blood pressure, they can exacerbate genetic predispositions (Sawicka et al., 2011). Additional factors contributing to primary hypertension include hyperactivity of the renin-angiotensin-aldosterone system and sympathetic nervous system, and a deficiency in substances that dilate blood vessels (Sawicka et al., 2011).

Approximately 5-10% of hypertension cases are secondary, meaning they have identifiable underlying causes. Recognizing secondary hypertension is crucial as its treatment focuses on addressing the root cause of the elevated blood pressure. Causes include renal disease, obstructive sleep apnoea, pregnancy-associated hypertension, and oestrogen use (Sawicka et al., 2011).

Even though primary and secondary hypertension are the two main forms of hypertension, other forms of hypertension also exist. For instance, white coat hypertension, also known as isolated clinical or office hypertension, is used to describe individuals with high blood pressures in a medical environment, but whose blood pressure is normal outside of the clinic or at home (Huang et al., 2017; Verdecchia et al., 2002). Patients with high blood pressure in a medical environment and normal blood pressure at home can be further characterised by three characteristics: lack of organ damage caused by hypertension, absence of cardiovascular diseases related to hypertension, or absence of a decrease in blood pressure via antihypertensive medication (Verdecchia et al., 2002).

Patients with normal office blood pressure but high home blood pressure or ambulatory blood pressure measurements (ABPM) are considered to have masked hypertension (Oparil et al., 2018; Papadopoulos & Makris, 2007). The occurrence in the population for both masked and white coat hypertension is about 1 in 7 or 8 individuals with normal office blood pressure (Papadopoulos & Makris, 2007).

Moreover, resistance hypertension occurs when the blood pressure remains high even after the administration of 3 different antihypertensive medications of different

classes, including a diuretic, an angiotensin-converting enzyme inhibitor or angiotensin receptor blocker, and a long-acting calcium channel blocker (Carey et al., 2018).

1.1.3. Hypertension the ‘‘silent killer’’

As previously mentioned, even though hypertension is often presented without early symptoms, it remains the most significant risk factor for a range of critical health outcomes, including heart failure, stroke, and chronic kidney disease (Sawicka et al., 2011; Fatima & Mahmood, 2021). The complications of hypertension arise from prolonged elevated blood pressure, which causes changes in blood vessels and the heart, and from atherosclerosis accelerated by chronic hypertension (Sawicka et al., 2011).

Hypertension is a recognised risk factor that contributes to the onset of left ventricular hypertrophy, impairments in both systolic and diastolic function, and coronary flow disturbances. This combination of abnormalities, referred to as hypertensive heart disease, ultimately progresses to heart failure (Sawicka et al., 2011).

Hypertension is not only a risk factor for heart diseases, but it is also a risk factor for stroke (Sawicka et al., 2011; Kim et al., 2016). Hypertension is a major contributor to the development of large artery atherosclerosis, which can lead to ischemic stroke through thrombotic arterial blockage, artery-to-artery embolism, or a combination (Kim et al., 2016). There are various factors involved in the hypertension-induced stroke, including, inflammation, oxidative stress, and arterial baroreflex dysfunction (Yu et al., 2011).

1.2. Regulating Hypertension

Since hypertension is affected by environmental factors, the blood pressure can be lowered by changing the lifestyle of hypertensive individuals. Alterations in lifestyle include change in diet, weight control, exercise, stress management, and limited alcohol consumption (Gupta & Guptha, 2010; Verma, 2021). High potassium intake is also associated with reduced blood pressure, since hypertensive individuals might have a deficiency in potassium, by balancing the total body fluid volume, acid, and electrolyte, and keeping normal cell function (Chan et al., 2024).

However, in case the blood pressure remains high despite these lifestyle changes, then the individual needs to be treated by antihypertensive drugs.

1.2.1. Modes of Treatment

Hypertension can be treated using a variety of drugs. Such drugs include angiotensin-converting enzyme (ACE) inhibitors, angiotensin receptor blockers (ARBs), calcium channel blockers, diuretics and β-blockers (Aronow, 2018; Laurent, 2017).

1.2.2. ACE Inhibitors

Angiotensin-converting enzyme (ACE) inhibitors inhibit the formation of angiotensin II from angiotensin I and thus the effects of angiotensin II type 1 (AT1) receptor and angiotensin II type 2 (AT2) receptor, including cell growth, sodium and water retention, amongst others (Messerli et al., 2018). This inhibition results in decreased generation of angiotensin II, lowering the blood pressure, since angiotensin II is the main effector molecule of Renin-Angiotensin System (RAS) and a vasoconstrictor, thereby it increases blood pressure (Benigni et al., 2010). ACE inhibitors inhibit also the breakdown of bradykinin, a vasodilator, elevating the levels of bradykinin in the blood (Messerli et al., 2018; Brown & Vaughan, 1998). ACE inhibitors also change the degradation and formation of other vasoactive substances, for instance substance P (Brown & Vaughan, 1998). Examples of ACE inhibitors include captopril, fosinopril, and trandolapril (Brown & Vaughan, 1998).

1.2.3. ARBs

Angiotensin II receptor blockers (ARBs) are inhibitors that also act on the renin-angiotensin-aldosterone system. However, rather than inhibiting the formation of angiotensin II like ACE inhibitors, they replace angiotensin II from the AT1 receptor. They also enable the stimulation of AT2, triggering vasodilation and natriuresis (Messerli et al., 2018). These inhibitors were developed to overcome the disadvantages of ACE inhibitors, such as elevated levels of renin and angiotensin I due to competitive inhibition which will eventually overcome the blockade effect (Barreras & Gurk-Turner, 2003). An example of ARB inhibitor is Losartan (Barreras & Gurk-Turner, 2003).

1.2.4. CCBs

Calcium Channel blockers (CCBs) are used in the treatment of hypertension, arrythmias, and coronary vasospasm. Through ion-specific channels, CCBs inhibit the movement of extracellular calcium inwards, reducing the peripheral vascular resistance, causing the vascular smooth muscle cells to relax and thus resulting in vasodilation and a

decrease in the blood pressure (Lee, 2023; Elliott & Ram, 2011). Examples of CCBs include verapamil and diltiazem (Elliott & Ram, 2011).

1.2.5. Diuretics

Diuretics are used as a treatment for hypertension by reducing both systolic and diastolic blood pressures, heart failure, or oedema. These drugs raise the rate of urine flow, by facilitating the excretion of water and electrolytes by the kidneys (Kehrenberg & Backmann, 2022). The luminar-cellular osmotic gradient is reduced through the decrease in the reabsorption in the renal tubular sodium, which limits the reabsorption of water (Wile, 2012). The reduction of sodium resorption is achieved by the interference with the $Na\text{-}K^{+}\text{-}2Cl^{-}$ cotransporter in the thick ascending loop of Henle (Shah et al., 2004). There are five classes of diuretics: thiazide diuretics, loop diuretics, potassium-sparing, osmotic diuretics, and carbonic anhydrase inhibitors (Kehrenberg & Beckmann, 2022). Thiazide is the most commonly used diuretic (Shah et al., 2004).

1.2.6. Beta-blockers

Beta-blockers can be used for myocardial infarction, angina, and high sympathetic tone, since they reduce the myocardial workload by decreasing the heart rate and high blood pressure to lower oxygen demand (Johri et al., 2023; Foëx & Sear, 2004). In acute myocardial infarction, beta-blockers can decrease arrythmias. Beta-blockers bind to β-adrenergic receptors (ARs), but they are not able to induce a response. They inhibit the activity of β-AR agonists, since they compete with β-AR agonists for the binding site, classifying them as competitive antagonists (Oliver et al., 2019). There are three different types of β-adrenergic receptors, specifically β1 in heart, β2 found in smooth muscles, and β3 in adipocytes (Johri et al., 2023). Even though β-blockers can be used for cardiovascular diseases, this therapy is associated with side effects, including fatigue, depression, and sexual dysfunction (Foëx & Sear, 2004).

1.2.7. Response to treatment

Even though there are different antihypertensive drugs, around 50% of individuals with hypertension manage to lower their blood pressure to normal levels. This is because variations in genes might unable hypertensive patients to lower their blood pressure upon medication as such interindividual genetic variations can affect the response to the antihypertensive treatment (Cuevas et al., 2019). It was also shown that hypertension arise

from both genetic and environmental factors, as well as gene interactions, and gene-environmental interactions (Wu et al., 2015).

1.3. Human XOR

Xanthine oxidoreductase (XOR) is a metalloflavoprotein firstly found in fresh milk (Dixon & Thurlow, 1924). In humans, XOR is a homodimer with a mass of 290 kDa with three domains per monomer, with one molybdenum, which is incorporated as a molybdenum cofactor (Moco) containing a mononuclear Mo atom coordinated to a molybdopterin (MPT) (Figure 1.1). The molybdenum is an organic cofactor containing two non-identical iron-sulphur [2Fe-2S] centres, and one flavin adenine dinucleotide (FAD) (Nishino et al., 2005; Mendel, 2013). Human XOR can be expressed in different organs, including brain, liver, kidney, and muscle (Cuevas et al., 2019). XOR is a rate-limiting enzyme in purine metabolism, since it catalyses the last two steps of uric acid production, due to the loss of uricase in humans through evolution (Chen et al., 2016).

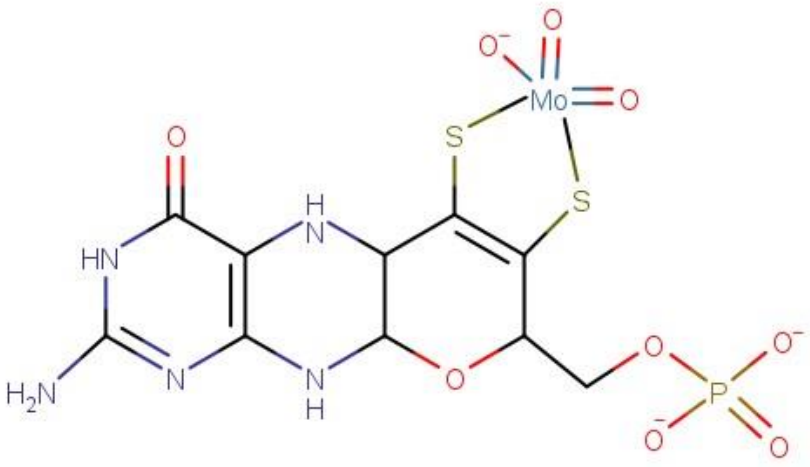

Figure 1.1: Moco cofactor. Structure drawn using Marvin Sketch 19.3 (ChemAxon).

The activity of XOR in humans was found to be high only in liver and intestine. Jarasch *et al.* observed using human anti-XOR antibodies, that XOR is also found in the epithelial and capillary endothelial cells (Jarasch et al., 1981). Even though XOR is a cytosolic enzyme, it is also present in extracellular compartments, such as blood and milk (Bortolotti et al., 2021). When it is released into the circulation, xanthine oxidase (XO) can bind extracellularly to glycosaminoglycans (GAGs) on the surface of endothelial cells by proteoglycan heparin sulphate anchor (Adachi et al., 1993; Kelley, 2015).

The human XOR gene is located on chromosome 2p22 and it is composed of 36 exons which result in the formation of a protein made up of 1,333 amino acids (Wu et al.,

2015; Yang et al., 2008). XOR is a metabolic enzyme involved in purine degradation. It converts purines, such as hypoxanthine and xanthine, into uric acid (Furuhashi, 2020).

Inactive forms of XOR have been observed in mammalian tissues, with 60% of purified bovine milk XOR being inactive towards xanthine (Ventom et al., 1988; Harrison 2002). The inactive forms include demolybdo XOR, which is the enzyme without Moco, or desulpho XOR, which is the XOR with a Moco bonded to an oxygen instead of a sulphur (Harrison, 2002).

Human XOR has been purified from liver tissue (Krenitsky et al., 1986) and breast milk (Abadeh et al., 1992) and has been recombinantly expressed in bacteria (Yamaguchi et al., 2007). The activity of human milk XO was only 5%, compared to the activity of bovine milk, likely due to the low molybdenum content that showed that human milk XOR was 95% in the demolybdo form, whereas bovine XOR was between 30% and 40% (Godber et al., 2005; Godber et al., 1997; Harrison, 2002).

1.3.1. Structure of human XOR

XOR protein is a homodimer (Figure 1.2) with each subunit consisting of one Moco domain, two non-identical [2Fe-2S] centres and one FAD centre, as shown in Figure 1.3, all of which have the role of facilitating electron transfer during substrate oxidation, enabling catalysis (Nishino et al., 2005; Kuwabara et al., 2003). The human XOR can be divided into three domains; the 25 kDa amino terminal domain that encompasses residues 1 to 166 and houses the [2Fe-2S] centres, the central 40 kDa domain from residues 228 to 542 containing the FAD cofactor, and the carboxy-terminal 85 kDa domain from residues 557 to 1333 in which the Moco-binding site is located (Seychell, 2019; Terao et al., 2016).

The homodimer is formed when the two monomers of the protein interact with each other via molybdenum centres with a distance of around 50 Å (Urarte et al., 2015). This indicates that the two monomers act as separate catalytic subunits, since there is no electron exchange between them (Enroth et al., 2000; Urarte et al., 2015) (Figure 1.4). The Moco domain contains a molybdenum ion bound to a pterin ring through two sulphur atoms. There is also another sulphur atom and two oxygen atoms bound to the molybdenum through coordinate bonds. The [2Fe-2S] can be divided into two groups according to their redox potential, with Fe/S II having higher redox potential (Okamoto et al., 2013).

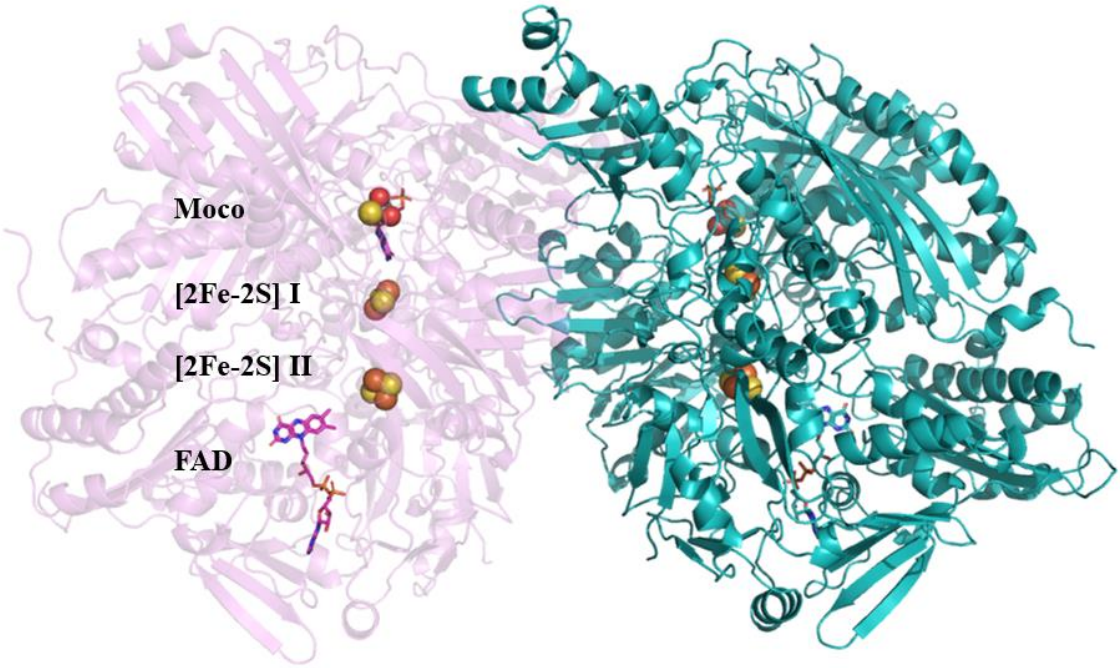

Figure 1.2: Structure of human XOR. Subunit of XOR is divided into three domains: the Moco domain, the [2Fe-2S] domain, and the FAD domain. The figure was generated using PyMol Molecular Graphics System (Schrödinger & DeLano, 2020).

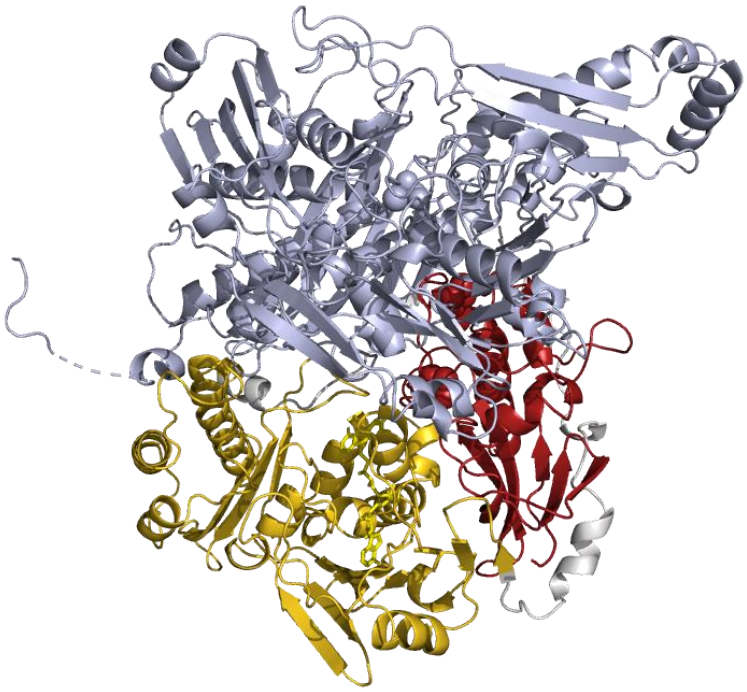

Figure 1.3: Domains of human XOR. The monomer of hXOR is divided into three domains: the Moco domain shown in grey, the [2Fe-2S] domain shown in red, and the FAD domain shown in yellow. The figure was generated using PyMol Molecular Graphics System (Schrödinger & DeLano, 2020).

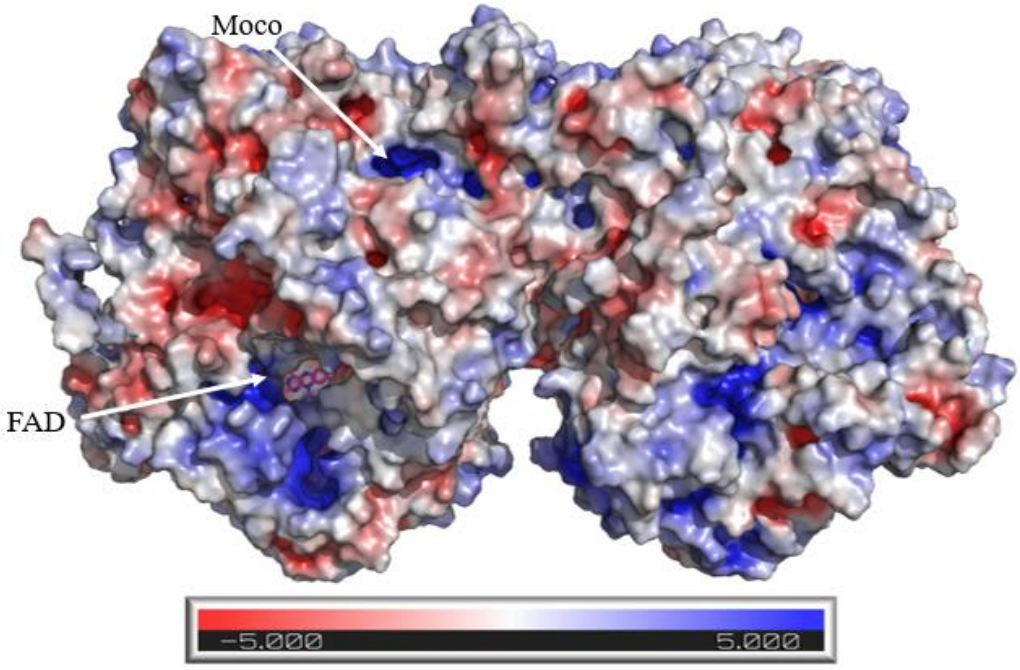

Figure 1.4: Vacuum electrostatics of the dimer unit. Electrostatic surface coloured red shows the negative regions while electrostatic surface coloured blue shows the positive regions. The figure was generated by PyMol Molecular Graphics System (Schrödinger &

1.3.2. Comparison of bovine and human XOR

Bovine XOR can be divided into three domains; the [2Fe-2S] centres which are in residues 1 to 165 in the 25 kDa amino terminal domain, the FAD in 226 to 531 bovine residues in the central 40kDa domain, and the Moco-binding site found in the carboxy-terminal 85kDa domain from 590 to 1332 residues in bovine (Terao et al., 2016).

Human XOR was structurally aligned with bovine XOR (3UNC) using PyMol Molecular Graphics System. As shown in Figure 1.5, hXOR and bovine XOR share a highly conserved structure, each with three domains in each subunit. The structural alignment of the two enzymes yielded a root-mean-square deviation (RMSD) of 0.989 Å and a match alignment of 12,235, indicating a strong structural similarity (Shamsian et al., 2023). Subtle differences in loop regions and surface were observed.

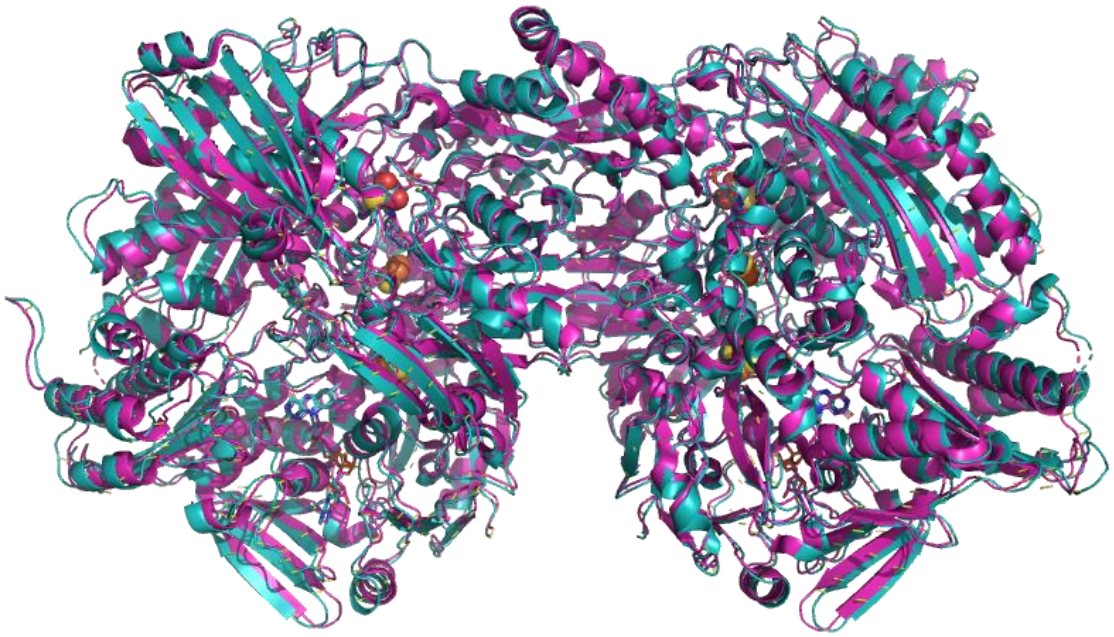

Figure 1.5: Structural based alignment of hXOR (pink) with bovine XOR (cyan). The figure was generated using PyMol Molecular Graphics System (Schrödinger & DeLano, 2020).

1.3.3. Conversion from Xanthine Dehydrogenase to Xanthine Oxidase

Mammalian XOR can occur in two interconvertible forms; the reduced form known as xanthine dehydrogenase (XDH) (EC 1.17.3.2) and the oxidised form known as xanthine oxidase (XO) (EC 1.17.1.4) (Stirpe & Della Corte, 1969; Ferdaus et al., 2025).

XOR, under physiological conditions, is mainly in the XDH form within cells such as endothelial cells, but when it is released into the blood circulation, it can be converted into the XO form (Lee et al., 2019). The conversion from XDH to XO can be either irreversible through limited proteolysis or reversible by oxidation of cysteine residues to form a disulphide bond (Nishino et al., 2005; Corte & Stirpe, 1972; Nishino, 1994). The conversion can be reversed through thiol-based reducing systems *in vivo*, including glutathione, which maintain a reducing intracellular environment (Hellsten, 2000; Cighetti et al., 1993). The irreversible and reversible conversions can take place under physiological conditions, such as lactation as well as under pathophysiological conditions, including ischemia-reperfusion injury or inflammatory tissue damage (Kusano et al., 2023; Haga et al., 2017). XDH is the predominant form in all organisms, while XO is found only in mammals (Zarepour et al., 2010; Kusano et al., 2023).

While XDH is able to reduce both oxygen and NAD^+ at the FAD reaction site, XO uses solely oxygen as a substrate in order to produce hydrogen peroxide and superoxide anion, since it is unable to catalyse the reaction with NAD^+ as substrate (Nishino, 1994; Hille & Nishino, 1995; Kuwabara et al., 2003).

The inability of XO to use NAD^+ as an electron acceptor is due to a conformational change involving a specific linker peptide loop (Gln422 – Lys432). In the oxidase form, this loop shifts position and physically blocks the NAD^+ binding channel at the FAD site, preventing NAD^+ from accessing the redox centre. This is caused by the formation of disulphide bond between Cys535 and Cys992. On the other hand, this loop is stable in the dehydrogenase form, thus preventing the obstruction of the FAD active site and allowing the interaction with both NAD^+ and oxygen molecules, even though NAD^+ is the preferred substrate (Nishino et al., 2005; Ferdaus et al., 2025). This structural change alters the size and the electrostatic environment of the cleft surrounding the FAD isoalloxazine ring. In the dehydrogenase form, the cleft is wide enough and solvent-accessible, allowing NAD^+ to bind with its nicotinamide ring oriented parallel to the isoalloxazine ring. Conversely, in the oxidase form, the cleft narrows due to the loop movement, enabling molecular oxygen to be the sole electron acceptor at the exposed isoalloxazine ring (Enroth et al., 2000).

1.3.4. Function and Catalysis of XOR

In a two-step reaction XOR firstly hydrolyses the reaction of hypoxanthine to xanthine and then xanthine to uric acid (Furuhashi, 2020). This reaction occurs at the 2-

position, where there is the addition of a carbonyl group to the ring forming xanthine. Following this, the second and slowest step occurs, where xanthine is hydrolysed at the 8-position forming uric acid (Okamoto et al., 2013) (Figure 1.6).

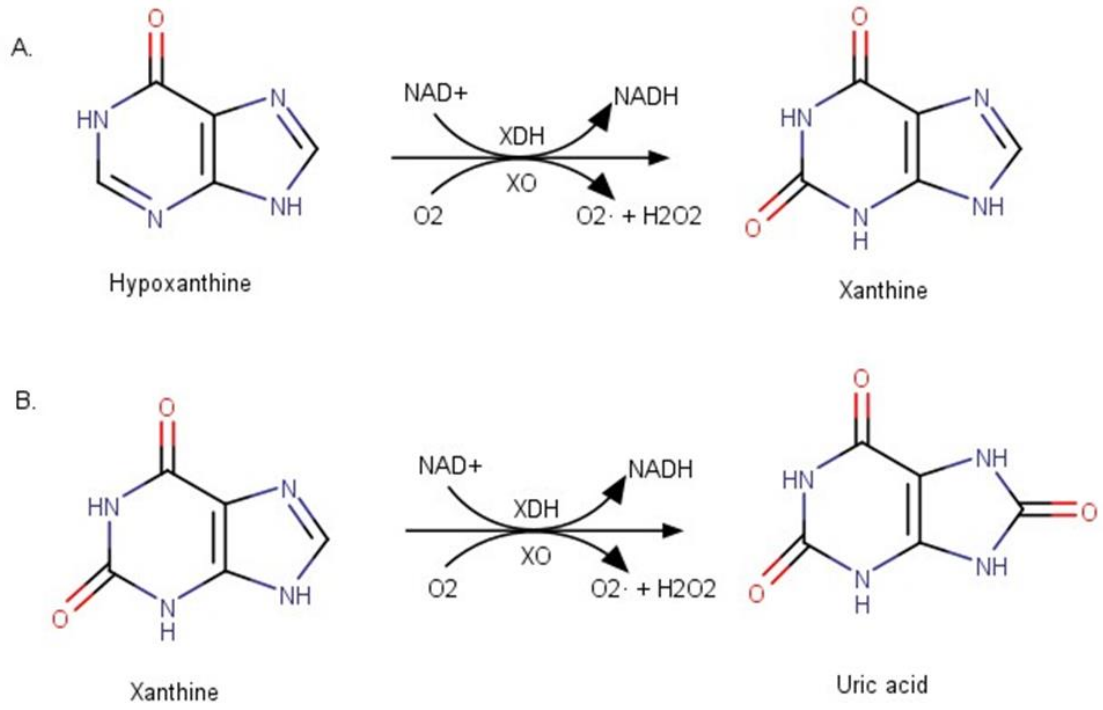

Figure 1.6: The last two steps of purine metabolism catalysed by XOR. A. The hydroxylation of hypoxanthine to xanthine and B. The hydroxylation of xanthine to uric acid. Structures drawn using MarvinSketch 19.3 (ChemAxon).

In the FAD domain, XDH reduces NAD^+ to NADH, while XO reduces oxygen from water molecules to form superoxide (O_2^-) and hydrogen peroxide (H_2O_2), both of which are known as reactive oxygen species (ROS). In more detailed, as shown in Figure 1.7, the oxidation of xanthine takes place at the Moco domain, by reducing the Mo(VI) to Mo(IV) with the donation of the electrons to the molybdenum, and subsequently to the [2Fe-2S] centres, ending at the FAD site (Nishino et al., 2008). The deprotonation of the Mo-OH by glutamic acid at Glu1261 residue initiates catalysis. When the hydroxyl group is transferred to the substrate, it creates free oxygen electron pairs that attack the electrophilic carbon, generating the hydroxylated product (Okamoto et al., 2013). The protonation of Glu1261 residue and the hydrogen bond with the N-1 atom maintain the state. This allows the nucleophilic attack on the adjacent carbon (Nishino et al., 2008).

The rate-limiting function of the enzyme ensures that the generation of the products is irreversible. This inhibits the salvage pathway, which recycles hypoxanthine to generates purines (Battelli et al., 2016 a).

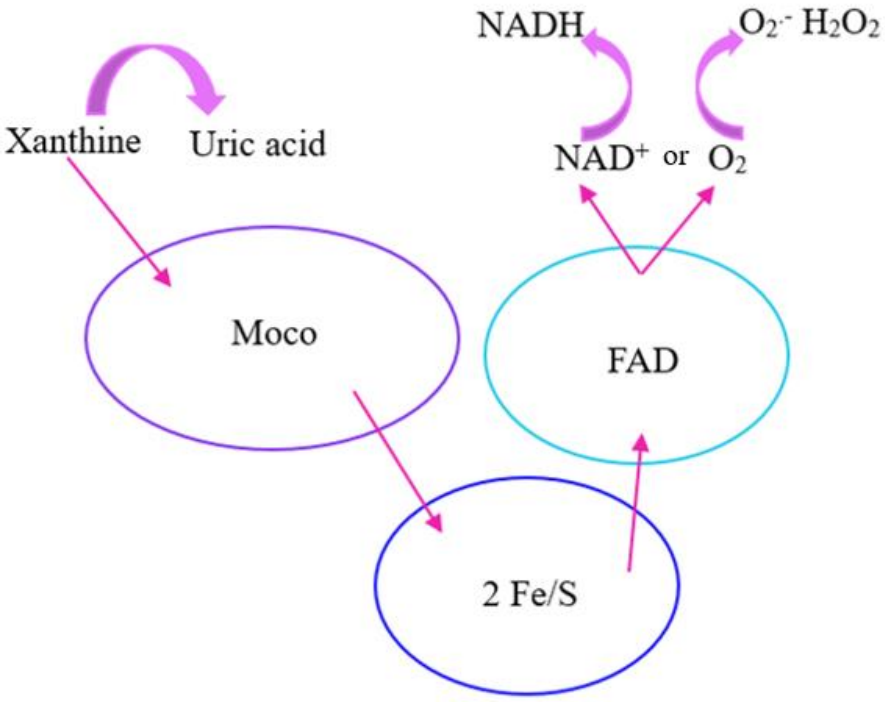

Figure 1.7: Transfer of electrons in XOR. The arrows show the electron transfer. Xanthine donates a pair of electrons at the Moco domain which move through the two [2Fe-2S] clusters to the FAD domain. The electrons are then accepted by either NAD^+ or oxygen depending on the form of the enzyme. Figure reproduced from Bortolotti et al., 2021.

1.3.5. Expression and Regulation of human xanthine oxidoreductase

The levels of human XOR are regulated during transcription and post-translation modifications. Although XOR activity is detected in all mammalian tissue, it is in small amounts due to the occurrence of repressor elements in non-coding regions (Xu et al., 2000; Berry & Hare, 2004). Even though the XOR transcription in most cells is downregulated, elevated transcription of XOR have been observed in mammary gland, intestine, liver, and kidney, and the expression levels of XOR in these cells can be elevated via low oxygen tension, growth factors, and cytokines (Battelli et al. a, 2016 a; Han et al., 2025).

Post-translational modifications include the conversions of XDH and XO forms and demolybdo- or desulpho- forms, that even though they are inactive during catalysis,

they can lead to oxidation of reduced nicotinamide adenine dinucleotide (NADH) (Battelli et al. a, 2016 a). Through these modifications, production of ROS can be elevated through the inactivation of the dehydrogenase form and enhancement of the oxidase with high oxygen tension (Terada et al., 1997; Battelli et al., 2018).

Apart from the modifications at transcriptional and post-translational levels, the activity of the enzyme can also be altered by nitric oxide (NO) that has an important role in regulating different biological processes. NO can lead to cellular damage upon the interaction with superoxide forming peroxynitrite, a highly reactive oxidant (Li et al., 2001; Li et al., 2004).

1.3.6. Xanthine Oxidoreductase and Reactive Oxygen Species (ROS)

XDH can be irreversibly or reversibly converted into the XO form in certain physiological and pathophysiological conditions, such as tissue damage caused by inflammation and under ischemic/hypoxic and reperfusion conditions (Haga et al., 2017). Ischemia is a condition where the blood supply to an organ is restricted, whereas reperfusion is the restoration of perfusion and simultaneous reoxygenation (Eltzchig & Eckle, 2011).

Under ischemic conditions, the energy in the oxygen-starved cells decreases and there is an elevation of the calcium inside the cell. This in turn, activates calpain, a calcium-dependent protease, further converting XDH to XO irreversibly. ATP is also degraded into hypoxanthine (Figure 1.8), a substrate for XO, causing an increase in the generation of ROS, specifically superoxide anion radicals and hydrogen peroxide, when the oxygen is available during reperfusion (Robert & Robert, 2014).

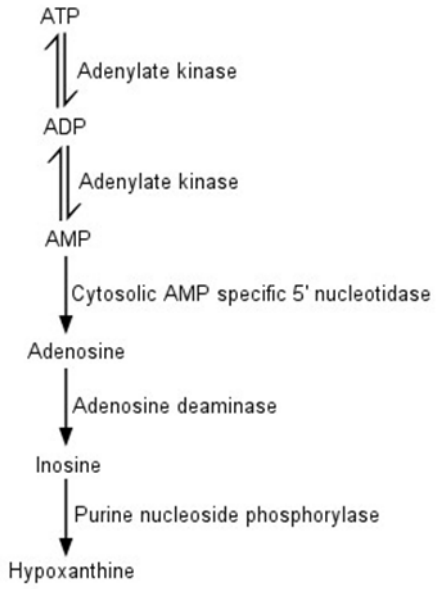

Figure 1.8: ATP catabolism pathway. Figure reproduced from Barsotti & Ipata (2004).

Inflammatory conditions, due to cytokines, such as tumour necrosis factor-alpha (TNFα), type 1 interferons (IFNs), and interleukin-1 (IL-1), and hypoxia enhance the expression of XDH, where it is converted to XO in the circulation and then it binds to negatively charged endothelial glycosaminoglycans (GAGs) (Kelley, 2015; Kany et al., 2019). This causes the amplification of local XO concentration and the production of ROS (Kelley, 2015). Sickle cell disease can cause low oxygen tension resulting in the release of XDH in the blood, increasing the amount of XO (Kotozaki et al., 2023).

XDH can produce ROS, such as superoxide anions ($O_2^{\bullet-}$), and hydrogen peroxide (H_2O_2) at the FAD site by the oxidation of NADH under hypoxic conditions transferring electrons to oxygen (Battelli et al., 2016a) (Figure 1.9). Unlike typical substrates, NADH transfers its electrons directly to the FAD centre rather than the molybdenum site, with oxygen subsequently accepting these electrons as the terminal electron acceptor (Maia et al., 2007).

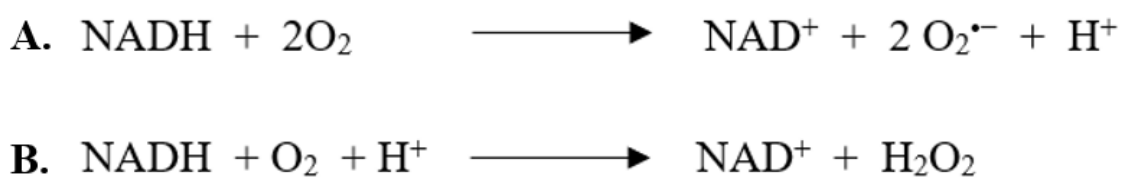

Figure 1.9: Reactions showing ROS generation from NADH oxidation by XDH at the FAD site. A. – NADH oxidation leading to the formation of superoxide anion radicals through the reduction of O_2. B. – NADH oxidation resulting in hydrogen peroxide formation via the reduction of O_2 (Vinogradov & Grivennikova, 2016).

The XO form transfers monovalent electrons to O_2 through a one-electron reduction, producing $O_2^{\bullet-}$, and divalent electrons in a two-electron reaction to O_2, generating H_2O_2 (Battelli et al., 2014; Kotozaki et al., 2023). ROS cause cytotoxicity in both pathophysiological and physiological conditions, since there is the formation of hydroxyl radicals when iron is present through the Haber-Weiss and Fenton reactions (Battelli et al., 2014; Battelli et al., 2016a). Under normal physiological conditions, and under ischemic/hypoxic conditions, hydrogen peroxide is favoured over superoxide anion, since the generation of ROS by XO are dependent on the oxygen tension, pH and the concentration of purine (Battelli et al., 2016a).

Low oxygen tension and acidic pH caused by hypoxia decrease the formation of nitric oxide (NO) by NO synthase and produce $O_2^{\bullet-}$. The formation of $O_2^{\bullet-}$ from XOR can produce reactive nitrogen species (RNS) by reacting with NO, specifically peroxynitrite ($ONOO^-$). Superoxide anion, hydroxyl, and nitric oxide radicals as well as hydrogen peroxide, and peroxynitrite, contribute to oxidative stress due to their oxidising effect (Battelli et al., 2016 b).

1.3.7. XOR and Nitrate

Nitric oxide (NO) is produced by NO synthase (NOS), in an oxidation reaction of arginine in the presence of oxygen and nicotinamide adenine dinucleotide phosphate (NADPH). NO is an intracellular, as well as an extracellular messenger able to regulate physiologic processes such as neural, immune, and cardiovascular activities (Godber et al., 2000; Andrabi et al., 2023).

NO binds to soluble guanylyl cyclase (sGC) which converts guanosine triphosphate (GTP) to cyclic guanosine monophosphate (cGMP) when it is activated. This binding enables the NO to exert its biological effect as a cell signalling molecule (Bryan, 2022).

NO acts as a vasodilator and controls hypertension by regulating the mean blood pressure. Beyond the role where insufficient NO bioavailability is implicated in hypertension linked to cardiovascular disease, it has also an important role in neurotransmission, apoptosis, immune responses. However, NO can also lead to oxidative stress that can cause cancer. The loss of NO generation by NOS in the endothelium, is known as endothelial dysfunction. This causes arterial stiffness and plaque deposition in the vessels that in turn lead to blood pressure, inflammation and oxidative stress due to the loss of regulation of blood flow (Andrabi et al., 2023; Bryan, 2022).

XOR is able to generate beneficial $NO^{\bullet}$, using xanthine or NADH as a reducing substrate, under hypoxic conditions. At the Moco domain, NO_2^- is reduced directly by xanthine to $NO^{\bullet}$, whereas NADH indirectly donates electrons to the FAD centre, which afterwards flow backwards to the Moco domain (Cantu-Medellin & Kelley, 2013).

1.3.8. Reactive Nitrogen Species

Even though NO has an important role as a vasodilator, it is also attributed with cytotoxicity during host defence, due to its ability to generate the powerful oxidant peroxynitrite ($ONOO^-$) by reacting with oxygen free radicals (Tuteja et al., 2004). NO is also highly reactive and by producing nitrogen oxides results in a lower bioavailability (Andrabi et al., 2023).

Reactive nitrogen species (RNS) are highly reactive free radicals and include peroxynitirite, nitrogen dioxide, and dinitrogen trioxide. XOR can produce $NO^{\bullet}$ and $O_2^{\bullet-}$ and cause a deficiency in NO that contribute to hypertension and atherosclerosis amongst others (Godber et al., 2000; Murad, 2006). Even though, $ONOO^-$ has a short half-life under normal pH conditions, it is still able to diffuse across cell membranes and react with molecules (Marla et al., 1997).

The highly reactive $ONOO^-$ can cause damage to cellular structures, such as mitochondria, by inactivating manganese superoxide dismutase (MnSOD) enzyme. This enzyme protects mitochondria from oxidative stress (Marla et al., 2007; Li & Zhou, 2011; MacMillan-Crow et al., 1996). Nitration induced by $ONOO^-$ modifies tyrosine residues

and oxidises cysteine residues in membrane channels, impairing ionic balance in cells (MacMillan-Crow et al., 1996; Ghosh et al., 2013).

1.4. Disease states related to Xanthine Oxidoreductase

1.4.1. Hyperuricemia related to Hypertension

Uric acid (7, 9-dihydro-1H-purine-2,6,8 (3H)-trione) is a heterocyclic organic compound with the formula $C_5H_4N_4O_3$ (Liu et al., 2021) and is the final product of purine degradation. Around 70% of uric acid is excreted in urine and 30% from the gastrointestinal route. An overproduction or under-excretion of uric acid can cause hyperuricemia (Chen et al., 2016).

In humans and higher primates, serum uric acid levels are higher compared to other mammals, since it is not degraded to allantoin, due to variants in the uricase gene that rendered it nonfunctional (Watanabe et al., 2002; Ndrepepa, 2025). Uric acid has both antioxidant and pro-oxidant properties, and it can also regulate sodium retention and blood pressure. However, high serum uric acid levels pose a risk for various diseases, such as cardiovascular diseases, gout, and atherosclerosis (Sekizuka et al., 2022; Chen et al., 2016). Hyperuricemia may be caused by increased consumption of alcohol, purine-rich foods, amongst others, that cause an elevated production of uric acid (Chen et al., 2016). Renal dysfunction and certain medications cause the underexcretion of uric acid from the kidney might also result in hyperuricemia (Chen et al., 2016).

Uric acid scavenges carbon-centred radicals and peroxyl radicals, including peroxynitrite ($ONOO^-$) under hydrophilic conditions. On the other hand, in a hydrophobic environment, uric acid becomes a strong pro-oxidant, causing inflammation, oxidative stress, and endothelial dysfunction (Chen et al., 2016; Sautin & Johnson, 2010).

Hyperuricemia is associated with cardiovascular diseases, obesity and metabolic conditions, including hypertension, and insulin resistance, due to the pro-oxidant activity that can decrease the bioavailability of NO (Furuhashi, 2020; Battelli et al., 2018).

Studies suggest that the potential mechanism of uric acid-induced hypertension, is the induction of oxidative stress by uric acid, that causes a decrease in the availability of endothelial NO. This in turn activates the plasma renin and intra-kidney angiotensin activity, which leads to vasoconstriction, ischemia, and oxidative stress in the kidneys. This activates the immune system causing persistent kidney vasoconstriction and

hypertension (Sanchez-Lozada et al., 2020). Uric acid can also induce hypertension by activating NADPH oxidase and consequent cellular oxidative stress (Battelli et al., 2018).

The elevated serum uric acid levels have been also associated with polymorphisms of the XOR. An increased generation of reactive oxygen species (ROS) has been linked to variants of XOR that have been implicated with increased risk of hypertension (Cuevas et al., 2019).

1.4.2. Xanthine Oxidoreductase Variants linked to Diseases

Various variants in the gene encoding XOR may lead to different diseases and disorders, since they may influence the regulation and function of the enzyme, resulting in altered levels of purines and their metabolites (Ichida et al., 2012).

A Japanese population study identified three missense variants in XDH gene, specifically G172R, A932T, and N1109T, that are associated with hypertension in a heterozygous state. The A932T and N1109T variants are located in the conserved functional domain, where the binding of the molybdopterin takes place. However, G172R variant is not found in the functional domain, but it is present between the Fe_2S_2 centres and the FAD domain, since 1 to 166 amino acids are in the Fe_2S_2 centres and 228 to 542 amino acids are found in the FAD domain in hXOR (Seychell, 2019). Patients harbouring the A932T or the N1109T variant were observed to be associated with high blood pressure, indicating that these two variants might be functional risk factors for hypertension (Yang et al., 2008).

From this study it was also observed that certain patients harboured the G172R or the N1109T variant in the homozygous state. These individuals had a more severe form of hypertension compared to other individuals with variants in the heterozygous form. They were diagnosed with resistant hypertension that remained untreated even with antihypertensive medication (Yang et al., 2008).

Furthermore, it was also showed that N1109T variant was positively correlated with hypertension in men, indicating that this variant might increase the risk of hypertension in men (Yang et al., 2008).

In another study, three single nucleotide polymorphisms (SNP), associated with hypertension, were identified, rs2043013, rs11904439, and rs148756340. These three SNPs are intron variants and the presence of any of these in an individual appeared to increase the susceptibility of hypertension (Scheepers et al., 2016).

Moreover, a further three SNPs were identified in the rural Han Chinese population that are associated with hypertension, specifically rs1042039, rs1054889, and rs2073316. These may be linked to essential hypertension (Wu et al., 2015).

Apart from hypertension, other variants appeared to be associated with other conditions, as well as low and high enzymatic activity. For instance, seven variants, p.R149C, p.R228X, p.K722X, p.T910K, p.T910M, c.2567del1 and c.1664dup1, are associated with classical xanthinuria type I, whereas five variants lead to low enzymatic activity, specifically p.P555S, p.R607Q, p.T623I, p.N909K, p.R1150P, p.C1318Y. On the contrary, two variants are associated with high activity, i.e. p.I703V and p.H1221R (Stiburkova et al., 2012; Sakamoto et al., 2001).

1.4.2.1. hXOR I646V and I703V variants

An elevated enzymatic activity is usually caused by variants located at the active sites or at the surface close to the active sites. These variants might cause an increased enzymatic activity due to an increased in the maximal reaction rate, V_{max} (Ichida et al.,2012).

In the Maltese Acute Myocardial Infarction Study (MAMI) conducted by *Attard et al.*, 2021, several already known variants as well as novel variants were detected within the Maltese population. These variants were associated with elevated uric acid levels. Amongst these variants were known variants I646V and I703V (Prof Stephanie Bezzina Wettinger, personal communication), where the amino acid isoleucine is substituted to valine at position 646 and 703, respectively. In the cohort they were found both in the heterozygous as well in the homozygous. These variants are going to be further characterised in this study. Positions 646 and 703 are located at the surface of the hXOR, close to the Moco domain. Even though isoleucine and valine have similar amino acid properties, it was identified from previous studies done in the Protein Science and Biochemistry laboratory (University of Malta) that both variants cause an increase in the activity of hXOR.

1.4.2.2. Comparison of variants in hXOR and bovine XOR

A notable difference between the human and bovine XOR sequences is observed around the region of Ile646. In the bovine enzyme, a glutamic acid is present at position 645 instead of an isoleucine at position 646 in the human enzyme (Figure 1.10). This

substitution introduces additional interactions, as Glu645 forms three specific contacts with Ser643, Asn650, and Lys779, as shown in Figure 1.11.

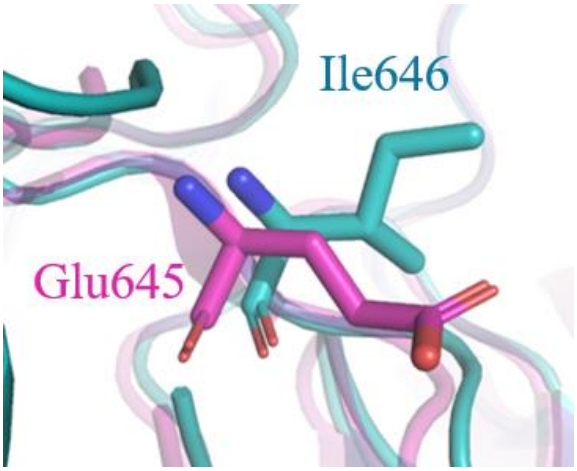

Figure 1.10: Ile646 hXOR and Glu645 bovine XOR aligned. Cyan – Ile646 hXOR, Pink – Glu645 bovine XOR. The figure was generated by PyMol Molecular Graphics System (Schrödinger & DeLano, 2020).

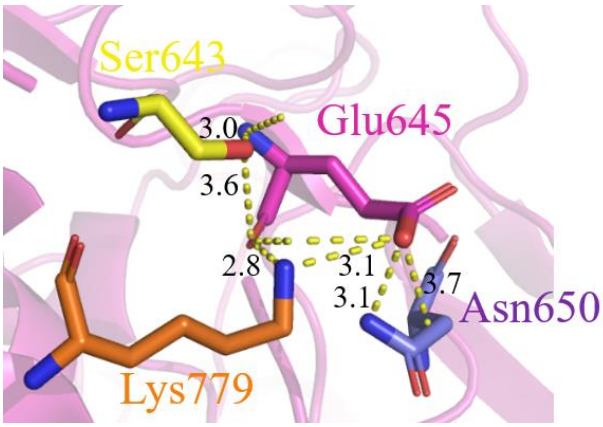

Figure 1.11: Interactions of the residue Glu645 with the surrounding residues. The figure was generated by PyMol Molecular Graphics System (Schrödinger & DeLano, 2020).

Another difference is observed for the Ile703 residue in human XOR, which corresponds to Ile702 in the bovine enzyme. In the bovine structure, Ile702 is involved in interactions with Ile698 and Asn705 (Figure 1.12). However, apart the positional shift of the amino acid there is no significant difference between this residue in the bovine and human XOR structures.

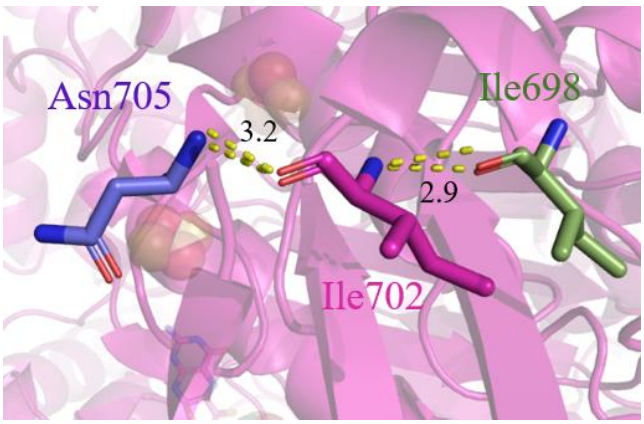

Figure 1.12: Interactions of the residue Ile702 with the surrounding residues. The figure was generated by PyMol Molecular Graphics System (Schrödinger & DeLano, 2020).

Human and bovine XOR sequences were aligned using EMBOSS-EBI shown in Figure 1.13 (Madeira et al., 2024).

```
EMBOSS_001      601 ENELSLRLVTSTRAHAKIKSIDTSEAKKVPGFVCFISADDVPGSNITGIC    650
                    ||||.||||||||||||||||.|||:||||||||:||||:|||||.||:.
EMBOSS_001      600 ENELFLRLVTSTRAHAKIKSIDVSEAQKVPGFVCFLSADDIPGSNETGLF    649

EMBOSS_001      651 NDETVFAKDKVTCVGHIIGAVVADTPEHTQRAAQGVKITYEELPAIITIE    700
                    |||||||||.||||||||||||||||||.:|||..||:|||:||||||||
EMBOSS_001      650 NDETVFAKDTVTCVGHIIGAVVADTPEHAERAAHVVKVTYEDLPAIITIE    699

EMBOSS_001      701 DAIKNNSFYGPELKIEKGDLKKGFSEADNVVSGEIYIGGQEHFYLETHCT    750
                    ||||||||||.||||||||||||||||||||||:|||||:|||||||||
EMBOSS_001      700 DAIKNNSFYGSELKIEKGDLKKGFSEADNVVSGELYIGGQDHFYLETHCT    749
```

Figure 1.13: Human and bovine XOR alignment. Amino acids in red box represent the position of the Ile646 (top) and Glu645 (bottom), while the amino acids in the blue box represent the position of the Ile703 (top) and Ile702 (bottom) in human and bovine XOR respectively.

1.5. Inhibitors of XOR

As already mentioned, XOR is implicated in several pathological conditions, including gout, cardiovascular diseases, and hypertension (Sekine & Ichida, 2025; Attard et al., 2021). Since certain high-activity variants of XOR appear to be associated with hypertension, XOR inhibitors may be considered for treatment. Currently, clinically approved XOR inhibitors such as allopurinol, febuxostat, and topiroxostat, effectively

reduce uric acid formation and have also shown benefits in managing hypertension (Bove et al., 2017; Sekine & Ichida, 2025).

1.5.1. Allopurinol

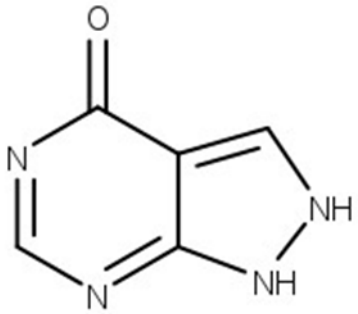

Figure 1.14: Allopurinol

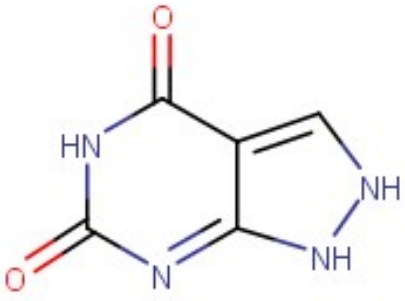

Figure 1.15: Oxypurinol

Allopurinol, also known as 1,5-dihydro-4*H*-pyrazolo[3,4-*d*]pyrimidin-4-one, was the first xanthine oxidoreductase inhibitor (XOI) drug discovered in the drug discovery program at Burroughs Wellcome by Gertrude B. Elion and George H. Hitchings (Pacher et al., 2006). Allopurinol is used as an antigout drug and for the treatment of conditions related to hyperuricemia, specifically primary and secondary hyperuricemia, since it lowers the levels of uric acid in the blood (Sekine et al., 2023; Pacher et al., 2006). Since XOR catalyses the last two steps of purine catabolism, allopurinol can control the levels of uric acid in serum and urine as it is an analogue of hypoxanthine (Pacher et al., 2006; Sekine et al. 2023). Allopurinol is hydroxylated by oxidation to oxypurinol at the molybdenum centre in the XOR, as the reaction of hydroxylation of purines takes place, resulting in the reduction of the active site molybdenum centre from Mo(VI) to Mo(IV), inhibiting the synthesis of uric acid (Sekine et al., 2023; Chen et al., 2016).

Hyperuricemia might cause hypertension through the upregulation of the renin-angiotensin-aldosterone system, oxidative stress and endothelial dysfunction (Macdonald et al., 2024). Hypertensive patients with hyperuricemia have an increased risk of coronary or cerebrovascular disease (Agarwal et al., 2012). Since allopurinol inhibits the synthesis of uric acid, studies showed that the reduction of uric acid decreased the risk of adverse cardiovascular events (Macdonald et al., 2024). Allopurinol is also associated with a

significant decrease in systolic blood pressure and it might have other effects on blood pressure independent of the reduction in urate (Agarwal et al., 2012; Macdonald et al., 2024).

Even though, allopurinol is the most prescribed drug for the treatment of gout, it has various side effects. The most dangerous side effects are life threatening hypersensitivity reactions, such as toxic epidermal necrolysis (TEN) and Stevens-Johnson syndrome (SJS) (Dillman et al., 2024; Chen et al., 2016). Moreover, asymptomatic hyperuricemia, and other related cardiovascular diseases cannot be treated by allopurinol, due to its side effects. Asymptomatic hyperuricemia occurs when the uric acid levels are high without any signs of uric acid crystal deposition diseases (Chen et al., 2016).

Tumour lysis syndrome (TLS) is a condition that occurs in hematologic cancer patients and it arises when the tumour cells burst, resulting in the release of phosphate, potassium, and uric acid in the blood, as well as acute renal failure (Mahfooz et al., 2023; Alakel et al., 2017). Allopurinol lowers the formation of uric acid but it has no effect on the current uric acid levels (Mahfooz et al., 2023). In another words, allopurinol is incapable of lowering preexisting uric acid levels, consequently elevating the levels of both hypoxanthine and xanthine in serum which might cause xanthine nephropathy. For this reason, allopurinol should only be used in low or intermediate risk for TLS (Alakel et al., 2017).

1.5.2. Febuxostat

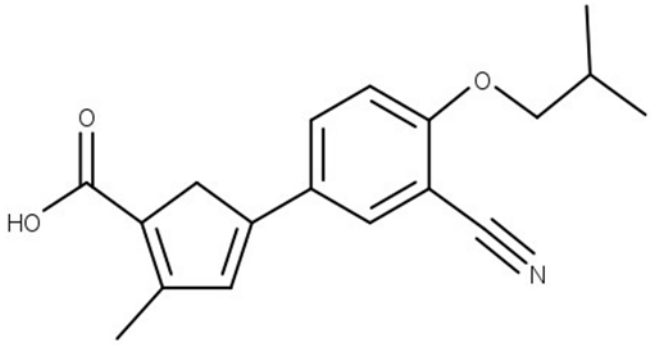

Figure 1.16: Febuxostat

Febuxostat, 2-(3-cyano-4-(2-methylpropoxy)phenyl)-4-methylthiazole-5-carboxylic acid, is a novel, selective, and potent non-purine XO inhibitor for the treatment hyperuricemia and gout (Takano et al., 2005). This drug acts as a structure-based

inhibitor, by ionic bonding of the carboxylic group with Arg880, and hydrogen bonding of nitrogen of thiazole with Glu802. Febuxostat fills most of the binding pocket of XOR (Kikuchi et al., 2012).

Febuxostat inhibits only xanthine oxidase or xanthine dehydrogenase, unlike allopurinol, and not any other enzymes found in metabolic pathways (Kraev et al., 2023). It is more effective in blocking the production uric acid and ROS, since it inhibits both oxidised Mo (VI) and reduced Mo (IV) forms of XOR (Chen et al., 2016; Noda et al., 2023). By inhibiting XO, febuxostat impedes the conversion of hypoxanthine and xanthine to uric acid, thereby reducing the production of uric acid in the body. This lowers the serum uric acid levels (Kraev et al., 2023).

Febuxostat is less toxic and has greater hypouricemic activity compared to allopurinol. However, febuxostat, similarly to allopurinol, is associated with hypersensitivity reactions, including SJS and anaphylactic shock, but it has higher occurrence of hepatotoxicity, and rhabdomyolysis. For these adverse effects, febuxostat is not used for the treatment of asymptomatic hyperuricemia (Chen et al., 2016).

1.5.3. Topiroxostat

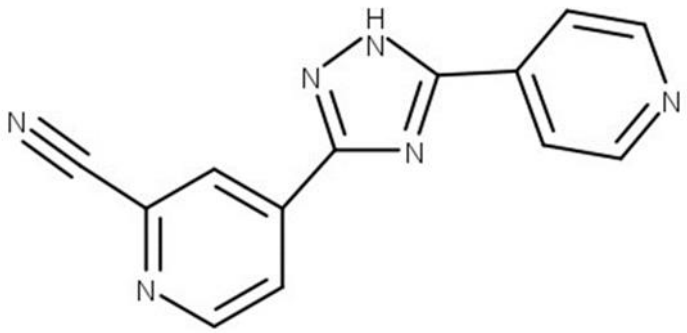

Figure 1.17: Topiroxostat

Another XOR inhibitor is a non-purine drug, called topiroxostat [4-[5-(4-Pyridinyl)-1H-1,2,4-thiazol-3-yl]-2-pyridinecarbonitrile]. It was approved in Japan for the treatment of gout and hyperuricemia (Hosoya et al., 2016). Topiroxostat reduces the production of uric acid, in a chemical structure-based inhibition of XO. Unlike febuxtostat, topiroxosat interacts with amino acid residues of the solvent channel, and, like allopurniol, binds through oxygen to molybdenum via covalent bonds in the hydroxylation reaction intermediate (Hosoya et al., 2014; Igel et al., 2019). Topiroxostat

inhibits both structurally and mechanistically, displaying high affinity and stable binding to the enzyme (Noda et al., 2023).

Even though, in animals it has high bioavailability and safety, the adverse effects in humans are still unknown (Chen et al., 2016). Topiroxostat exerts milder hypouricemic effect compared to febuxostat (Li et al., 2024). There are no serious side effects linked to topiroxostat when compared with placebo (Igel et al., 2019).

1.6. Aims and Objectives

The recent MAMI study in the Maltese population identified already known variants as well as novel variants, specifically I646V and I703V. It was also identified that certain cases harboured both variants. According to data collected as part of this study, preliminary studies show that singly each variant is associated elevated uric acid levels (Prof Stephanie Bezzina Wettinger, Dr Francesca Carabott, personal communication). Preliminary *in silico* structural bioanalysis indicated that the I646V and I703V variants are located close to the active site of XOR, potentially altering its activity and ROS production.

Recent research also shows that XOR can form filaments under different experimental conditions. Filament formation might indicate some kind of enzymatic regulation related to the localisation of XOR especially since in endothelial cells, the protein also occurs extracellularly anchored to the cell surface to heparin proteoglycan. This is significant because during reperfusion, the influx of highly oxygenated blood can activate XOR, increasing ROS levels in the bloodstream and triggering a cascade of adverse reactions (Seychell, 2019).

The hypothesis is that I646V and I703V variants lead to altered enzymatic activity, increased ROS production and increased uric acids levels.

This project aims to investigate the impact of two specific variants, I646V and I703V, on the enzymatic activity, stability and oligomer formation, comparing single variants of each, and the double variant with the wild type XOR.

To reach these aims, the following objectives will be undertaken. First, the variants will be produced from the pTrcHis-hXOR clone via site-directed mutagenesis using polymerase chain reaction (PCR). Following PCR, Sanger-sequencing will be done to confirm the variants. Subsequently, XOR wild type, as well as the singly and doubly mutated variants will be transformed into *E. coli* TP1000 cells and cultured under

optimised conditions. The cultures will be then harvested using centrifugation and lysed. Cell fractionation will then be carried out. Clarification via centrifugation will be used to remove any insoluble and/or misfolded proteins. The soluble recombinant proteins will then be purified using immobilised metal affinity chromatography. SDS-Page gel electrophoresis will be performed to check the purity and yield of the sample obtained. Native-Page electrophoresis will be used to assess quality of the samples. The purified XOR proteins will be characterised for activity, stability and structure. XOR activity will be measured spectrophotometrically using the uric acid assays. XOR stability will be measured using circular dichroism temperature ramps. XOR structure will be investigated using circular dichroism, and dynamic light scattering. Thioflavin T (ThT) assay will also be used to examine the fibrils formed in the protein samples.

Chapter 2 Methodology

2.1. Materials

2.1.1. General chemicals

Acetic acid, ammonium persulfate (APS), glycine, isopropyl alcohol, magnesium chloride, methanol, sodium hydroxide and tris(2-carboxyethyl)phosphine hydrochloride (TCEP) were bought from VWR chemicals. 1,4-dithiothreitol (DTT), ethylenediaminetetraacetic acid (EDTA), glycerol, nitro blue tetrazolium chloride (NBT), tetramethylethylenediamine (TEMED), tris base and xanthine were purchased from Sigma Aldrich/Merck. Bacterial agar, tryptone, and yeast extract were purchased from Oxoid. di-Sodium hydrogen phosphate anhydrous (Na_2HPO_4), sodium dihydrogen phosphate anhydrous (NaH_2PO_4), sodium dodecyl sulphate (SDS), magnesium chloride were Fluka molecular biology grade. Sodium chloride (NaCl) was Biochem Chemopharma. Isopropyl-β-D-thiogalactopyranoside and Ampicillin Sodium were Apollo Scientific. Chemicals not listed here were purchased from Sigma Aldrich/Merck unless otherwise stated. Unless specified, water was deionised following reverse osmosis treatment.

2.1.2. General Buffers

All buffers and solutions were prepared according to Table 2.1. All solutions were sterilised by autoclaving at 121°C and 15 psi for 20 minutes unless otherwise stated.

Table 2.1: List of buffers and solutions

Buffer/Solution	**Composition of working solution**
General Buffers	
10x PBS	1.37 M NaCl 27 mM KCl 100 mM Na_2HPO_4 anhydrous 18 mM KH_2PO_4
500 mM Sodium Phosphate Buffer pH 7.4 (NaP)	Ratio of 19:81, NaH_2PO_4 : Na_2HPO_4 anhydrous

1 M HEPES pH 8.0	25 mL of 50 mM HEPES pH was adjusted to 8.0 with sodium hydroxide pellets dH_2O adjusted to 500 mL Solution was filtered with a 0.2 µm filter.
5 M Sodium Chloride	146.1 g Sodium Chloride Deionised H_2O to a final volume of 500 mL
Transformation and Expression	
Agar	3.75 g bacterial agar 2xTY media adjusted to 200 mL
Ampicillin	4 g ampicillin Na salt Deionised H_2O adjusted to 40 mL. Solution was filtered with a 0.2 µm filter.
IPTG	2.38 g IPTG Deionised H_2O adjusted to 10 mL. Solution was filtered with a 0.2 µm filter.
2xTY media	16g/L tryptone 10g/L yeast extract 5 g/L NaCl in deionised H_2O
Chromatography	
Buffer A	50 mM HEPES pH 8.0 (25 mL of 1 M stock) 500 mM NaCl (50 mL of 5 M stock) Deionised H_2O adjusted to 500 mL
Buffer B	50 mM HEPES pH 8.0 500 mM NaCl 1 M imidazole
Start buffer	10 mM imidazole, 50 mM HEPES pH 8, 500 mM NaCl
Strip Buffer	100 mM EDTA (5 mL of 1 M) in Buffer A to a final volume of 50 mL
0.5 M TCEP	5.73 g TCEP-HCl

	pH was adjusted to 7.0 dH_2O topped up to 40 mL
Buffer Exchange	
Dialysis Buffer	50 mM NaP 150 mM NaCl dH_2O topped it up to 2 L
Dialysis tubing	8g $NaHCO_3$ Deionised H_2O adjusted to 400 mL
Protein Analysis	
10x Tris-Glycine running Buffer	151 g tris 720 g glycine Deionised H_2O adjusted to 5 L final volume
Blue Native-PAGE running buffer	20x Native PAGE running buffer (10 mL) (Thermo scientific) 20x Native PAGE cathode buffer additive (10 mL) (Thermo scientific) dH_2O to a final volume of 200 mL
Blue Native-PAGE anode buffer	20x Native PAGE running buffer (50 mL) Deionised H_2O topped up to 1 L
Protein Characterisation	
Circular Dichroism Dialysis Buffer	10 mM sodium phosphate buffer, pH 7.4 50 mM Na_2SO_4 Deionised H_2O to a final volume of 3 L

2.1.3. *E. coli* Bacterial strains

2.1.3.1. XL-1 Blue Cells

XL-1 Blue cells (originally purchased from Stratagene) are deficient in endonuclease and recombination genes, denoted by the *endA1* and *recA1* genes. These cells were used for the extraction of plasmid DNA. Competent XL-1 Blue cells were transformed with WT hXOR plasmid DNA or hXOR I646V plasmid DNA or hXOR

I703V plasmid DNA or hXOR 1646V-I703V plasmid DNA or hXOR I646A plasmid DNA for the extraction of DNA.

Genotype: *recA1 endA1 gyrA96 thi-1 hsdR17 supE44 relA1 lac [F' proAB lacIq ZΔM15 Tn10 (Tet1)].*

2.1.3.2. TP1000 cells

TP1000 cells (provided by Professor Tracy Palmer) are derived from the parental strain of MC4100 cells. In these cells, the *mobA* and *mobB* genes were replaced by a kanamycin resistant gene (denoted by *ΔmobAB::Kan* in the genotype). This mutation stops the conversion of molybdopterin-to-molybdopterin guanine dinucleotide. This allows the molybdopterin to bind with molybdenum, forming the molybdenum cofactor (Moco) and to be incorporated into the protein.

Genotype: *ΔmobAB::Kan [F′ araD139]B/r, Del(argF-lac)169, lambda-, e14-, flhD5301, Δ(fruK-yeiR)725(fruA25), relA1, rpsL150(strR), rbsR22, Del(fimB-fimE)632(::IS1), deoC1]*

The plasmid encoding hXOR, pTrc99a-hXOR, was donated by Professor Arwen Pearson. An N-terminal 6xhistidine tag was incorporated into the clone by Dr Brandon Seychell. The modified plasmid was designated pTrcHis-hXOR (Figure 2.1).

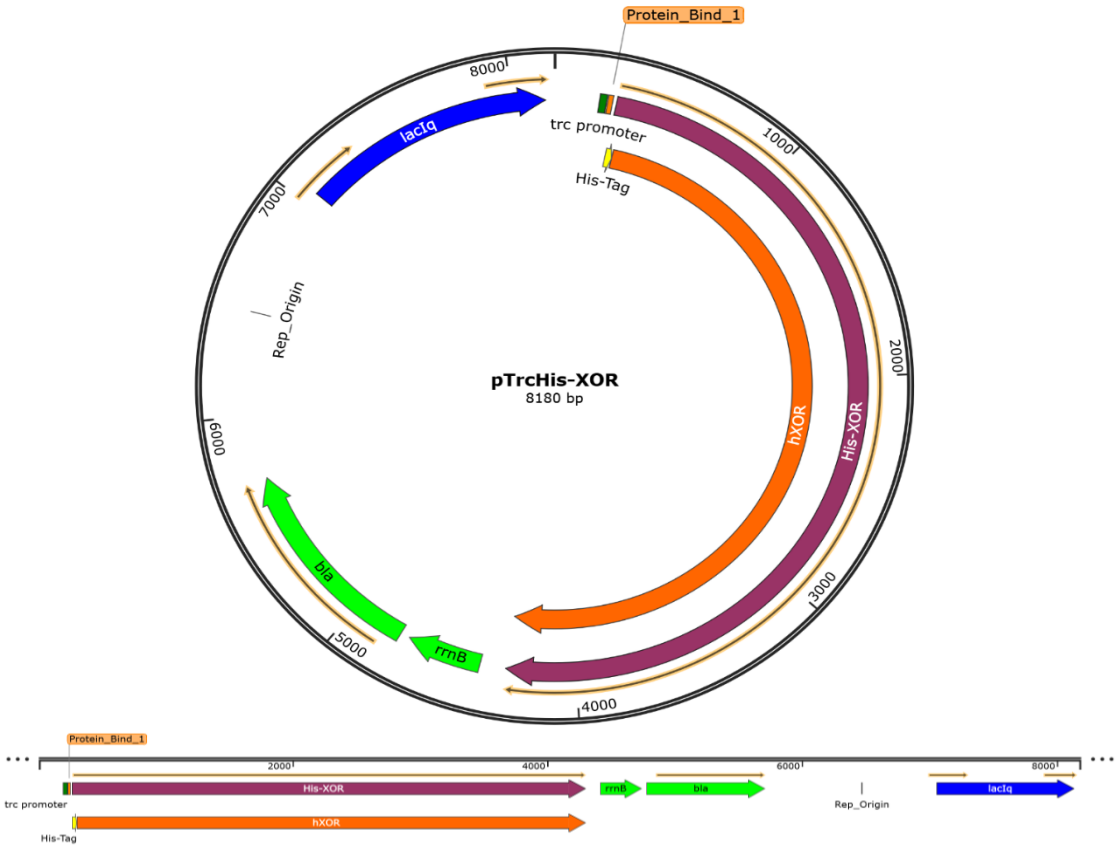

Figure 2.1: pTrcHis-hXOR plasmid map. Reproduced using SnapGene® software (from Dotmatics; available at snapgene.com).

2.2. Recombinant DNA Methodology

2.2.1. Transformation of XL-1 Blue competent cells

XL-1 Blue competent cells were thawed on ice, and once thawed, 10 ng of plasmid DNA (pTrcHis-hXOR WT, I646V, I703V, I646V-I703V or I646A), was added to 100 µL XL-1 cells. Subsequently, the cells were left on ice for 35 minutes and heat-shocked for 45 seconds in a heat block at 42˚C. 2xTY (300 µL) was added, and the cells were placed in the water bath at 37˚C for 1 hour. The transformed cells were spread on agar plates supplemented with 100 µg/mL ampicillin and incubated overnight at 37˚C (Sambrook et al., 2012).

2.2.2. Isolation of Plasmid DNA

Plasmid DNA was extracted from XL-1 Blue transformants using the ZR Plasmid Miniprep^{TM}-Classic (Zymo Research) following the manufacturer's instructions. The concentration of the DNA was measured at A260 and the ratio of A260/A280 and

A260/A230 were measured using the Eppendorf BioSpectrometer® kinetic. The quality of purified DNA was assessed through agarose gel electrophoresis.

2.2.3. Agarose gel electrophoresis

The 0.7 % (w/v) agarose gel was prepared by adding 0.7 g of agarose in 100 mL of TAE buffer (20 mM Tris base, 1.14% (v/v) glacial acetic acid, 10 mM EDTA). The solution was boiled and left to cool. Once it cooled to roughly 50˚C, it was poured into a casting tray with a well comb. Once the gel had solidified, TAE buffer was poured into the casting tray. The samples were then loaded with a 1:5 of loading dye to DNA solution (10x loading dye composed of 20% (w/v) Ficoll 400, 1% (v/v) SDS, 20% (v/v) 0.5M EDTA, 0.25% (w/v) bromophenol blue, 0.25% (w/v) xylene cyanol). Electrophoresis was carried out at a constant voltage of 75 V until the dye front reached two thirds of the gel. The gel was then stained with ethidium bromide, destained in water and visualised using a ChemiDoc™ Imaging System (Bio-Rad).

2.2.4. Lambda *Hind*III DNA preparation

To 1 μg of lambda (λ) DNA, 1 μL (10 units) of *Hind*III restriction enzyme in SuRE/Cut™ Buffer B (Sigma-Aldrich) was added and incubated for 2 hours at 37ºC. The digested fragments were utilised as a molecular weight standard for agarose gel electrophoresis.

2.2.5. Restriction digest of plasmid DNA

The pTrcHis-WT hXOR and I646V plasmids DNA were linearized by double digestion using *SalI* or *EcoRV* restriction enzymes for 2 hours at 37°C in SuRE/Cut^{TM} Buffer H and B, respectively. *Sal*I was expected to cut the DNA at position 4307 while *Eco*RV was expected to cut the DNA at position 7859 (Figure 2.2). The composition of the reaction mix of each restriction digest is shown in Table 2.2.

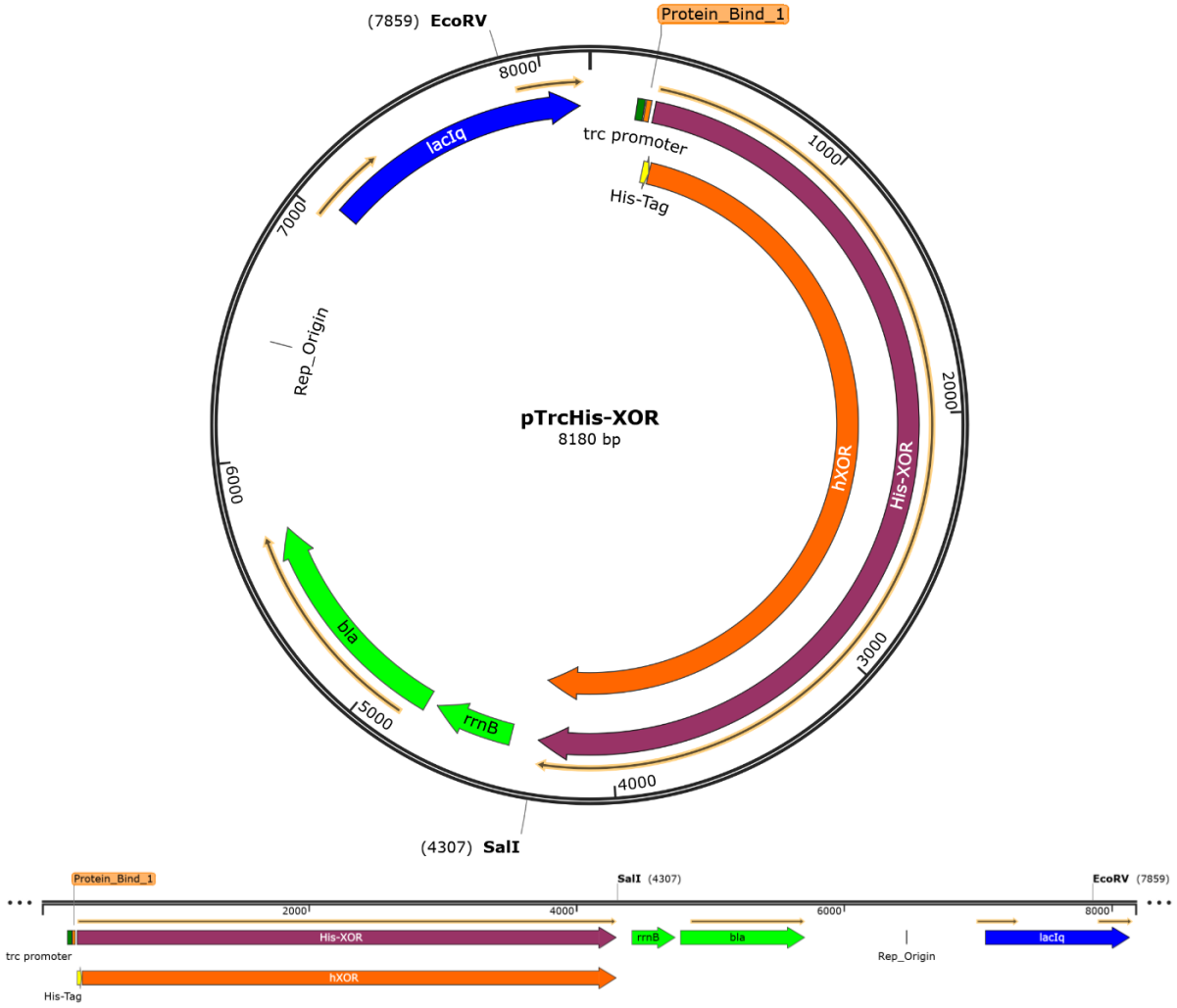

Figure 2.2: Restriction enzymes SalI and EcoRV cleavage sites on pTrcHis-hXOR plasmid map.

Table 2.2: Table summarising the reactants, and the volumes, involved in the restriction digest reactions 1, 2, 3, and 4

Reaction 1		Reaction 2		Reaction 3		Reaction 4	
Reactants	Volume (µL)	Reactants	Volume (µL)	Reactants	Volume (µL)	Reactants	Volume (µL)
pTrcHis-WT hXOR DNA (100 ng/µL)	2	pTrcHis-WT hXOR DNA (100 ng/µL)	2	PTrcHis-hXOR I646V DNA(180 ng/µL)	1.1	pTrcHis-hXOR I646V DNA(180 ng/µL)	1.1
10X Buffer H	2	10X Buffer B	2	10X Buffer H	2	10X Buffer B	2
Deionized Water	15	Deionized Water	15	Deionized Water	15.8	Deionized Water	15.8
*Sal*I	1	*Eco*RV	1	*Sal*I	1	*EcoR*V	1

Agarose gel electrophoresis (0.7%) was then used to assess the DNA fragments produced by the restriction digest.

2.2.6. DNA oligonucleotides

The primers required for the mutagenesis were designed according to the instructions of the QuikChange II XL site-directed mutagenesis kit and they were synthesised by Humanizing Genomic Macrogen Europe. The sequences of the primers are listed in Table 2.3.

Table 2.3: Primers

Primer name	Primer Sequence (5' → 3')	N	GC ratio/ %	T_M/ °C
hXOR_I646A_FOR	GATGATGTTCCTGGGAGTAACG CAACTGGAATTTGTAATGATGA G	45	42.2	79.4
hXOR_I646A_REV	CTCATCATTACAAATTCCAGTTG CGTTACTCCCAGGAACATCATC	45	42.2	79.4
hXOR_I646V_FOR	GATGTTCCTGGGAGTAACGTAA CTGGAATTTGTAATG	37	40.5	77.2
hXOR_I646V_REV	CATTACAAATTCCAGTTACGTTA CTCCCAGGAACATC	37	40.5	77.2
hXOR_I703V_FOR	CATTATCACAATTGAGGATGCTG TAAAGAACAACTCCTTTTATGG	45	35.6	78.9
hXOR_I703V_REV	CCATAAAAGGAGTTGTTCTTTAC AGCATCCTCAATTGTGATAATG	45	35.6	78.9

2.2.7. *In-vitro* site-directed mutagenesis

In-vitro site-directed mutagenesis was done via the QuikChange II XL Site-Directed Mutagenesis Kit (Stratagene). The pTrc-His-hXOR I646V clone (available in laboratory) was used as the template for both reactions of the *in vitro* site-directed mutagenesis, specifically I646V-I793V and I646A. The reaction mixture was prepared as shown in Table 2.4. The PCR parameters used for Tprofesional Thermocycler (Biometra) PCR machine are described in Table 2.5.

Table 2.4: Components of the in-vitro site-directed mutagenesis reaction

Reagent	Amount
10x reaction buffer	5 µL
DNA template	10 ng
Forward primer	125 ng
Reverse primer	125 ng
dNTP mix	1 µL
QuickSolution	3 µL
ddH_2O	Top up to 50 µL
2.5 U/µL *Pfu*Ultra HF DNA polymerase	1 µL

Table 2.5: QuikChange XL cycling parameters

Segment	Cycles	Temperature/ºC	Time
1	1	95ºC	1 minute
2	18	95ºC	50 seconds
		60ºC	50 seconds
		68ºC	1 minute/ kb of plasmid length
3	1	68ºC	7 minutes

Following the amplification reaction, 1 µL of *Dpn*I was added and aspirated gently. The solution was then centrifuged for 1 minute and incubated at 37°C. From this solution, 2 µL were used to transform competent XL-1 cells. The transformants were next cultured for subsequent plasmid DNA extraction and DNA sequencing.

2.3. Human XOR Expression and Purification

2.3.1. TP1000 transformation

TP1000 competent cells were thawed on ice, and then 10 ng of pTrc-His-hXOR DNA were placed in a tube with 100 µL of TP1000 cells. The cells were left on ice for 35 minutes and then they were heat-shocked for 45 seconds in a heat block at 42˚C. The transformed cells were then spread on agar plates supplemented with 100 µg/mL ampicillin and incubated overnight at 37˚C.

2.3.2. Expression of Recombinant XOR under Optimised Conditions

A starter culture was inoculated with a colony from freshly prepared transformants and grown at 37°C in 5 mL 2xTY media supplemented with 100 µg/mL ampicillin and grown overnight.

This starter culture was used to inoculate 500 mL of 2xTY media containing 100 µg/mL ampicillin and 1 mM of sodium molybdate. The culture was incubated at 37°C with shaking until an OD_{600} of 0.4-0.6 was reached. It was then induced with 40 µM of isopropyl-β-D-thiogalactopyranoside (IPTG) and incubated overnight at 30°C.

For heat-shocked treated cultures, the cells were left growing until they reached an OD_{600} of 0.3, after which the flask was incubated for 20 minutes at 42°C. Induction was conducted using 40 µM of IPTG and left overnight at 30°C.

The cells were harvested using the F12-6x500 LEX (Thermo Scientific) rotor and the Sorvall Lynx 6000 (Thermo Scientific) centrifuge at 4000 x g for 10 minutes at 4°C. The supernatant was decanted and the cell pellets were frozen at -20°C until required.

2.3.3. Cell Lysis

The frozen cell pellet was resuspended in 40 mL Start Buffer with 1 mM TCEP, 5 mM $MgCl_2$, 5 µg/mL DNase (Roche, prepared as a 1000x stock solution containing 5 mg DNase in 1 mL of 0.15 M NaCl), and 10 mM phenylmethylsulphonyl fluoride (PMSF) in ethanol (Sigma). Lysis was performed on the cell suspension using a French® Pressure Cell Press at 1,000 PSIG and sonicated on ice using Soniprep 150 (MSE) for 15 cycles of 3 seconds on/47 seconds off. The lysed cells were centrifuged for 35 minutes at 20,000 x g and 4°C using the T29-8x50 (Thermo Scientific) rotor. The supernatant was then collected and filtered with a 0.45 µm cellulose acetate Whatman™ filter.

2.3.4. Immobilised metal affinity chromatography

A 5 mL HisTrap™ Chelating HP column (Cytivia) was used to purify the protein. The column was washed with 20 mL of strip buffer, followed by 25 mL of deionised water, and finally charged with 100 mM nickel (II) sulphate. The column was equilibrated with 25 mL of cold start buffer. The cold clarified lysate was loaded on the column and the flow through was collected. All solutions were maintained at 4˚C. The column was then washed in a stepwise fashion with 50 mL of 20 mM imidazole/ 50 mM HEPES and 500 mM NaCl, then 50 mL of 50 mM imidazole/ 50 mM HEPES and 500 mM NaCl, and 25 mL of 75 mM imidazole/ 50 mM HEPES and 500 mM NaCl. The protein of interest

was eluted using 250 mM imidazole/50 mM HEPES and 500 mM NaCl. The flow rate was 1 mL/min. Buffers were prepared as listed in Table 2.6. All buffers and collected fractions were kept on ice.

Table 2.6: Preparation of imidazole solutions

Imidazole concentration (mM)	Total Volume (mL)	Volume of Buffer A (mL)	Volume of Buffer B (1 M imidazole)
20	50	49	1
50	50	47.5	2.5
75	25	23.125	1.875
250	25	18.75	6.25

Collected samples were analysed by 8% SDS-PAGE.

2.3.5. Buffer exchange

Buffer exchange was performed by dialysis. The eluted sample was dialysed three times against 2 Liters of 500 mM Na phosphate buffer pH 7.4 and 5 M NaCl at 4°C. The purity and concentration of the samples were measured using the Eppendorf BioSpectrometer® kinetic spectrophotometer using the 280 nm and 450 nm wavelengths, where tyrosine and tryptophane and flavin adenine dinucleotide (FAD) absorb, respectively. Concentration was calculated using an ε_{280} of 102,680 $M^{-1}cm^{-1}$, which is the extinction coefficient at 280 nm calculated from the amino acid sequence of hXOR from SnapGene® (from Dotmatics; available at snapgene.com). Purity was calculated using the ratio of the absorbance at 280 nm to the absorbance at 450 nm (A280:A450), for which a value between 4 – 6 indicates a pure hXOR sample. The dialysed samples were aliquoted and stored with 1 mM TCEP at -80°C until required.

2.4. Protein Analysis Methodology

2.4.1. SDS-Polyacrylamide Gel Electrophoresis (SDS-PAGE)

Protein samples were separated and assessed using SDS-PAGE according to manufacturer's instructions and according to the method described in *Sambrook et al.* (Sambrook et al., 2012). An 8% resolving gel was prepared and poured between two glass plates. The resolver gel was then layered with 300 µL of water-equilibrated butanol, to

avoid oxygen from affecting the polymerisation of the gel. The gel was left to polymerise for approximately 20 minutes. Once the gel had set, the butanol was removed using a filter paper.

Table 2.7: SDS-PAGE Gel Composition of 8% Resolving Gel

Reagents	Volume/mL
Deionised Water	4.6
1.5M TrisCl pH 8.8	2.5
30%t, 3.3%c Acrylamide/Bisacrylamide [29:1]	2.7
Trichloroethanol	0.05
10% (w/v) SDS	0.1
10% (w/v) APS	0.1
TEMED	0.004

A 5% stacking gel was then prepared and poured over the resolver gel between the two glass plates. A gel comb was inserted, and the gel was left to polymerise for approximately 20 minutes. Once the gel polymerised, the glass plates were removed from the casting tray and placed into the electrophoresis chamber.

Table 2.8: SDS-PAGE Gel Composition of 5% Stacking Gel

Reagents	Volume/mL
Deionised Water	2.7
1.0M TrisCl pH 8.8	0.5
30%t, 3.3%c Acrylamide/Bisacrylamide [29:1]	0.67
10% (w/v) SDS	0.04
10% (w/v) APS	0.04
TEMED	0.004

The protein samples were prepared by adding 2x SDS loading dye (100 mM Tris.Cl pH 6.8, 20% (v/v) glycerol, 0.2% (w/v) bromophenol blue, and 4% (w/v) SDS)

with 200 mM DTT. Following the addition of the dye to the protein samples, the samples were boiled for approximately 10 minutes. The 1x Tris-Glycine SDS buffer (Table 2.1) was placed to the electrophoresis chamber and the comb from the gel was removed. The samples were loaded on the gel, along with the Precision Plus Protein^{TM} ladder (BioRad), and electrophoresis was carried out for approximately 55 minutes at a constant voltage of 200 V. The gel was then viewed by the ChemiDoc^{TM} Imaging System (Bio-Rad) using the 'Stain Free' setting. Following electrophoresis, the gel was stained overnight with Coomassie Brilliant Blue stain solution (40% (v/v) methanol, 10% (v/v) acetic acid, 0.2% (w/v) Coomassie 25 Brilliant Blue R250, 0.2% (w/v) cupric acetate). The stain was then removed and the gel was washed with water to remove excess stain and destained using 20% (v/v) isopropyl alcohol and 10% (v/v) acetic acid. After destaining, the gel was then visualised again using the ChemiDoc^{TM} system using the 'Coomassie Blue Stain' setting.

2.4.2. Native-Polyacrylamide Gel Electrophoresis (Native-PAGE)

The oligomeric state of the XOR samples was assessed using native-PAGE. A 5% native gel was prepared as shown in Table 2.9, poured between the two glass plates and a well comb was inserted. The gel was left to solidify for approximately 20 minutes.

Table 2.9: 5% Native-PAGE Gel Composition

Reagents	Volume/mL
Deionised Water	6.1
1.5M TrisCl pH 8.8	2.5
30%t, 3.3%c Acrylamide/Bisacrylamide [29:1]	1.3
10% (w/v) APS	0.1
TEMED	0.01

The samples were prepared for loading through the addition of 6x native dye (20% (v/v) 1.5 M Tris pH 8.8, 60% (v/v) glycerol and 0.6% (w/v) bromophenol blue) in a 5:1 ratio (dye: protein sample). The samples were loaded onto the gel and electrophoresis was carried out for approximately 50 minutes at 200 V using 1x Tris Glycine buffer as the running buffer. Following electrophoresis, the gel was stained with Coomassie Brilliant Blue stain overnight and destained as described in section 2.4.1.

2.4.3. Blue Native Gel

The NativePAGE™ Novex® Bis-Tris Gel System (Thermo Scientific) was set up according to the manufacturer instructions using the XCell *SureLock*™ Mini-Cell. The samples were prepared at a final amount of 12.5 µg and loaded, along with uricase and Bovine Serum Albumin (BSA) markers and the gel was left to run for 120 minutes at 150 V. The gel was destained using destain solution.

2.5. Enzymatic Assays

2.5.1. In-gel nitro blue tetrazolium (NBT) Assay

When XOR catalyses the reaction of hypoxanthine to xanthine and subsequently to uric acid, reactive oxygen species (ROS) are produced as by-products, including superoxide ions and hydrogen peroxide. Superoxide reduces NBT from yellow to blue formazan (Tvrda, 2019). This assay indirectly measures the activity of XO through the generation of ROS.

The gel obtained from Native-PAGE was placed in a container with 25 mL of XOR activity solution made up of 300 µM of 150 mM xanthine stock, 5mL of 100 mM NaP, 15 µM of nitro blue tetrazolium (NBT), and topped up to 25 mL with dH_2O (Fried, 1966). The gel was left in the incubator at 37ºC in the dark for 15 minutes and then it was viewed using ChemiDoc™.

2.5.2. NBT Assay

The NBT assay was also carried out in a 96-well microtiter plate, by placing 0.50 mg/ml of protein sample, 100 µL of NBT solution, containing 300 µM of 150 mM xanthine stock, 5 mL of 100 mM NaP, 15 µM of NBT, topped up to 25 mL with dH_2O, and 1x PBS to fill up the wells to 200 µL. Apart from hXOR samples, bovine hXOR was also used as a positive control. A buffer was also included in the plate with NBT solution and 1x PBS buffer. Each sample was prepared in duplicates. The plate was placed in the Tecan Spark® Multimode Microtiter Plate Reader and the activity of each sample was monitored.

2.5.3. Uric acid activity assay

Two uric acid activity assays were performed, one for the measurement of xanthine oxidase (XO) activity and the other for xanthine dehydrogenase (XDH) activity.

2.5.3.1. Xanthine Oxidase Activity

The determination of the activity of xanthine oxidase was achieved by monitoring the rate of oxidation of xanthine to uric acid at a wavelength of 295 nm and pathlength 1 cm at a temperature control-environment of 25ºC (Avis et al., 1956). This was done using the Olis Spectrophotometer Conversion. A stock solution of 150 mM xanthine was prepared by dissolving xanthine with sodium hydroxide and adjusting the pH to 7.4 before use. The actual concentration of xanthine was calculated by first preparing 1:1000 and 1:2000 dilution and then checking the absorbance at 277 nm. The Beer Lambert's Law equation was used to calculate the actual concentration of xanthine using $\varepsilon = 9.3\ mM^{-1}cm^{-1}$.

To check the XOR activity, 2x Master Mix Buffer was prepared, containing 100 mM sodium phosphate pH 7.5, 300 µM of xanthine stock in deionised water. The reaction mixtures were composed of the following reagents: 500 µL 2x Master Mix Buffer; 0.15 mg/mL hXOR; x µL deionised water (adjusted to 1000 µL final volume).

The 2x Master Mix Buffer, water and lastly the protein samples, were combined in 1.5 mL microfuge tubes. Before adding the protein samples to the mixture, they were removed from ice and allowed to equilibrate at room temperature for a few minutes. The change in absorbance caused by the generation of uric acid was checked over a period of 2 minutes by transferring the contents of the Eppendorf tubes into 1 mL glass cuvette. A blank solution was also prepared containing only 1x Master Mix buffer and dH_2O, omitting the enzyme.

2.5.3.2. Xanthine Dehydrogenase Activity

Xanthine dehydrogenase catalyses the same conversion of xanthine to uric acid but transfers electrons to nicotinamide adenine dinucleotide (NAD^+) rather than O_2. The activity of xanthine dehydrogenase was also measured using the same set up as described in Section 2.5.3.1., by monitoring the rate of oxidation of xanthine to uric acid at a wavelength of 295 nm for 2 minutes. The only difference between the two assays was the inclusion of NAD^+ in the latter. Specifically, 33 mg of NAD^+ (free acid, grade I, approx. 100%, Roche) was dissolved in 1 mL of dH_2O. The actual concentration of NAD^+ was

then determined spectrophotometrically using the Beer Lambert's Law with ε = 17.6 $mM^{-1}cm^{-1}$.

In this case, 2x Master Mix Buffer, was prepared as previously described (Section 2.5.3.1.). This was placed in the Eppendorf tubes, followed by 0.5 mM NAD^+, water (adjusted to 1000 µL final volume) and lastly 0.15 mg/mL of hXOR sample. A blank solution was prepared with buffer, deionised water, and NAD^+.

2.5.4. Thermal inactivation analysis

The protein samples were incubated for 10 minutes at different temperatures (30, 37, 42, 50°C). The samples were allowed to equilibrate at room temperature after heating and the uric acid assay was then performed at 25ºC to determine the final residual activity.

2.6. Colorimetric Assays

2.6.1. Bicinchoninic Acid (BCA) Protein Assay

The PierceTM BCA Protein Assay Kit (Thermo Scientific) was used to carry out the BCA protein assay in order to quantify the total amount of protein in each sample. The standards (STD) ranging from 0 to 50 µg/mL were prepared using the bovine serum albumin (BSA) (2mg/mL). Before and after clarification, a serial dilution of 1:20 of whole lysates was prepared using PBS buffer. For approximately 70 samples, the working reagent was prepared by mixing 14 mL of Reagent A and 280 µL of Reagent B. In a 96-well microtiter plate, 25 µL of the standards were prepared as shown in Table 2.10. The wells of the plate were filled with 25 µL of either standard or cell lysates as well as 200 µL of working reagent. All the samples, including standards were prepared in duplicates. The plate was then placed in the incubator at 37°C for 30 minutes. Then, the plate was allowed to cool down to room temperature and the absorbances were measured using the Tecan Spark® Multimode Microtiter Plate Reader. A standard curve was generated using the standards and the total protein concentration of each well was calculated.

Table 2.10: Volumes of BSA and PBS used to produce standards

Column number	1	2	3	4	5	6	7	8
STD (µg)	0	5	10	15	20	30	40	50
2 mg/mL of BSA(µL)	0	2.5	5	7.5	10	15	20	25
PBS (µL)	25	22.5	20	17.5	15	10	5	0

2.7. Protein Characterisation

2.7.1. Circular Dichroism

The samples were left on ice to thaw and buffer exchanged by dialysis against 10 mM sodium phosphate buffer pH 7.4 and 50 mM Na_2SO_4. The 1 mL samples were left stirring overnight at 4°C in 3 L of buffer. Following the buffer exchange, the samples were centrifuged for 10 minutes at 16,000 x g. The concentration of the protein samples was measured and they were diluted with dialysis buffer to a concentration of around 0.2 – 0.3 mg/mL.

Circular Dichroism (CD) was performed using the Chirascan V100 circular dichroism spectrometer (Applied Photophysics). The aim of this experiment was to assess secondary structure content and overall folding of the protein samples. A 0.1 cm cuvette was washed five times with dH_2O and a blank reading of the dialysis buffer was taken. Then each protein sample was read using the setting in Table 2.11, washing the cuvette with dH_2O five times between the samples.

Table 2.11: Settings used for circular dichroism

Setting	Value
Monochromator wavelength	222 nm
Bandwidth	4
Step size	0.5
Wavelength range	180 – 260 nm
Time per point	0.5
Repeats	5

2.7.2. Melting Temperature

Melting temperatures of the protein samples were measured using the Chirascan V100 circular dichroism spectrometer (Applied Photophysics), using the setting described in Table 2.12. Between each sample, the cuvette was washed five times with dH_2O between the samples.

Table 2.12: Settings used for melting temperature ramps.

Setting	Value
Monochromator wavelength	222 nm
Bandwidth	4
Step	1.0°C
Rate step	1°C per minute
Temperature range	20 – 90°C
Time per point	5 seconds
Tolerance	0.2
Repeats	5

2.7.3. Thioflavin T Assay

The propensity of protein fibrillization was assessed using Thioflavin T (ThT) fluorescent dye, having a maximum excitation wavelength of 440 nm and a maximum emission wavelength of 480 nm. A stock solution of 10 mM ThT was prepared. The actual concentration was measured spectrophotometrically using the Beer Lambert's Law with ε=36 $mM^{-1}cm^{-1}$. The wells of the black 96-well plate (Themo Scientific) were first

blocked with 200 µL of a solution consisting of 1x PBS, 1% Casein Blocker and 0.05% Tween. The plate was wrapped and left shaking overnight at 4˚C. The blocking solution was removed from the wells and 1x PBS buffer, XOR protein within a concentration range of 0.5 to 12 µM , and 20 µM of ThT were added in each well. The measurements were performed in duplicate, and blanks composed of 1xPBS and ThT, as well as ThT alone, were included in the plate. The fluorescence was detected with excitation and emission wavelengths of 430 nm and 485 nm, respectively, using the Tecan Spark® Multimode Microtiter Plate Reader. The concentration range of the protein between 0.5 µM and 12 µM was done as a preliminary optimisation experiment using only the WT and I646V protein samples. Based on the results obtained, 8 µM and 12 µM were used in the actual ThT assay for all the protein samples at 37˚C. The plate was subjected to orbital shaking at a frequency of 510 rpm with a shaking amplitude of 1mm. Shaking was performed in 600 s intervals following each fluorescence measurement. To evaluate the aggregation of the WT hXOR specifically, the assay was repeated at room temperature. The shaking parameters were modified to a double orbital shaking with 1mm amplitude at 270 rpm with 600 s intervals between measurements.

2.7.3.1. Native Agarose Gel Electrophoresis

The migration of positively and negatively charged proteins was assessed using Native agarose gel electrophoresis according to the method described by *Kim* in Cold Spring Harbor Protocols (Kim, 2011). The 0.8% (w/v) agarose gel was prepared by adding 0.8 g of agarose in 125 mL of Native gel buffer, containing 25 mM Tris-Cl (pH 8.5) and 19.2 mM glycine. The solution was boiled and left to cool. Once it cooled to approximately 50˚C, it was poured into a casting tray and the comb was inserted in the centre of the gel-casting assembly. The agarose gel was left to solidify and native gel buffer was poured into the casting tray. The samples obtained from the ThT assay were then loaded with a 1:1 of loading dye to protein solution (2x loading dye composed of 20% glycerol, 0.2% bromophenol blue, and 0.12 M Tris-Cl). Electrophoresis was carried out at a constant voltage of 50 V for 1 hour. The gel was stained in gel-staining solution composed of 0.12% Coomassie Brilliant Blue R, 45% methanol, and 10% acetic acid. Then the stain was removed and the gel was destained using gel destaining solution made up of 45% methanol, and 10% acetic acid. The destained gel was visualised using the ChemiDoc^{TM} system.

2.7.3.2. Uric acid activity assay

Following the ThT assay, the samples that showed fibrillization were then incubated in the water bath at 37ºC for 24 hours, and their activity was subsequently measured at 25˚C using the uric acid activity assay. In parallel, the enzymatic activity of identical samples that were not subjected to the 37˚C incubation, was also measured for comparison.

2.7.3.3. ZipperDB

The aggregation propensity of selected regions within the hXOR protein sequence was analysed using ZipperDB, an online computational tool that predicts the likelihood of amyloid fibril formation based on steric formation energies (Goldschmidt et al., 2010). The entire amino acid sequence of WT hXOR, as well as the sequences including the variants (I636V, I703V, and I646A) were submitted to the ZipperDB server.

2.7.4. Dynamic Light Scattering

Dynamic Light Scattering (DLS) was used to assess the size distribution of the XOR protein. The protein samples were diluted to a final concentration of 0.25 mg/mL in 1x PBS buffer to a 1 mL final volume and placed in microfuge tubes. Prior to measurement, the samples were centrifuged for 30 minutes at 16,000 x g at 4°C and the supernatant was transferred to a new tube. DLS measurements were performed using a Zetasizer Advance Red® (Malvern Instruments, UK).

2.8. Structural Analysis of hXOR

2.8.1. Molecular Modelling

The structure of WT hXOR, as well as the variants hXOR were analysed using the PyMol Molecular Graphics System (Schrödinger & DeLano, 2020). The site-directed mutagenesis and the energy minimisation were performed using Swiss-PDBviewer (Guex & Peitsch, 1997).

2.8.2. Molecular Docking of hXOR with ThT

Molecular docking of hXOR with ThT was performed using the online server SwissDock (SwissDrugDesign) (Bugnon et al., 2024; Eberhardt et al., 2021). The docking simulations were executed using the AutoDock Vina method with a sampling

exhaustivity of 4. The ligand of ThT was used as a SMILES notation CC1=CC2=C(C=C1)[N+](=C(S2)C3=CC=C(C=C3)N(C)C)C.[Cl-].

2.8.3. Protein-Protein Interactions

To investigate protein-protein interactions between two dimers of hXOR, protein-protein docking was performed using the HDOCK Server (Yan et al., 2020; Yan et al., 2017, Yan et al., 2017; Huang & Zhou, 2014; Huang & Zhou, 2008).

Chapter 3 Results

TP1000 cells were transformed with pTrcHis-WT hXOR and the variant clones, specifically I646V, I703V, I646V-I703V, and I646A. The I646A variant was studied to identify any differences in activity, stability, and function resulting from substituting isoleucine with a smaller amino acid. Cells were cultured and expression was induced under aerobic conditions, with and without heat shock treatment. In response to heat shock, cells release chaperones that promote better protein folding. The protein samples recovered from cells treated with heat shock were annotated either as '+HS' or 'treated samples' in the following sections. Following expression, the cells were lysed as described in Section 2.3 and all the different cell lysates were subjected to immobilised metal affinity chromatography (IMAC). The purity and yield of the recombinant hXOR proteins were evaluated using SDS-PAGE and densitometry. Oligomerisation states were assessed using Native-PAGE while enzymatic activity was monitored using photometric enzymatic assays and NBT assays. Furthermore, biophysical characterisations were carried out to assess the secondary structure and stability of hXOR. Thioflavin T (ThT) assay was used to determine the propensity of protein fibrillization. Figure 3.1 summarises the results obtained from this project.

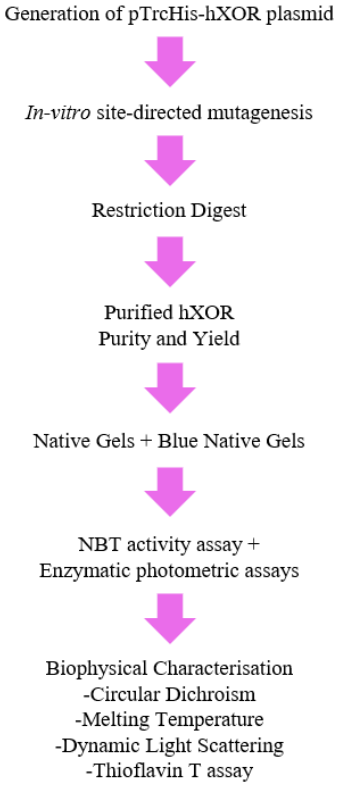

Figure 3.1: Summary of the results.

3.1. pTrcHis-hXOR

3.1.1. Plasmid Map

The pTrcHis-WT hXOR clone in Figure 3.2 was generated by Dr Brandon Seychell (Laboratory of Biochemistry and Protein Science, University of Malta). The WT clone was produced by modifying the pTrc-hXOR clone (donated by Prof Arwen Pearson, University of Hamburg) and inserting a 6xHis-tag with the nucleotide sequence CACCACCACCACCAC using a polymerase chain reaction (PCR). The I646V, I703V, I646V-I703V and I646A variants were generated using the pTrcHis-XOR WT clone as a template for *in-vitro* site-directed mutagenesis.

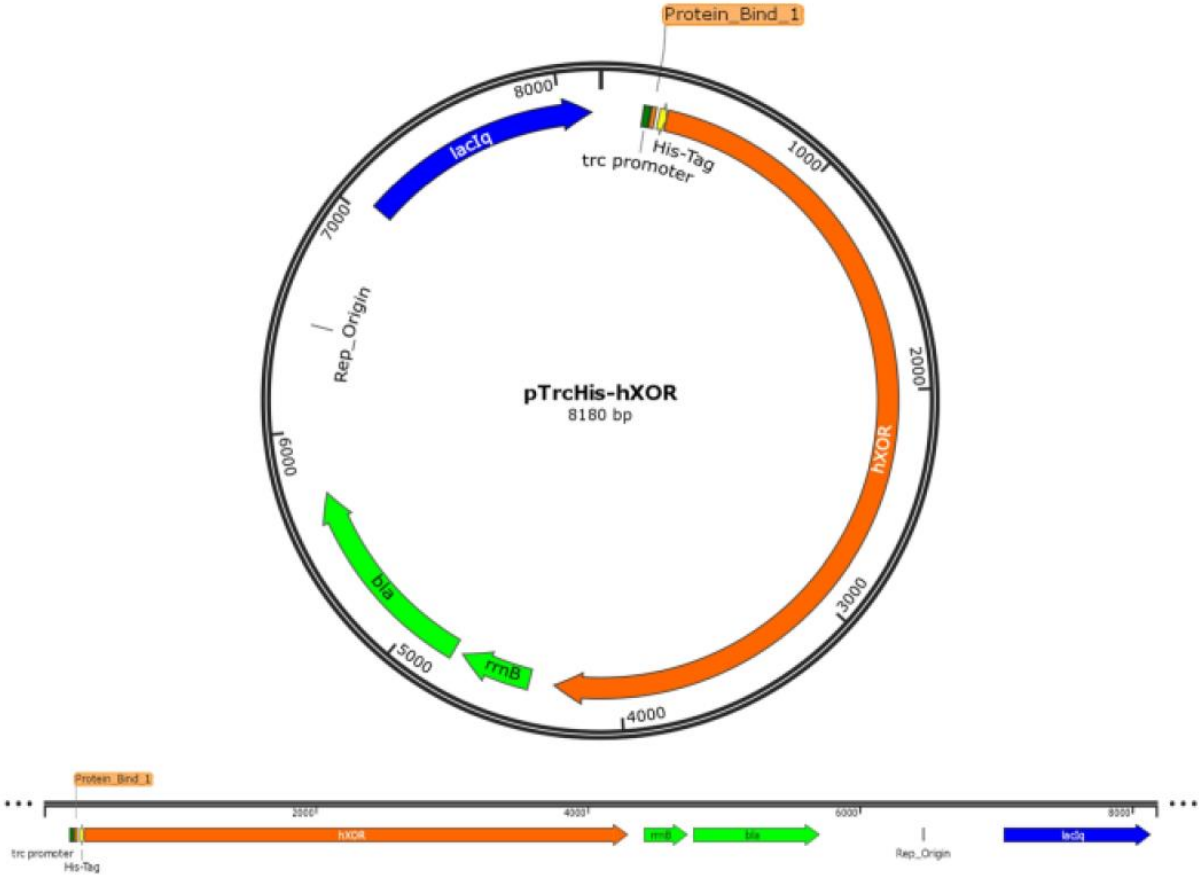

Figure 3.2: pTrcHis-hXOR plasmid map. Reproduced using SnapGene® software (from Dotmatics; available at snapgene.com).

3.2. *In-vitro* site-directed mutagenesis

Figure 3.3 shows the nucleotide and amino acid positions where the *in-vitro* site-directed mutagenesis was performed using the primers hXOR_I646V_FOR and hXOR_I646V_REV and hXOR_I703V_FOR and hXOR_I703V_REV for the I646V-I703V variant and hXOR_I646A_FOR and hXOR_I646A_REV for the I646A variant as described in Section 2.2.6 Table 2.3. A number of colonies from each mutagenesis reaction were selected for plasmid DNA extraction followed by Sanger sequencing.

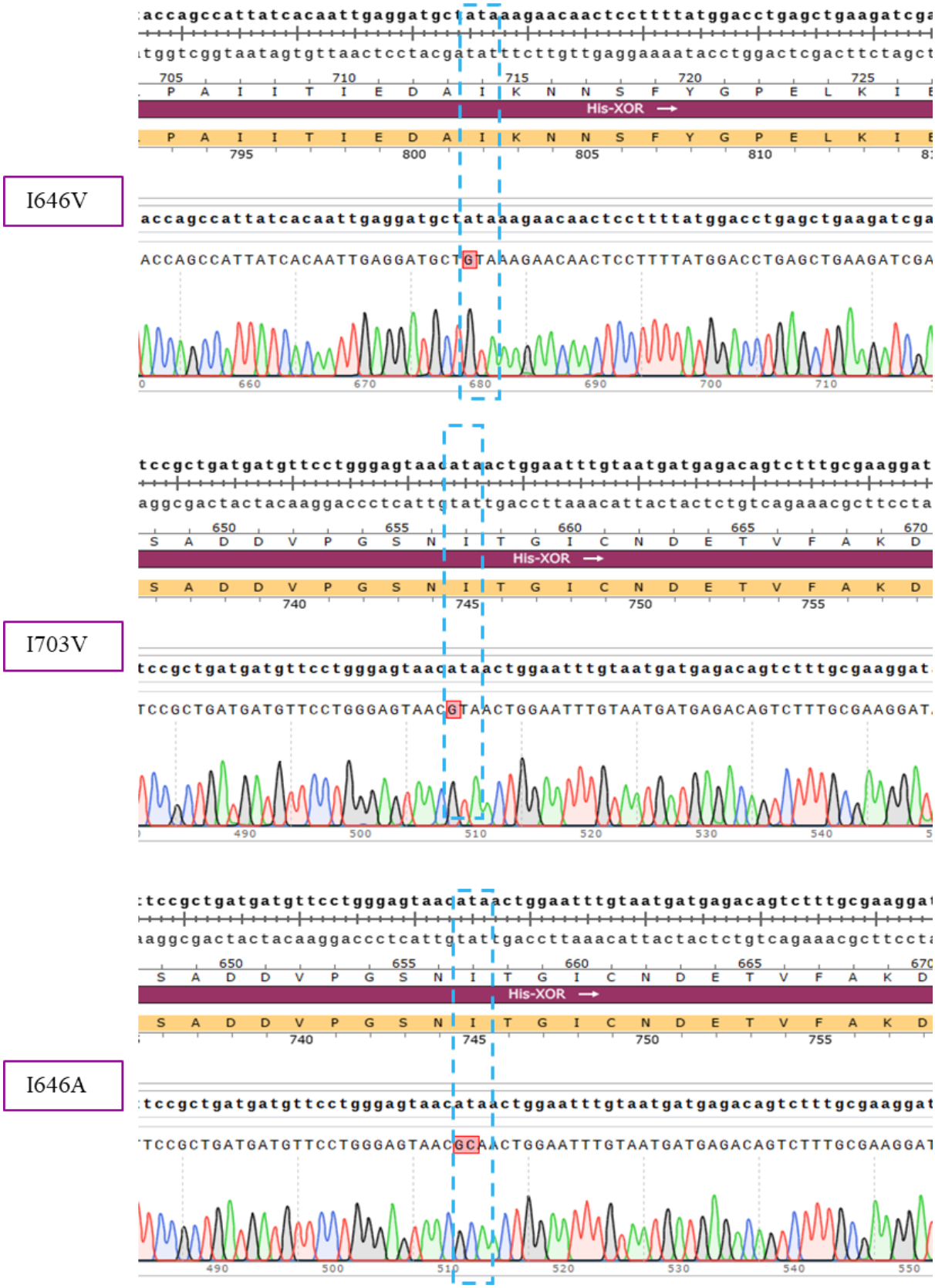

Figure 3.3: Sequencing results confirming the mutations in the pTrcHis-hXOR clone. The nucleotide in red represents the nucleotide that was mutated. The boxed blue nucleotides represent the codons where the nucleotide is found.

3.3. Restriction Digest

The WT hXOR and I646V underwent restriction enzyme digest as described in Section 2.2.3. The restriction enzymes were chosen using SnapGene Viewer. The DNA pTrcHis-WT hXOR and pTrcHis I646V was linearised by single enzyme digest using *Sal*I and *Eco*RV.

Agarose gel electrophoresis was then used to assess the DNA fragments produced by the restriction digest (Figure 3.4). Two bands can be observed in lanes 2 and 5, showing that the plasmids DNA are present in both their relaxed (top band) and supercoiled form (bottom band), since they did not undergo restriction digest. Both pTrcHis-WT hXOR and pTrcHis-I646V were efficiently linearised by the *Sal*I and *Eco*RV restriction enzymes as can be observed in lanes 3,4,6 and 7, with one band at 8,180 bp.

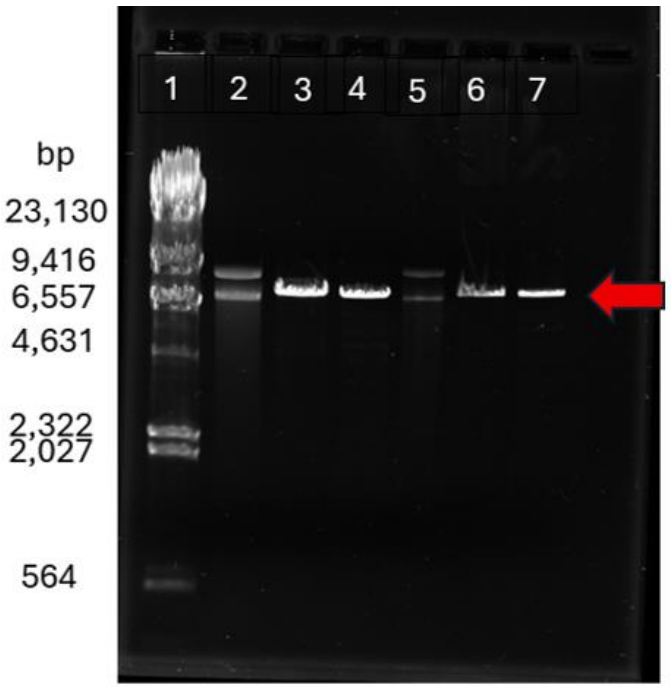

Figure 3.4: Agarose gel (0.7% w/v) of pTrcHis-WT hXOR and I646V DNA. Lane 1 – HindIII λ DNA ladder (1 µg); Lane 2 – uncut pTrcHis-WT hXOR DNA; Lane 3 – pTrcHis-WT hXOR vector digested by SalI restriction enzyme; Lane 4 – restriction digest of pTrcHis-WT hXOR DNA by EcoRV; Lane 5 – uncut pTrcHis-hXOR I646V DNA; Lane 6 – restriction digest of pTrcHis-hXOR I646V DNA by SalI; Lane 7 – restriction digest of pTrcHis-hXOR I646V DNA by EcoRV. The red arrow indicated the pTrcHis-hXOR linear plasmid (size: 8180 bp).

The restriction enzyme digest was also performed using pTrcHis-hXOR I703V DNA, and agarose gel electrophoresis was used to assess the DNA fragments produced by the restriction digest (Figure 3.5). Two bands can be observed in lane 2, with a major band at approximately 8,180 bp, indicating successful linearisation of the plasmid by *Sal*I restriction enzyme, and a smaller band representing residual uncut or partially digested DNA.

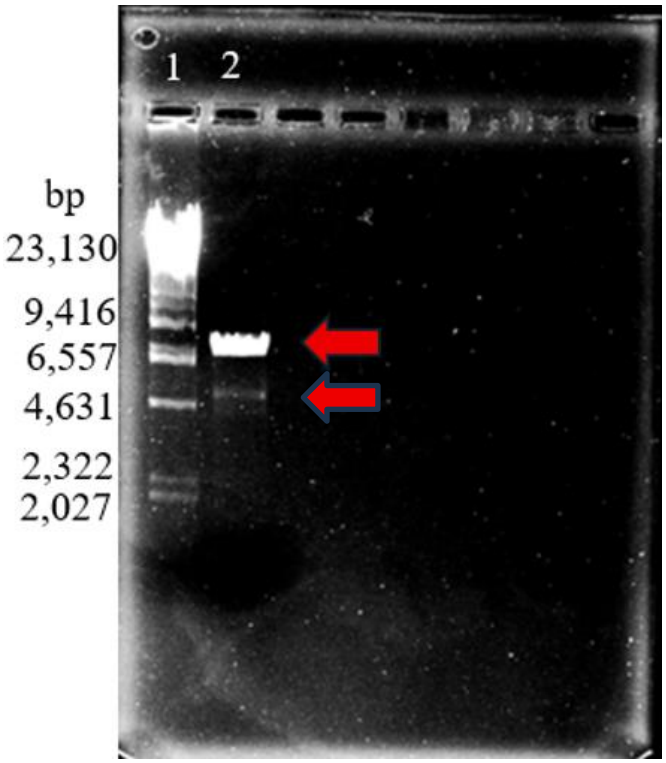

Figure 3.5: Agarose gel (0.7% w/v) of pTrcHis-hXOR I703V DNA. Lane 1 – HindIII λ DNA ladder (1 μg); Lane 2 – pTrcHis-hXOR I703V vector digested by SalI restriction enzyme.

The purified pTrcHis-hXOR I646V-I703V DNA was also subjected restriction enzyme digest using *Sal*I. Agarose gel electrophoresis confirmed that the plasmid DNA extracted from 6 colonies linearised by *Sal*I as it can be observed in lanes 2,3,4,5,6 and 7.

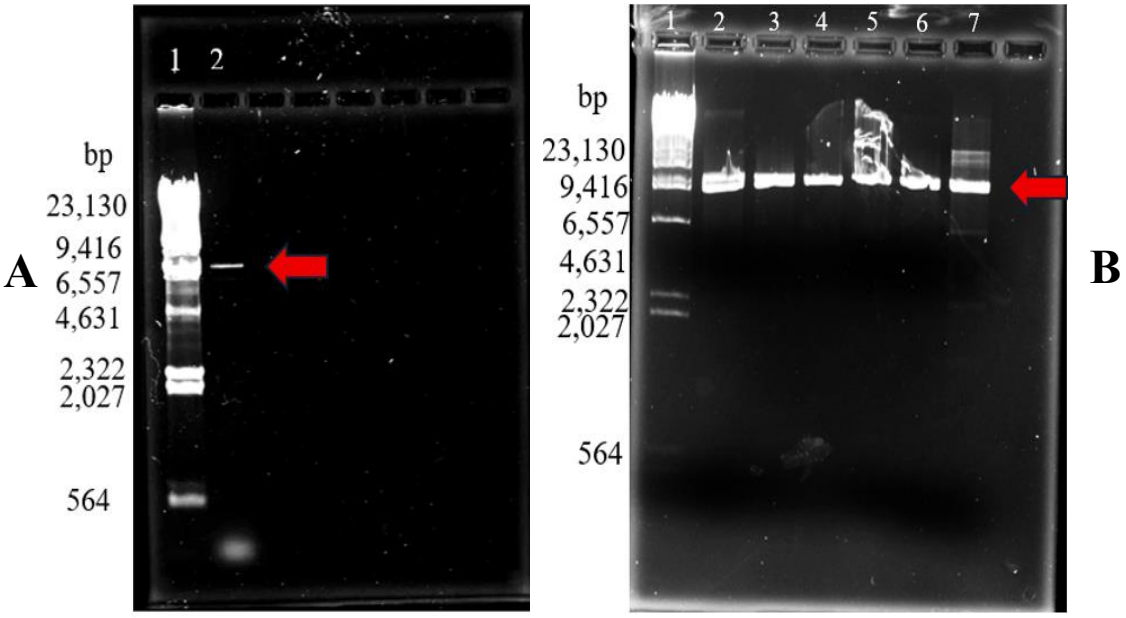

Figure 3.6: A – Agarose gel (0.7%, w/v) of the PCR product. Lane 1 – HindIII λ DNA ladder; Lane 2 – 10 µL pTrcHis-hXOR I646V-I703V. The red arrow indicates the amplified pTrcHis-hXOR plasmid. B – Agarose gel (0.7%, w/v) of pTrcHis-hXOR I646V-I703V DNA. Lane 1 – HindIII λ DNA ladder; Lanes 2, 3, 4, 5, and 6 – restriction digest of pTrcHis-hXOR I646V-I703V DNA by SalI. The red arrow indicated the pTrcHis-hXOR linear plasmid (size: 8180 bp).

3.4. Purification of human xanthine oxidoreductase

3.4.1. Purification of WT human xanthine oxidoreductase

His-tagged WT hXOR was shown to bind to the nickel-charged IMAC column (Figure 3.7). In each of these gels, lanes 1 and 2 show the lysate and the clarified lysate respectively while lane 3 shows the flowthrough of the column, which contains the proteins that did not bind to the column. It can be observed that in lane 3 that there is a missing band when compared to lane 1 and lane 2, suggesting that WT hXOR bound to the column. The column was then washed with three different concentrations of imidazole, 20 mM, 50 mM, and 75 mM imidazole, in order to remove any weakly bound

proteins from the column. The eluates are shown in lanes 4, 5, and 6 respectively. For the WT samples, the 250 mM imidazole was used to elute hXOR in three different fractions, shown in lanes 7, 8, and 9. The highest yield of hXOR resulted in the second 250 mM imidazole fracture and had a molecular weight of approximately 150 kDa (lane 8).

In the two gels, miscellaneous faint bands can also be observed, indicating either a lack of purity or slight proteolysis. Previous research has shown that this is typical for XOR and these bands might be due to the hXOR domains, which are the Moco domain (90 kDa) and FAD with [2Fe-2S] (60 kDa) (Gadave et al., 2014).

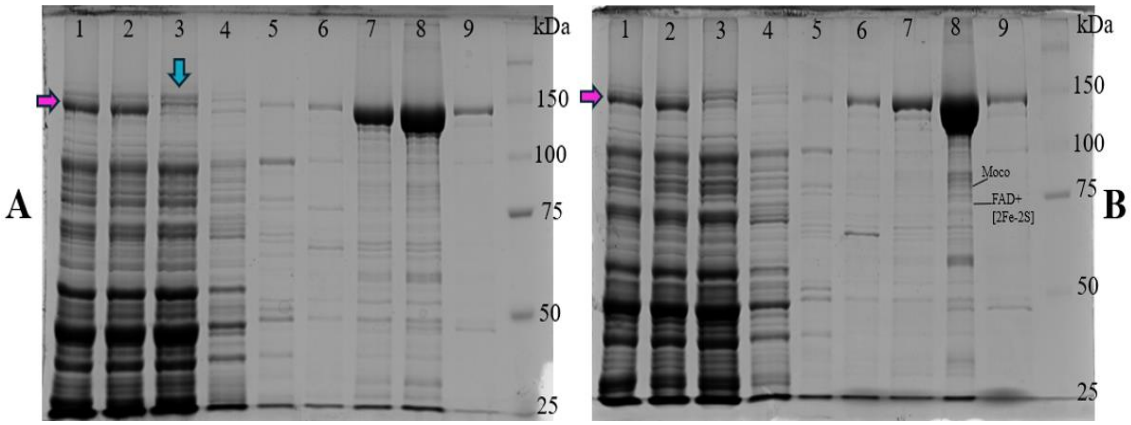

Figure 3.7: SDS-PAGE Gels (8%) of WT hXOR after IMAC chromatography. A – WT purification. Lane 1 – 8.4 µg lysate; Lane 2 – 6.4 µg clarified; Lane 3 – FT; Lane 4 – 20 mM IM wash; Lane 5 – 50 mM IM wash; Lane 6 – 75 mM IM wash; Lane 7 – elution 1 with 250 mM IM; Lane 8 – 10.5 µg elution 2 with 250 mM IM; Lane 9 – elution 3 with 250 mM IM. B – WT + HS purification. Lane 1 – 10.5 µg lysate; Lane 2 – 8 µg clarified; Lane 3 – FT; Lane 4 – 20 mM IM wash; Lane 5 – 50 mM IM wash; Lane 6 – 75 mM IM wash; Lane 7 – elution 1 with 250 mM IM; Lane 8 – 8.1 µg elution 2 with 250 mM IM; Lane 9 – elution 3 with 250 mM IM.

3.4.2. Purification of I646V hXOR

hXOR I646V, shown in Figure 3.8, bound well to the column, with lane 1 and 2 showing lysate and clarified lysate respectively, and with lane 3 showing the flowthrough. In both instances (with and without HS) the hXOR I646V protein bound to the column and was absent on the lane 3. The column was then washed with 20 mM, 50 mM, and 75 mM imidazole (lanes 4, 5, 6 respectively) to remove any weakly bound proteins from the column. If any hXOR was eluted at this stage, the eluted sample was not used further. This was done as a precaution as low binding to the column may be indicative of protein misfolding that disrupts the interaction of his tag with the column. Similar to the WT hXOR, elution with 250 mM imidazole yielded pure protein as shown in Figure 3.8. However, in contrast with WT hXOR, hXOR I646V sample contained no proteolysis products.

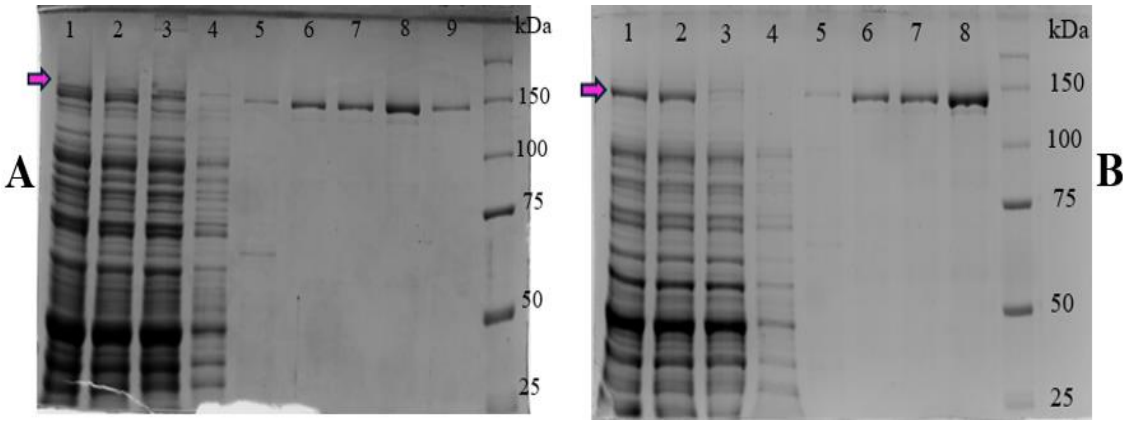

Figure 3.8: SDS-PAGE Gels (8%) of hXOR I646V after IMAC chromatography. A – I646V purification. Lane 1 – 8.6 µg lysate; Lane 2 – 6.6 µg clarified; Lane 3 – FT; Lane 4 – 20 mM IM wash; Lane 5 – 50 mM IM wash; Lane 6 – 75 mM IM wash; Lane 7 – elution 1 with 250 mM IM; Lane 8 – 4.7 µg elution 2 with 250 mM IM; Lane 9 – elution 3 with 250 mM IM. B – I646V + HS purification. Lane 1 – 5.1 µg lysate; Lane 2 – 4.25 µg clarified; Lane 3 – FT; Lane 4 – 20 mM IM wash; Lane 5 – 50 mM IM wash; Lane 6 – 75 mM IM wash; Lane 7 – elution 1 with 250 mM IM; Lane 8 – 5.8 µg elution 2 with 250 mM IM.

3.4.3. Purification of I703V hXOR

As shown in Figure 3.9, I703V hXOR bound well to the IMAC column. The protein samples were eluted at 250 mM imidazole, as shown in lanes 8 and 9, yielding a pure protein sample of approximately 150 kDa. When purifying I703V hXOR, the sample with HS produced a thicker and darker band for the eluted protein in lane 8 (Gel B), indicating a more concentrated eluted protein. In the case of hXOR I703V, it can be observed that at this high protein concentration some degree of limited proteolysis of hXOR was visible.

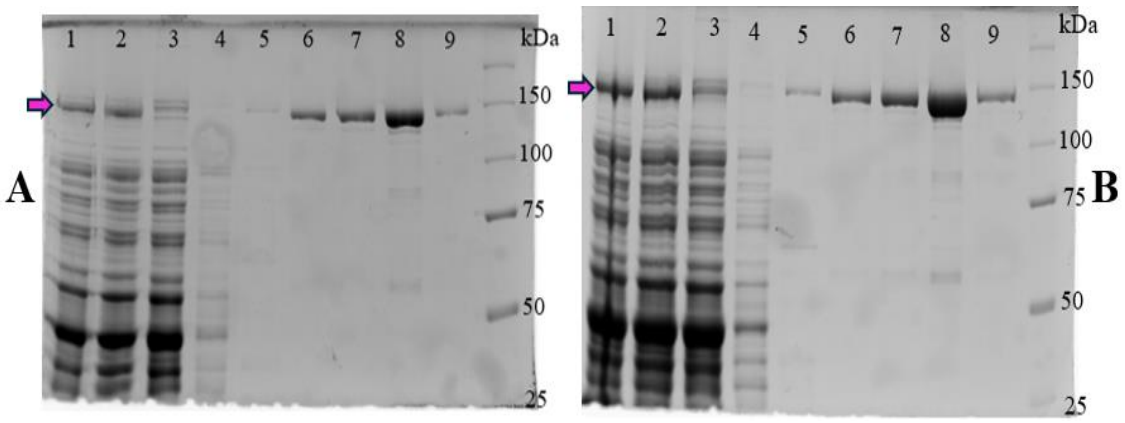

Figure 3.9: SDS-PAGE Gels (8%) of hXOR I703V after IMAC chromatography. A – I703V purification. Lane 1 – 10 µg lysate; Lane 2 – 8.7 µg clarified; Lane 3 – FT; Lane 4 – 20 mM IM wash; Lane 5 – 50 mM IM wash; Lane 6 – 75 mM IM wash; Lane 7 – elution 1 with 250 mM IM; Lane 8 – 7.2 µg elution 2 with 250 mM IM; Lane 9 – elution 3 with 250 mM IM. B – I703V + HS purification. Lane 1 – 11.5 µg lysate; Lane 2 – 7.5 µg clarified; Lane 3 – FT; Lane 4 – 20 mM IM wash; Lane 5 – 50 mM IM wash; Lane 6 – 75 mM IM wash; Lane 7 – elution 1 with 250 mM IM; Lane 8 – 5.1 µg elution 2 with 250 mM IM; Lane 9 – elution 3 with 250 mM IM.

3.4.4. Purification of I646V-I703V hXOR

hXOR I646V-I703V was shown to fully bind to the IMAC column as shown in Figure 3.10. This protein sample too eluted with 250 mM imidazole as shown in lanes 7, 8, and 9, yielding a pure protein sample with a size of approximately 150 kDa.

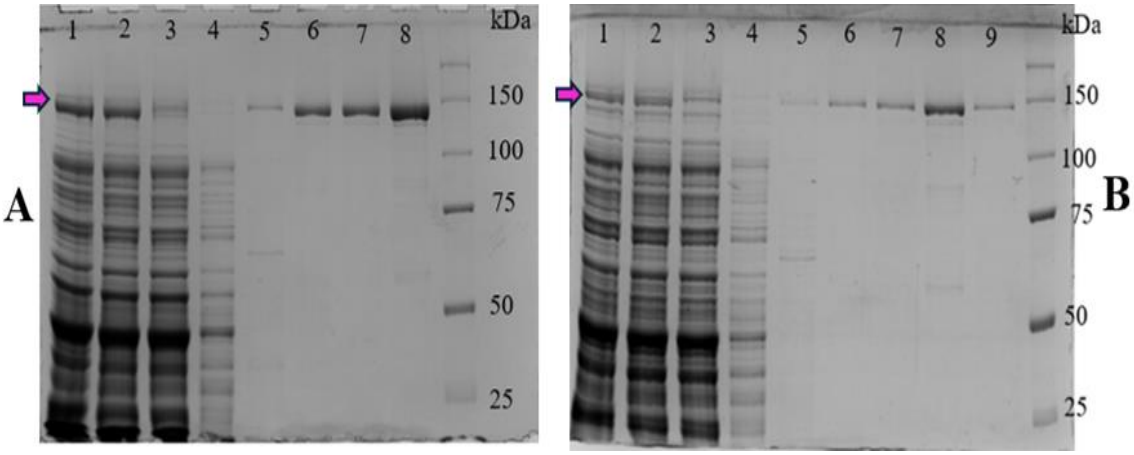

Figure 3.10: SDS-PAGE Gels (8%) of hXOR I646V-I703V after IMAC chromatography. A – I646V-I703V purification. Lane 1 –8.4 µg lysate; Lane 2 – 6.9 µg clarified; Lane 3 – FT; Lane 4 – 20 mM IM wash; Lane 5 – 50 mM IM wash; Lane 6 – 75 mM IM wash; Lane 7 – elution 1 with 250 mM IM; Lane 8 – 8.3 µg elution 2 with 250 mM IM. B – I646V-I703V + HS purification. Lane 1 – 12 µg lysate; Lane 2 – 7.9 µg clarified; Lane 3 – FT; Lane 4 – 20 mM IM wash; Lane 5 – 50 mM IM wash; Lane 6 – 75 mM IM wash; Lane 7 – elution 1 with 250 mM IM; Lane 8 – 5.7 µg elution 2 with 250 mM IM; Lane 9 – elution 3 with 250 mM IM.

3.4.5. Purification of I646A hXOR

hXOR I646A was shown to bind well to the IMAC column and eluted at 250mM IM to yield a pure protein as shown in Figure 3.11, lanes 7 and 8.

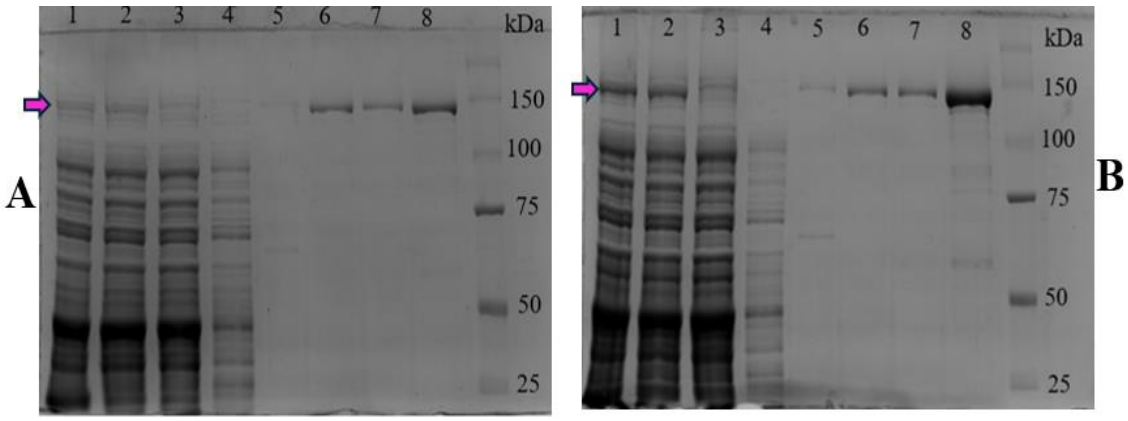

Figure 3.11: SDS-PAGE Gels (8%) of hXOR I646A after IMAC purification. Lane 1 – 12.8 µg lysate; Lane 2 – 8.9 µg clarified; Lane 3 – FT; Lane 4 – 20 mM IM wash; Lane 5 – 50 mM IM wash; Lane 6 – 75 mM IM wash; Lane 7 – elution 1 with 250 mM IM; Lane 8 – 8.6 µg elution 2 with 250 mM IM. B – I646A + HS purification. Lane 1 – 11.1 µg lysate; Lane 2 – 10.2 µg clarified; Lane 3 – FT; Lane 4 – 20 mM IM wash; Lane 5 – 50 mM IM wash; Lane 6 – 75 mM IM wash; Lane 7 – elution 1 with 250 mM IM; Lane 8 – 8.2 µg elution 2 with 250 mM IM.

3.4.6. Bicinchoninic acid (BCA) assay

The total protein in the lysate and the clarified lysate samples was determined using the BCA assay (2.6.1). The standard curve was plotted using a serial dilution of BSA ranging from 0 to 40 µg. The concentration of the protein samples was measured using a 1:20 dilution of sample. The amount of protein in micrograms was calculated using the line equation obtained from the standard curve, where x is the concentration of the total amount of proteins and y is the absorbance obtained. The concentration of pure hXOR was calculated through the absorbance at 280 nm using an extinction coefficient of 102,680 M^{-1} cm^{-1}. The extinction coefficient was calculated from the amino acid sequence using SnapGene® (from Dotmatics; available at snapgene.com).

The total yield from the lysate, clarified lysate, and pure hXOR fractions are summarised in Tables 3.1 and 3.2. The purity was assessed through densitometry analysis of SDS-PAGE gels using ImageJ (Schneider et al., 2012). The total yield was calculated by first multiplying the concentration by the volume of the samples. Since 500 mL cultures were used for all purifications, the value obtained was then multiplied by 2 to get the yield per L of culture.

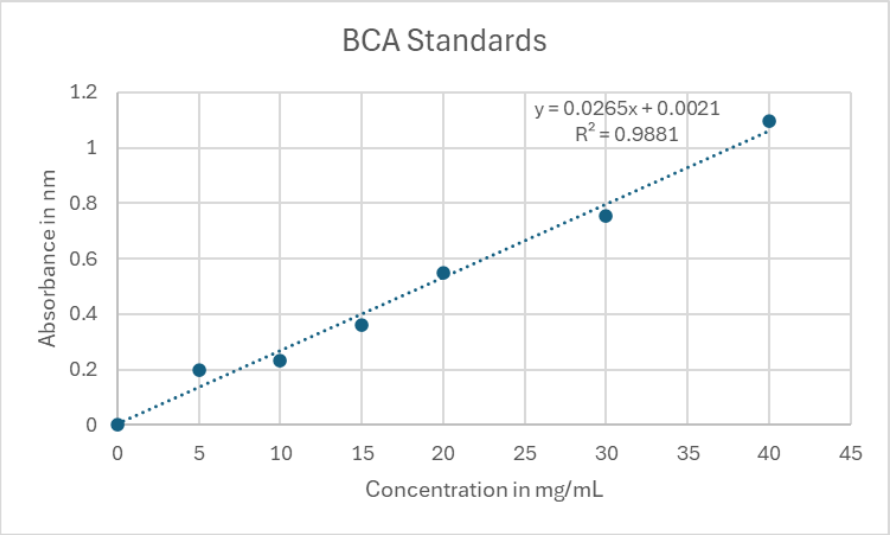

Figure 3.12: Standard curve for BCA using concentration of bovine serum albumin ranging from 0 to 40 mg/mL.

Analysis of the purification table of all the hXOR proteins demonstrate an inverse relationship between the increase in purity and a decrease in yield. This decrease can be linked to the clarification step, during which insoluble and/or denatured proteins are removed in the pellet, accounting for the initial reduction in yield. During the elution step, however, hXOR becomes the predominant protein in the sample, explaining the further drop in total yield but an increase in purity. The percentage purity of hXOR samples produced without and with HS is similar, with WT and WT+HS showing the lowest purity percentages, possibly due to protein fragmentation.

Table 3.1: Purification Table of samples without HS was constructed by scanning SDS-PAGE gels using ImageJ software.

Protein	Sample	Volume (mL)	Concentration (mg/mL)	Yield (mg/L culture)	Purity (%)
WT	Full Lysate	40	1.68	134.4	14.29
	Clarified	35	1.27	88.9	12.24
	Elution	6	2.09	25.08	90.33
I646V	Full Lysate	40	1.72	137.6	11.27
	Clarified	35	1.32	92.4	10.41
	Elution	5	0.93	9.3	97.92
I703V	Full Lysate	40	2.00	160	10.80
	Clarified	35	1.74	121.8	11.34
	Elution	8	1.44	23.04	98.91
I646V-I703V	Full Lysate	40	1.68	134.4	22.30
	Clarified	35	1.38	96.6	17.63
	Elution	5	1.65	16.5	98.83
I646A	Full Lysate	40	2.56	204.8	8.99
	Clarified	35	1.77	123.9	8.43
	Elution	8	1.71	27.36	99.61

Table 3.2: Purification Table of samples with HS was constructed by scanning SDS-PAGE gels with ImageJ software.

Protein	Sample	Volume (mL)	Concentration (mg/mL)	Yield (mg/L culture)	Purity (%)
WT + HS	Full Lysate	40	2.09	167.2	10.08
	Clarified	35	1.60	112	14.17
	Elution	15	1.61	48.3	89.73
I646V + HS	Full Lysate	40	1.02	81.6	11.90
	Clarified	35	0.85	59.5	10.08
	Elution	5	1.15	11.5	98.90
I703V + HS	Full Lysate	40	2.29	183.2	26.30
	Clarified	35	1.49	104.3	23.66
	Elution	7.5	1.01	15.15	94.74
I646V-I703V + HS	Full Lysate	40	2.40	192	7.38
	Clarified	35	1.58	110.6	7.10
	Elution	5.5	1.14	6.27	92.50
I646A + HS	Full Lysate	40	2.22	177.6	28.23
	Clarified	35	2.03	142.1	18.57
	Elution	7.5	1.64	24.6	92.27

3.4.7. UV-Vis Spectrum of hXOR

The A_{280}:A_{450} ratio was calculated using the Eppendorf BioSpectrometer® kinetic spectrophotometer for each sample and a typical scan of hXOR was plotted, to check the absorbance of tyrosine and tryptophane residues at A_{280}, the absorption of [2Fe-2S] centres at A_{350}, and the absorption of FAD domain at A_{450}. The A_{280}:A_{450} ratio was used to determine the purity of the samples, with values 4-6 indicating a pure sample (Bray, 1975). The purity values of 4–6 were calculated under the assumption that the content of FAD is 100%.

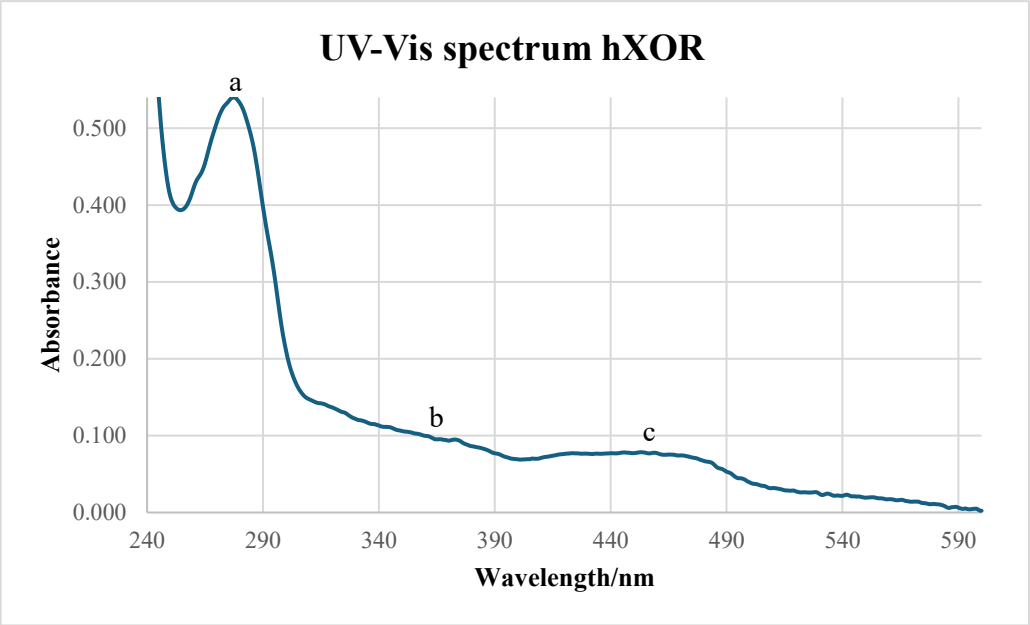

Figure 3.13: Typical plot of hXOR. Peak a has maximum at A_{280} due to the UV absorption from tyrosine and tryptophan residues. Peak b has a maximum at A_{350} due to the absorption of the [2Fe-2S] centres. Peak c has a maximum at A_{450} due to the UV absorption of the FAD domain.

Table 3.3: A_{280}:A_{450} Ratio of hXOR samples was measured using the BioSpectrometer® from Eppendorf to determine the purity of the samples.

Protein	A_{280}	A_{450}	A_{280}:A_{450} Ratio
WT	1.53	0.24	6.4
WT + HS	1.18	0.20	5.9
I646V	0.55	0.11	5.0
I646V + HS	0.84	0.22	3.8
I703V	1.09	0.21	5.2
I703V + HS	0.74	0.13	5.7
I646V-I703V	1.21	0.28	4.3
I646V-I703V + HS	0.84	0.21	4.0
I646A	1.23	0.24	5.1
I646A + HS	1.20	0.25	4.8

3.5. Protein Characterisation

3.5.1. In-gel Nitro Blue Tetrazolium Assay

The NBT assay using 5% (w/v) Native-PAGE gel showed that hXOR I646V with no HS, I703V+HS and I646V-I703V without and with HS were the most active compared to the other protein samples (lanes 3,6,7, and 8, respectively). The bands shown in the NBT assay gel indicate the presence and the activity of oligomers particularly in the samples that are most active.

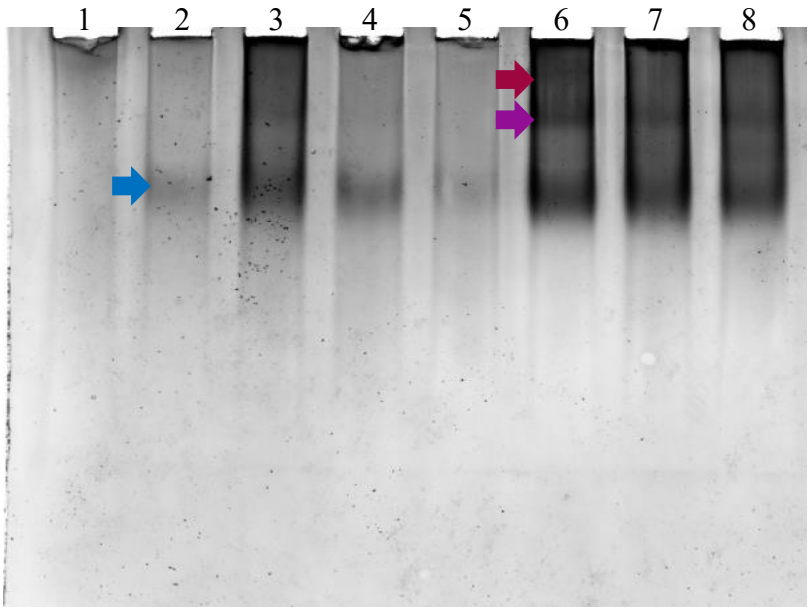

Figure 3.14: 5%(w/v) Native-PAGE gel NBT Assay (10 µg). Lane 1 –WT; Lane 2 – WT+HS; Lane 3 –I646V; Lane 4 –I646V+HS; Lane 5 –I703V; Lane 6 –I703V+HS; Lane 7 –I646V-I703V; Lane 8 – I646V-703V+HS. The blue arrow indicates the supposed dimeric state while the purple and red arrow possibly show the oligomeric states.

The Coomassie Blue stained 5% (w/v) Native-PAGE gel was prepared in parallel. This gel showed the presence of higher molecular weight bands that suggests oligomerisation. The in-gel assay (Figure 3.15) showed that these bands also exhibit XOR activity.

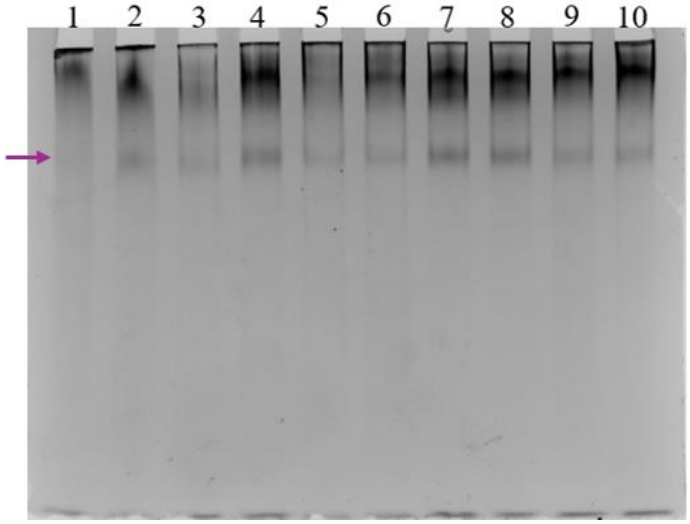

Figure 3.15: 5% Native gel (10 µg). Lane 1 – WT, Lane 2 – WT+HS, Lane 3 – I646V, Lane 4 – I646V+HS, Lane 5 – I703V, Lane 6 – I703V+HS, Lane 7 – I646V-I703V, Lane 8 – I646V-I703V + HS, Lane 9 – I646A, Lane 10 – I646A + HS.

3.5.2. NBT Based Colorimetric Assay

The NBT based colorimetric assay was also used to assess the activity of the hXOR samples (Section 2.5.2). In a 96-well microtiter plate, 100 µL of the protein sample was mixed with 100 µL of the NBT solution. The reaction mixture was placed in the Tecan Spark® Multimode Microtiter Plate Reader and the XOR activity was monitored at room temperature for 20 minutes. A positive control, the bovine XOR, was also included in the experiment. XOR activity was observed in almost all hXOR samples to different degrees, with WT+HS having the lowest activity on Figure 3.16.

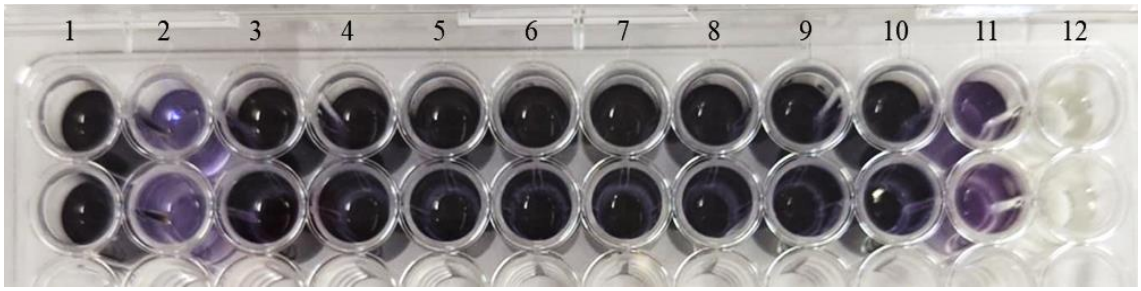

Figure 3.16: NBT Assay of hXOR samples (50 µg). Lane 1 – WT, Lane 2 – WT+HS, Lane 3 – I646V, Lane 4 – I646V+HS, Lane 5 – I703V, Lane 6 – I703V+HS, Lane 7 – I646V-I703V, Lane 8 – I646V-I703V+HS, Lane 9 – I646A; Lane 10 – I646A+HS; Lane 11 – bovine XOR; Lane 12 – PBS buffer.

Table 3.4: Amount of reactive oxygen species produced by hXOR samples using nitro blue tetrazolium assay. This table displays the concentration of product measured in µM at time 0 and after 20 minute incubation period. Measurements were performed using the Tecan Spark® Multimode Microtiter Plate Reader.

XOR samples	Amount of Product produced at time 0/µM	Amount of Product produced after 20 min/µM
WT	1.15	7.69
WT+HS	0.43	0.60
I646V	0.57	9.97
I646V+HS	1.86	29
I703V	1.28	13.9
I703V+HS	1.66	24.7
I646V-I703V	2.67	53
I646V-I703V+HS	1.18	20.1
I646A	0.97	20.2
I646A+HS	0.79	12.7
Bovine XOR	43	55.7

As shown in Table 3.4, product formation was already detectable immediately after mixing the protein with NBT. This occurred because there was a delay between pipetting the reaction mixture and placing the plate in the Tecan Spark® Multimode

Microtiter Plate Reader, allowing some product to form before the time-zero measurement. The amount of product produced (µM) was calculated by using the absorbance and the extinction coefficient of NBT at 12,800 $M^{-1}cm^{-1}$.

3.5.3. Blue Native-PAGE Gel

Blue-Native PAGE was used to resolve the proteins in their native conformation by mass and not by charge. hXOR samples were electrophoresed in a Blue Native-PAGE (Thermo Fisher Scientific) gel to determine the oligomerisation state of the purified protein and the approximate size of the oligomers. The dimer state is shown in the blue native gel close to 272 kDa. There are also oligomeric states in the samples, with a prominent band at 545 kDa, which is approximately twice the size of the dimer. Protein deposits are also visible in the wells.

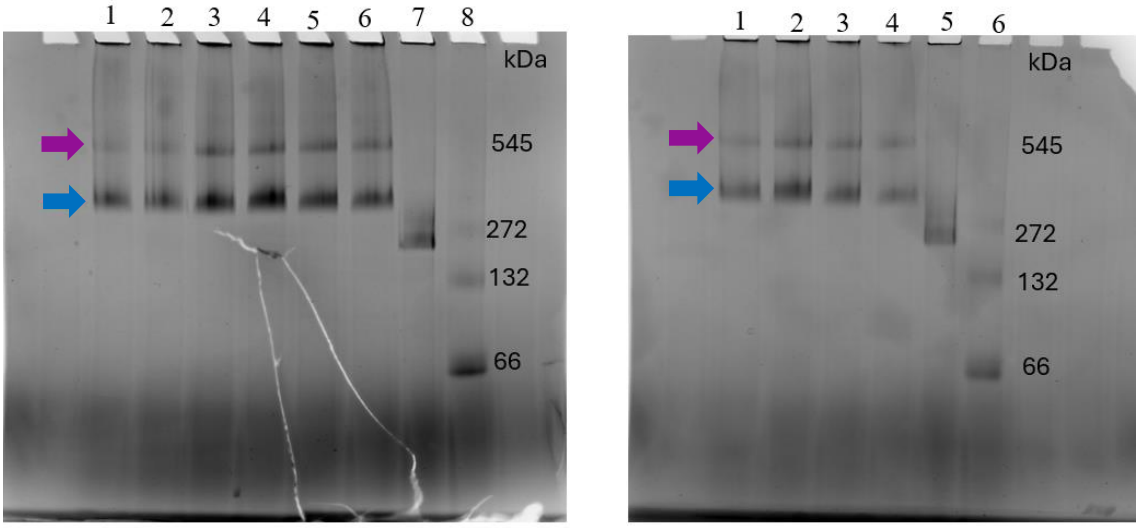

Figure 3.17: Blue Native Gel hXOR samples (12.5 µg). A – Lane 1 – WT, Lane 2 – WT+HS; Lane 3 – I646V; Lane 4 – I646V+HS; Lane 5 – I703V; Lane 6 – I703V+HS; Lane 7 – 5 µg molecular markers urease from Jack Bean; Lane 8 – 2.5 µg molecular weight marker albumin from bovine serum (Sigma-Aldrich). B – Lane 1 – I646V-I703V; Lane 2 – I646V-I703V+HS; Lane 3 – I646A; Lane 4 – I646A+HS; Lane 5 - 5 µg molecular markers urease from Jack Bean; Lane 6 – 2.5 µg molecular weight marker albumin from bovine serum (Sigma-Aldrich). The blue arrow shows the dimer state, while the purple arrow indicates the oligomeric state.

3.5.4. Enzymatic Activity

The activity of the XOR protein samples was measured by monitoring the rate of oxidation of xanthine to uric acid through a spectrophotometric assay at a wavelength of 295 nm. From the equation below, one unit of hXOR is the amount of XOR that will convert 1.0 µmole of xanthine to uric acid per minute at 25°C. The extinction coefficient of uric acid at A_{295} is 9.6 mM^{-1} cm^{-1} and [W] denotes the concentration in mg/mL of the hXOR sample, which in this case was 0.15 mg/mL for all the samples used (Avis et al., 1956).

$$\text{Units per mg enzyme} = \frac{\Delta A295/minTest - \Delta A295/minBlank}{9.6(W)}$$

The activity assay was conducted for both XO and XOR forms of the enzyme. XOR form represents the activity of both XO and XDH forms together. The XOR form activity assay was conducted to determine the amount of XO and XDH in the samples tested. For all activity assays the absorbance increased over time.

For the XO form activity assay, all of the variants exhibited higher enzymatic activities compared to WT hXOR, with I646A showing the highest activity. I703V had the lowest activity out of all variants tested. In general, all samples without HS (Figure 3.18) showed a positive correlation with high R-squared values.

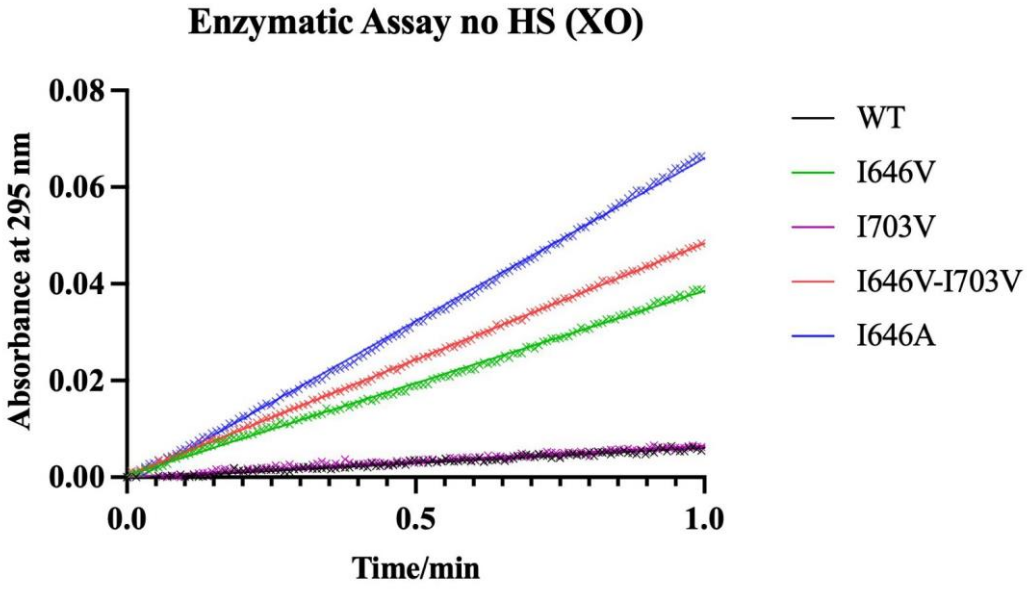

Figure 3.18: Activity assay of untreated hXOR samples in XO form (n=3). Activity was determined by monitoring the production of uric acid via absorbance at 295 nm over 1 minute using oxygen as the substrate. All assays were performed using 0.15 mg/mL.

Similar to the untreated samples, the treated hXOR samples (Figure 3.19) also exhibited a strong positive correlation, with R-squared shown in Table 3.6. Overall, HS treatment exhibited both negative and positive impacts on the activity, since it decreased the activity of I646A and I646V, but increased the activity of the other variants and WT. The activity of WT remained the lowest among all samples.

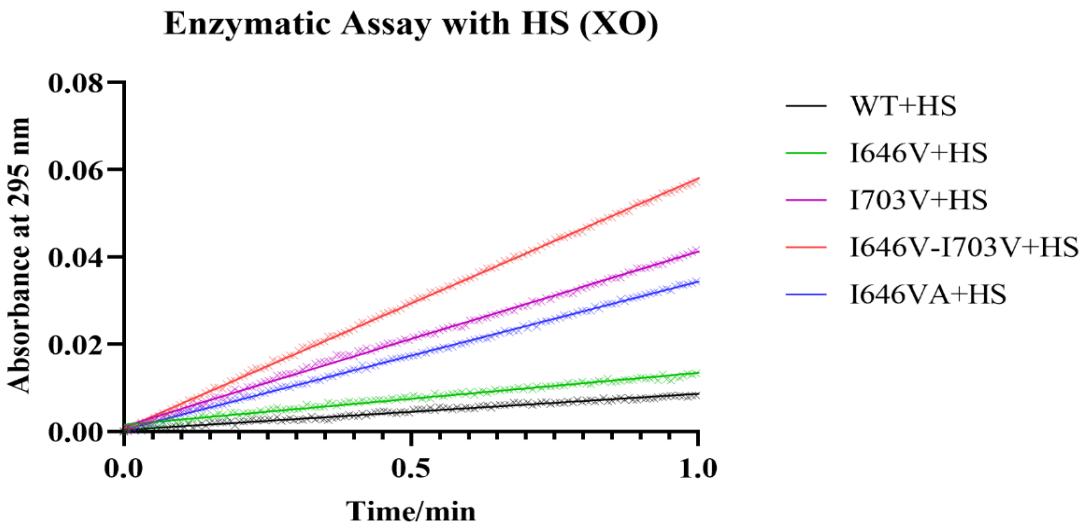

Figure 3.19: Activity assay of HS treated hXOR samples in XO form (n=3). Activity was determined by monitoring the production of uric acid via absorbance at 295 nm over 1 minute using oxygen as the substrate. All assays were performed using 0.15 mg/mL.

The activity for samples in the XO form without and with HS, which was performed in triplicates, was calculated and the results are shown in Table 3.5.

Table 3.5: The specific activity of all the hXOR samples was calculated (XO form).

hXOR	Activity (U/mg)	R-squared values
WT	0.00452 ± 0.00006	0.9779
WT+HS	0.00569 ± 0.00007	0.9836
I646V	0.02660 ± 0.00011	0.9988
I646V+HS	0.00715 ± 0.00009	0.9810
I703V	0.00625 ± 0.00015	0.9623
I703V+HS	0.02750 ± 0.00010	0.9987
I646V-I703V	0.03278 ± 0.00006	0.9995
I646V-I703V+HS	0.03896 ± 0.00001	0.9996
I646A	0.04604 ± 0.00015	0.9995
I646A+HS	0.02243 ± 0.00006	0.9989

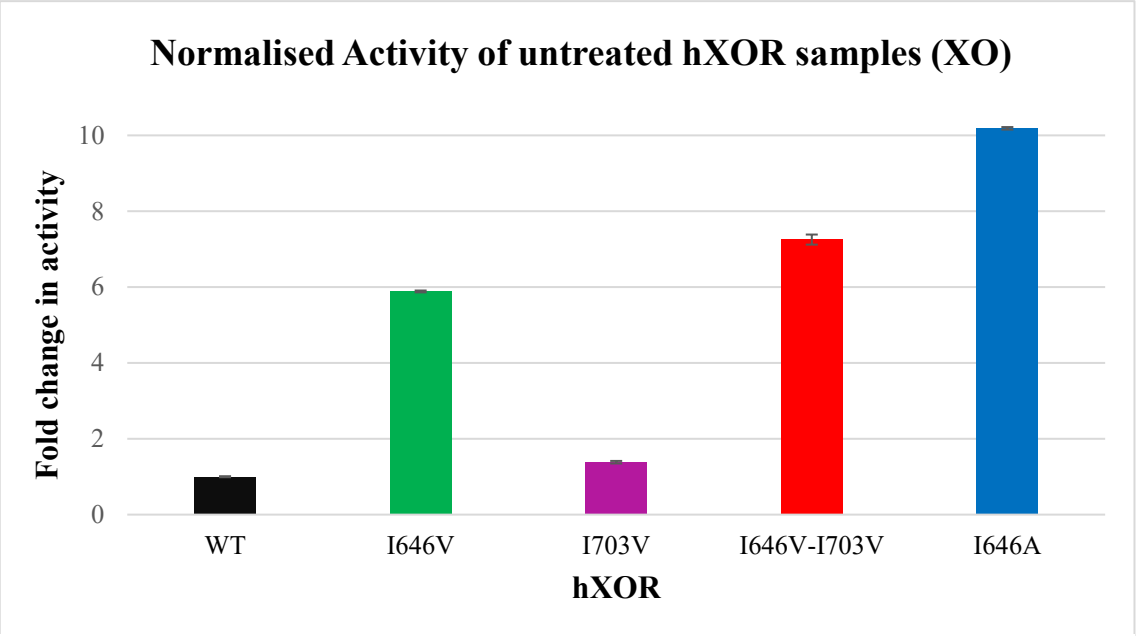

Figure 3.20: Fold change in enzymatic activity of untreated hXOR samples in Xanthine Oxidase form. Activities were normalised to the wild type hXOR, which is set to a value of 1.

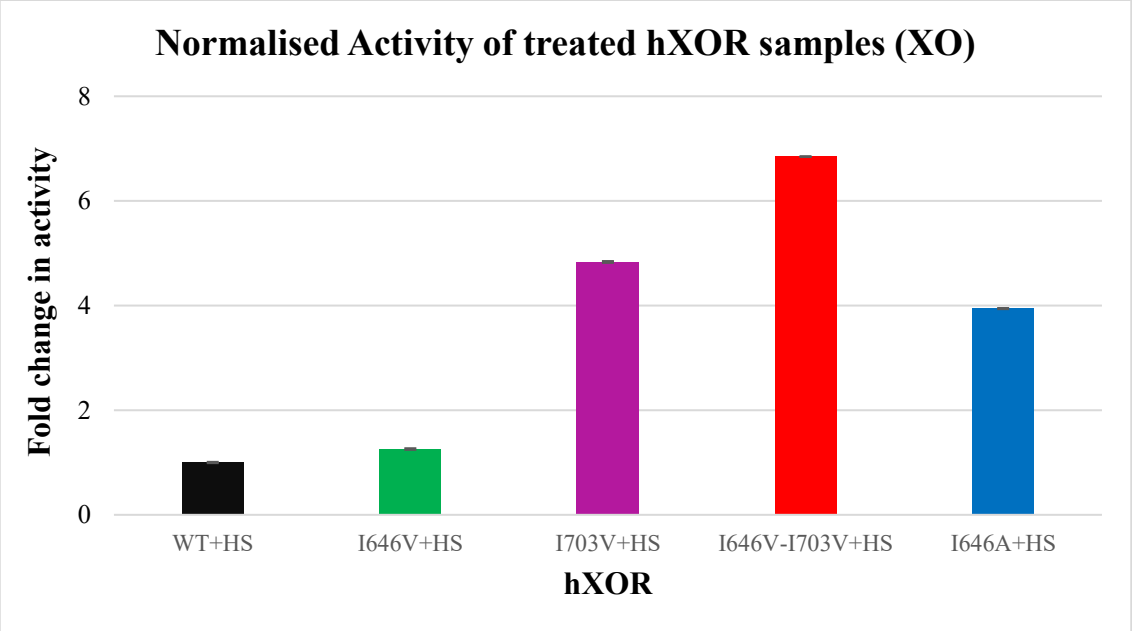

Figure 3.21: Fold change in enzymatic activity of treated hXOR samples in Xanthine Oxidase form. Activities were normalised to the wild type hXOR, which is set to a value of 1.

For the XOR activity assay, the activity of both untreated and treated samples for total XOR was calculated, with the results presented in Table 3.6 and Figures 3.22 and 3.23. Like the untreated samples in the XO form, the untreated I646A exhibited the highest enzymatic activity. Overall, all variants exhibited higher enzymatic activities compared to the WT hXOR.

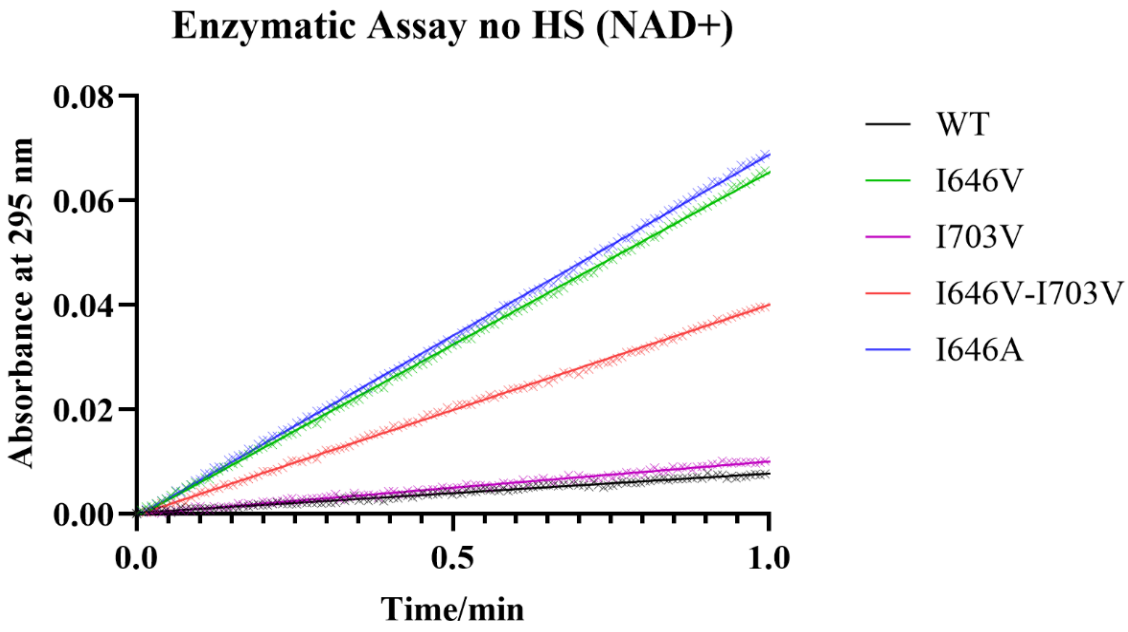

Figure 3.22: Activity assay of untreated hXOR samples of total XOR (n=3). Activity was determined by monitoring the production of uric acid via absorbance at 295 nm over 1 minute using NAD^+ as the substrate. All assays were performed using 0.15 mg/mL.

Amongst the HS samples, I703V+HS was the most active. The treatment with HS in this case had a positive impact on the activity regarding most of the samples, except I646V and I646A, for which it caused a lower activity.

In both the XO form and total XOR, the variant samples exhibited higher enzymatic activities than the WT. However, HS treatment showed a similar effect with XOR and XO forms, decreasing the activity of the same samples. In all samples, the XOR form exhibited higher enzymatic activity than the XO form since it shows the activity of XO and XDH combined.

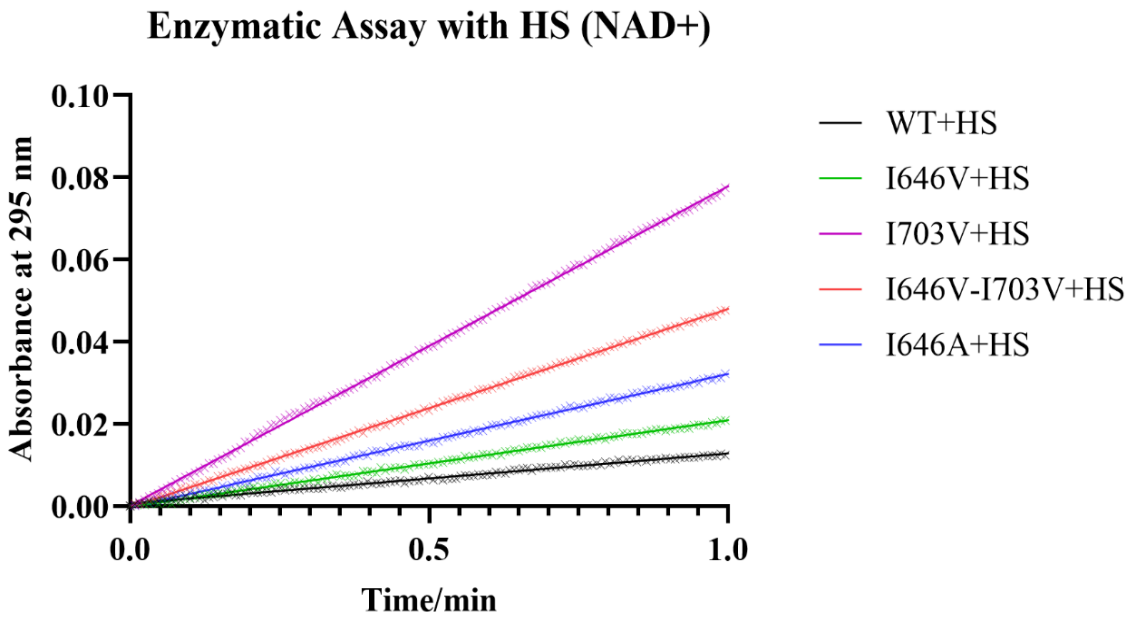

Figure 3.23: Activity assay of treated hXOR samples of total XOR (n=3). Activity was determined by monitoring the production of uric acid via absorbance at 295 nm over 1 minute using NAD^+ as the substrate. All assays were performed using 0.15 mg/mL.

Table 3.6: The specific activity of all the hXOR samples was calculated (total hXOR).

hXOR	Activity (U/mg)	R-squared values
WT	0.00521 ± 0.00005	0.9864
WT+HS	0.00847 ± 0.00006	0.9936
I646V	0.04556 ± 0.00009	0.9995
I646V+HS	0.01458 ± 0.00006	0.9979
I703V	0.00715 ± 0.00006	0.9899
I703V+HS	0.05326 ± 0.00010	0.9995
I646V-I703V	0.02833 ± 0.00008	0.9989
I646V-I703V+HS	0.03340 ± 0.00006	0.9996
I646A	0.04806 ± 0.00010	0.9995
I646A+HS	0.02243 ± 0.00006	0.9989

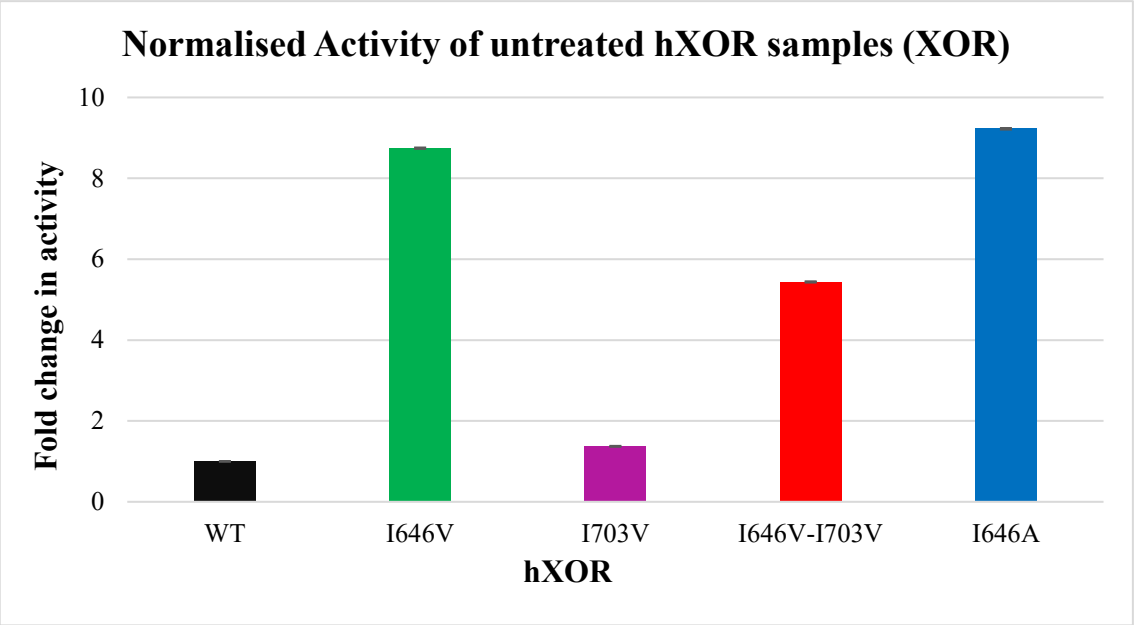

Figure 3.24: Fold change in enzymatic activity of untreated hXOR samples for total XOR. Activities were normalised to the wild type hXOR, which is set to a value of 1.

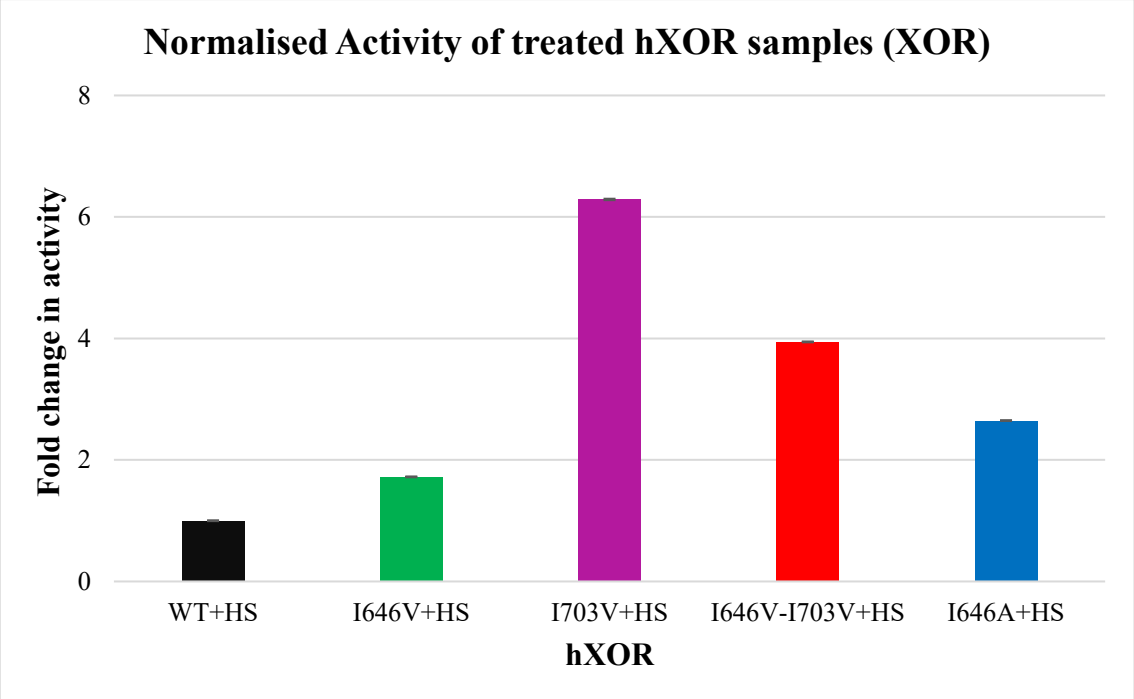

Figure 3.25: Fold change in enzymatic activity of treated hXOR samples for total XOR. Activities were normalised to the wild type hXOR, which is set to a value of 1.

To calculate the percentage of hXDH (Table 3.7), the below equation was used:

$$\%hXDH = \frac{U_{hXOR}}{(U_{hXO} \times \frac{350}{452}) + U_{hXOR}} \times 100$$

Where:

U_{hXOR} is the total activity of hXOR

U_{hXO} is the activity of hXO

350 and 452 are the assumed activities of typical reduced and oxidised XOR forms.

Table 3.7: The percentage composition of XDH and XO forms was determined based on the total activity of hXOR samples.

Sample	%hXDH	%hXO	Normalised activity (hXO 100%)	% Activity change against WT
WT	59.83788	40.16212	0.011241	100
WT+HS	65.76976	34.23024	0.016636	148
I646V	68.86627	31.13373	0.085429	760
I646V+HS	72.47461	27.52539	0.025986	231
I703V	59.64436	40.35564	0.003739	138
I703V+HS	71.4394	28.5606	0.096287	857
I646V-I703V	52.74816	47.25184	0.069368	617
I646V-I703V+HS	52.54518	47.45482	0.082096	730
I646A	57.40905	42.59095	0.108102	962
I646A+HS	56.3591	43.6409	0.051398	457

As shown in Table 3.7, most samples displayed a predominance of hXDH form over hXO form, indicating that the enzyme exists mainly in its dehydrogenase form. To ensure a meaningful comparison amongst the samples, the measured XO activity was normalised. This normalisation was calculated by taking the activity of the XO form and extrapolating it to an assumed 100% XO protein amount. This was calculated based on a direct proportionality for the estimated percentages of the XO form, determining the activity if the hXOR was 100% present as XO. The XO form was chosen as it is the main contributor for ROS production. Furthermore, the activity of the XO can be directly

calculated using the XO assay, while this is not possible for the XDH form. The activities were then compared with the WT activity. The results showed that I646A was the most active out of all the samples, with 962% greater activity than the WT. Conversely, out of all the variants, I703V showed the least activity, with 138% greater activity than the WT.

The uric acid enzymatic assay was also conducted to assess the activity of all hXOR samples after a 10-minute incubation at different temperatures, specifically at 25ºC, 30ºC, 37ºC, 42ºC, and 50ºC. The data was normalised within each temperature to allow direct comparison between the samples. For each hXOR sample, the temperature yielding the highest activity was set to 1, and all other activities at different temperatures for that specific sample were expressed as a proportion of this maximum. For the untreated samples, WT, I703V, and the double variant I646V-I703V hXOR exhibited their highest enzymatic activity after 25ºC incubation, whereas I646A variant showed peak activity after the 30ºC incubation, and I646V after the 37ºC incubation (Figure 3.26). In general, I646V-I703V and I646A samples are more resistant to high temperatures compared to the rest of the samples.

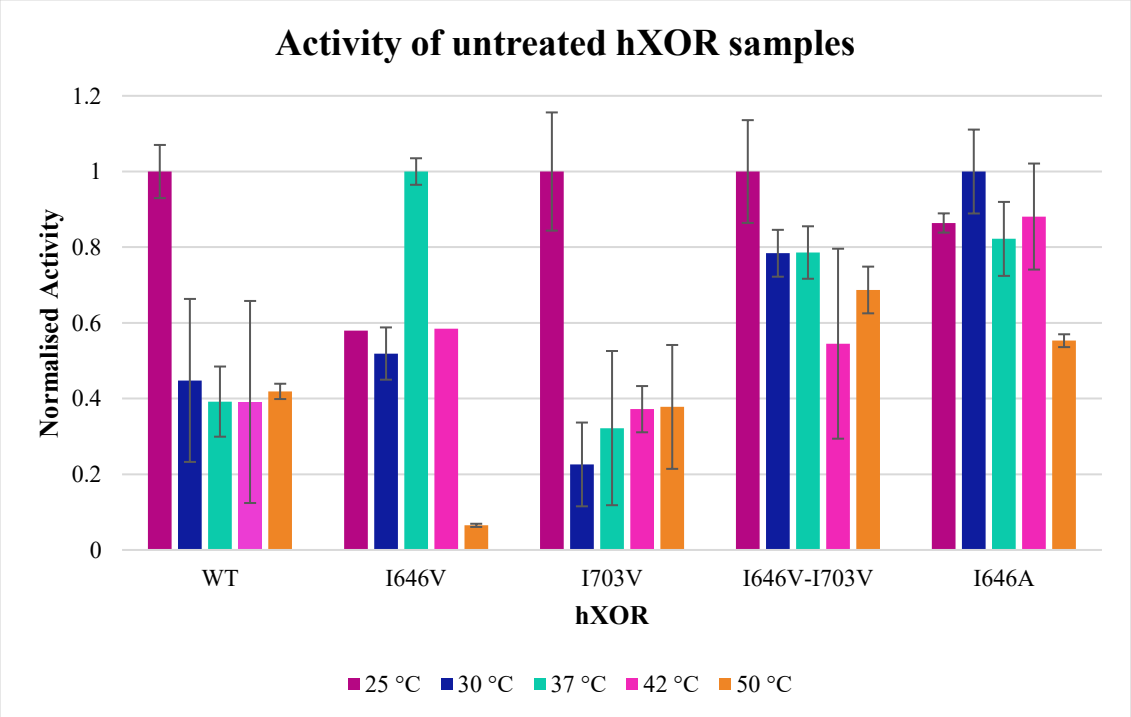

Figure 3.26: Activity assay of untreated hXOR samples at different temperatures (n=3). Normalised activity was measured across a temperature range of 25°C to 50°C**.** For each sample, the temperature at which it exhibited maximum activity was set to value of 1.

In contrast, heat-shocked hXOR samples displayed altered activity patterns compared to their untreated counterparts, except from WT hXOR. Specifically, WT+HS, I646V+HS, I646V-I703V+HS maintained their highest activity after 25°C incubation, whereas I703V+HS and I646A+HS exhibited maximal activity after 30°C incubation.

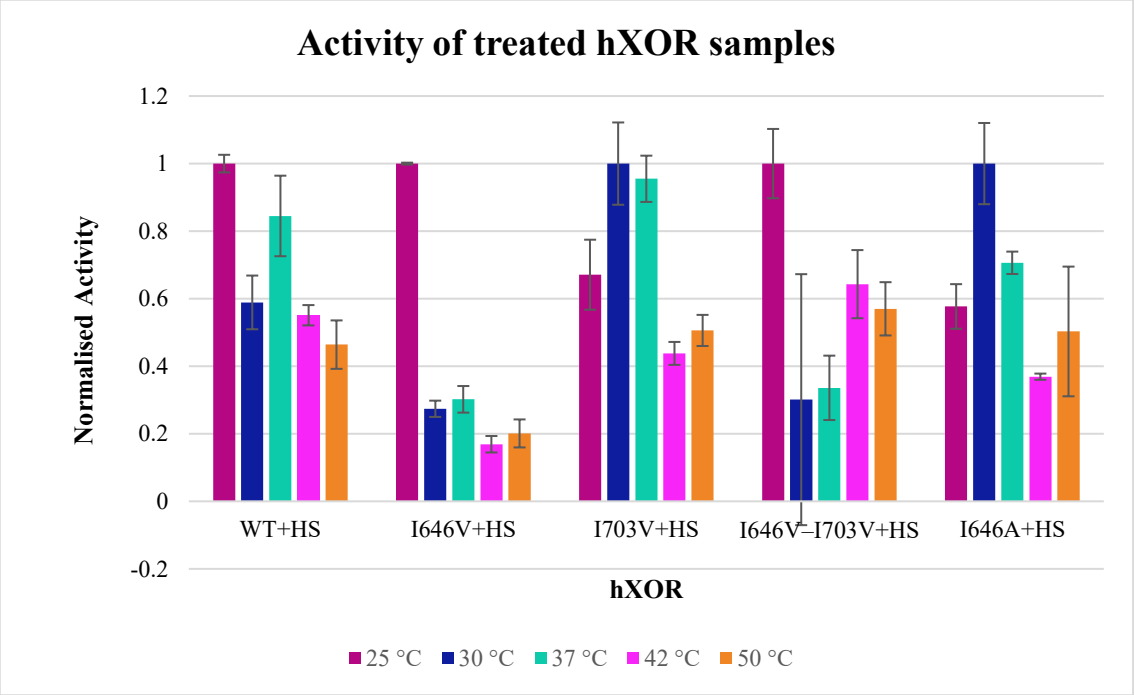

Figure 3.27: Activity assay of treated hXOR samples at different temperatures (n=3). Normalised activity was measured across a temperature range of 25°C to 50°C**.** For each sample, the temperature at which it exhibited maximum activity was set to value of 1.

3.5.5. Circular Dichroism

Circular dichroism was carried out across a wavelength range between 180 and 260 nm, with a monochromator wavelength of 222 nm, bandwidth of 4, step size of 0.5, time per point at 0.5 and 5 repeats. The raw data was analysed using the BestSel software. 'Helix' refers to the alpha helices, 'Antiparallel' and 'Parallel' refer to beta sheets, 'Turn' refers to beta turns, and 'Others' refer to the intrinsically disordered, or flexible regions of the protein.

Table 3.8: hXOR secondary structure content (n=5). The data shows the percentage of structural components for untreated and treated hXOR samples.

Protein	Helix (%)	Antiparallel (%)	Parallel (%)	Turn (%)	Others (%)
WT	7.4	32.1	0.6	13.6	46.4
WT + HS	11.9	22.7	7.5	12.4	45.5
I646V	5.9	31.5	3.9	12.8	45.9
I646V + HS	10.1	21	7.1	14.1	47.7
I703V	11.8	27.4	5.1	12.2	43.5
I703V + HS	16.6	19.4	7.1	13.5	43.3
I646V-I703V	5.9	34.1	0.7	13.3	45.9
I646V-I703V + HS	25	0.7	9.4	13.7	51.2
I646A	13.9	21.4	8.2	12.6	43.9
I646A + HS	8.9	29.6	4.8	12.7	44

In general, when grown without HS, the hXOR samples exhibited similar secondary structures. The highest percentage of alpha helices is 13.9%, observed in I646A, whilst the rest of the samples have lower percentages of alpha helices from 5.9 – 11.8%. With respect to antiparallel beta strands, the samples had close percentages of 21.4 – 34.1%, with I646V-I703V having the highest amount, whereas I646A had the lowest amount. WT hXOR, as well as I646V-I703V, had very low percentages of parallel beta strands, compared to the rest of the samples, specifically 0.6% and 0.7% respectively, whereas I646A had the highest number with 8.2%. All samples had similar percentages of beta turns, while the largest percentage in each case is found in others, but with similar values amongst the samples.

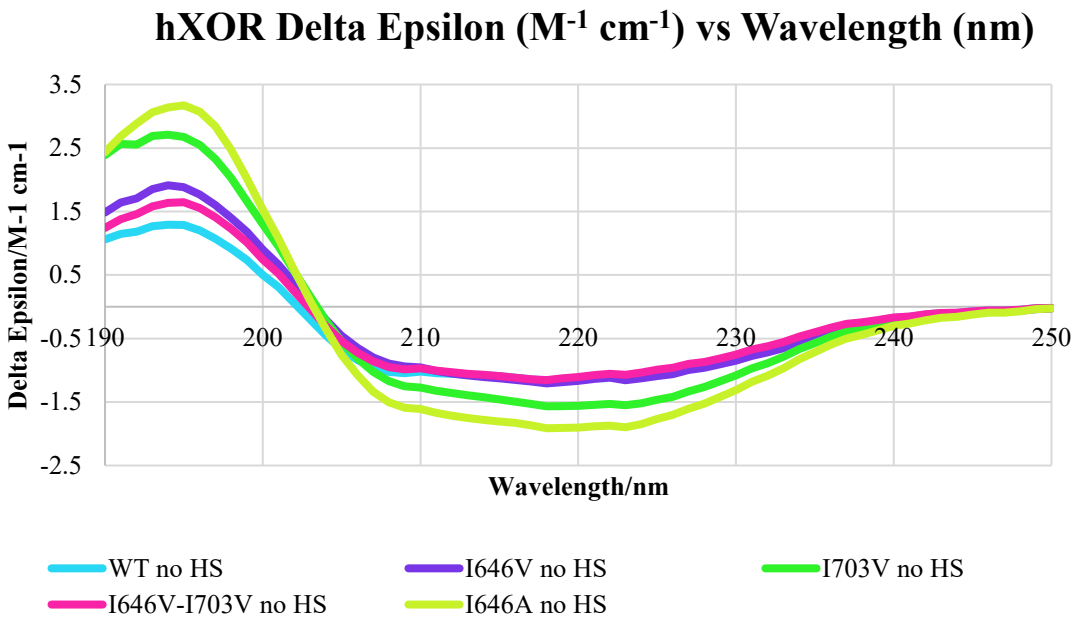

Figure 3.28: CD spectrum of untreated hXOR samples. All protein samples were prepared at a concentration of 0.2-0.3 mg/mL.

Upon the treatment with HS, some changes in the secondary structure composition of hXOR samples were observed. The highest alpha helix content (25%) was found in I646V-I703V+HS, while the other samples ranged between 8-9 – 16.6%. In contrast, the proportion of antiparallel beta strands generally decreased following HS treatment, with values ranging from 0.7 – 29.6%, and I646V-I703V+HS showing the lowest content. Parallel beta strands increased across most treated samples, ranging from 4.8 – 9.4%, relative to the untreated forms. The percentages of beta turns remained largely unchanged after treatment, while the 'others' continued to account for the largest fraction of the secondary structure, showing only minor variation among the samples.

In general, the variants did not have major effects on the contents of the secondary structure, since the percentages were similar to the WT hXOR.

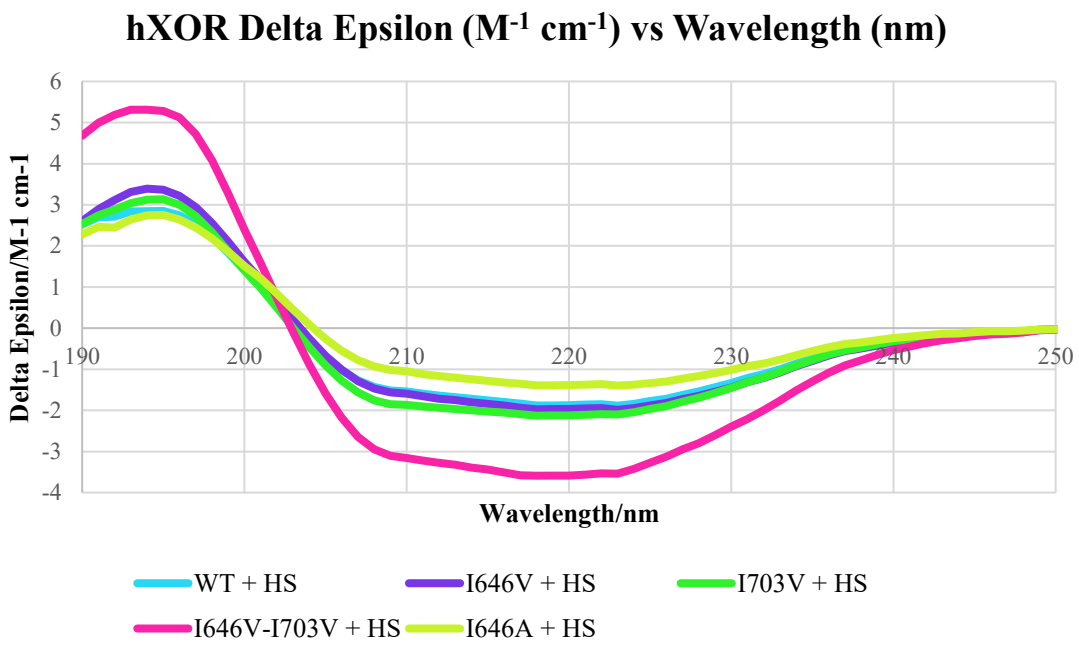

Figure 3.29: CD spectrum of treated hXOR samples. All protein samples were prepared at a concentration of 0.2-0.3 mg/mL.

3.5.6. Melting temperatures

A temperature gradient of 1°C.min-1, ranging from 20°C to 90°C was applied. The increase in the unfolded fraction of the protein was monitored, by measuring the fluorescent signal at 222 nm. The melting temperature was calculated by fitting the signal ratio to a Boltzmann sigmoidal equation using non-linear regression.

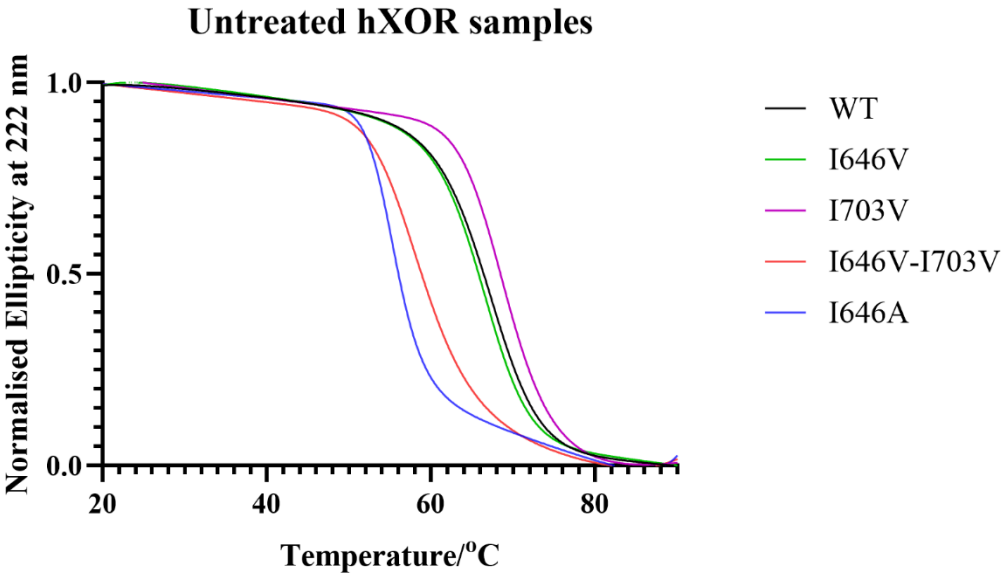

Figure 3.30: Melting temperature of untreated hXOR samples (n=1). The samples were subjected to temperatures ranging from 20°C to 90°C.

The melting temperature (T_M) obtained from temperature ramps is extrapolated at an unfolded fraction of normalised ellipticity at 222 nm of 0.5. This shows that the melting temperature is the temperature require to unfold by 50%.

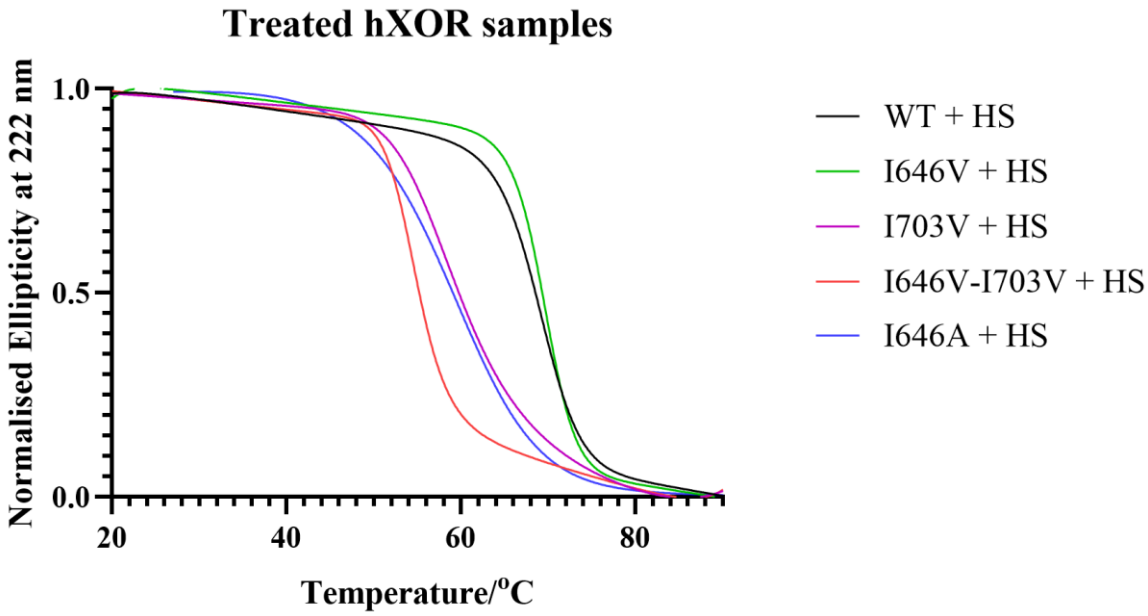

Figure 3.31: Melting temperature of treated hXOR samples (n=1). The samples were subjected to temperatures ranging from 20°C to 90°C.

Table 3.9: Melting Temperatures (T_m) for hXOR samples (n=1). The table shows the Tm values derived from the midpoint of the protein unfolding curve.

hXOR samples	Tm (°C)	+/- Tm	R squared value
WT	66.8	0.18	0.9997
WT+HS	68.89	0.21	0.9994
I646V	66.08	0.14	0.9997
I646V+HS	69.5	0.13	0.9995
I703V	69.74	0.73	0.9988
I703V+HS	59.55	0.91	0.999
I646V-I703V	59.04	0.64	0.9988
I646V-I703V+HS	54.79	0.20	0.999
I646A	55.49	0.21	0.9989
I646A+HS	58.37	1.57	0.9993

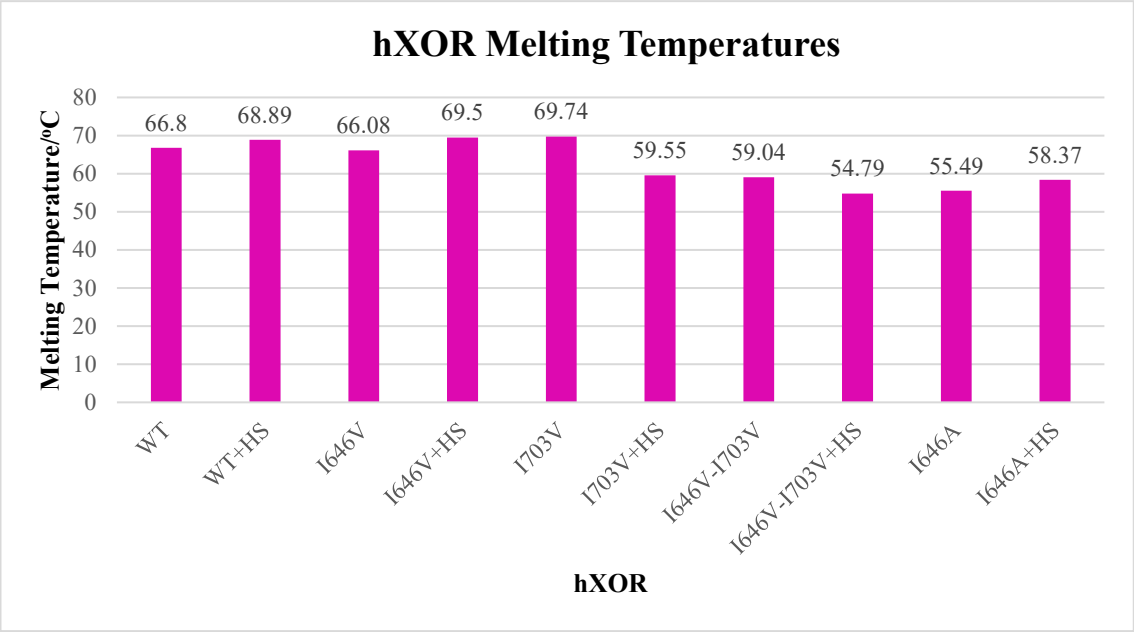

Figure 3.32: Melting Temperatures for hXOR. The Tm values reflect the thermal stability of each protein sample.

The most thermally unstable sample was I646V-I703V+HS, with a melting temperature of 54.79ºC while the most thermally stable protein sample was I703V, with a melting temperature of 69.74ºC. The rest of the samples had either high melting temperatures ranging between 66.08 – 69.5ºC or lower melting temperatures between 55.49 – 59.55ºC.

3.5.7. Thioflavin T (ThT) Assay

Thioflavin T (ThT) dye fluorescence was used to monitor the formation of amyloid fibrils (Section 2.7.3). Amyloid fibrils are very stable and are composed predominantly of β-sheet secondary structures, forming a cross-β core in which β-strands assemble into sheets that are oriented at right angles to the long axis fibre (Gras, 2009). Amyloid aggregation is divided into three distinct phases: an initial lag or nucleation phase, during which monomers associate to form nuclei; an exponential phase, characterised by polymerisation and fibril elongation; and a final saturation phase, where monomer depletion leads to fibril maturation through lateral association (Invernizzi et al., 2012).

In the presence of protein samples rich in cross-β-sheets, ThT gives fluorescence intensity at the excitation wavelength of 440 nm and emission at 480 nm. However, in the absence of amyloid, ThT exhibits excitation peak at 350 nm and emission peak at 438 nm (Chandel et al., 2018).

To optimise the concentration of protein used for the ThT assays, different concentrations of WT hXOR were used. The samples were incubated at 37°C in PBS buffer with shaking. The fluorescence values were normalised by subtracting the first reading so that each curve began at zero. The data was then fitted using a hyperbola fit with GraphPad. This fit was used as it produced the best R-squared values as well as this fit is used to study ligand binding, which in this case it was the ThT binding to the fibrils.

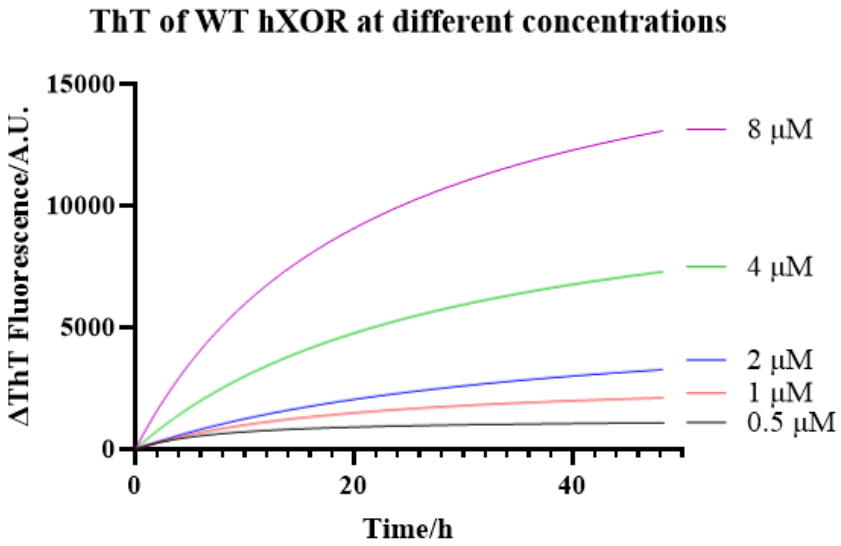

Figure 3.33: ThT assay of WT hXOR at different concentrations (n=2). The assay was done at 37°C with orbital shaking at a frequency of 510 rpm with a shaking amplitude of 1 mm.

As shown in Figure 3.33, 8 μM of hXOR had the highest ThT fluorescence as well as the highest R-squared value and thus this concentration was adopted for the ThT assays of all the hXOR samples.

Table 3.10: R-squared value for each concentration of WT hXOR.

Concentration of WT (μM)	R-squared value
0.5	0.9328
1	0.9661
2	0.9838
4	0.9936
8	0.9979

Thus, the ThT assay was performed at a protein concentration of 8 µM for both untreated and heat-shocked hXOR samples. Under these conditions, WT, WT+HS, I646V, I646V-I703V, and I703V+HS formed amyloid fibrils at 37°C in PBS buffer, as indicated by the increase in the ThT fluorescence signal over time (Figures 3.34 and 3.35) while, under these conditions I703V and I646V do not.

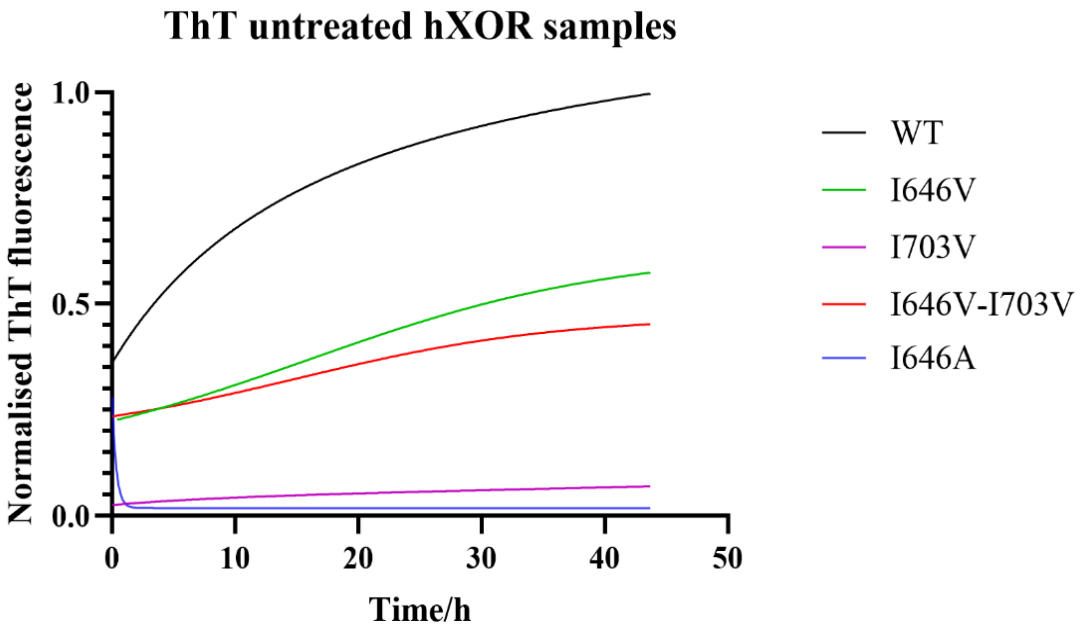

Figure 3.35: ThT assay of untreated hXOR samples. The assay was done at 37°C with orbital shaking at a frequency of 510 rpm with a shaking amplitude of 1 mm.

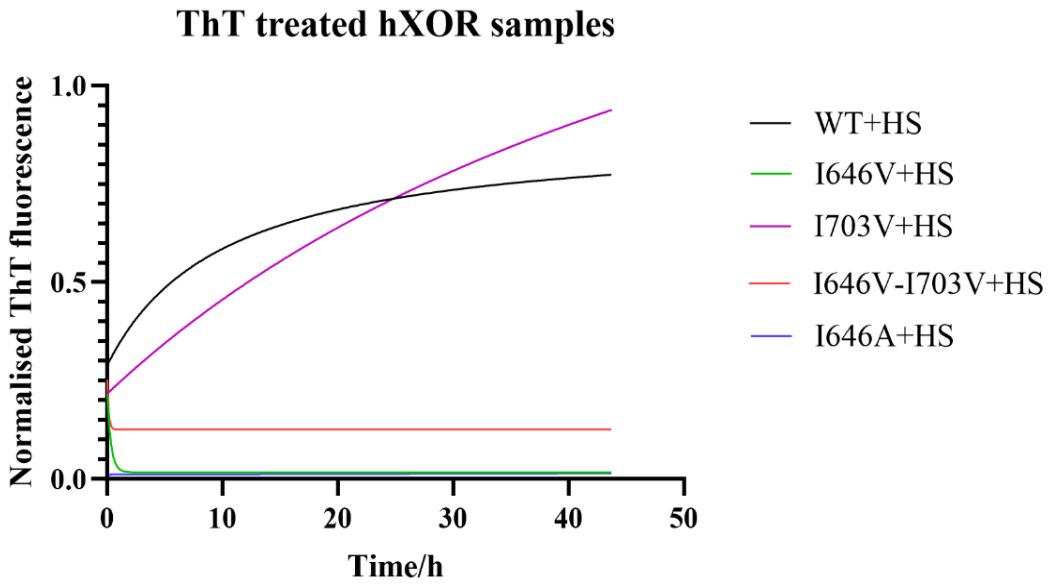

Figure 3.34: ThT assay of treated samples. The assay was done at 37°C with orbital shaking at a frequency of 510 rpm with a shaking amplitude of 1 mm.

To obtain a typical sigmoidal aggregation curve, the ThT assay was repeated at room temperature using 1 µM WT hXOR (Figure 3.36). A low concentration and temperature were used to slow down the initial fibril formation to obtain the first lag segment. The curve features a lag phase, a rapid exponential growth phase, and a plateau phase. The time it took for 50% the fibrils to form was 18.3 ± 0.4 h.

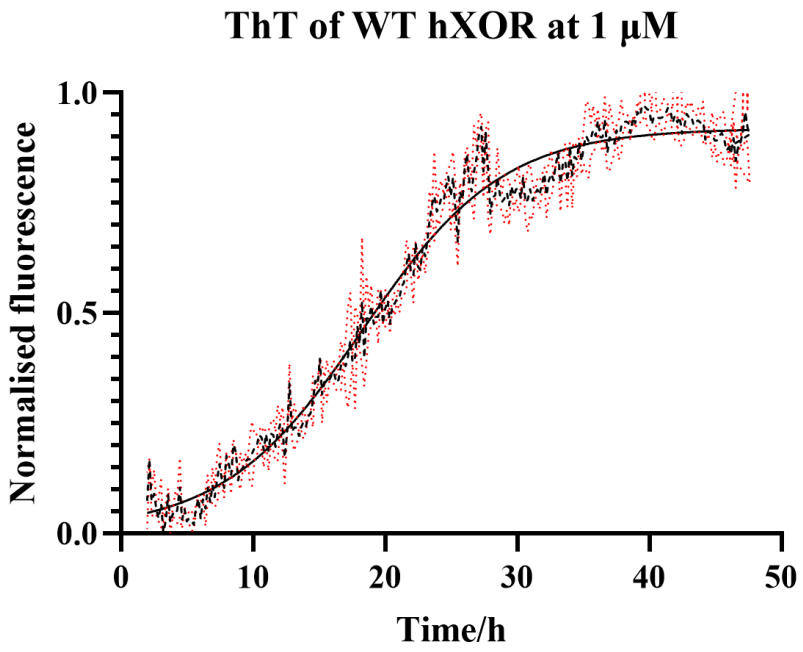

Figure 3.36: Sigmoidal curve of 1 µM WT. The black line represents the fitted values of normalised fluorescence, the black dotted line indicates the normalised fluorescence data, and the red dotted line represents the error bars. R-squared value is 0.9736, n=2.

3.5.8. Native-PAGE gel of samples following ThT incubation

The protein samples used in the ThT assay were collected from the microtiter plate and subsequently loaded onto a 5% native gel to examine their oligomeric state. The Coomassie Blue stained 5% Native-PAGE gel (Figure 3.37) showed multiple bands that indicate that oligomers were present in the samples. Various bands of hXOR samples exhibited different mobility in the Native PAGE gel compared to WT, indicating differences in overall charge, size and shape. The gel shows that all the samples are possibly present in both dimeric and oligomeric state. However, since it is a native gel it cannot be concluded that the dimeric form of the protein samples is present. Protein deposits were observed in the wells.

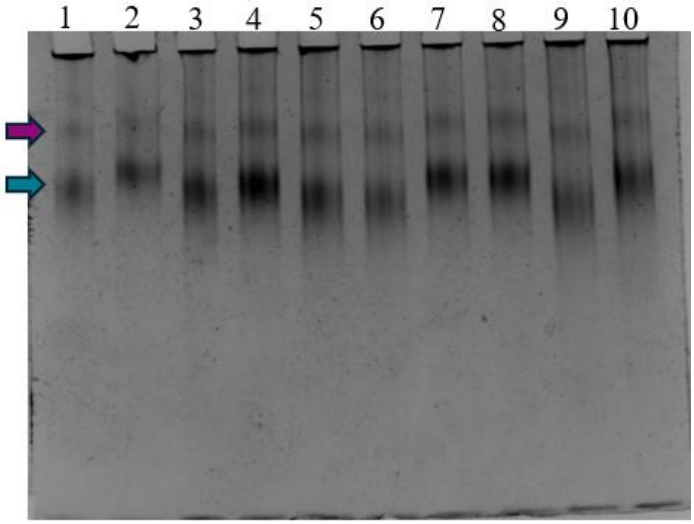

Figure 3.37: 5% Native Gel ThT samples (12.5 µg). Lane 1 –WT, Lane 2 – WT+HS, Lane 3 – I646V, Lane 4 – I646V+HS, Lane 5 – I703V, Lane 6 – I703V+HS, Lane 7 – I646V-I703V, Lane 8 – I646V-I703V + HS, Lane 9 – I646A, Lane 10 – I646A + HS. The blue arrow might indicate the dimer form. The purple arrow might show the oligomeric state.

3.5.9. Blue Native-PAGE gel following ThT assay

Blue Native-PAGE gel was also used to resolve the proteins from ThT assay in their native conformation and not by charge. This provides an estimate of molecular mass. hXOR samples were electrophoresed in a Blue Native-Page gel (4–16%) to determine the approximate size. In all hXOR samples, the dimer state is shown in the blue native gel close to the 272 kDa. There are also oligomeric states in the samples of approximately

545 kDa indicating the formation of a dimer of dimers. This gel also showed presence of protein in wells.

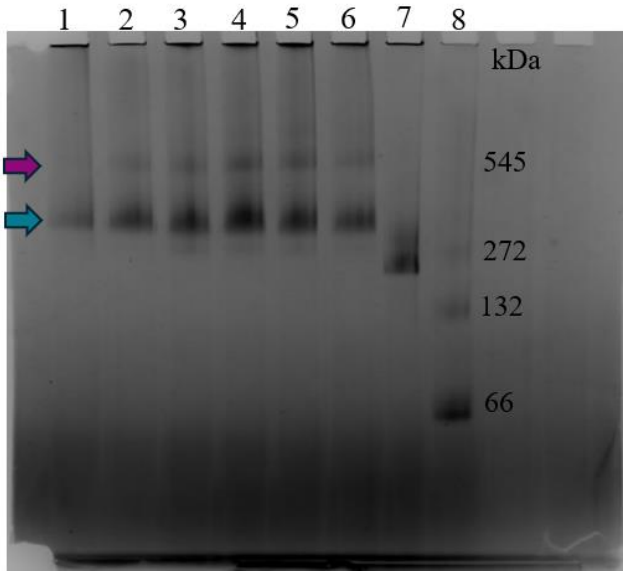

Figure 3.38: Blue Native Gel hXOR ThT samples. Lane 1 – 12.5 µg WT, Lane 2 – 12.5 µg WT + HS, Lane 3 – 12.5 µg I646V, Lane 4 – 12.5 µg I646V + HS, Lane 5 – 12.5 µg I703V, Lane 6 – 12.5 µg I703V + HS, Lane 7 – 5 µg molecular with markers urease from Jack Bean; Lane 8 – 2.5 µg molecular weight marker albumin from bovine serum (Sigma-Aldrich). The blue arrow indicates the dimer, whereas the purple arrow shows the oligomeric state.

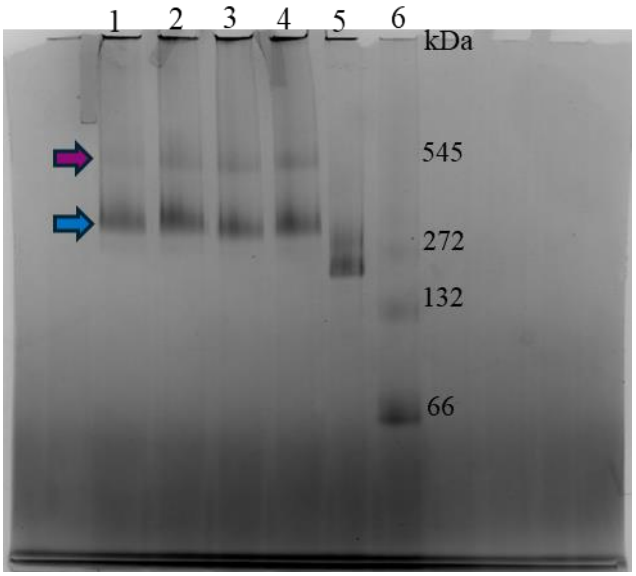

Figure 3.39: Blue Native Gel hXOR ThT samples. Lane 1 – I646V-I703V, Lane 2 – I646V-I703V + HS, Lane 3 – I646A, Lane 4 – I646A + HS, Lane 5 – 5 µg molecular with markers urease from Jack Bean; Lane 6 – 2.5 µg molecular weight marker albumin from bovine serum (Sigma-Aldrich). The blue arrow shows the dimer form. The purple arrow indicates the oligomeric state.

3.5.10. Agarose Gel following ThT Assay

Agarose gel electrophoresis was performed by loading the hXOR samples obtained from the ThT assay in the middle of the gel to assess their net change. All samples migrated towards the positive electrode, as they carry a negative charge. It can also be observed that in the gel some bands appeared lower (lanes 5, 6, and 9), possibly due to the difference in the charge in the variants I646V, I646V+HS, and I646A respectively.

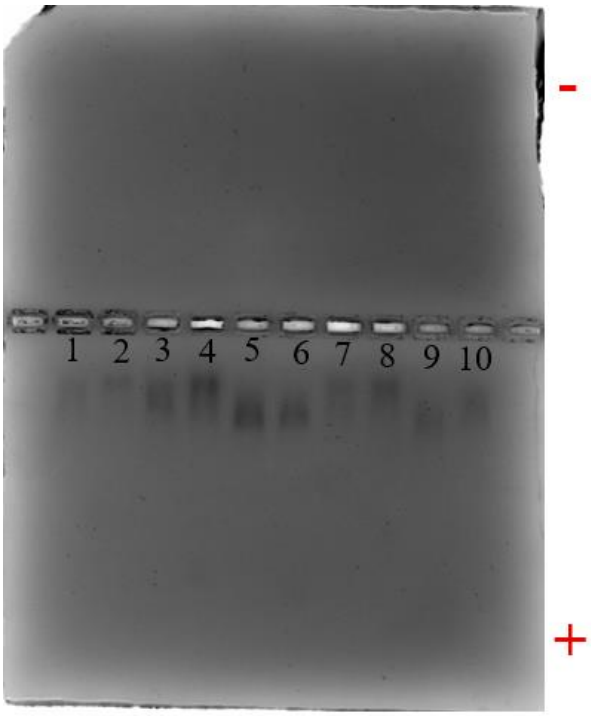

Figure 3.40: Agarose gel of ThT samples. Lane 1 – 10 µg WT, Lane 2 – 10 µg WT+HS, Lane 3 – 10 µg I646V, Lane 4 – 10 µg I646V+HS, Lane 5 – 10 µg I703V, Lane 6 – 10 µg I703V+HS, Lane 7 – 10 µg I646V-I7 03V, Lane 8 – 10 µg I646V-I703V + HS, Lane 9 – 10 µg I646A, Lane 10 – 10 µg I646A + HS.

3.5.11. Enzymatic activity following ThT assay

To assess the effect of prolonged incubation at physiological temperature on enzymatic activity, WT hXOR and variants that exhibited fibrillization propensity in the ThT assay were incubated at 37ºC for 24 hours. Their enzymatic activity was subsequently measured at 25ºC using the uric acid activity assay and expressed as a percentage relative to the activity measured before incubation. As shown in Figure 3.41, WT hXOR retained the highest activity after incubation, maintaining approximately 42.5% of its initial activity. Similarly, I646V preserved 41.7% activity, indicating relatively stable enzymatic activity. WT+HS sample showed moderate decrease, retaining 38.7% of its activity. In contrast, I703V+HS displayed the most pronounced loss, retaining only 25.7% after incubation at 37ºC.

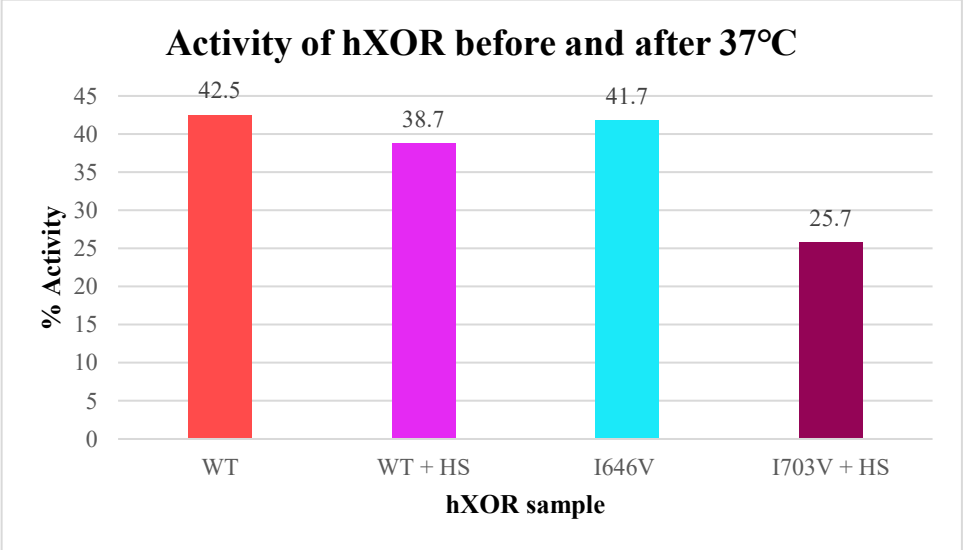

Figure 3.41: Activity of hXOR samples following incubation at 37ºC. The activity was determined via uric acid assay at 295 nm using a 0.15 mg/mL protein concentration. Data is expressed as a percentage of activity retained relative to the initial activity measured prior to incubation.

3.5.12. Circular Dichroism (CD) following ThT assay

CD was performed on WT hXOR sample recovered after a 48-hour ThT assay at room temperature. Untreated WT hXOR, which had not been exposed to ThT or the assay conditions, was used as a control to compare secondary structure changes. Following incubation at room temperature for 48 hours in the presence of ThT, WT had higher parallel percentage compared to the untreated WT, with 4.5% and 0.6% respectively. This

shows that ThT managed to bind to beta sheets on the WT due to the high amount of parallel beta sheets present in the protein.

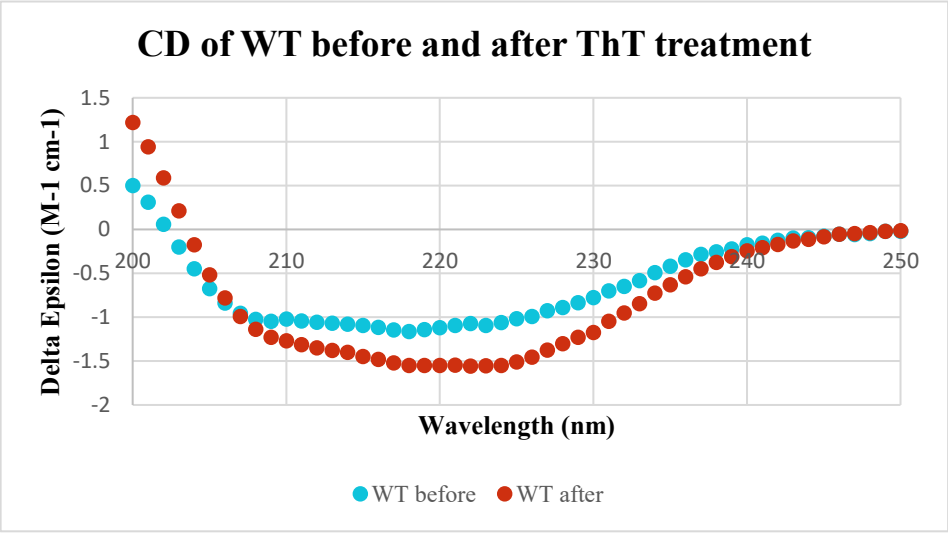

Figure 3.42: CD spectrum of WT before and after exposure at 37°C. The graph shows the change in the structural conformation of WT hXOR over a wavelength range of 200-250 nm. All protein samples were prepared at a concentration of 02-0.3 mg/mL.

Table 3.11: hXOR secondary structure content.

	Helix (%)	Antiparallel (%)	Parallel (%)	Turn (%)	Others (%)
WT before incubation	7.4	32.1	0.6	13.6	46.4
WT after incubation	9.6	30.8	4.5	16.8	38.3

3.5.13. Dynamic Light Scattering

Dynamic Light Scattering (DLS) is an established and effective technique for assessing the size and distribution of particles in a suspension. The measurements of particle size and size distribution are based on the analysis of diffusion behaviour of particles undergoing Brownian motion within a small scattering volume (Wang et al., 2021). It can also monitor how particles aggregate or assemble over time (Rodriquez-Loya et al., 2023).

To investigate the size of different hXOR proteins, DLS measurements were performed on WT hXOR and each variant protein both before and after incubation with

ThT (2.7.4). Figure 3.43 displays one plot of the intensity generated from the DLS experiment without and with ThT.

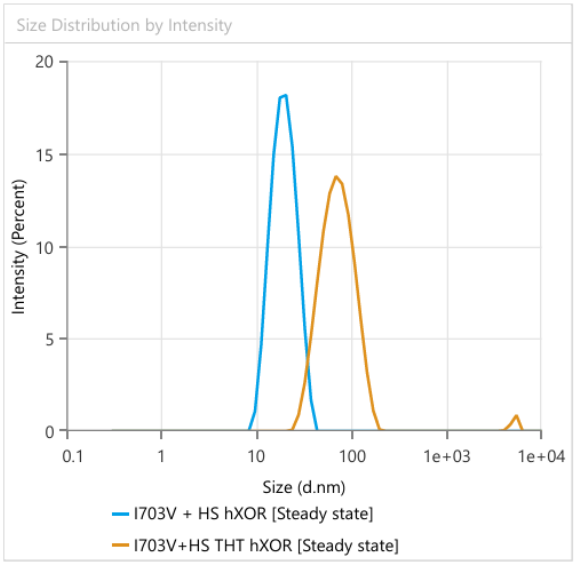

Figure 3.43: Dynamic Light Scattering (DLS) analysis of I703V+HS hXOR in the absence and presence of Thioflavin T (ThT). The plot shows the size distribution by intensity.

Table 3.12 includes the relative area (%) of each scattering population together with its corresponding mean hydrodynamic diameter (nm), providing an overview of the size distribution and the dominant particle species in each sample.

Prior to the 48 h, 37°C ThT incubation, all samples exhibited relatively small particle sizes, with mean intensity diameters ranging between 10 and 26 nm, consistent with the expected size of hXOR dimer of around 14 nm. However, WT and WT+HS samples displayed a high polydisperse population, with the dominant species having over 91% of the total area. This major species for WT and WT+HS samples had a mean diameter of 107 nm and 142.7 nm, respectively, indicating the presence of higher-order oligomers. The smaller species, which is the dimer form, was present at much lower proportion. The plots for the rest of the samples will be shown in appendix 6.1.

After the ThT incubation, clear differences were observed among the variant XORs. WT and WT+HS showed the appearance of large particle populations, with mean intensities of 141.4 nm and 193 nm, respectively, indicating the formation of higher-order oligomers. I646V+HS, I703V and I703V+HS also displayed a pronounced shift, with a major species between 60 – 75 nm, which reflects dimer of dimers of dimers of dimers. Other variants, including I646V, I646V-I703V, I646V-I703V+HS, I646A, and I646A+HS also showed an increase in particle size but to a lesser extent. Their post-ThT

distributions were dominated by populations around 30 – 50 nm, indicating moderate aggregation compared to WT and WT+HS. No samples retained a major population near the expected native size after ThT incubation. Overall, DLS measurements showed that prolonged incubation under ThT assay conditions leads to widespread formation of larger assemblies in all hXOR variants, consistent with fibril or aggregate formation. WT+HS sample had the highest mean with 193 nm, whereas I646V-I703V had the lowest with 100% of the population at 30.08 nm.

Table 3.12: DLS results of hXOR samples before and after the exposure under ThT conditions. Values were calculated using size distribution by intensity.

Protein	**DLS**			
	Before ThT		After ThT	
	Area (%)	Mean diameter (nm)	Area (%)	Mean diameter (nm)
WT	8.22	17.66	98.1	141.4
	91.78	107	1.901	5303
WT + HS	8.319	17.3	100	193
	91.68	142.7		
I646V	87.8	10.9	5.279	6.883
	12.2	96.3	94.72	37.48
I646V + HS	56.8	12.57	100	63.32
	43.2	44.75		
I703V	96.89	26.45	100	70.01
	0.01003	170.5		
	3.103	4997		
I703V + HS	100	12.17	98.75	75.66
			1.25	5203
I646V-I703V	100	10.09	100	30.08
I646V-I703V + HS	100	16.59	6.069	7.391
			93.93	39.64
I646A	100	13.07	100	43.69
I646A + HS	100	17.43	2.572	11.6
			70.95	46.84
			26.47	156

3.5.14. ZipperDB

To assess whether the observed oligomerisation or fibrillization tendencies correlate with intrinsic sequence propensities, ZipperDB analysis was performed on the WT and variant hXOR sequences (Brumshtein et al., 2018). ZipperDB predicts the formation of steric zipper, fibril-forming segments based on Rosetta energy calculations, with segments scoring below -23 kcal/mol considered likely to form amyloid fibrils (Zink et al., 2025; Rosenberg et al., 2022).

For the WT sequence, a strong aggregation-prone segment was identified around residues Gly642 and Ser643, which is adjacent to Ile646 (Figure 3.44). This region displays several segments with energies below the threshold, suggesting an intrinsic tendency to form fibrillar structures.

Substitution of Ile646 to Val646 did not abolish the predicted fibril propensity of this region. The variant slightly altered the local energy landscape (Figure 3.45), since the contribution of serine appeared to be less, but the overall predicted amyloidogenic segment remained present.

For the I646A variant, ZipperDB analysis revealed a reduction in predicted aggregation propensity in the same region (residues Gly642-Cys654) compared to WT and I646V (Figure 3.46). The substitution of isoleucine to alanine lead to higher calculated energies for several segments, indicating a lower likelihood of steric zipper formation.

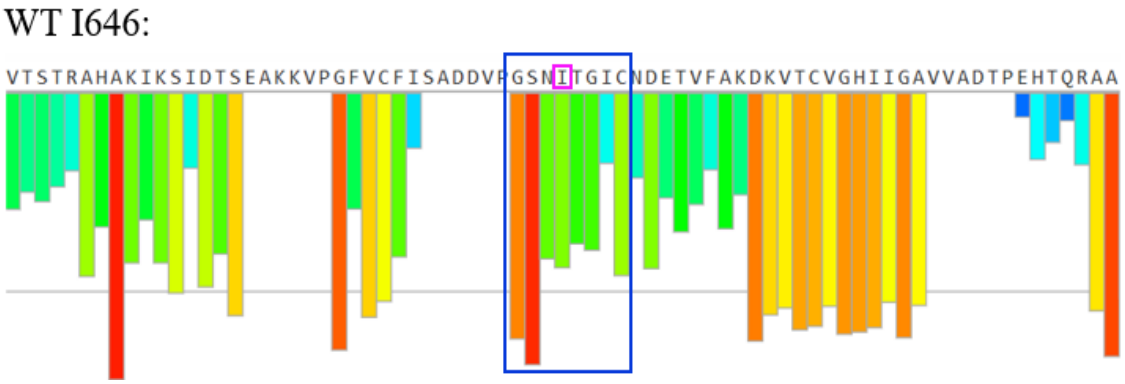

Figure 3.44: Prediction of propensity fibrillation of WT hXOR at position 646. Red and orange colours represent a higher propensity for fibrillization, while blue and green represent higher energy values with lower likelihood of fibril formation. Image generated using ZipperDB.

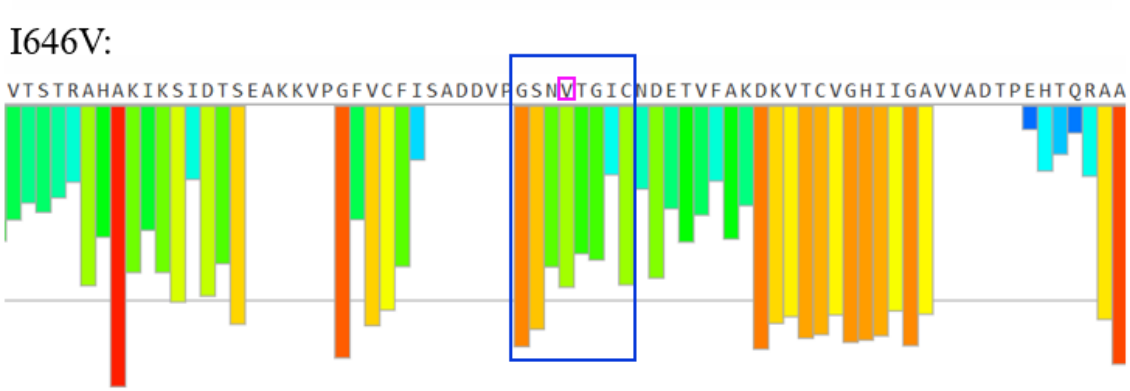

Figure 3.45: Prediction of propensity fibrillation of I646V mutant at position 646. Red and orange colours represent a higher propensity for fibrillization, while blue and green represent higher energy values with lower likelihood of fibril formation. Image generated using ZipperDB.

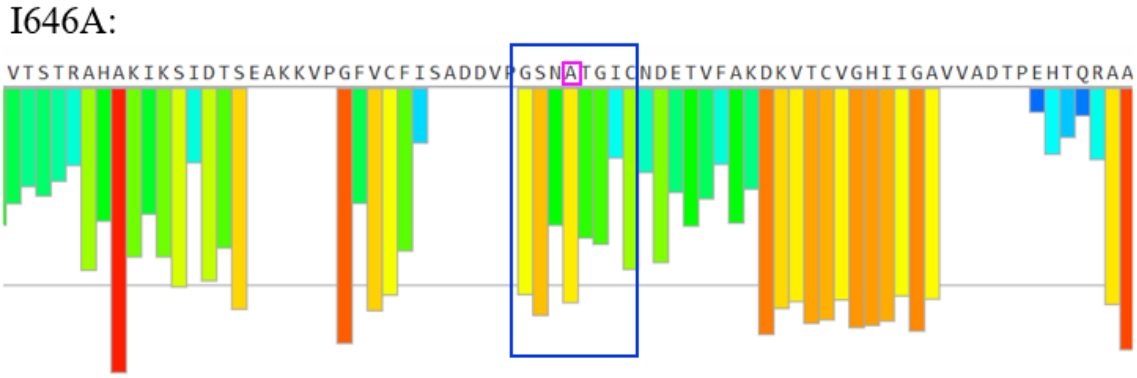

Figure 3.46: Prediction of propensity fibrillation of I646A hXOR at position 646. Red and orange colours represent a higher propensity for fibrillization, while blue and green represent higher energy values with lower likelihood of fibril formation. Image generated using ZipperDB.

ZipperDB analysis of the second aggregation-prone region (residues 696-707) showed a strong predicted amyloidogenic segment centred around Ile703 in the WT sequence (Figure 3.47). Substitution of isoleucine with valine at position 703 did not substantially alter the predicted aggregation propensity of this region (Figure 3.48). Both WT and I703V retained a deep energy minimum indicative of high steric zipper potential, suggesting that this segment remains strongly prone to fibril formation regardless of the variant.

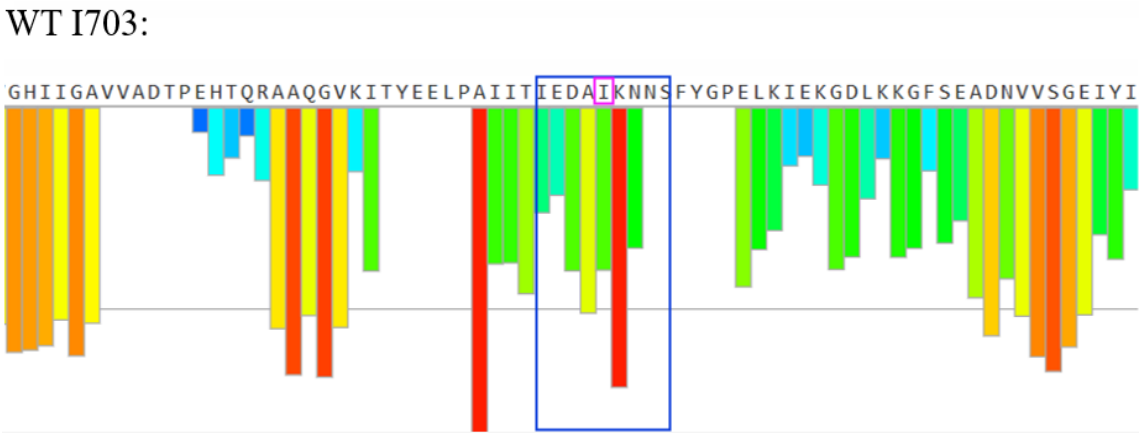

Figure 3.47: Prediction of propensity fibrillation of WT hXOR at position 703. Red and orange colours represent a higher propensity for fibrillization, while blue and green represent higher energy values with lower likelihood of fibril formation. Image generated using ZipperDB.

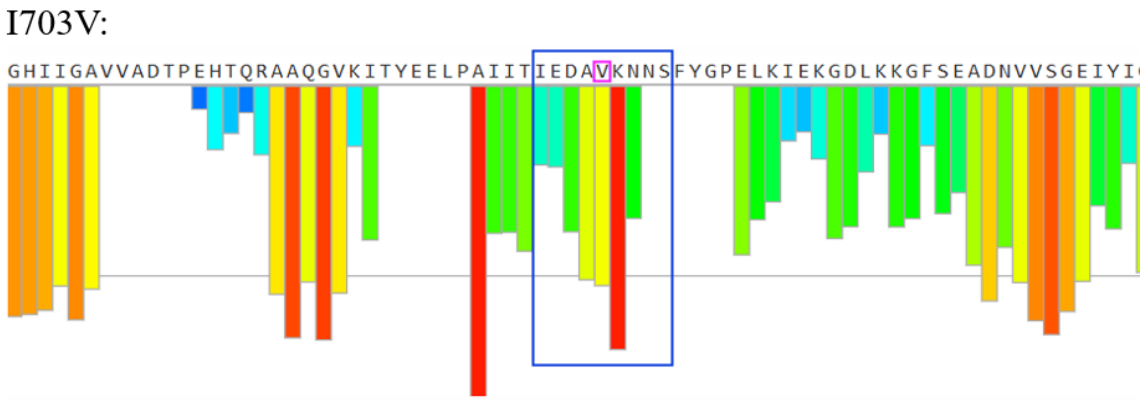

Figure 3.48: Prediction of propensity fibrillation of I703V mutant at position 703. Red and orange colours represent a higher propensity for fibrillization, while blue and green represent higher energy values with lower likelihood of fibril formation. Image generated using ZipperDB.

The bovine XOR (bXOR) WT sequence did not show aggregation-prone sequence around the residues adjacent to E645. This region displays all the segments with energies above threshold (Figure 3.49).

Figure 3.49: Prediction of propensity fibrillation of WT bXOR at position 645. Red and orange colours represent a higher propensity for fibrillization, while blue and green represent higher energy values with lower likelihood of fibril formation. Image generated using ZipperDB.

3.6. Structural analysis of hXOR

3.6.1. Molecular modelling of the hXOR variants

The variants were analysed using the cryoEM structure of human XOR (Seychell, unpublished) using The PyMol Molecular Graphics System (Schrödinger & DeLano, 2020). The polar hydrogen bonds were computed and the site directed mutagenesis was performed for each variant using Swiss-PDBviewer (Guex & Peitsch, 1997). The mutated residue was selected and each variant was energy minimised. The energy minimised structure was saved and transferred to PyMOL for analyses.

3.6.1.1. The I646V variant

The WT hXOR and the I646V variant structures were aligned (Figure 3.50) and the mutated residue was analysed. The variant, present on the surface of hXOR, close to the Moco domain, changed an isoleucine residue, a non-polar amino acid, with a valine residue, also a non-polar amino acid. A vacuum electrostatic surface analysis showed no observable change in electrostatics due to this variant (Figure 3.51).

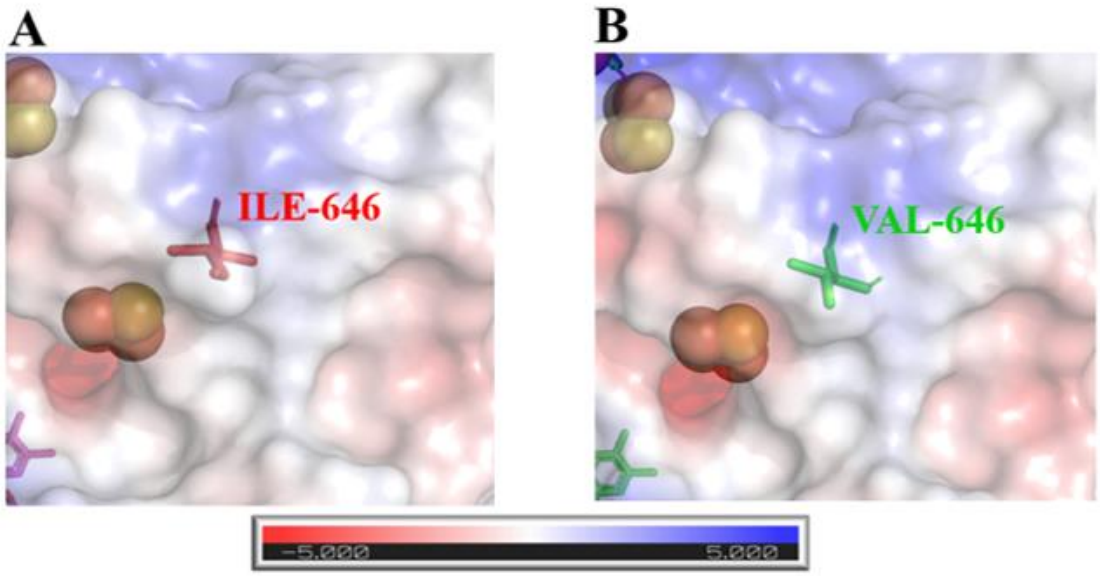

Figure 3.50: Vacuum electrostatics around the residue 646. Electrostatic surface-coloured red shows negative regions while electrostatic surface coloured blue represents positive regions. A – wild type. B – I646V mutant. The figure was generated by PyMOL Molecular Graphics System using the CryoEM structure (Schrödinger & DeLano, 2020).

In the wild type, a moderate electrostatic hydrogen bond of 3.0 Å forms between Ile^{646} and Lys^{779} while in the I646V variant, the Val^{646} residue forms a strong hydrogen bond of 2.1 Å with Lys^{779} (Figure 3.52).

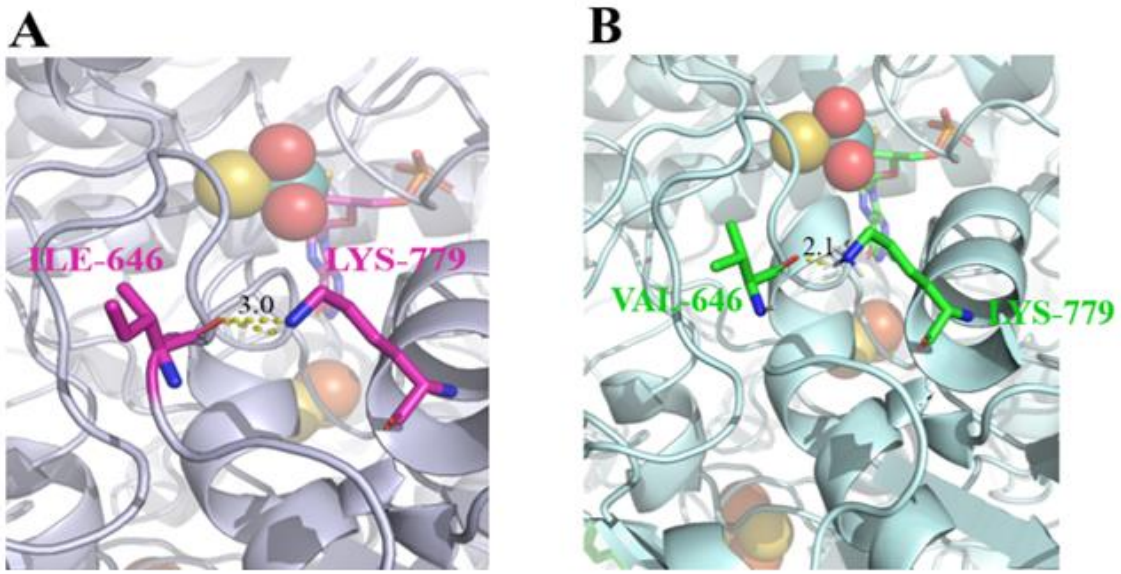

Figure 3.52: Interactions of the residue 646 with the surrounding residues. A – wild type residue. B – I646V residue. The figure was generated by PyMOL Molecular Graphics System using the CryoEM structure (Schrödinger & DeLano, 2020).

3.6.1.2. The I703V variant

The wild-type protein was also aligned with I703V variant (Figure 3.53). The variant changed an isoleucine residue, a non-polar amino acid, with a valine residue, a non-polar amino acid, as well. When vacuum electrostatic surfaces were applied, there was no change in the electrostatic charge around the mutated residue (Figure 3.54).

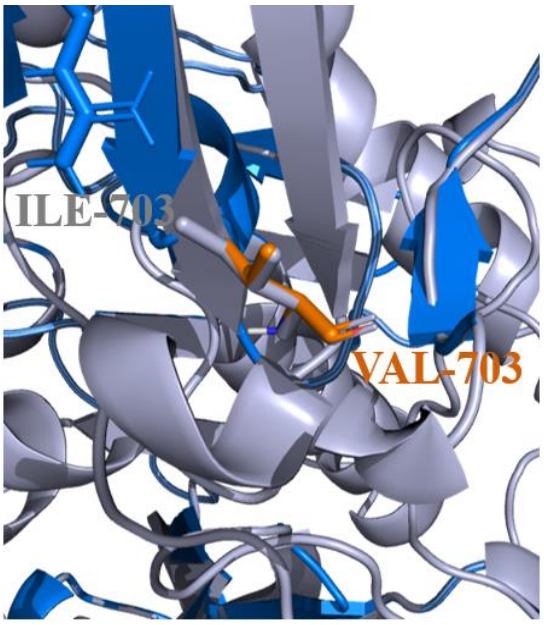

Figure 3.53: Wild type and mutant I703V hXOR aligned. Grey – wild type hXOR, Orange – I703V mutant. The figure was generated by PyMOL Molecular Graphics System using the CryoEM structure (Schrödinger & DeLano, 2020).

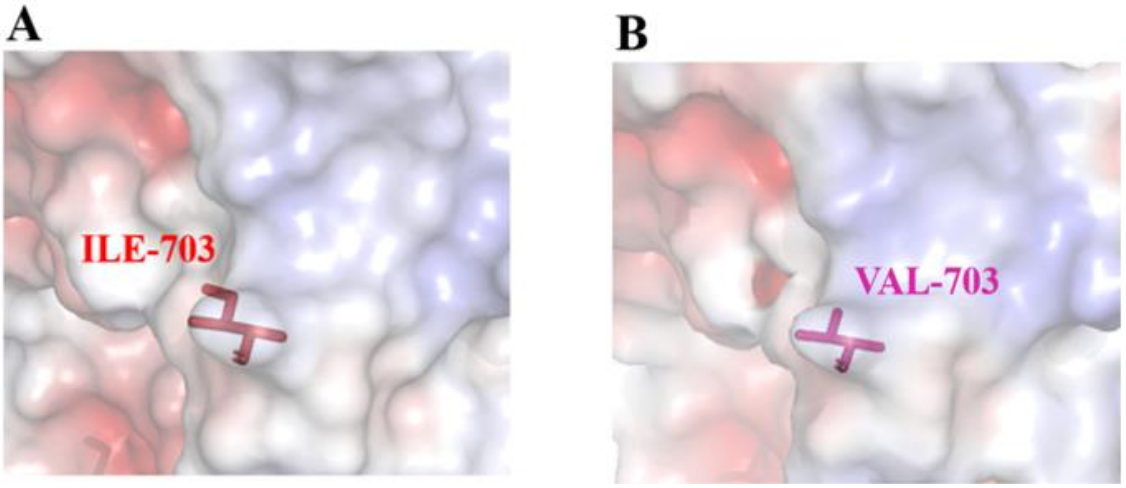

Figure 3.54: Vacuum electrostatics around the residue 703. Electrostatic surface coloured red represents negative regions while electrostatic surface coloured blue shows positive regions. A – wild type. B – I703V mutant. The figure was generated by PyMOL Molecular Graphics System using the CryoEM structure (Schrödinger & DeLano, 2020).

The I703V variant forms stronger electrostatic hydrogen bonds with Asn^{706} and Ile^{699} to Val^{703} (2.3 and 2.0 Å respectively) compared to the wild-type protein where moderate electrostatic hydrogen bonds of 3.3 Å and 2.9 Å are formed between Ile^{703} and Asn^{706} and Ile^{699}, respectively (Figure 3.55).

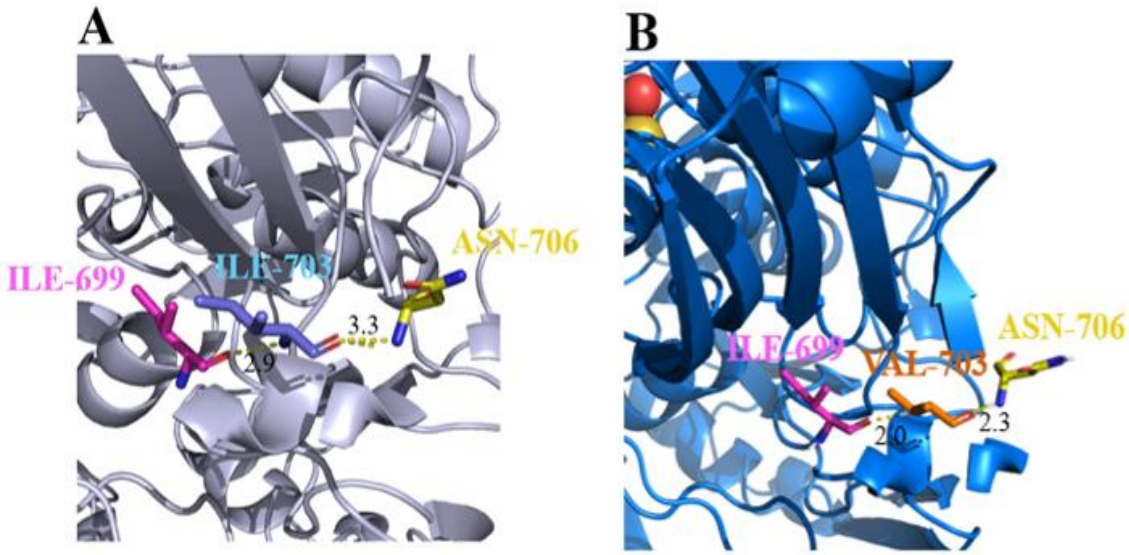

Figure 3.55: Interactions of the residue 703 with the surrounding residues. A – Wild type residue. B – I703V mutant residue. The figure was generated by PyMOL Molecular Graphics System using the CryoEM structure (Schrödinger & DeLano, 2020).

3.6.1.3. The I646A variant

The I646A variant caused no change in the overall alignment of wild type with variant (Figure 3.56). The variant changed a non-polar isoleucine residue, with another non-polar alanine residue. When vacuum electrostatic surfaces were applied, a slight increase in positive electrostatic charge around the mutated residue was observed (Figure 3.57).

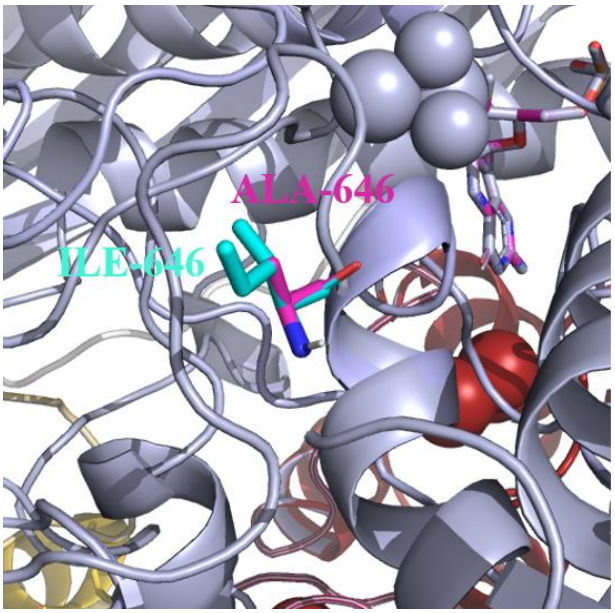

Figure 3.56: Wild type and I646A mutant hXOR aligned. Cyan – wild type hXOR, Pink – I646A mutant. The figure was generated by PyMOL Molecular Graphics System using the CryoEM structure (Schrödinger & DeLano, 2020).

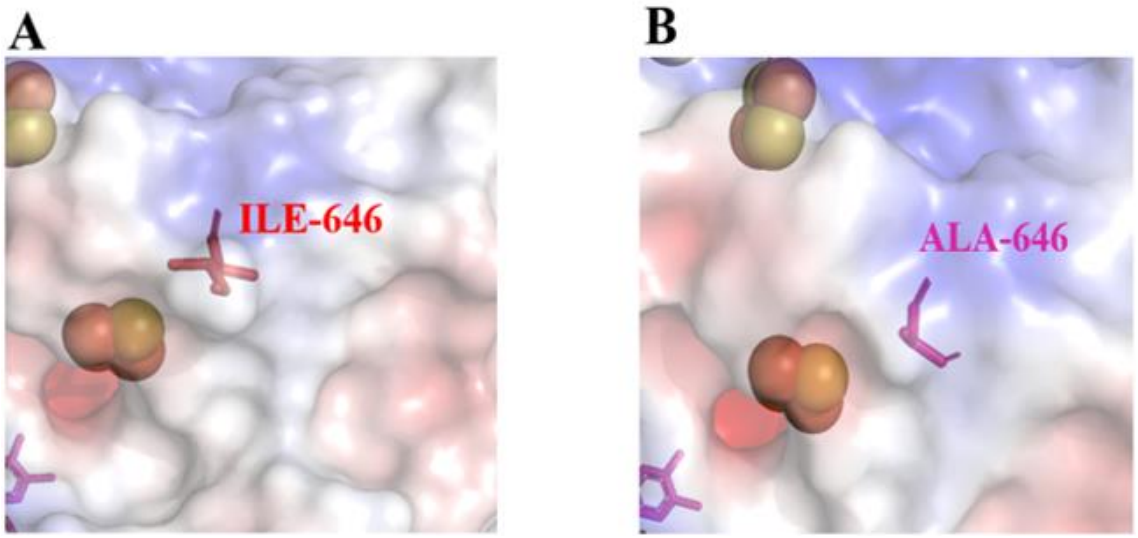

Figure 3.57: Vacuum electrostatics around the residue 646. Electrostatic surface coloured red signifies negative regions while electrostatic surface coloured blue shows positive regions. A – wild type. B – I646A mutant. The figure was generated by PyMOL Molecular Graphics System using the CryoEM structure (Schrödinger & DeLano, 2020).

The hydrogen bonds between the residues remained the same in both wild-type and mutated protein, both forming a moderate 3.0 Å hydrogen bond of the carbonyl oxygen of isoleucine and alanine with Lys^{779} (Figure 3.58).

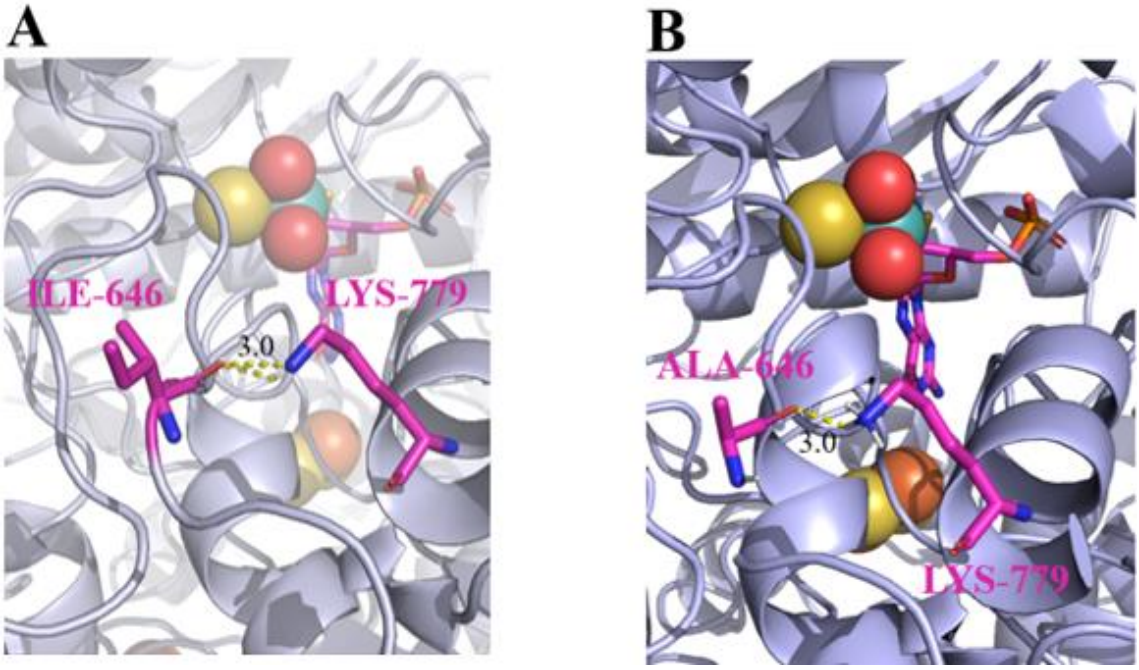

Figure 3.58: Interactions of the residue 646 with the surrounding residues. A – wild type residue. B – I646A mutant residue. The figure was generated by PyMOL Molecular Graphics System using the CryoEM structure (Schrödinger & DeLano, 2020).

3.6.2. Molecular Docking of hXOR with ThT

Due to a high fluorescence value observed at the start of the ThT assay, molecular docking was conducted to check whether ThT binds to native hXOR. The molecular docking simulation of the ligand ThT onto hXOR using SwissDock showed two binding poses. The most stable pose exhibited a calculated binding affinity of -5.611 kcal/mol (Figures 3.59 and 3.60), while the other one had an affinity of -5.647 kcal/mol (Figure 3.61 and 3.62). Both binding orientations of ThT ligands occurred in the active site of hXOR. The calculated binding affinities of -5.647 kcal/mol and -5.611 kcal/mol are considered to represent a favourable, moderate binding affinity between hXOR and ThT (Alsedfy et al., 2024). The variants are not found closely to the binding of ThT.

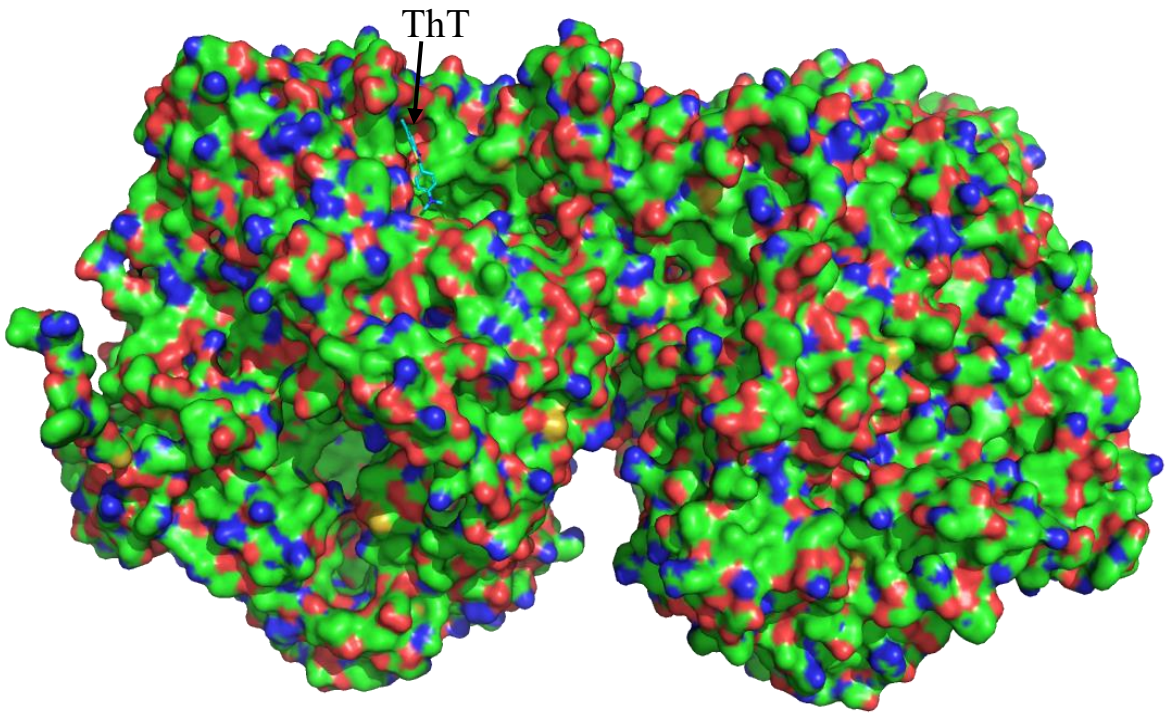

Figure 3.59: Molecular docking of ThT binding to the hXOR in the dimer structure. The figure was generated using PyMOL Molecular Graphics System (Schrödinger & DeLano, 2020).

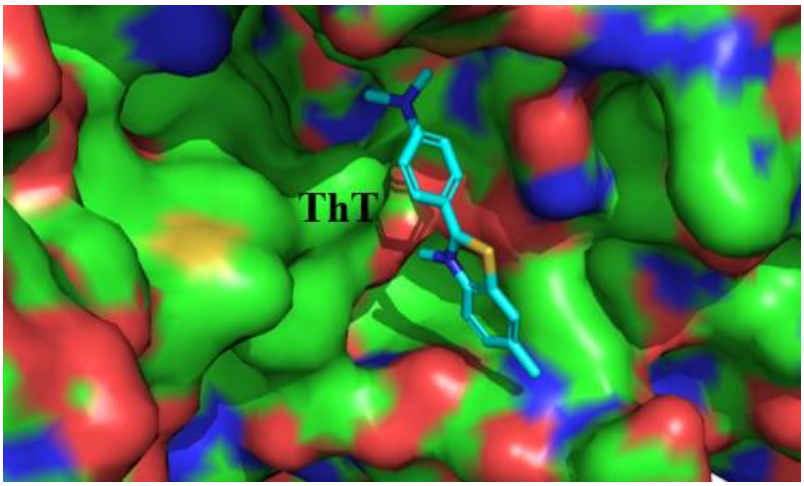

Figure 3.60: Docking of ThT with hXOR of -5.611 kcal/mol. Cyan – ThT ligand. The figure was generated using PyMOL Molecular Graphics System (Schrödinger & DeLano, 2020).

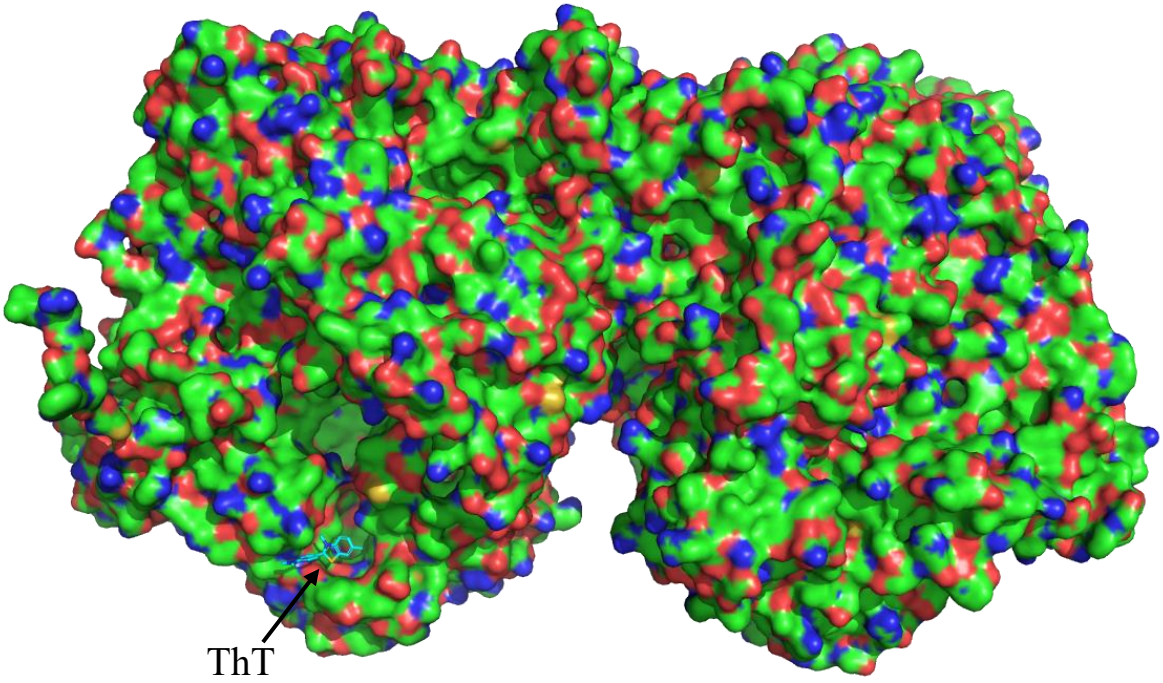

Figure 3.61: Molecular docking of ThT binding at another position to the hXOR in the dimer structure. The figure was generated using PyMOL Molecular Graphics System (Schrödinger & DeLano, 2020).

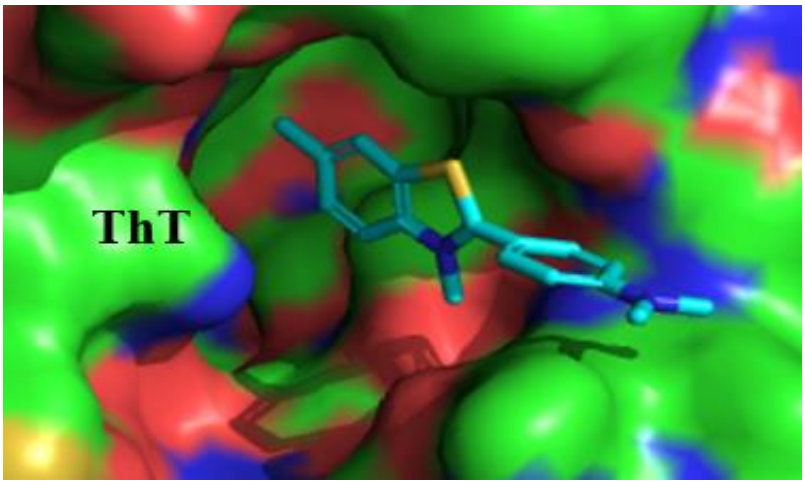

Figure 3.62: Docking of ThT with hXOR of -5.647 kcal/mol. Cyan – ThT ligand. The figure was generated using PyMOL Molecular Graphics System (Schrödinger & DeLano, 2020).

3.6.3. Dimer-dimer Interactions

The computational modelling of the dimer-dimer interactions of hXOR was performed using the HDOCK server (Yan et al., 2017) This generated multiple binding models but based on the predicted docking score, which reflects the overall favourability of the interaction, one was selected. The top-ranked model, formed by the interaction of two hXOR dimers, representing an XOR tetramer, exhibited the most favourable HDOCK score of -254.62 kcal/mol (Figure 3.63). The interaction involved the FAD site of one subunit from each interacting dimer (Figure 3.64) . This model suggests that the FAD active site in each of these two monomer subunits is blocked and hence unable to participate in the catalytic mechanism. However, since the two chains within the hXOR homodimer function independently of each other, the remaining two hXOR monomeric subunits in the dimer of dimer oligomer are hypothesised to retain their full catalytic activity. ThT molecule is found in the vicinity of the interaction between the hXOR dimers.

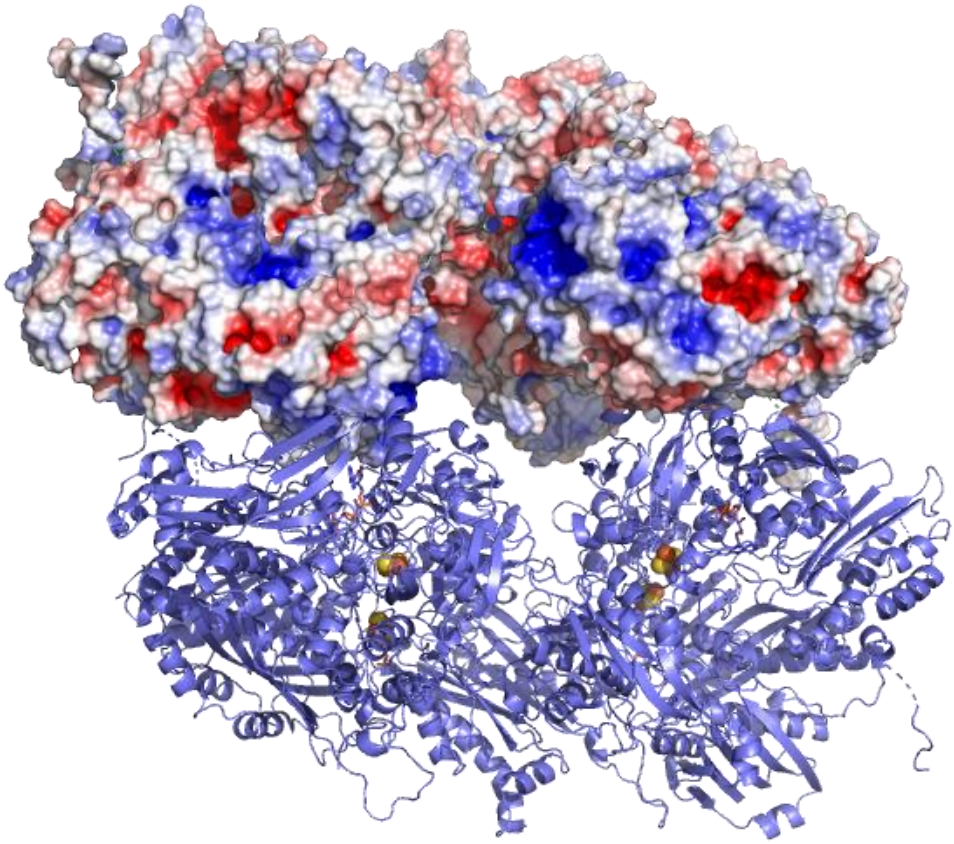

Figure 3.63: Computational modelling of the protein-protein interactions between hXOR dimers. The electrostatic surface representation (top) of hXOR and ribbon diagram (bottom) of modelled structure illustrate the interaction between two hXOR dimers, resulting in the formation of an XOR tetramer. The figure was generated using PyMOL Molecular Graphics System (Schrödinger & DeLano, 2020).

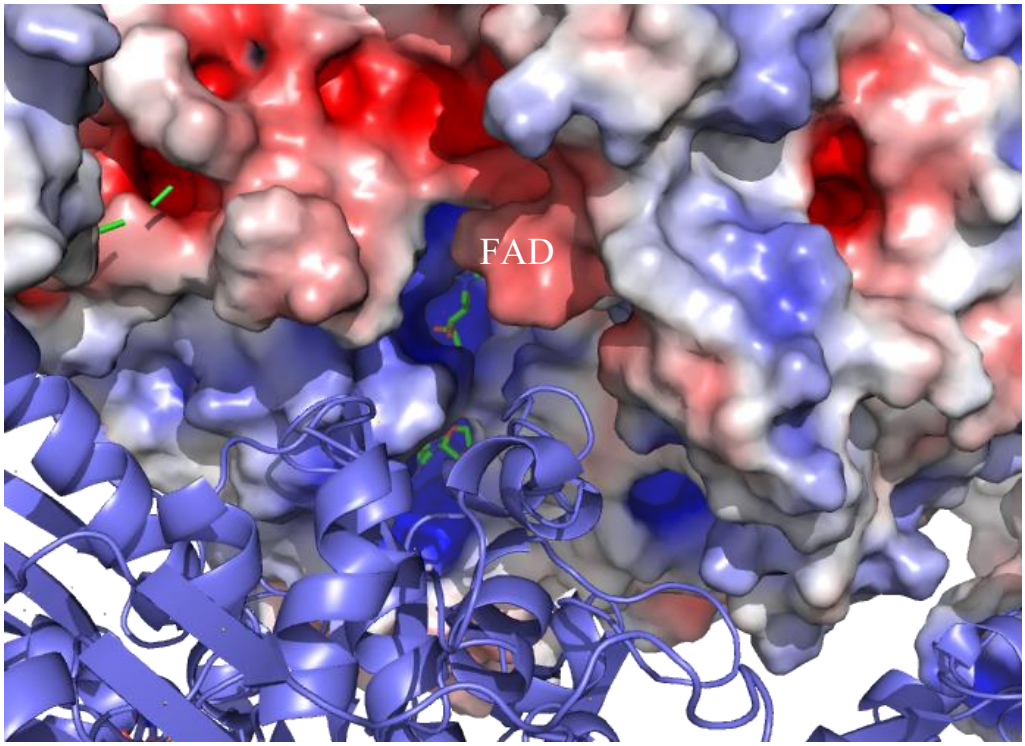

Figure 3.64: Interaction at the FAD domain of hXOR. The electrostatic surface representation highlights the binding interface (top), while the ribbon structure (bottom) shows the position of the interacting dimer. The figure was generated using PyMOL Molecular Graphics System (Schrödinger & DeLano, 2020).

3.6.3.1. Interface

The binding interface between two interacting monomeric subunits was determined by identifying all residues in the receptor chain and the ligand chain within a cut-off distance of 4.0 Å (Figure 3.65). The interactions of the residues contributing to the stability of the predicted hXOR dimer of dimer were then analysed for this specific interface (Figure 3.66). Interactions, including polar contacts and salt bridges were determined using PyMol. Specifically, the residues mediating the interaction were identified (Table 3.13), and the intermolecular contacts are listed in Table 3.14, whereas the distance of the bond lengths are shown in Table 3.15.

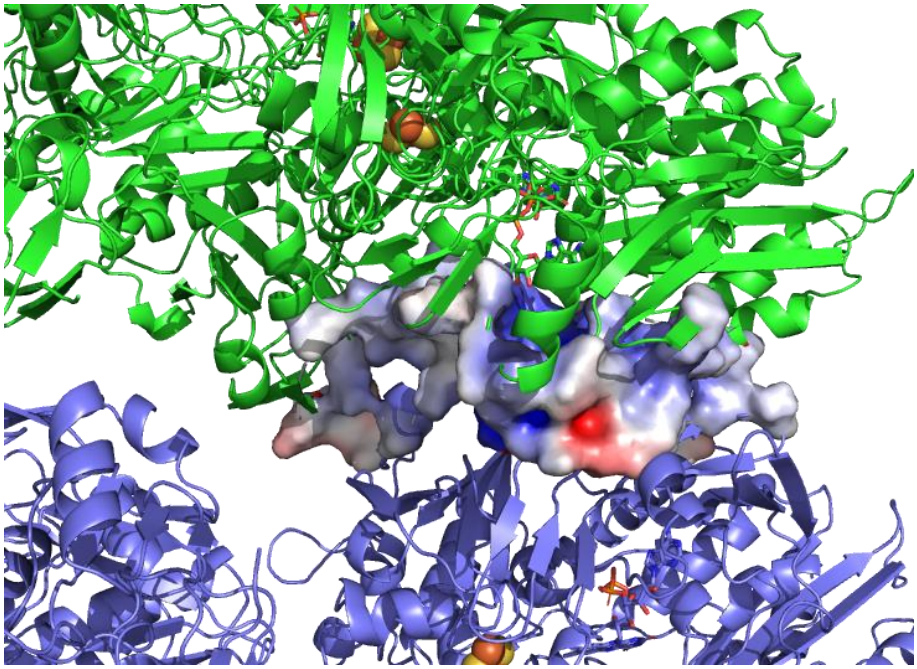

Figure 3.65: Binding interface between two interacting hXOR monomers. The electrostatic surface representation highlighting the interaction site. Green – hXOR monomer, Purple – modelled hXOR monomer The figure was generated by PyMOL Molecular Graphics System (Schrödinger & DeLano, 2020).

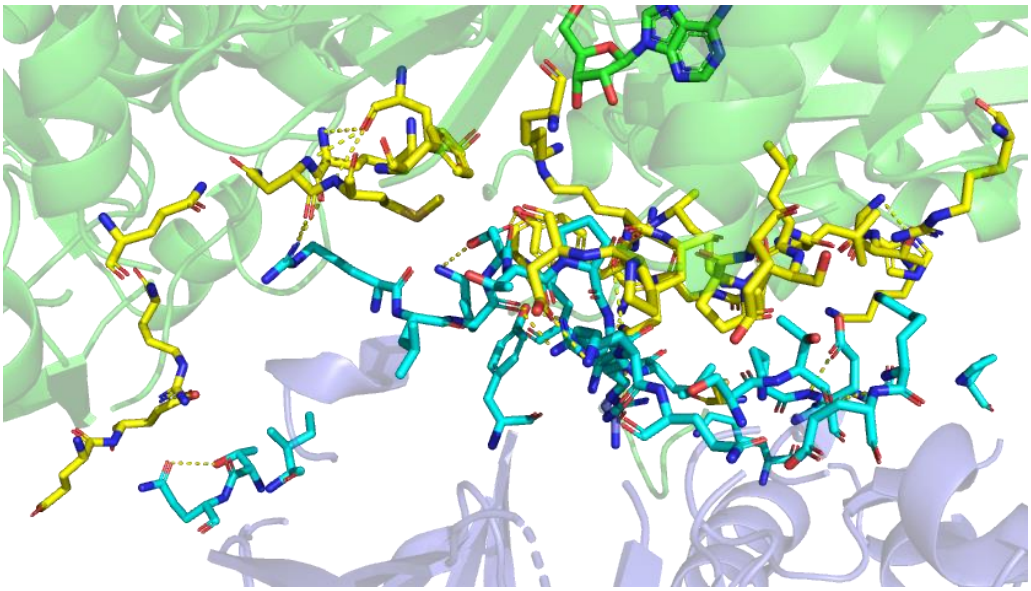

Figure 3.66: Interacting residues at the interface between two hXOR monomers. Yellow – Chain A interacting residues, Cyan – Chain D interacting residues. The figure was generated by PyMOL Molecular Graphics System (Schrödinger & DeLano, 2020).

Table 3.13: Interface Residues of two monomers of hXOR.

Interface Residues	
Chain A	**Chain D**
Tyrosine-58 (Y)	Proline-253 (P)
Arginine-60 (R)	Aspartic acid-254 (D)
Leucine-61 (L)	Lysine-256 (K)
Arparagine-63 (N)	Glutamic acid-267 (E)
Threonine-207 (T)	Lysine-271 (K)
Glutamine-208 (Q)	Asparagine-272 (N)
Isoleucine-211 (I)	Methionine-273 (M)
Arginine-218 (R)	Phenylalanine-275 (F)
Leucine-219 (L)	Arginine-381 (R)
Lysine-220 (K)	Histidine-387 (H)
Threonine-222 (T)	Threonine-388 (T)
Proline-223 (P)	Proline-391 (P)
Arginine-224 (R)	Glycine-392 (G)
Lysine-225 (K)	Tyrosine-393 (Y)
Glutamic acid-226 (E)	Arginine-394 (R)

Serine-240 (S)	Lysine-395 (K)
Threonine-241 (T)	Leucine-397 (L)
Lysine-243 (K)	Leucine-398 (L)
Glutamic acid-244 (E)	Serine-399 (S)
Proline-285 (P)	Proline-400 (P)
Glutamic acid-286 (E)	Glutamic acid-401 (E)
Histidine-292 (H)	Alanine-460 (A)
Proline-294 (P)	Asparagine-461 (N)
Lysine-318 (K)	Arginine-462 (R)
	Lysine-468 (K)
	Proline-501 (P)
	Arginine-613 (R)
	Glutamine-684 (Q)
	Glutamic acid-691 (E)
	Glutamic acid-692 (E)
	Cysteine-1326 (C)

Table 3.14: Interactions of interface residues of two monomers of hXOR.

Interactions	
Polar contacts	**Salt bridges**
R60-K220	K220-D221
R60-N63	K225-D254
R60-N461	R613-E692
N63-N461	
Q208-T207	
Q208-E692	
R218-K271	
R218-N272	
K220-D221	
D221-Y393	
K225-D254	
T241-E244	
P285-P391	
E286-E286	
E267-K271	
E267-N272	
E267-M273	
K271-E267	
N272-E267	
M273-E267	
H387-H387	
G392-K395	
Y393-K395	

Table 3.15: Bond Lengths of interactions between interface residues.

Bond Lengths of Interactions	
Interactions	**Bond length (Å)**
R60-K220	2.4
R60-N63	3.5
R60-N461	2.6
N63-N461	2.9
Q208-T207	3.4
Q208-E692	2.6
R218-K271	2.6
R218-N272	3.2
K220-D221	3.1
D221-Y393	2.9
K225-D254	4.0
T241-E244	3.2
P285-P285	2.5
E286-E286	2.7
E267-K271	3.4
E267-N272	3.3
E267-M273	3.5
H387-H387	3.1
G392-K395	3.4
Y393-K395	3.4
R613-E692	3.1

Chapter 4 Discussion

The main biological role of hXOR is to catalyse the last two steps of purine catabolism, oxidizing hypoxanthine to xanthine and subsequently to uric acid. When oxygen is used as a substrate, ROS, specifically H_2O_2 and O_2^-, are generated. Apart from its role in purine catabolism, hXOR can also function as a nitrite reductase to generate the vasodilator, nitric oxide (NO), when nitrite is used as the substrate, especially under anaerobic conditions (Cantu-Medellin & Kelley, 2014; Miah et al., 2022). Various health conditions have also been linked to abnormal activity of hXOR. An elevated enzymatic activity can cause hyperuricemia that can lead to cardiovascular diseases. Moreover, high hXOR activity can result in oxidative stress due to its ability to produce ROS. ROS produced by hXOR can form the potent oxidant species, peroxynitrite ($ONOO^-$), through the reaction of superoxide with NO. This can lead to hypertension and heart failure (Miah et al., 2022).

Presently, a total of 21 XOR polymorphisms have been identified (Ichida et al., 2012; Kudo et al., 2008; Sekine et al., 2021; Stiburkova et al., 2012; Yang et al., 2008). Variants such as, I703V, K617N, H1221R, and R1296W have been shown to have a higher activity compared to wild type protein with higher intrinsic clearance (CLint) or Vmax values, while E133K, G172R, I646V, V1091L, and N1109T generally show similar activity to WT hXOR. In contrast, variants like R149C, T235M, K395M, P555S, D584A, R607Q, T623I, N909K, T910K, P1150R, and C1318Y exhibit a decrease in enzymatic activity (Kudo et al., 2008; Massimo et al., 2023). The more severe loss-of-function variants are associated with xanthinuria type I (Ichida et al., 2012).

Certain clinical hXOR variants exhibiting altered enzymatic activity, and structural stability of hXOR have been associated with an elevated risk of hypertension, hyperuricemia, and xanthinuria. Among these mutations, only a few have been observed in hypertensive patients cohorts or are thought to influence cardiovascular risk. In the literature, G172R, A932T, and N1109T have been reported to be associated with hypertension. A932T and N1109 are both located in the Moco domain, whereas G172R is found close to the Fe-S cluster (Yang et al., 2008). These three human variants were functionally analysed in the Protein and Biochemistry Laboratory (University of Malta) for their potential impact on enzyme activity. Among these, A932T was found to exhibit a notable increase in enzymatic activity compared to the wild-type enzyme. In contrast,

the activity of the G172R and N1109T variants was similar to that of the WT hXOR (Seychell, personal communication, 2019).

In a study conducted by Attard et al. (2021) involving cardiac patients known as the Maltese Acute Myocardial Infarction Study (MAMI Study), four hXOR polymorphisms were identified in the Maltese population notably G172R, I646V, and I703V, and a novel variant, V1163A. Interestingly, this also identified that some cases of patients harboured a compound heterozygote (I646V-I703V) (Prof. Stephanie Bezzina Wettinger, personal communication). In this project, I646V and I703V variants, as well as the I646V-I703V double mutant, were characterised. To our knowledge, this was the first time the double mutant was identified. These variants were chosen as there was an occurrence of the single mutants and the double mutant was statistically significant with high uric acid level (Prof. Stefanie Bezzina Wettinger, personal communication). Previous studies have shown that the I703V mutation has a higher activity than the wild type hXOR (Kudo et al., 2008; Massimo et al., 2023), however, Kudo et al. (2008) did not observe much difference between the WT and the I646V mutation (with a Vmax of 41.4 nmol/mg protein/min and 38.5 nmol/mg protein/min respectively). Structural *in silico* bioanalysis confirmed that these residues are located close to the active site of hXOR, may therefore potentially alter enzyme activity and ROS production. Each single mutation, as well as the double mutation, were further characterised in this project, studying their catalytic and biophysical characteristics. Apart from the mutations that were identified in the study, I646A mutant was also studied, to assess the consequences of substituting an isoleucine with a smaller nonpolar amino acid.

Although previous studies have reported that the activity of I703V was higher than that of the WT XOR, while the activity of I646V was comparable to WT XOR (Kudo et al., 2008), the findings of this project differ from these observations. Specifically, I703V demonstrated an activity similar to the WT, whereas the activity of I646V was 7.6-fold that of the WT. These discrepancies may be explained by differences in experimental approaches; Kudo et al. (2008) expressed the enzyme in COS-7 cells (eukaryotic cells derived from African green monkey kidney cells) and only partially fractionated the proteins. Moreover, the protein concentration used in this study was the total protein concentration of the fraction even though the expression of the different hXOR variants in the COS-7 cells varied as evidenced by the Western Blots (Kudo et al, 2008). This may have introduced a discrepancy in the activity assay measurements. Lastly, the XOR

activity was measured using different methodology for the XO protein and importantly, no determination of the amount of XO against XDH was conducted.

In this study both the WT and the mutants were expressed recombinantly in bacterial cells and purified to homogeneity. The activity of the pure protein was assessed using a photometric enzymatic activity assay and the amount of XO and XDH was determined. The activities of the WT and mutants were then compared by normalising the XO activity against a calculated 100% XO protein amount.

As the human XOR protein is a large complex protein with multiple cofactors, it was necessary to optimise culture conditions to improve yield, solubility and activity for the wild type XOR and for each of the mutant proteins. The main condition tested was involved exposing the bacterial culture briefly to elevated temperature to induce the cellular heat shock response. TP1000 *E.coli* cells culture harbouring the different hXOR cDNAs were each grown aerobically without and with heat shock (HS). Subjecting cells to heat shock induces the production of heat shock chaperones that could potentially improve the molecular folding of the recombinant hXOR protein in bacterial cells (Oganesyan et al., 2007). Hence for each hXOR sample (WT, I646V, I703V, I646V-I703V, and I646A), two conditions were tested: aerobic production without and with HS.

Heat shock treatment and the DnaJ/K and GroEL/ES bacterial chaperone systems proved effective for improving the yield and activity of some proteins, but not all of them. These systems typically facilitate proper folding, where DnaK (assisted by DnaJ) binds to an early-stage folding intermediates to prevent them from clumping together, while the GroEL/ES complex functions as a chaperonin cage, providing a protected environment for proteins to fold in isolation (Fourie & Wilson, 2020). For certain proteins, the elevated temperature required during heat shock might have caused them to partially unfold, exposing hydrophobic regions that are usually found in the core of the protein. This might have encouraged the formation of inclusion bodies or aggregates (Kedzierska et al., 2001). In terms of activity, WT, I703V, and I646V-I703V all showed higher enzymatic activities following HS treatment (Table 4.1).

This resulted in a total of 10 protein samples, and the purification, stability, secondary structure, enzymatic activity, and propensity of fibrillization, of all the samples were analysed and compared.

Table 4.1: Summary of purity, yield, activity, stability, and fibril formation without and with HS.

Samples	Purity	Yield	Activity	Stability	Fibril formation
WT	90.33	High	Low	Stable	Yes
WT+HS	89.73	High	Moderate	Stable	Yes
I646V	97.92	Low	High	Stable	Yes
I646V+HS	98.90	Low	Moderate	Very stable	No
I703V	98.91	High	Moderate	Very stable	No
I703V+HS	94.74	Low	High	Less stable	Yes
I646V-I703V	98.83	Low	High	Less stable	Yes
I646V-I703V+HS	92.50	Low	High	Least stable	No
I646A	99.61	High	Very high	Less stable	No
I646A+HS	92.27	High	High	Less stable	No

4.1. hXOR Mutations

4.1.1. hXOR I646V Mutation

I646V is a conservative mutation that was identified in the MAMI study (Prof. Stephanie Bezzina Wettinger, personal communication) associated with elevated serum uric acid levels. The I646V hXOR mutation is a conservative amino acid change as both isoleucine and valine are both non-polar, uncharged, aliphatic, and branched amino acids. This substitution is located on the surface of the Moco domain close to the molybdenum centre. Despite being a conservative amino acid change, I646V surprisingly exhibited an activity that was 7-fold higher than that of the WT protein with very little change in the melting temperature and the secondary content.

4.1.2. hXOR I703V

I703V is also a conservative mutation that was identified in the MAMI study (Prof. Stephanie Bezzina Wettinger, personal communication) associated with elevated serum uric acid levels. Although this mutation is also located in the Moco domain, it is positioned at a distance from the molybdenum centre. The secondary structure content,

activity and the melting temperatures of I703V and WT hXOR were observed to be similar.

4.1.3. hXOR I646V-I703V

I646V-I703V is a novel double mutation that was identified in the MAMI study, associated with elevated serum uric acid levels. The double mutant exhibited 6-fold increase in enzymatic activity when compared to WT hXOR. The melting temperature of I646V-I703V was slightly lower than WT, with a difference of around 6ºC, while the secondary content was similar. Whether the single and double mutations are associated with hypertension cannot be determined at this stage without further analysis of the MAMI participant data to assess, for example, how many harbouring the compound heterozygous variant were on hypertension medication.

4.1.4. hXOR I646A

The hXOR I646A mutation is not a known clinical variant. It was constructed to assess whether the replacement of a large non-polar branched amino acid such as isoleucine with a smaller non-polar amino acid would affect the protein properties. Surprisingly this residue change resulted in a hyperactive enzyme, with a 9-fold increase in activity when compared to the WT. Of all the studied XOR proteins, CD results showed that the I646A protein had the highest alpha helix content and the lowest melting temperature. This clearly indicates that as the residue at 646 changes from a larger, more hydrophobic amino acid such as isoleucine, to a smaller amino acid with lower hydrophobic character/index such valine and alanine, the activity increases. Furthermore, as assessed through ThT assays and DLS, the I646A did not form fibrils which may a contributing factor to observe the elevated enzyme activity.

4.1.5. Mutation Analysis

Although the bovine hXOR has 89.6% sequence identity and 95.2% sequence similarity to the human hXOR, the isoleucine at position 646 is not conserved in the bovine XOR. This position is in fact occupied by a glutamate instead of an isoleucine, thereby replacing a large hydrophobic amino acid with a polar amino acid. Hence, an unpublished hXOR cryogenic electron microscopy (cryo EM) structure (Seychell, 2019) at a resolution of 2.8 Å was used since it contains all the domains, especially molybdenum, which is of particular significance for the mutations I646V, I703V, and I646A.

The *in-silico* mutagenesis of I646V, I703V, and I646A residues was performed using PyMOL while the energy minimisation was done using SwissPBD viewer. The changes in nearby structures of these mutations were considered. This includes the effect of the mutations on the backbone, hydrogen bonding, position of residue, or access to the substrate sample. Following the energy minimisation of the mutants and the structural alignment with the WT hXOR, the interactions were analysed. The I646V and I703V mutations did not change the conformation of the neighbouring residues and no surface electrostatic change was observed. These mutations are present on a loop at the surface of the protein. However, the hydrogen bonds formed between Val^{646} with Lys^{779} and Val^{703} with Ile^{699} and Asn^{706} were shorter than the hydrogen bonds of WT hXOR. Moreover, there was no change in the length of hydrogen bond of Ala^{646} and Lys^{779} in the mutation compared to WT, but there was a slight difference in the electrostatic surface charge. As these amino acid changes appear to exert minimal structural changes, this may infer that the difference in catalytic activity may not be a consequence to changes in neighbouring residue interaction.

4.2. Protein Purification

Purification of hXOR was conducted using nickel-chelated Immobilised Metal Affinity Chromatography (IMAC), as the recombinant proteins were designed with an N-terminal six histidine tag that forms a dative covalent bond with the nickel chelated to the column. Weakly bound proteins were eluted from the column using a step gradient of low concentrations of imidazole, specifically 20 mM, 50 mM, and 75 mM, whereas all the his-tagged hXOR proteins eluted at high purity using 250 mM imidazole.

Amongst the untreated hXOR samples, the I646A protein showed the highest protein yield (27.36 mg/L), followed by the WT sample. The I703V produced slightly less protein than the WT, while the I646V-I703V showed a further decrease. The lowest yield was observed for the I646V mutant. Overall, all mutations except I646A resulted in lower yields compared to WT hXOR.

One possible explanation for the low yield of some of the hXOR samples could be that those variants are more active than the WT counterpart. In general, except I646A, hXOR protein samples with lower yield, had higher enzymatic activity. Since hXOR has the ability to generate ROS with antimicrobial properties, the elevated activity may have resulted in higher ROS levels, which could have been toxic to the bacterial host during the production of protein. However, this is not the case with all the samples, and this

hypothesis cannot be verified, due to the fact that the cell pellet was not weighed after cell harvesting.

The protein yield in this case was obtained from the soluble fraction. Although some of the protein may also be present in the insoluble fraction or in inclusion bodies, the pellets were not analysed. Therefore, it is not possible to determine whether this impacted the overall yield of pure protein,

Purity was calculated using ImageJ based on densitometry. WT hXOR exhibited the lowest percentage purity of 90.33% after chromatography. This could be related to the limited proteolysis shown in Figure 3.10. On average, the purity achieved by the hXOR mutants was higher when compared to WT hXOR. Untreated I646A hXOR exhibited the highest percentage purity at 99.61%. I646V, I703V, and I646V-I703V exhibited also comparably high percentage purities (97.92%, 98.91%, and 98.83%, respectively).

4.3. Biophysical Characterisation

4.3.1. Melting temperature

Circular dichroism (CD) spectroscopy provides information about the composition of the secondary structure of proteins as the peptide backbone absorbs light in the far-UV region (190-250 nm) and generates characteristic CD signals based on the arrangement of the protein secondary structure (Section 2.7.1). A CD spectrum is produced by the difference in the absorption of left- and right-circularly polarized light (Rocha et al., 2023). CD spectroscopy is also frequently used to assess the thermal stability of proteins by determining the melting temperature (Tm). The CD signal decreases as the temperature increases, and the protein starts unfolding. The Tm is characterised as the midpoint between the folded state and the unfolded state of the protein, corresponding to the temperature at which half of the protein population is unfolded (2.7.2) (Greenfield, 2009).

The melting temperatures of the various hXOR proteins ranged between 69.74^{o}C and 55.49^{o}C (Section 3.5.6). I703V hXOR was the most stable, with the highest melting temperature followed by WT and I646V (Tm of 66.8^{o}C, and 66.08^{o}C respectively). On the other hand, I646V-I703V, and I646A were both less stable (Tm 59.04^{o}C and 55.49^{o}C respectively). Despite that I646A was one of the least stable protein samples (55.49^{o}C),

it showed the highest activity compared to the untreated samples. It is possible that this low melting temperature might be due to the fact that, as observed in the DLS results, I646A showed no high-level oligomeric states, thus making it less thermodynamically stable compared to the other mutant proteins and the WT.

4.3.2. Secondary Structure

Far-UV circular dichroism (190-250 nm) provides useful information about the secondary structure content of protein that permits a rapid analysis of the structural consequences of known mutations. It is standard good laboratory practice to employ far-UV CD to assess the secondary structure of the purified recombinant protein prior to proceeding to further characterisation. Analysis of the secondary structure of hXOR, including alpha helices, beta sheets, beta turns and random coils, provided important insights into the structural stability. A higher content of alpha helices (negative minima at 208 nm, 222 nm, and positive peak near 190 nm) and beta sheets is generally associated with elevated enzyme stability, as these structures promote proper protein folding, provide rigidity, and enhance resistance to denaturation and proteolytic degradation (Rathi et al., 2015; Ahmed et al., 2022; Yakimov et al., 2016).

A comparison of the secondary structure composition of the untreated proteins (Section 3.5.5., Table 3.5) showed an overall greater proportion of antiparallel beta sheets compared to parallel beta sheets and alpha-helices, with this being more pronounced in I646V-I703V and WT proteins and least pronounced in I646V. Apart from these observations, there were no significant differences in the secondary structures between any of the samples, indicating that the mutations, did not have a considerable effect on the secondary structure of hXOR proteins. This implies that differences in the activity of the candidate proteins are not a direct consequence of gross misfolding. However, a typical CD secondary structure spectrum does not exclude the occurrence of minor changes in structure in localised regions within the protein, especially one as large and complex as hXOR,

4.4. Enzymatic Activity

The enzymatic activity of hXOR was measured based on the rate of uric acid formation. Two protocols of the uric acid assay were performed, one to measure the activity of the XO form of the enzyme using oxygen as a substrate, and the second to

obtain the activity of the complete hXOR enzyme, using NAD^+ as a substrate, which was then used to estimate the amount of XDH form (Nakamura and Yamazaki, 1982).

When comparing the normalised XO activity, the WT protein exhibited the lowest activity (0.011241 U/mg), while the activity of I646A was 9-fold higher (0.108102 U/mg), with a 962% increase compared to WT (Section 3.5.4.). In general, the mutants exhibited higher enzymatic activities compared to the WT hXOR. I646V and I646V-I703V also had high enzymatic activities with 0.085429 U/mg and 0.069368 U/mg, respectively, with 760% and 617% compared to WT. Interestingly, untreated I703V, although previously reported to enhance activity (Kudo et al., 2008), exhibited the lowest enzymatic activity amongst the mutants at 0.015487 U/mg, which was still higher than the activity of WT, by 138%. Surprisingly, the protein with the highest activity, I646A, was one of the least stable proteins (55.49^{o}C and exhibited no fibrillisation. This may suggest that higher Tm of the other proteins may be a consequence of oligomerisation states these may adopt.

The uric acid assay was also performed to measure the total hXOR form for the enzymatic activity with NAD^+, which serves as an electron acceptor and is reduced when uric acid is formed (Hille, 2005). The proteins followed the same pattern in activity to those measured for the XO form of the enzyme.

As already mentioned, in contrast to the findings of this project, previous studies reported different catalytic behaviours for the I646V and I703V mutations. It was observed that I646V exhibited a Vmax value nearly identical to WT hXOR, indicating no meaningful change in catalytic capacity while the I703V mutation had an increase of 210% in Vmax when compared to the WT. As noted before, these differences between the results in this project and the study might be due to different experimental approaches, including the use of impure sample and no normalisation in the published study (Kudo et al., 2008). The fact that the recombinant proteins were produced in different host cells, mammalian versus bacterial may contribute to the observed differences. The *E.coli* host cells used for this study were designed to improve molybdenum uptake into XOR and the cells were also supplemented with molybdenum ions during cell culturing. Moreover, Vmax was not calculated in this project. This further re-enforces the importance of testing different culture conditions for the optimisation of the production of recombinant proteins and that different proteins, including mutants of the same protein may benefit from different treatments.

The higher enzymatic activities observed are physiologically significant. An elevated hXOR activity enhances uric acid production and promotes the generation of ROS, especially when the enzyme shifts toward the XO form. Even relatively small increases in activity may contribute to endothelial dysfunction, and the increase in superoxide may lead to hypertension due to the production of peroxynitrite (Cai & Harrison, 2000; Battelli et al., 2014). When XDH is converted to XO, it can be released into the bloodstream, whether it can bind to glycosaminoglycans on the surface of the endothelium. Due to this the products of the XOR reaction are released directly into the blood (Bortolotti et al., 2021) and can exert their effect on the blood vessel wall.

Apart from the uric acid assays for XO and total hXOR activities at 25ºC, the activity of the samples was also measured at different temperatures (25ºC, 30ºC, 37ºC, 42ºC, and 50ºC). This showed that I646V-I703V and I646A were the most kinetically stable, meaning that they retained their activity at the higher temperatures. This is curious as I646A was also observed to be the least thermostable according to the CD results. However, thermostability and kinetic stability might not always be directly proportional to each other. In fact, an increase in flexibility, which might result into a lower thermostability, can lead to a higher catalytic activity (Quezada et al., 2017). This concept might explain why I646A is the most kinetically stable while being the least thermostable. In general, the activity of the WT, I646V, and I703V decreased inversely with temperature. According to this enzymatic assay, at physiological temperature (37ºC), many samples exhibited high or the highest enzymatic activities. This is not favourable, since higher enzymatic activity is attributed to health conditions related to high uric acid and ROS levels.

Additionally, the NBT in-gel assay was used to assess the activity of the hXOR samples, showing that they exhibited varying levels of enzymatic activity. The NBT assay is based on the direct measure of the amount of superoxide radicals by the XOR reaction.

As already mentioned, the high activity of the mutants observed in hXOR may have biological relevance under ischemic and hypoxic conditions in the human body. If the hXOR produced is highly active, reperfusion could result in the generation of a significant amount of ROS. This elevated ROS production may contribute to the development of health conditions, such as hypertension as previously discussed (Section 1.4.2). However, the activity measured in this project reflects that of the recombinant, purified enzyme and may not be identical to the enzymatic activity of hXOR *in vivo*. Under physiological conditions, hXOR is tightly regulated by several additional factors.

These include post-translational, such as the interconversion between the XDH and XO forms, which shifts in response to oxidative stress, through thiol oxidation or proteolysis, phosphorylation and intracellular redox environment (Berry & Hare, 2004; Harrison, 2002; Kayyali et al., 2001).

4.5. Propensity of Fibrillization

Thioflavin T (ThT) assay was used to validate the presence of amyloid fibrils (section 3.5.7). This assay was performed since negative staining conducted by Seychell (2019), showed that WT hXOR can form filaments under various pH's including physiological conditions.

Amyloidogenesis refers to the process of forming amyloid fibrils, which are highly order protein aggregates associated with various diseases, including Alzheimer's disease and type II diabetes melitus (Perez et al., 2023). Amyloidogenic sequences are short peptide segments found in proteins that self-assemble into stable, β-sheet-rich aggregates. These form intermolecular cross-β-sheet structures, which are usually found in amyloid fibrils (Beerten et al., 2015; Sebate & Ventura et al., 2013). The amyloidogenic sequences can promote protein misfolding and unwanted aggregation under physiological conditions (Kwiatkowski et al., 2024). Large proteins may also form amyloid structures due to the formation of proteolytic fragments or misfolding. The WT XOR did in fact exhibit proteolytic fragments in every purification made. These fragments in the sample may have contributed to the fibrillization propensity of this protein. Misfolding of normally soluble globular proteins is another cause of amyloid formations, with β-macroglobulin and transthyretin as known examples (Almeida & Brito, 2020). However, the presence of fibrils in the WT hXOR does not automatically classify them as pathogenic amyloids.

Glycine residues can play an important role in turns between β-strands and within β-sheets. Studies have shown that glycine can have an effect on aggregation, since the β-amyloid peptide contains GxxxG motif in the C-terminal region, which leads to the generation of toxic Aβ oligomers (Fonte et al., 2011). In fact, Ile646, is present between two glycines residues, G643 and G648, within this residue sequence: GSN**I**TG. Hydrophobic residues such as isoleucine and leucine have an important role in amyloid formation. In the islet amyloid polypeptide, these amino acids influence the kinetics of the formation of amyloids (Azriel & Gazit, 2001). In general, hydrophobic and aromatic

amino acids have high propensity of forming β-sheets, whereas glycine and proline have lower propensity of forming β-sheets (Burdukiewicz et al., 2017).

The ZipperDB server was used to predict the propensity of fibrillization based on the amino acid sequence of the hXOR samples. This showed that the sequence of WT around Ile646 is prone to support aggregation, as well as the Val646 but to a lesser extent. Compared to the WT and I646V, I646A presents a lower likelihood of fibrils formation. Similarly to WT, I703V indicates a high likelihood of fibril formation. The predictability of ZipperDB server correlated with the results obtained from the ThT assay. Moreover, when comparing isoleucine with valine, valine has a shorter, more branched R group which makes it less hydrophobic than isoleucine. Alanine has an even smaller R group, thus decreasing the hydrophobic character even further. This also correlates to the fact that the fibril formation decreased when going from isoleucine to valine to alanine (Kyte & Doolittle, 1982). When compared to the bovine amino acid sequence ZipperDB showed that the bovine XOR showed less propensity for fibril formation. This might be due to the change of residue from the hydrophobic isoleucine to the polar glutamate.

In fact, the ThT assay showed that the WT protein exhibited the greatest propensity towards amyloid fibril formation at 37ºC. I646V, and I646V-I703V formed fibrils to a less extent whereas no fibril formation was detected in the I646A and the I703V samples. The formation of amyloid fibrils may be a factor affecting the enzymatic activity. In fact, WT hXOR, showed the highest amount of fibril content while having the lowest activity. I646V variant had lower amount of fibrils and higher enzymatic activity compared to WT hXOR. On the other hand, I646A, showed no fibril formation while having the highest enzymatic activity. Overall, XOR protein variants produced under their respective optimal conditions exhibited higher enzymatic activity and either no or reduced fibril formation when compared to the WT hXOR. I703V upon HS, which was the optimised condition, appeared as an outlier, exhibiting both high enzymatic activity and high amount of amyloid fibrils. This variant displayed a predominant XDH composition (71%) relative to the XO form (28%), whereas the majority of the samples, were composed of approximately 50% of XDH form and 50% of the XO form. Given this distribution, further investigation is required to determine if fibril formation and high activity shown by I703V are caused by the XDH form. It would also be interesting to devise a method of separating the I703V fibrils from the dimeric fraction of the protein then conducting the enzyme assay to determine if the activity is due to only a fraction of

the protein molecules in the sample. The formation of amyloid filaments was thus overall, in agreement with the ZipperDB predictions.

As shown in Section 3.5.7, each of the hXOR samples started at a high fluorescence value, including the samples that did not show any fibril formation through ThT analysis. To assess the reason this occurred, *in silico* molecular docking was conducted using HDOCK and the WT hXOR cryoEM structure with the ThT molecule as a ligand. Docking showed that the ThT molecule does bind to the native hXOR molecule (Section 3.6.2), which may explain why the fluorescence started at high values for all hXOR proteins. ThT can bind to protein regions that do not form classical amyloid structures however the interaction is weak. Although ThT is the considered as the gold standard for amyloid detection, there are rare instances where it interacts with native globular proteins such serum albumins and acetylcholinesterases (Ferrari et al., 2001; Sen et al., 2009). The decrease in fluorescence over the course of time in some of the mutant proteins, such as the I646A, may also be explained by the dissociation of the ThT molecules from the protein dimer at higher temperatures.

Following the ThT assay, the recovered samples were analysed on a Blue-Native PAGE gel to confirm the presence of oligomers. Two prominent bands were observed at approximate molecular weights of 272 kDa and 545 kDa respectively that are representative of the dimer of hXOR and the dimer of dimers that is twice the mass expected for hXOR. In addition, there clearly were protein deposits in the wells, suggesting the occurrence of even higher molecular weight aggregates. It is important to note that even though all the samples did show higher molecular weight aggregates in the Blue-Native gel (Section 3.5.10), this only shows that higher oligomeric states are present and does not discriminate between amyloid fibrils and aggregates.

The secondary structure of the WT following ThT was also analysed using CD. This showed that following a 48-hr incubation at 37^{o}C in the presence of ThT, the WT hXOR had a higher proportion of parallel beta sheets when compared to the WT protein prior to incubation (Section 3.5.12). This further supports fibril formation, as fibrillization is normally linked to an increase in parallel beta sheet formation (Hoshino, 2016; Tompa, 2009).

4.6. Dynamic Light Scattering

Dynamic light scattering (DLS) is a technique used for the characterisation of the size of particles and aggregation behaviour. In a DLS instrument, the laser beam hits the macromolecules and the light scatters in many directions. A detector measures how the scattered light changes over time. The autocorrelator then analyses the intensity fluctuations, which compares the signal over time to determine how quickly the intensity changes. The rate of these fluctuations corresponds to the diffusion properties of the macromolecules (Rodriguez-Loya et al., 2024; Stetefeld et al., 2016). However, DLS measurements may not be accurate, as the technique is best suited for spherical molecules (Arenas-Guerrero et al., 2018; Langevin et al., 2018). Since XOR is non-spherical and relatively large, the data obtained from DLS may not accurately reflect its true hydrodynamic properties.

A minor species with a mean diameter of 18 nm, represents the dimer form. The WT hXOR protein appears largely polydisperse, showing a major species (91.78%) with a mean diameter of 107 nm, which represents a higher-order oligomeric state far larger than the native state.

In contrast, all the mutant proteins show greater initial monodispersity and smaller sizes. These results suggest that the particles present in the mutant protein samples are mostly in their native dimer form.

DLS was also conducted on samples recovered immediately after completion of the ThT assay. The results of these proteins were dramatically different. The particles observed for all the ThT samples were predominantly higher order oligomers. It is important to note that DLS results only show the formation of higher order oligomers, but do not show the formation of amyloid fibrils. This means that even though certain variants such as the I646A, showed a higher order oligomers, this does not exclusively translate to fibril formation. The smaller size was observed for the I646V-I703V with 100% of the population having a mean by intensity 30.08 nm, which represents a dimer of dimers, whereas the WT population is 141.4 nm, which suggests that very large oligomers had formed, supporting the results of the ThT assay. The rest of the samples are found between 40 – 70 nm, likely representing assemblies in the range of hexamers to decamers. The DLS data obtained after the ThT assay is consistent with the findings from the ThT assay for the WT hXOR. WT displayed very large particle sizes, reflecting the formation of substantial higher-order oligomers, which correlates with the high ThT fluorescence. However, even though some of the mutants showed weaker but still

measurable ThT signals (I646V, I646V-I703V), the sizes of the particles were similar to those of the mutants that did not show ThT fluorescence.

4.7. Treated Samples

Heat shock treatment of expressing recombinant proteins is a standard experimental optimisation step (Oganesyan et al., 2007). Heat shock of the bacterial culture was included in the protocol to trigger the heat shock response as the heat shock proteins maintain protein homeostasis, promote desirable protein folding and cofactor acquisition under stressful conditions. Heat shock proteins bind to an unfolded or incorrectly folded part of the enzyme to help in their proper folding. This prevents the development of non-functional conformations. However, proteins treated with HS can possibly be incompatible with the folding pathways favoured under stress (Becker & Craig, 1994; Oganesyan et al., 2007). Furthermore, it cannot be assumed that all recombinant protein expression improves upon HS as was clearly demonstrated by the results obtained in variants. The experiments related with heat shock are relevant as, in response to cellular stress such as oxidative stress and ischaemia, heat shock proteins are also expressed. This is applicable to hXOR as during oxidative stress and ischaemia, hXOR is also being produced. When coupled with the heat shock proteins, hXOR might fold in a different way, affecting its activity and stability as shown in the current work (Szyller & Bil-Lula, 2021).

The treatment of the bacterial culture with heat shock had variable effects on the hXOR samples. In terms of yield, although exposure to heat-shock caused a substantial improvement in the yield of the WT hXOR (193%), it had a negative effect on the yield of most of the other proteins. Specifically, it improved the production of WT (48.3 mg/L) and slightly the I646V mutant (11.5 mg/L), whereas all other mutants showed reduced yields compared to their untreated counterparts. Treatment with HS in cultures can cause the release of heat shock proteins that affect the folding of proteins (Mikhailova et al., 2025). This may be reflected in the rise in the yield for certain samples in the soluble fraction. If the damage to proteins is high, the heat shock response may direct misfolded protein towards degradation. However, the decrease in the yield after HS may indicate instability of the mutated recombinant proteins that may cause the protein to aggregate in inclusion bodies. The heat shock response also increases proteases, such as Lon and Clp, that degrade misfolded proteins. This would also have a negative effect on the yield (Meyer & Baker, 2011; Simmons et al., 2008).

The application of HS had either a positive or a negative impact on thermal stability depending on the mutation. For instance, HS caused an increase in the melting temperature of WT, I646V, and I646A hXOR samples, improving their thermostability. However, the difference of the Tm was not significant.

However, HS drastically decreased the melting temperature of I703V (59.55ºC), by approximately 10ºC and it also reduced the thermostability of I646V-I703V. Even though I646V-I703V+HS showed the lowest thermostability, after heat shock, it was the most active between the treated hXOR samples. I646V-I703V+HS had minimal fibrillization according to the ThT assay and this may explain the reduction in thermostability and increase in activity. In this case the exposure of the cells to heat shock may have improved protein folded and correct assembly of the quaternary structure.

Furthermore, a comparison of the untreated proteins with their HS counterparts revealed that the protein recovered from cells subjected to heat shock contained a higher proportion of alpha helices and parallel beta sheets whilst a smaller percentage of antiparallel beta sheets. I646A was the exception as the HS sample had a lower component of both alpha helices and parallel beta sheets and more anti-parallel beta sheets with respect to the untreated sample. In addition, the CD results indicate that heat shock treatment appears to have adversely affected the folding of the I646V-I703V protein as there was a sharp drop in the anti-parallel beta sheets (0.7%) component together with an increase in random coils (to 51.2%). However, the percentage of secondary structure motifs derived from Circular Dichroism (CD) data is generally not considered an absolute, high-resolution measure as it relies on comparisons with structure in the database and CD is also sensitive to experimental deviations. One would have to resort to structural data to confirm actual proportions of secondary structure motifs (Khrapunov, 2009; Micsonai et al., 2015; Nagy & Grubmüller, 2020).

Enzymatic activity was also differentially affected. Even though, HS increased the activity of WT (0.016636 U/mg) by 148%, the activity was still the lowest compared to the mutants. Treated WT also showed lower degree of fibrillization according to the ThT assay when compared to WT without HS but was still high compared to the other protein samples. Treatment with HS had a negative impact on the activity of both I646A and I646V resulting in a decrease of activity but overall, their activity remained higher than that of the WT XOR. Both the I646A+HS and I646V+HS showed no ThT fluorescence upon incubation, therefore the decrease in activity may be due to misfolding and aggregation or cofactor loss of some of the protein. However, the application of HS

improved the enzymatic activity of both I703V and I646V-I703V. In fact, the activity of I703V increased 7-fold although the fibrillization propensity of this protein increased also. The I646V-I703V protein on the other hand, retained the high activity whilst exhibiting no ThT signal upon incubation and appearing to be predominantly in the dimer state according to DLS data. Thereby the I646V-I703V protein appears to have benefitted further from heat shock exposure.

With the exception of I646V, all of the samples retained around 50% of their activity after incubation at 50ºC. I646V lost around 70% of its activity even after the 30ºC incubation. This shows that I646V is the least kinetically stable mutant out of all of them. Interestingly, when comparing these findings to the non-treated samples, one can observe that only the WT and I703V with HS retained their activity better after incubation than the non-treated counterparts.

According to the ThT assay, amongst the HS samples, only WT+HS, and I703V+HS formed amyloid fibrils at 8 μM. Moreover, in the DLS, similarly to WT hXOR, WT+HS major species population was very similar. Overall, the treatment with HS did not affect the size of the particles, since no significant changes were observed. Following the ThT assay, DLS results showed that WT+HS formed large oligomers with a population of 193 nm, which correlates with the high fluorescence of ThT. However, even though I703V+HS showed also high ThT signal the sizes of the particles were similar to the those of the mutants that did not show ThT fluorescence.

4.8. Concluding Remarks

Analysis of the whole genome sequencing data of the MAMI cohort revealed polymorphisms of the XDH gene (Stephanie Bezzina Wettinger, personal communication). The single variants I646V and I703V had previously been reported in the literature (Kudo et al., 2008). These variants were also reported in the MAMI study, with a statistically significant association with hyperuricaemia (Stephanie Bezzina Wettinger, personal communication). Surprisingly, analysis in the MAMI study also identified the occurrence of both I646V and I703V polymorphisms on the same gene, that was both statistically significant and associated with hyperuricaemia. Association with hypertension for the single polymorphisms and the double polymorphisms was difficult to confirm as many participants may have been on hypertension treatment at the time of

recruitment. Following analysis of the results of the current study, the following are the most pertinent observations.

The activity of all variants was higher than that of the WT protein. Analysis of DLS data confirmed that the native proteins of these mutants predominantly occur in the native dimer conformation. The protein of the WT hXOR (and the HS WT hXOR) exhibited the lowest activity whilst forming the largest oligomeric structures, according to the DLS data. Transmission electron microscopy that was conducted as part of a previous study showed that the WT hXOR appeared as filamentous structures whose formation was pH dependent, being more pronounced at pH 7.0 and above (Seychell, 2019). This information was the basis for the decision to perform the ThT assay for amyloid fibrils. According to the ThT fluorescence results, the WT hXOR formed amyloid fibrils that increased with both concentration and time period of incubation. A classical sigmoidal curve was observed when lowering the temperature and concentration of the protein. The ZipperDB server was used to assess if there were any amyloidogenic stretches within the amino acid sequence of the WT hXOR that combine properties of hydrophobicity, low overall charge and a high propensity to form beta sheets. In the neighbourhood of Ile646, a region of 6 amino acids was identified (GSNITG) where the glycine and serine formed the amyloidogenic core. Substitution of the Ile646 with valine reduced the amyloidogenic potential of both the glycine and the serine. This was reduced even further when Ile646 was replaced by alanine. This prediction was in fact supported by the ThT assay analysis of I646V (HS treated sample) and I646A as fibril formation was negligible. The amyloidogenic stretch detected in the region of Ile703 was EDAVKN, where K was the amyloidogenic hot spot. According to the ZipperDB prediction, substitution of Ile703 with valine had no significant effect on the amyloidogenic propensity of this stretch. The ThT assay for the I703V mutant confirmed this, especially for I703V+HS, as this exhibited high ThT fluorescence similar to that of the WT hXOR. In contrast to the WT protein, the native I703V protein predominantly adopted the dimer configuration as the favoured quaternary structure whilst formed fibrils upon incubation with ThT at 37˚C. In the dimer state, the activity of I703V was 8-fold higher than that of the WT. Again, similar to I646A and I646V proteins, the prevalence of the dimer state of I703V appears to influence the higher activity in these samples. The fact that the replacement of the Ile with a Val did not affect the amyloidogenic core was substantiated by the observation that the I703V retained its ability to form fibrils upon incubation. This suggests the amyloidogenic stretch associated with Ile646 has a greater

contribution to fibril formation as replacement of the Ile with an Ala or a Val removed or decreased the ability to form fibrils. The mutations also appeared to have an overall effect that stabilised the dimer. In this context, the properties exhibited by the I646V-I703V double mutant were analysed. This protein had an activity approximately 7-fold that of the WT XOR, in its native state it was predominately dimeric and according to the DLS data. After ThT incubation, it formed the quaternary structure of a dimer of dimers, that according to in-gel zymology for XOR activity, was still an active form of the protein. The presence of the two substitutions on the protein seems to have stabilised the protein as the dimer and dimer of dimer species. Although this was also observed in the single I646V and I703V mutant proteins, these two proteins did also form higher oligomeric structures and possible aggregates as DLS showed presence of particles in the absence of ThT signal. Although the genetical analysis of the polymorphisms is not part of the current study and an explanation of the prevalence of the double mutant cannot be explained at this stage, it is interesting to observe that the double mutant is both highly active and is stable in its native dimeric conformation. The lower Tm exhibited by the double mutant may also reflect the absence of higher hierarchy structures. When this mutant was produced in bacterial cells under conditions of the heat shock response, the protein that was formed was more active and predominately in the native quaternary structure. This may infer that under physiological conditions the I646V-I703V enzyme is not only hyperactive but also that under conditions of stress that trigger the heat shock response, its activity may possibly increase, thereby compounding the problems arising from the excess of reactive oxygen species and uric acid in blood. Conducting functional studies on mammalian cells would be an interesting follow-up to this current study.

Chapter 5 Conclusion

5.1. Conclusions

The aim of this project was to investigate the impact of two known clinical variants and one novel variant, specifically I646V and I703V, and I646V-I703V, as well as I646A, on the enzymatic activity, stability and oligomer formation. This is significant since the clinical variants may alter enzymatic activity and contribute to the development of hypertension and high uric acid levels. Moreover, ROS generated from the conversion of XDH to XO might react with NO to form peroxynitrite, which is linked to hypertension.

In this study, TP1000 *E.coli* cells were grown under aerobic conditions, and the effect of HS on the hXOR samples was assessed. Following the purification of protein samples, the enzymatic activity of hXOR was measured spectrophotometrically, via uric acid assays and NBT assay. The presence of higher order oligomers was obtained through blue native gel. Further characterisation was carried out, by determining the secondary structure, melting temperatures, and amyloid formation. The primary findings from this study were as follows:

hXOR WT

- WT with HS produced the highest yield.
- WT without HS showed limited activity on the uric acid assay. The hXOR activity increased by 148% upon HS.
- WT formed amyloid fibrils as it can be observed from the ThT assay.
- Most of the population of WT and WT+HS was found as high-order oligomers.

hXOR I646V

- I646V had the lowest yield compared to all the samples.
- I646V showed high activity with an increase of 760% compared to WT.
- The application of HS decreased the activity of I646V, but it increased slightly the yield and the stability.
- I646V formed amyloid fibrils but to a lesser extent compared to WT hXOR.

- I646V was found mostly in the native dimeric state, whereas I646V+HS was found in a mixture of dimeric and higher-order oligomeric state.

hXOR I703V

- I703V was the most stable, but the activity was only 138% higher than the WT.
- HS decreased the stability of I703V but it had higher activity, with an increase of 857% compared to the WT.
- The I703V+HS formed fibrils, whereas the I703V did not.
- I703V was found mostly in a dimer of dimer state, whereas I703V+HS was found in the native dimeric state.

hXOR I646V-I703V

- I646V-I703V had low melting temperature, and high enzymatic activity of 617% compared to WT.
- The application of HS decreased the yield and the stability but it increased slightly the activity.
- I646V-I703V formed fibrils but to a lesser extent compared to WT and I646V.
- The I646V-I703V+HS did not form fibrils.
- I646V-I703V, as well as I646V-I703V were present in the native dimeric state.

hXOR I646A

- I646A was one of the least thermostable samples, but with the highest activity, with an increase of 962% compared to the WT.
- I646A+HS was less active than I646A but still moderate activity and the stability was slightly higher.
- Under both conditions, hXOR I646A did not form amyloid fibrils.
- I646A and I646A+HS were found in the native dimeric state.

5.2. Limitations and Future work

In the enzymatic activity assays the reaction starts instantly when the protein is added to the mixture containing xanthine. Because of this, the enzymatic activity in the first milliseconds of the reaction was not monitored.

In this project, no statistical tests were conducted, since there were no biological replicates. More replicates are needed so that statistical tests, such as T-tests and ANOVA can be performed.

Other further work can include Transmission Electron Microscopy (TEM), and Cryo Electron Microscopy (EM) to characterise the structure of the higher-order oligomers in the hXOR. Furthermore, the corresponding mutation in bovine XOR, substituting isoleucine at position 645 with glutamate (I645E), which parallels the human I646V mutation, can be tested to determine whether this position contributes to functional differences between the bovine and human XOR. This is particularly relevant because bovine XOR exhibits higher enzymatic activity and does not form amyloids. Moreover, a study expressing the mutant XOR in human cell lines such as colon cells can be conducted. This can confirm whether WT hXOR forms fibrils *in vivo* and how the fibrils are using staining.

References

Abadeh, S., Killacky, J., Benboubetra, M., & Harrison, R. (1992). Purification and partial characterization of xanthine oxidase from human milk. *Biochimica et biophysica acta, 1117*(1), 25–32. https://doi.org/10.1016/0304-4165(92)90157-p

Adachi, T., Fukushima, T., Usami, Y., & Hirano, K. (1993). Binding of human xanthine oxidase to sulphated glycosaminoglycans on the endothelial-cell surface. *The Biochemical journal, 289 (Pt 2)*(Pt 2), 523–527. https://doi.org/10.1042/bj2890523

Agarwal, V., Hans, N., & Messerli, F. H. (2013). Effect of allopurinol on blood pressure: a systematic review and meta-analysis. *Journal of clinical hypertension (Greenwich, Conn.)*, *15*(6), 435–442. https://doi.org/10.1111/j.1751-7176.2012.00701.x

Alakel, N., Middeke, J. M., Schetelig, J., & Bornhäuser, M. (2017). Prevention and treatment of tumor lysis syndrome, and the efficacy and role of rasburicase. *OncoTargets ac and therapy*, *10*, 597–605. https://doi.org/10.2147/OTT.S103864

Almeida, Z. L., & Brito, R. M. M. (2020). Structure and Aggregation Mechanisms in Amyloids. *Molecules (Basel, Switzerland), 25*(5), 1195. https://doi.org/10.3390/molecules25051195

Alraawi, Z., Banerjee, N., Mohanty, S., & Kumar, T. K. S. (2022). Amyloidogenesis: What Do We Know So Far?. *International journal of molecular sciences, 23*(22), 13970. https://doi.org/10.3390/ijms232213970

Alsedfy, M. Y., Ebnalwaled, A. A., Moustafa, M., & Said, A. H. (2024). Investigating the binding affinity, molecular dynamics, and ADMET properties of curcumin-IONPs as a mucoadhesive bioavailable oral treatment for iron

deficiency anemia. *Scientific reports, 14*(1), 22027. https://doi.org/10.1038/s41598-024-72577-8

Andrabi, S. M., Sharma, N. S., Karan, A., Shahriar, S. M. S., Cordon, B., Ma, B., & Xie, J. (2023). Nitric oxide: Physiological functions, delivery, and biomedical applications. *Advanced Science, 10*(30), 2303259. https://10.1002/advs.202303259

Andrews, S. S., & Tretton, J. (2020). Physical Principles of Circular Dichroism. *Journal of Chemical Edication 97*(12). 4370-4376. 10.1021/acs.jchemed.0c01061

Arenas-Guerrero, P., Delgado, Á.V., Donovan, K.J., Scott, K., Bellini, T., Mantegazza, F., & Jiménez, M. L. (2018). Determination of the size distribution of non-spherical nanoparticles by electric birefringence-based methods. *Scientific Reports 8. https://doi.org/10.1038/s41598-018-27840-0*

Aronow W. S. (2018). Antihypertensive drug therapy. *Annals of translational medicine*, *6*(7), 123. https://doi.org/10.21037/atm.2018.01.26

Attard, R., Dingli, P., Spek, A. C., Cassar, K., Farrugia, R., & Wettinger, S. B. (2021). The impact of metabolic factors on inflammatory mrna expression profiles: Findings from the MAMI study. *Atherosclerosis, 331*(91), e91. https://doi.org/10.1016/j.atherosclerosis.2021.06.264

Avis, P. G., Bergel, F. and Bray, R. C. (1956) Cellular constituents. The chemistry of xanthine oxidase. Part III. Estimations of the cofactors and the catalytic function sof enzyme fractions of cows' milk. *J. Chem. Soc.*, 1219–1226.

Azriel, R., & Gazit, E. (2001). Analysis of the minimal amyloid-forming fragment of the islet amyloid polypeptide. An experimental support for the key role of the phenylalanine residue in amyloid formation. *The Journal of biological chemistry, 276*(36), 34156–34161. https://doi.org/10.1074/jbc.M102883200

Baldelli, A., Shi, J., Singh, A., Guo, Y., Fathordoobaby, F., Amiri, A., & Pratap-Singh, A. (2024). Effect of high-pressure on protein structure refolding, and crystallization. *Food Chemistry Advances, 5*. https://doi.org/10.1016/j.focha.2024.100741

Barreras, A., & Gurk-Turner, C. (2003). Angiotensin II receptor blockers. *Proceedings (Baylor University. Medical Center)*, *16*(1), 123–126. https://doi.org/10.1080/08998280.2003.11927893

Barsotti, C., & Ipata, P. L. (2004). Metabolic regulation of ATP breakdown and of adenosine production in rat brain extracts. *The international journal of biochemistry & cell biology, 36*(11), 2214–2225. https://doi.org/10.1016/j.biocel.2004.04.015

Battelli, M. G. (1980). Enzymic conversion of rat liver xanthine oxidase from dehydrogenase (D form) to oxidase (O form). *FEBS Letters, 113*(1), 47–51. https://doi.org/10.1016/0014-5793(80)80491-1

Battelli, M. G., Bolognesi, A., & Polito, L. (2014). Pathophysiology of circulating xanthine oxidoreductase: New emerging roles for a multi-tasking enzyme. *Biochimica et Biophysica Acta (BBA) - Molecular Basis of Disease, 1842*(9), 1502–1517. https://doi.org/10.1016/j.bbadis.2014.05.022

Battelli, M. G., Polito, L., Bortolotti, M., & Bolognesi, A. (2016a). Xanthine Oxidoreductase in Drug Metabolism: Beyond a Role as a Detoxifying Enzyme. *Current medicinal chemistry, 23*(35), 4027–4036. https://doi.org/10.2174/0929867323666160725091915

Battelli, M. G., Polito, L., Bortolotti, M., & Bolognesi, A. (2016b). Xanthine Oxidoreductase-Derived Reactive Species: Physiological and Pathological Effects. *Oxidative medicine and cellular longevity*, *2016*, 3527579. https://doi.org/10.1155/2016/3527579

Battelli, M. G., Bortolotti, M., Polito, L., & Bolognesi, A. (2018). The role of xanthine oxidoreductase and uric acid in metabolic syndrome. *Biochimica et biophysica*

acta. Molecular basis of disease, *1864*(8), 2557–2565. https://doi.org/10.1016/j.bbadis.2018.05.003

Becker, J., & Craig, E. A. (1994). Heat-shock proteins as molecular chaperones. *European journal of biochemistry, 219*(1-2), 11–23. https://doi.org/10.1007/978-3-642-79502-2_2

Beerten, J., Van Durme, J., Gallardo, R., Capriotti, E., Serpell, L., Rousseau, F., & Schymkowitz, J. (2015). WALTZ-DB: a benchmark database of amyloidogenic hexapeptides. *Bioinformatics (Oxford, England), 31*(10), 1698–1700. https://doi.org/10.1093/bioinformatics/btv027

Benigni, A., Cassis, P., & Remuzzi, G. (2010). Angiotensin II revisited: new roles in inflammation, immunology and aging. *EMBO molecular medicine*, *2*(7), 247–257. https://doi.org/10.1002/emmm.201000080

Benboubetra, M., Baghiani, A., Atmani, D., & Harrison, R. (2004). Physicochemical and kinetic properties of purified sheep's milk xanthine oxidoreductase. *Journal of dairy science, 87*(6), 1580–1584. https://doi.org/10.3168/jds.S0022-0302(04)73311-1

Berry, C.E. and Hare, J.M. (2004), Xanthine oxidoreductase and cardiovascular disease: molecular mechanisms and pathophysiological implications. *The Journal of Physiology, 555*, pp. 589-606. https://doi.org/10.1113/jphysiol.2003.055913

Bortolotti, M., Polito, L., Battelli, M. G., & Bolognesi, A. (2021). Xanthine oxidoreductase: One enzyme for multiple physiological tasks. *Redox Biology, 41*, 101882. https://10.1016/j.redox.2021.101882

Bove, M., Cicero, A. F. G., & Borghi, C. (2017). The Effect of Xanthine Oxidase Inhibitors on Blood Pressure and Renal Function. *Current hypertension reports, 19*(12), 95. https://doi.org/10.1007/s11906-017-0793-3

Brown, N. J., & Vaughan, D. E. (1998). Angiotensin-converting enzyme inhibitors. *Circulation, 97*(14), 1411–1420. https://10.1161/01.CIR.97.14.1411

Brumshtein, B., Esswein, S. R., Sawaya, M. R., Rosenberg, G., Ly, A. T., Landau, M., & Eisenberg, D. S. (2018). Identification of two principal amyloid-driving segments in variable domains of Ig light chains in systemic light-chain amyloidosis. *The Journal of biological chemistry, 293*(51), 19659–19671. https://doi.org/10.1074/jbc.RA118.004142

Bray, R. C. (1975). Molybdenum-containing enzymes. *Journal of The Less-Common Metals 54*(2), 527–536.

Bryan, N. S. (2022). Nitric oxide deficiency is a primary driver of hypertension. *Biochemical Pharmacology, 206*, 115325. https://10.1016/j.bcp.2022.115325

Bugnon, M., Röhrig, U. F., Goullieux, M., Perez, M. A. S., Daina, A., Michielin, O., & Zoete, V. (2024). SwissDock 2024: major enhancements for small-molecule docking with Attracting Cavities and AutoDock Vina. *Nucleic acids research, 52*(W1), W324–W332. https://doi.org/10.1093/nar/gkae300

Burdukiewicz, M., Sobczyk, P., Rödiger, S., Duda-Madej, A., Mackiewicz, P., & Kotulska, M. (2017). Amyloidogenic motifs revealed by n-gram analysis. *Scientific reports, 7*(1), 12961. https://doi.org/10.1038/s41598-017-13210-9

Cantu-Medellin, N., & Kelley, E. E. (2013). Xanthine oxidoreductase-catalyzed reduction of nitrite to nitric oxide: Insights regarding where, when and how. *Nitric Oxide, 34*, 19–26. https://10.1016/j.niox.2013.02.081

Carey, R. M., Muntner, P., Bosworth, H. B., & Whelton, P. K. (2018). Prevention and Control of Hypertension: JACC Health Promotion Series. *Journal of the American College of Cardiology*, *72*(11), 1278–1293. https://doi.org/10.1016/j.jacc.2018.07.008

Carey, R. M., Calhoun, D. A., Bakris, G. L., Brook, R. D., Daugherty, S. L., Dennison-Himmelfarb, C., Egan, B. M., Flack, J. M., Gidding, S. S., Judd, E., Lackland, D. T., Laffer, C. L., Newton-Cheh, C., Smith, S. M., Taler, S. J., Textor, S. C., Turan, T. N., White, W. B., on behalf of the American Heart Association Professional/Public Education and Publications Committee of the Council on Hypertension, . . . and, S. C. (2018). Resistant hypertension: Detection, evaluation, and management: A scientific statement from the american heart association. *Hypertension, 72*(5), e53–e90. https://10.1161/HYP.0000000000000084

Carretero, O. A., & Oparil, S. (2000). Essential hypertension. *Circulation, 101*(3), 329–335. https://10.1161/01.CIR.101.3.329

Chan, R. J., Parikh, N., Ahmed, S., Ruzicka, M., & Hiremath, S. (2024). Blood pressure control should focus on more potassium: Controversies in hypertension. *Hypertension, 81*(3), 501–509. https://10.1161/HYPERTENSIONAHA.123.20545

Chandel, T. I., Zaman, M., Khan, M. V., Ali, M., Rabbani, G., Ishtikhar, M., & Khan, R. H. (2018). A mechanistic insight into protein-ligand interaction, folding, misfolding, aggregation and inhibition of protein aggregates: An overview. *International journal of biological macromolecules, 106*, 1115–1129. https://doi.org/10.1016/j.ijbiomac.2017.07.185

Chen, C., Lü, J. M., & Yao, Q. (2016). Hyperuricemia-Related Diseases and Xanthine Oxidoreductase (XOR) Inhibitors: An Overview. *Medical science monitor : international medical journal of experimental and clinical research*, *22*, 2501–2512. https://doi.org/10.12659/msm.899852

Cighetti, G., Debiasi, S., & Paroni, R. (1993). Effect of glutathione depletion on the conversion of xanthine dehydrogenase to oxidase in rat liver. *Biochemical pharmacology, 45*(11), 2359–2361. https://doi.org/10.1016/0006-2952(93)90213-g

Corte, E. D., & Stirpe, F. (1972). The regulation of rat liver xanthine oxidase. Involvement of thiol groups in the conversion of the enzyme activity from dehydrogenase (type D) into oxidase (type O) and purification of the enzyme. *The Biochemical journal, 126*(3), https://doi.org/10.1042/bj1260739

Cuevas, S., Villar, V. A. M., & Jose, P. A. (2019). Genetic polymorphisms associated with reactive oxygen species and blood pressure regulation. *The pharmacogenomics journal*, *19*(4), 315–336. https://doi.org/10.1038/s41397-019-0082-4

De Ferrari, G. V., Mallender, W. D., Inestrosa, N. C., & Rosenberry, T. L. (2001). Thioflavin T is a fluorescent probe of the acetylcholinesterase peripheral site that reveals conformational interactions between the peripheral and acylation sites. *The Journal of biological chemistry, 276*(26), 23282–23287. https://doi.org/10.1074/jbc.M009596200

Dillman, K. M., Hawkins, A. M., Ragland, A. R., Wester, G. C., Greene, D. R., Varrassi, G., Moore, P., Behara, R., Ahmadzadeh, S., Siddaiah, H., Shekoohi, S., & Kaye, A. D. (2024). Allopurinol: Clinical Considerations in the Development and Treatment of Stevens-Johnson Syndrome, Toxic Epidermal Necrolysis, and Other Associated Drug Reactions. *Cureus*, *16*(7), e64654. https://doi.org/10.7759/cureus.64654

Dotmatics. (2025). *SnapGene® software*. https://www.snapgene.com

Eberhardt, J., Santos-Martins, D., Tillack, A. F., & Forli, S. (2021). AutoDock Vina 1.2.0: New Docking Methods, Expanded Force Field, and Python Bindings. *Journal of chemical information and modeling, 61*(8), 3891–3898. https://doi.org/10.1021/acs.jcim.1c00203

Elliott, W. J., & Ram, C. V. (2011). Calcium channel blockers. *Journal of clinical hypertension (Greenwich, Conn.)*, *13*(9), 687–689. https://doi.org/10.1111/j.1751-7176.2011.00513.x

Eltzschig, H. K., & Eckle, T. (2011). Ischemia and reperfusion--from mechanism to translation. *Nature medicine*, *17*(11), 1391–1401. https://doi.org/10.1038/nm.2507

Enroth, C., Eger, B. T., Okamoto, K., Nishino, T., Nishino, T., & Pai, E. F. (2000). Crystal structures of bovine milk xanthine dehydrogenase and xanthine oxidase: Structure-based mechanism of conversion. *Proceedings of the National Academy of Sciences,* *97*(20), 10723-10728. https://10.1073/pnas.97.20.10723

Fatima, S., & Mahmood, S. (2021). Combatting a silent killer - the importance of self-screening of blood pressure from an early age. *EXCLI journal*, *20*, 1326–1327. https://doi.org/10.17179/excli2021-4140

Ferdaus, S. A., Ohara, H., Matsuo, H., Kawakami, K., Takeuchi, F., Fujikawa, K., Kawakita, E., Kato, N., Nabika, T., & Kanasaki, K. (2025). NAD+ deficiency plays essential roles in the hyperuricemia of stroke-prone spontaneously hypertensive rat via xanthine dehydrogenase to xanthine oxidase conversion. Biochemical and biophysical research communications, 744, 151136. https://doi.org/10.1016/j.bbrc.2024.151136

Foëx, P., & Sear, J. W. (2004). Hypertension: Pathophysiology and treatment. *Continuing Education in Anaesthesia Critical Care & Pain, 4*(3), 71–75. https://10.1093/bjaceaccp/mkh020

Fonte, V., Dostal, V., Roberts, C. M., Gonzales, P., Lacor, P., Magrane, J., Dingwell, N., Fan, E. Y., Silverman, M. A., Stein, G. H., & Link, C. D. (2011). A glycine zipper motif mediates the formation of toxic β-amyloid oligomers *in vitro* and *in vivo*. *Springer Nature Link, 61*. https://doi.org/10.1186/1750-1326-6-61

Fourie, K. R., & Wilson, H. L. (2020). Understanding GroEL and DnaK Stress Response Proteins as Antigens for Bacterial Diseases. Vaccines, 8(4), 773. https://doi.org/10.3390/vaccines8040773

Fried, R. (1966) Calorimetric Determination of Xanthine Dehydrogenase by Tetrazolium Reduction. *Analytical Biochemistry, 16*, 427–432.

Furuhashi M. (2020). New insights into purine metabolism in metabolic diseases: role of xanthine oxidoreductase activity. *American journal of physiology. Endocrinology and metabolism*, *319*(5), E827–E834. https://doi.org/10.1152/ajpendo.00378.2020

Gabb G. (2020). What is hypertension?. *Australian prescriber*, *43*(4), 108–109. https://doi.org/10.18773/austprescr.2020.025

Gadave, K. S., Panda, S., Singh, S., Kalra, S., Malakar, D., Mohanty, A. K., & Kaushik, J. K. (2014). Structural and functional insights into the catalytic inactivity of the major fraction of buffalo milk xanthine oxidoreductase. *PloS one, 9*(1), e87618. https://doi.org/10.1371/journal.pone.0087618

Gras, Sally. (2009). Chapter 6 - Surface- and Solution-Based Assembly of Amyloid Fibrils for Biomedical and Nanotechnology Applications. *Advances in Chemical Engineering*, *35*. 161-209. 10.1016/S0065-2377(08)00206-8

Ghosh, S. M., Kapil, V., Fuentes-Calvo, I., Bubb, K. J., Pearl, V., Milsom, A. B., Khambata, R., Maleki-Toyserkani, S., Yousuf, M., Benjamin, N., Webb, A. J., Caulfield, M. J., Hobbs, A. J., & Ahluwalia, A. (2013). Enhanced vasodilator activity of nitrite in hypertension: critical role for erythrocytic xanthine oxidoreductase and translational potential. *Hypertension (Dallas, Tex. : 1979), 61*(5), 1091–1102. https://doi.org/10.1161/HYPERTENSIONAHA.111.00933

Godber, B. L. J., Doel, J. J., Sapkota, G. P., Blake, D. R., Stevens, C. R., Eisenthal, R., & Harrison, R. (2000). Reduction of nitrite to nitric oxide catalyzed by xanthine oxidoreductase*. *Journal of Biological Chemistry, 275*(11), 7757–7763. https://10.1074/jbc.275.11.7757

Godber, B. L., Schwarz, G., Mendel, R. R., Lowe, D. J., Bray, R. C., Eisenthal, R., & Harrison, R. (2005). Molecular characterization of human xanthine oxidoreductase: the enzyme is grossly deficient in molybdenum and substantially deficient in iron-sulphur centres. *The Biochemical journal, 388*(Pt 2), 501–508. https://doi.org/10.1042/BJ20041984

Godber, B., Sanders, S., Harrison, R., Eisenthal, R., & Bray, R. C. (1997). > or = 95% of xanthine oxidase in human milk is present as the demolybdo form, lacking molybdopterin. *Biochemical Society transactions, 25*(3), 519S. https://doi.org/10.1042/bst025519s

Goldschmidt L, Teng PK, Riek R, Eisenberg D (2010). Identifying the amylome, proteins capable of forming amyloid-like fibrils, *Proc. Natl. Acad. Sci. U.S.A. 107*(8): 3487-3492.

Greenfield N. J. (2006). Using circular dichroism spectra to estimate protein secondary structure. *Nature protocols, 1*(6), 2876–2890. https://doi.org/10.1038/nprot.2006.202

Guex, N., & Peitsch, M. C. (1997). SWISS-MODEL and the Swiss-PdbViewer: an environment for comparative protein modeling. *Electrophoresis, 18*(15), 2714–2723. https://doi.org/10.1002/elps.1150181505

Gupta, R., & Guptha, S. (2010). Strategies for initial management of hypertension. *The Indian journal of medical research*, *132*(5), 531–542.

Haga, Y., Ohtsubo, T., Murakami, N., Noguchi, H., Kansui, Y., Goto, K., Matsumura, K., & Kitazono, T. (2017). Disruption of xanthine oxidoreductase gene attenuates renal ischemia reperfusion injury in mice. *Life Sciences, 182*, 73–79. https://10.1016/j.lfs.2017.06.011

Han, C., Wu, Y., Rong, J., Xia, Q., & Du, D. (2025). Unveiling the Emerging Role of Xanthine Oxidase in Acute Pancreatitis: Beyond Reactive Oxygen Species.

Antioxidants (Basel, Switzerland), 14(1), 95. https://doi.org/10.3390/antiox14010095

Harrison R. (2002). Structure and function of xanthine oxidoreductase: where are we now? *Free radical biology & medicine, 33*(6), 774–797. https://doi.org/10.1016/s0891-5849(02)00956-5

Hille, R., & Nishino, T. (1995). Flavoprotein structure and mechanism. 4. Xanthine oxidase and xanthine dehydrogenase. *FASEB journal : official publication of the Federation of American Societies for Experimental Biology, 9*(11), 995–1003.

Hoshino M. (2017). Fibril formation from the amyloid-β peptide is governed by a dynamic equilibrium involving association and dissociation of the monomer. *Biophysical reviews, 9*(1), 9–16. https://doi.org/10.1007/s12551-016-0217-7

Kikuchi, H., Hiroshi, F., Tadaomi, F., Okamoto, K., Leimkühler S, & Nishino, T. (2012). Different inhibitory potency of febuxostat towards mammalian and bacterial xanthine oxidoreductases: Insight from molecular dynamics. *Scientific Reports 2, Article Number: 331*. https://https://doi.org/10.1038/srep00331

Hellsten, Y. (2000). The role of xanthine oxidase in exercise. In C. K. Sen, L. Packer, & O. O. P. Hänninen (Eds.). *Handbook of oxidants and antioxidants in exercise (pp. 153–176). Elsevier Science*. https://doi.org/10.1016/B978-044482650-3/50007-9

Hosoya, T., Ohno, I., Nomura, S., Hisatome, I., Uchida, S., Fujimori, S., Yamamoto, T., & Hara, S. (2014). Effects of topiroxostat on the serum urate levels and urinary albumin excretion in hyperuricemic stage 3 chronic kidney disease patients with or without gout. *Clinical and experimental nephrology*, *18*(6), 876–884. https://doi.org/10.1007/s10157-014-0935-8

Hosoya, T., Sasaki, T., Hashimoto, H., Sakamoto, R., & Ohashi, T. (2016). Clinical efficacy and safety of topiroxostat in Japanese male hyperuricemic patients with or without gout: an exploratory, phase 2a, multicentre, randomized, double-

blind, placebo-controlled study. *Journal of clinical pharmacy and therapeutics*, *41*(3), 298–305. https://doi.org/10.1111/jcpt.12392

Huang, Y., Huang, W., Mai, W., Cai, X., An, D., Liu, Z., Huang, H., Zeng, J., Hu, Y., & Xu, D. (2017). White-coat hypertension is a risk factor for cardiovascular diseases and total mortality. *Journal of hypertension*, *35*(4), 677–688. https://doi.org/10.1097/HJH.0000000000001226

Huang, S. Y., & Zou, X. (2014). A knowledge-based scoring function for protein-RNA interactions derived from a statistical mechanics-based iterative method. *Nucleic acids research, 42*(7), e55. https://doi.org/10.1093/nar/gku077

Huang, S. Y., & Zou, X. (2008). An iterative knowledge-based scoring function for protein-protein recognition. *Proteins, 72*(2), 557–579. https://doi.org/10.1002/prot.21949

Ichida, K., Amaya, Y., Okamoto, K., & Nishino, T. (2012). Mutations Associated with Functional Disorder of Xanthine Oxidoreductase and Hereditary Xanthinuria in Humans. *International Journal of Molecular Sciences*, *13*(11), 15475-15495. https://doi.org/10.3390/ijms131115475

Igel, T. F., Toprover, M., Krasnokutsky, S., & Pillinger, M. H. (2019). *Drugs in the Pipeline. Gout,* 185–195.

Invernizzi, G., Papaleo, E., Sabate, R., & Ventura, S. (2012). Protein aggregation: mechanisms and functional consequences. *The international journal of biochemistry & cell biology, 44*(9), 1541–1554. https://doi.org/10.1016/j.biocel.2012.05.023

Jarasch, E., Grund, C., Bruder, G., Heid, H. W., Keenan, T. W., & Franke, W. W. (1981). Localization of xanthine oxidase in mammary-gland epithelium and capillary endothelium. *Cell, 25*(1), 67-82. https://10.1016/0092-8674(81)90232-4

Johri, N., Matreja, P. S., Maurya, A., Varshney, S., & Smritigandha (2023). Role of β-blockers in Preventing Heart Failure and Major Adverse Cardiac Events Post Myocardial Infarction. *Current cardiology reviews*, *19*(4), e110123212591. https://doi.org/10.2174/1573403X19666230111143901

Kany, S., Vollrath, J. T., & Relja, B. (2019). Cytokines in Inflammatory Disease. *International journal of molecular sciences*, *20*(23), 6008. https://doi.org/10.3390/ijms20236008

Kayyali, U. S., Donaldson, C., Huang, H., Abdelnour, R., & Hassoun, P. M. (2001). Phosphorylation of xanthine dehydrogenase/oxidase in hypoxia. *The Journal of biological chemistry, 276*(17), 14359–14365. https://doi.org/10.1074/jbc.M010100200

Kedzierska, S., Jezierski, G., & Taylor, A. (2001). DnaK/DnaJ chaperone system reactivates endogenous E. coli thermostable FBP aldolase in vivo and in vitro; the effect is enhanced by GroE heat shock proteins. *Cell stress & chaperones, 6*(1), 29–37. https://doi.org/10.1379/1466-1268(2001)006<0029:ddcsre>2.0.co;2

Kehrenberg, M. C. A., & Bachmann, H. S. (2022). Diuretics: a contemporary pharmacological classification?. *Naunyn-Schmiedeberg's archives of pharmacology*, *395*(6), 619–627. https://doi.org/10.1007/s00210-022-02228-0

Kelley, E. E. (2015). A new paradigm for XOR-catalyzed reactive species generation in the endothelium. *Pharmacological Reports, 67*(4), 669–674. https://10.1016/j.pharep.2015.05.004

Khrapunov S. (2009). Circular dichroism spectroscopy has intrinsic limitations for protein secondary structure analysis. *Analytical biochemistry, 389*(2), 174–176. https://doi.org/10.1016/j.ab.2009.03.036

Kim, B.J., Bae, HJ., Wong, L.K.S. (2016). Pathophysiology and Mechanisms Whereby Hypertension May Cause Stroke. In: Aiyagari, V., Gorelick, P. (eds)

Hypertension and Stroke. *Clinical Hypertension and Vascular Diseases*. https://doi.org/10.1007/978-3-319-29152-9_6

Kim R. (2011). Native agarose gel electrophoresis of multiprotein complexes. *Cold Spring Harbor protocols, 2011*(7), 884–887. https://doi.org/10.1101/pdb.prot4558

Kotozaki, Y., Satoh, M., Nasu, T., Tanno, K., Tanaka, F., & Sasaki, M. (2023). Human Plasma Xanthine Oxidoreductase Activity in Cardiovascular Disease: Evidence from a Population-Based Study. *Biomedicines*, *11*(3), 754. https://doi.org/10.3390/biomedicines11030754

Kraev, K. I., Geneva-Popova, M. G., Hristov, B. K., Uchikov, P. A., Popova-Belova, S. D., Kraeva, M. I., Basheva-Kraeva, Y. M., Stoyanova, N. S., & Mitkova-Hristova, V. T. (2023). Celebrating Versatility: Febuxostat's Multifaceted Therapeutic Application. *Life*, *13*(11), 2199. https://doi.org/10.3390/life13112199

Kudo, M., Moteki, T., Sasaki, T., Konno, Y., Ujiie, S., Onose, A., Mizugaki, M., Ishikawa, M., & Hiratsuka, M. (2008). Functional characterization of human xanthine oxidase allelic variants. Pharmacogenetics and genomics, 18(3), 243–251. https://doi.org/10.1097/FPC.0b013e3282f55e2e

Kusano, T., Nishino, T., Okamoto, K., Hille, R., & Nishino, T. (2023). The mechanism and significance of the conversion of xanthine dehydrogenase to xanthine oxidase in mammalian secretory gland cells. *Redox biology*, *59*, 102573. https://doi.org/10.1016/j.redox.2022.102573

Kuwabara, Y., Nishino, T., Okamoto, K., Matsumura, T., Eger, B. T., Pai, E. F., & Nishino, T. (2003). Unique amino acids cluster for switching from the dehydrogenase to oxidase form of xanthine oxidoreductase. *Proceedings of the National Academy of Sciences 100*(14), 8170-8175. https://10.1073/pnas.1431485100

Kwiatkowski, W., Greenwald, J., Murzakhmetov, L., Robinson, R. C., & Riek, R. (2024). Short Peptide Amyloids Are a Potential Sequence Pool for the Emergence of Proteins. *Journal of molecular biology, 436*(6), 168495. https://doi.org/10.1016/j.jmb.2024.168495

Kyte, J., & Doolittle, R. F. (1982). A simple method for displaying the hydropathic character of a protein. *Journal of molecular biology, 157*(1), 105–132. https://doi.org/10.1016/0022-2836(82)90515-0

Langevin, D., Raspaud, E., Mariot, S., Knyazev, A., Stocco, A., Salonen, A., Luch, A., Haase, A., Trouiller, B., Relier, C., Lozano, O., Thomas, S., Salvati, A., & Dawson, K. (2018). Towards reproducible measuremtn of nanoparticle size using dynamic light scattering: Important controls and considerations. *NanoImpact, 10*, 161-167. https://doi.org/10.1016/j.impact.2018.04.002

Laurent, S. (2017). Antihypertensive drugs. *Pharmacological Research, 124*, 116–125. https://10.1016/j.phrs.2017.07.026

Lee, E. M. (2023). Calcium channel blockers for hypertension: old, but still useful. *Cardiovascular Prevention and Pharmacotherapy*, *5*(4), 113–125. DOI: https://doi.org/10.36011/cpp.2023.5.e16

Lee, J. H., Go, T. H., Lee, S. H., Kim, J., Huh, J. H., Kim, J. Y., Kang, D. R., Jeong, S., Koh, S. B., & Choi, J. R. (2019). Association between Serum Urate and Risk of Hypertension in Menopausal Women with XDH Gene. *Journal of clinical medicine, 8*(5), 738. https://doi.org/10.3390/jcm8050738

Li, C., & Zhou, H. M. (2011). The role of manganese superoxide dismutase in inflammation defense. *Enzyme research, 2011*, 387176. https://doi.org/10.4061/2011/387176

Li, H., Samouilov, A., Liu, X., & Zweier, J. L. (2001). Characterization of the magnitude and kinetics of xanthine oxidase-catalyzed nitrite reduction. Evaluation of its role in nitric oxide generation in anoxic tissues. *The Journal of*

biological chemistry, 276(27), 24482–24489. https://doi.org/10.1074/jbc.M011648200

Li, H., Samouilov, A., Liu, X., & Zweier, J. L. (2004). Characterization of the effects of oxygen on xanthine oxidase-mediated nitric oxide formation. *The Journal of biological chemistry, 279*(17), https://doi.org/10.1074/jbc.M314336200

Li, X., Chen, D., Qi, C., Yang, Y., Guo, K., Ma, C., Tian, J., Li, J., Zhang, L., Wang, B., Xiao, Z., & Ye, F. (2024). Identification of a novel xanthine oxidoreductase inhibitor for hyperuricemia treatment with high efficacy and safety profile. *Biomedicine & Pharmacotherapy, 178*, 117223. https://10.1016/j.biopha.2024.117223

Liu, N., Xu, H., Sun, Q., Yu, X., Chen, W., Wei, H., Jiang, J., Xu, Y., & Lu, W. (2021). The Role of Oxidative Stress in Hyperuricemia and Xanthine Oxidoreductase (XOR) Inhibitors. *Oxidative medicine and cellular longevity*, *2021*, 1470380. https://doi.org/10.1155/2021/1470380

Macdonald, A. S., McConnachie, A., Dickie, D. A., Bath, P. M., Forbes, K., Quinn, T., Broomfield, N. M., Dani, K., Doney, A., Muir, K. W., Struthers, A., Walters, M., Barber, M., Bhalla, A., Cameron, A., Guyler, P., Hassan, A., Kearney, M., Keegan, B., Lakshmanan, S., … Dawson, J. (2024). Allopurinol and blood pressure variability following ischemic stroke and transient ischemic attack: a secondary analysis of XILO-FIST. *Journal of human hypertension*, *38*(4), 307–313. https://doi.org/10.1038/s41371-024-00906-5

MacMillan-Crow, L. A., Crow, J. P., Kerby, J. D., Beckman, J. S., & Thompson, J. A. (1996). Nitration and inactivation of manganese superoxide dismutase in chronic rejection of human renal allografts. *Proceedings of the National Academy of Sciences of the United States of America*, *93*(21), 11853-11858. https://doi.org/10.1073/pnas.93.21.11853 93(21), 11853–11858

Madeira, F., Madhusoodanan, N., Lee, J., Eusebi, A., Niewielska, A., Tivey, A. R. N., Lopez, R., & Butcher, S. (2024). The EMBL-EBI Job Dispatcher sequence

analysis tools framework in 2024. *Nucleic acids research, 52*(W1), W521–W525. https://doi.org/10.1093/nar/gkae241

Mahfooz, K., Sohail, H., Gvajaia, A., Arif, U., Grewal, D., Muppidi, M. R., Vohra, V., Tarique, A., & Vasavada, A. (2023). Rasburicase in treating tumor lysis syndrome: An umbrella review. *Cancer Pathogenesis and Therapy, 1*(4), 262– 271. https://10.1016/j.cpt.2023.07.001

Maia, L., Duarte, R. O., Ponces-Freire, A., Moura, J. J., & Mira, L. (2007). NADH oxidase activity of rat and human liver xanthine oxidoreductase: potential role in superoxide production. *Journal of biological inorganic chemistry : JBIC : a publication of the Society of Biological Inorganic Chemistry, 12*(6), 777–787. https://doi.org/10.1007/s00775-007-0229-7

Marla, S. S., Lee, J., & Groves, J. T. (1997). Peroxynitrite rapidly permeates phospholipid membranes. *Proceedings of the National Academy of Sciences of the United States of America, 94*(26), 14243–14248. https://doi.org/10.1073/pnas.94.26.14243

Massimo, G., Dyson, N., Olotu, F., Khambata, R. S., & Ahluwalia, A. (2024). Potential Opportunities for Pharmacogenetic-Based Therapeutic Exploitation of Xanthine Dehydrogenase in Cardiovascular Disease. *Antioxidants, 13*(12), 1439. https://doi.org/10.3390/antiox13121439

McKelvey, T. G., Höllwarth, M. E., Granger, D. N., Engerson, T. D., Landler, U., & Jones, H.P. (1988). Mechanisms of conversion of xanthine dehydrogenase to xanthine oxidase in ischemic rat liver and kidney. *The American journal of physiology, 254*(5 Pt 1), G753– G760. https://doi.org/10.1152/ajpgi.1988.254.5.G753

Mendel R. R. (2013). The molybdenum cofactor. *The Journal of biological chemistry*, *288*(19), 13165–13172. https://doi.org/10.1074/jbc.R113.455311

Messerli, F. H., Bangalore, S., Bavishi, C., & Rimoldi, S. F. (2018). Angiotensin-converting enzyme inhibitors in hypertension: To use or not to use? *Journal of the American College of Cardiology, 71*(13), 1474–1482. https://10.1016/j.jacc.2018.01.058

Meyer, A. S., & Baker, T. A. (2011). Proteolysis in the Escherichia coli heat shock response: a player at many levels. *Current opinion in microbiology, 14*(2), 194–199. https://doi.org/10.1016/j.mib.2011.02.001

Miah, R., Fariha, K. A., Sony, S. A., Ahmed, S., Hasan, M., Mou, A. D., Barman, Z., Hasan, A., Mohanto, N. C., & Ali, N. (2022). Association of serum xanthine oxidase levels with hypertension: a study on Bangladeshi adults. *Scientific reports, 12*(1), 21727. https://doi.org/10.1038/s41598-022-26341-5

Micsonai, A., Wien, F., Kernya, L., Lee, Y. H., Goto, Y., Réfrégiers, M., & Kardos, J. (2015). Accurate secondary structure prediction and fold recognition for circular dichroism spectroscopy. *Proceedings of the National Academy of Sciences of the United States of America, 112*(24), E3095–E3103. https://doi.org/10.1073/pnas.1500851112

Mikhailova, E., Sokolenko, A., Combs, S. E., & Shevtsov, M. (2025). Modulation of Heat Shock Proteins Levels in Health and Disease: An Integrated Perspective in Diagnostics and Therapy. *Cells, 14*(13), 979. https://doi.org/10.3390/cells14130979

Murad F. (2006). Shattuck Lecture. Nitric oxide and cyclic GMP in cell signaling and drug development. *The New England journal of medicine, 355*(19), 2003–2011. https://doi.org/10.1056/NEJMsa063904

Nakamura, M., & Yamazaki, I. (1982). Preparation of bovine milk xanthine oxidase as a dehydrogenase form. *Journal of biochemistry, 92*(4), 1279–1286. https://doi.org/10.1093/oxfordjournals.jbchem.a134046

Nagy, G., & Grubmüller, H. (2020). How accurate is circular dichroism-based model validation?. *European biophysics journal : EBJ, 49*(6), 497–510. https://doi.org/10.1007/s00249-020-01457-6

Ndrepepa, G. (2025). Uric acid and cardiovascular disease—recent evidence on the association and underlying mechanisms. *Journal Of Laboratory And Precision Medicine, 10*. https://jlpm.amegroups.org/article/view/10145

Nishino T. (1994). The conversion of xanthine dehydrogenase to xanthine oxidase and the role of the enzyme in reperfusion injury. *Journal of biochemistry, 116*(1), 16. https://doi.org/10.1093/oxfordjournals.jbchem.a124480

Nishino, T., Okamoto, K., Eger, B. T., Pai, E. F., & Nishino, T. (2008). Mammalian xanthine oxidoreductase - mechanism of transition from xanthine dehydrogenase to xanthine oxidase. *The FEBS journal, 275*(13), 3278–3289. https://doi.org/10.1111/j.1742-4658.2008.06489.x

Nishino, T., Okamoto, K., Kawaguchi, Y., Hori, H., Matsumura, T., Eger, B. T., Pai, E. F., & Nishino, T. (2005). Mechanism of the Conversion of Xanthine Dehydrogenase to Xanthine Oxidase. Identification of the two cysteine disulfide bonds and crystal structure of a non-convertible rat liver xanthine dehydrogenase mutant. *Journal of Biological Chemistry, 280*(26), P24888-24894. https://www.jbc.org/article/S0021-9258(20)65640-X/fulltext

Noda, M., Kikuchi, C., Tarui, R., Nakamura, T., Murase, T., & Matsunaga, T. (2023). Effects of Xanthine Oxidoreductase Inhibitors on Reactive Oxygen Species Produced *In Vitro* from Xanthine Oxidase. *BPB Reports, 6*(6), Pages 189-192. https://doi.org/10.1248/bpbreports.6.6_189

Okamoto, K., Kusano, T., & Nishino, T. (2013). Chemical nature and reaction mechanisms of the molybdenum cofactor of xanthine oxidoreductase. *Current pharmaceutical design, 19(14),* 2606–2614. https://doi.org/10.2174/1381612811319140010

Oliver, E., Mayor Jr, F., & D'Ocon, P. (2019). Beta-blockers: Historical perspective and mechanisms of action. *Revista Española De Cardiología (English Edition), 72*(10), 853–862. https://10.1016/j.rec.2019.04.006

Oparil, S., Acelajado, M. C., Bakris, G. L., Berlowitz, D. R., Cífková, R., Dominiczak, A. F., Grassi, G., Jordan, J., Poulter, N. R., Rodgers, A., & Whelton, P. K. (2018). Hypertension. *Nature reviews. Disease primers*, *4*, 18014. https://doi.org/10.1038/nrdp.2018.14

Oganesyan, N., Ankoudinova, I., Kim, S. H., & Kim, R. (2007). Effect of osmotic stress and heat shock in recombinant protein overexpression and crystallization. *Protein expression and purification, 52*(2), 280–285. https://doi.org/10.1016/j.pep.2006.09.015

Pacher, P., Nivorozhkin, A., & Szabó, C. (2006). Therapeutic effects of xanthine oxidase inhibitors: renaissance half a century after the discovery of allopurinol. *Pharmacological reviews*, *58*(1), 87–114. https://doi.org/10.1124/pr.58.1.6

Papadopoulos, D. P., & Makris, T. K. (2007). Masked hypertension definition, impact, outcomes: a critical review. *Journal of clinical hypertension (Greenwich, Conn.)*, *9*(12), 956–963. https://doi.org/10.1111/j.1524-6175.2007.07418.x

Quezada, A. G., Díaz-Salazar, A. J., Cabrera, N., Pérez-Montfort, R., Piñeiro, Á., & Costas, M. (2017). Interplay between Protein Thermal Flexibility and Kinetic Stability. *Structure (London, England : 1993), 25*(1), 167–179. https://doi.org/10.1016/j.str.2016.11.018

Rathi, P. C., Jaeger, K. E., & Gohlke, H. (2015). Structural Rigidity and Protein Thermostability in Variants of Lipase A from Bacillus subtilis. *PloS one, 10*(7), e0130289. https://doi.org/10.1371/journal.pone.0130289

Robert, A. M., & R obert, L. (2014). Xanthine oxido-reductase, free radicals and cardiovascular disease. A critical review. *Pathology oncology research : POR*, *20*(1), 1–10. https://doi.org/10.1007/s12253-013-9698-x

Rodriguez-Loya, J., Lerma, M., & Gardea-Torresdey, J. L. (2023). Dynamic Light Scattering and Its Application to Control Nanoparticle Aggregation in Colloidal Systems: A Review. *Micromachines, 15*(1), 24. https://doi.org/10.3390/mi15010024

Rosenberg, G. M., Murray, K. A., Salwinski, L., Hughes, M. P., Abskharon, R., & Eisenberg, D. S. (2022). Bioinformatic identification of previously unrecognized amyloidogenic proteins. *The Journal of biological chemistry, 298*(5), 101920. https://doi.org/10.1016/j.jbc.2022.101920

Rysz, J., Franczyk, B., Rysz-Górzyńska, M., & Gluba-Brzózka, A. (2020). Pharmacogenomics of Hypertension Treatment. *International journal of molecular sciences*, *21*(13), 4709. https://doi.org/10.3390/ijms21134709

Sabaté, R., & Ventura, S. (2013). Cross-β-sheet supersecondary structure in amyloid folds: techniques for detection and characterization. *Methods in molecular biology (Clifton, N.J.), 932*, 237–257. https://doi.org/10.1007/978-1-62703-065-6_15

Sakamoto, N., Yamamoto, T., Moriwaki, Y., Teranishi, T., Toyoda, M., Onishi, Y., Kuroda, S., Sakaguchi, K., Fujisawa, T., Maeda, M., & Hada, T. (2001). Identification of a new point mutation in the human xanthine dehydrogenase gene responsible for a case of classical type I xanthinuria. *Human genetics, 108*(4), 279–283. https://doi.org/10.1007/s004390100477

Sambrook, J. and Green, M. R. (2012). Molecular Cloning: A Laboratory Manual. 4th edn. *Cold Spring Harbor Laboratory Press*.

Sanchez-Lozada, L. G., Rodriguez-Iturbe, B., Kelley, E. E., Nakagawa, T., Madero, M., Feig, D. I., Borghi, C., Piani, F., Cara-Fuentes, G., Bjornstad, P., Lanaspa, M.

A., & Johnson, R. J. (2020). Uric Acid and Hypertension: An Update With Recommendations. *American journal of hypertension*, *33*(7), 583–594. https://doi.org/10.1093/ajh/hpaa044

Sautin, Y. Y., & Johnson, R. J. (2008). Uric acid: the oxidant-antioxidant paradox. *Nucleosides, nucleotides & nucleic acids*, *27*(6), 608–619. https://doi.org/10.1080/15257770802138558

Sawicka, K., Szczyrek, M., Jastrzębska, I., Prasał, M., Zwolak, A., Daniluk, J. (2011). Hypertension – The Silent Killer. *J Pre Clin Clin Res., 5*(2), 43-46.

Scheepers, L. E., Wei, F. F., Stolarz-Skrzypek, K., Malyutina, S., Tikhonoff, V., Thijs, L., Salvi, E., Barlassina, C., Filipovský, J., Casiglia, E., Nikitin, Y., Kawecka-Jaszcz, K., Manunta, P., Cusi, D., Boonen, A., Staessen, J. A., & Arts, I. C. (2016). Xanthine oxidase gene variants and their association with blood pressure and incident hypertension: a population study. *Journal of hypertension*, *34*(11), 2147– 2154. https://doi.org/10.1097/HJH.0000000000001077

Schneider, C. A., Rasband, W. S., & Eliceiri, K. W. (2012). NIH Image to ImageJ: 25 years of image analysis. *Nature methods, 9*(7), 671–675. https://doi.org/10.1038/nmeth.2089

Schrödinger, L., & DeLano, W. (2020). *PyMOL*. Retrieved from http://www.pymol.org/pymol

Sekine, M., & Ichida, K. (2025). Metabolic Impact of XOR Inhibitors Use and Discontinuation. *Gout, Urate, and Crystal Deposition Disease, 3*(2), 9. https://doi.org/10.3390/gucdd3020009

Sekine, M., Okamoto, K., Pai, E. F., Nagata, K., Ichida, K., Hille, R., & Nishino, T. (2023). Allopurinol and oxypurinol differ in their strength and mechanisms of inhibition of xanthine oxidoreductase. *Journal of Biological Chemistry, 299*(9), 105189. https://10.1016/j.jbc.2023.105189

Sekizuka H. (2022). Uric acid, xanthine oxidase, and vascular damage: potential of xanthine oxidoreductase inhibitors to prevent cardiovascular diseases. *Hypertension research : official journal of the Japanese Society of Hypertension*, *45*(5), 772–774. https://doi.org/10.1038/s41440-022-00891-7

Sen, P., Fatima, S., Ahmad, B., & Khan, R. H. (2009). Interactions of thioflavin T with serum albumins: spectroscopic analyses. *Spectrochimica acta. Part A, Molecular and biomolecular spectroscopy, 74*(1), 94–99. https://doi.org/10.1016/j.saa.2009.05.010

Seychell, B. C. (2019). *Structural and biochemical analyses of human and sheep xanthine oxidoreductase* (Doctoral dissertation). https://www.um.edu.mt/library/oar/handle/123456789/71010

Shah, S. U., Anjum, S., & Littler, W. A. (2004). Use of diuretics in cardiovascular disease: (2) hypertension. *Postgraduate medical journal*, *80*(943), 271–276. https://doi.org/10.1136/pgmj.2003.010843

Shamsian, S., Sokouti, B., & Dastmalchi, S. (2024). Benchmarking different docking protocols for predicting the binding poses of ligands complexed with cyclooxygenase enzymes and screening chemical libraries. *BioImpacts : BI*, *14*(2), 29955. https://doi.org/10.34172/bi.2023.29955

Simmons, L. A., Grossman, A. D., & Walker, G. C. (2008). Clp and Lon proteases occupy distinct subcellular positions in Bacillus subtilis. *Journal of bacteriology, 190*(20), 6758–6768. https://doi.org/10.1128/JB.00590-08

Stetefeld, J., McKenna, S. A., & Patel, T. R. (2016). Dynamic light scattering: a practical guide and applications in biomedical sciences. *Biophysical reviews, 8*(4), 409–427. https://doi.org/10.1007/s12551-016-0218-6

Stiburkova, B., Krijt, J., Vyletal, P., Bartl, J., Gerhatova, E., Korinek, M., & Sebesta, I. (2012). Novel mutations in xanthine dehydrogenase/oxidase cause severe hypouricemia: biochemical and molecular genetic analysis in two Czech

families with xanthinuria type I. *Clinica chimica acta; international journal of clinical chemistry, 413(*1-2), 93–99. https://doi.org/10.1016/j.cca.2011.08.038

Stirpe, F., & Della Corte, E. (1969). The regulation of rat liver xanthine oxidase. Conversion in vitro of the enzyme activity from dehydrogenase (type D) to oxidase (type O). *The Journal of biological chemistry, 244*(14), 3855–3863.

Szyller, J., & Bil-Lula, I. (2021). Heat Shock Proteins in Oxidative Stress and Ischemia/Reperfusion Injury and Benefits from Physical Exercises: A Review to the Current Knowledge. *Oxidative medicine and cellular longevity, 2021*, 6678457. https://doi.org/10.1155/2021/6678457

Takano, Y., Hase-Aoki, K., Horiuchi, H., Zhao, L., Kasahara, Y., Kondo, S., & Becker, M. A. (2005). Selectivity of febuxostat, a novel non-purine inhibitor of xanthine oxidase/xanthine dehydrogenase. *Life sciences*, *76*(16), 1835–1847. https://doi.org/10.1016/j.lfs.2004.10.031

Terada, L. S., Piermattei, D., Shibao, G. N., McManaman, J. L., & Wright, R. M. (1997). Hypoxia regulates xanthine dehydrogenase activity at pre- and posttranslational levels. *Archives of biochemistry* https://doi.org/10.1006/abbi.1997.0367

Terao, M., Romão, M. J., Leimkühler, S., Bolis, M., Fratelli, M., Coelho, C., Santos Silva, T., & Garattini, E. (2016). Structure and function of mammalian aldehyde oxidases. *Archives of toxicology*. https://doi.org/10.1007/s00204-016-1683-1

Tompa P. (2009). Structural disorder in amyloid fibrils: its implication in dynamic interactions of proteins. *The FEBS journal, 276*(19), 5406–5415. https://doi.org/10.1111/j.1742-4658.2009.07250.x

Tuteja, N., Chandra, M., Tuteja, R., & Misra, M. K. (2004). Nitric Oxide as a Unique Bioactive Signaling Messenger in Physiology and Pathophysiology. *Journal of*

biomedicine & biotechnology, *2004*(4), 227–237. https://doi.org/10.1155/S1110724304402034

Tvrda, E. (2019). Chapter 3.2 – NBT Test. Oxidants, Antioxidants and Impact of the Oxidative Status in Malte Reproduction. *Academic Press*, 195-205. https://doi.org/10.1016/B978-0-12-812501-4.00018-3

Urarte, E., Esteban, R., Moran, J.F., Bittner, F. (2015). Established and Proposed Roles of Xanthine Oxidoreductase in Oxidative and Reductive Pathways in Plants. In: Gupta, K., Igamberdiev, A. (eds) Reactive Oxygen and Nitrogen Species Signaling and Communication in Plants. *Signaling and Communication in Plants, vol 23. Springer, Cham*. https://doi.org/10.1007/978-3-319-10079-1_2

Ventom, A. M., Deistung, J., & Bray, R. C. (1988). The isolation of demolybdo xanthine oxidase from bovine milk. *The Biochemical journal*, *255*(3), 949–956. https://doi.org/10.1042/bj2550949

Verdecchia, P., Staessen, J. A., White, W. B., Imai, Y., & O'Brien, E. T. (2002). Properly defining white coat hypertension. *European heart journal*, *23*(2), 106–109. https://doi.org/10.1053/euhj.2001.2657

Verma, N., Rastogi, S., Chia, Y., Siddique, S., Turana, Y., Cheng, H., Sogunuru, G. P., Tay, J. C., Teo, B. W., Wang, T., TSOI, K. K. F., & Kario, K. (2021). Non-pharmacological management of hypertension. *The Journal of Clinical Hypertension, 23*(7), 1275–1283. https://10.1111/jch.14236

Vinogradov, A. D., & Grivennikova, V. G. (2016). Oxidation of NADH and ROS production by respiratory complex I. *Biochimica et biophysica acta*, *1857*(7), 863–871. https://doi.org/10.1016/j.bbabio.2015.11.004

Wang, M., Shen, J., Thomas, J. C., Mu, T., Liu, W., Wang, Y., Pan, J., Wang, Q., & Liu, K. (2021). Particle Size Measurement Using Dynamic Light Scattering at Ultra- Low Concentration Accounting for Particle Number Fluctuations.

Materials (Basel, Switzerland), 14(19), 5683. https://doi.org/10.3390/ma14195683

Watanabe, S., Kang, D. H., Feng, L., Nakagawa, T., Kanellis, J., Lan, H., Mazzali, M., & Johnson, R. J. (2002). Uric acid, hominoid evolution, and the pathogenesis of salt-sensitivity. *Hypertension (Dallas, Tex. : 1979)*, *40*(3), 355–360. https://doi.org/10.1161/01.hyp.0000028589.66335.aa

Wile, D. (2012). Diuretics: A review. *Ann Clin Biochem, 49*(5), 419–431. https://10.1258/acb.2011.011281

World Health Organisation (2023). *Hypertension.* WHO. https://www.who.int/news-room/fact-sheets/detail/hypertension

Wu, B., Hao, Y., Shi, J., Geng, N., Li, T., Chen, Y. ... Sun, Y. (2015). Association between xanthine dehydrogenase tag single nucleotide polymorphisms and essential hypertension. *Molecular Medicine Reports, 12*, 5685-5690. https://doi.org/10.3892/mmr.2015.4135

Xia, K., & Wei, G. W. (2014). Persistent homology analysis of protein structure, flexibility, and folding. *International journal for numerical methods in biomedical engineering, 30*(8), 814–844. https://doi.org/10.1002/cnm.2655

Xu, P., LaVallee, P., & Hoidal, J. R. (2000). Repressed expression of the human xanthine oxidoreductase gene. E-box and TATA-like elements restrict ground state transcriptional activity. *The Journal of biological chemistry, 275*(8), 5918–5926. https://doi.org/10.1074/jbc.275.8.5918

Yamaguchi, Y., Matsumura, T., Ichida, K., Okamoto, K., & Nishino, T. (2007). Human xanthine oxidase changes its substrate specificity to aldehyde oxidase type upon mutation of amino acid residues in the active site: roles of active site residues in binding and activation of purine substrate. *Journal of biochemistry, 141*(4), 513 524. https://doi.org/10.1093/jb/mvm053

Yan, Y., Tao, H., He, J., & Huang S. (2020). The HDOCK server for integrated protein–protein docking. *Nature Protocols 15*, 1829–1852 https://doi.org/10.1038/s41596-020-0312-x

Yan, Y., Wen, Z., Wang, X., & Huang, S. Y. (2017). Addressing recent docking challenges: A hybrid strategy to integrate template-based and free protein-protein docking. *Proteins, 85*(3), 497–512. https://doi.org/10.1002/prot.25234

Yan, Y., Zhang, D., Zhou, P., Li, B., & Huang, S. Y. (2017). HDOCK: a web server for protein-protein and protein-DNA/RNA docking based on a hybrid strategy. *Nucleic acids research, 45*(W1), W365–W373. https://doi.org/10.1093/nar/gkx407

Yang, J., Kamide, K., Kokubo, Y., Takiuchi, S., Horio, T., Matayoshi, T., Yasuda, H., Miwa, Y., Yoshii, M., Yoshihara, F., Nakamura, S., Nakahama, H., Tomoike, H., Miyata, T., & Kawano, Y. (2008). Associations of hypertension and its complications with variations in the xanthine dehydrogenase gene. *Hypertension research : official journal of the Japanese Society of Hypertension, 31*(5), 931 940. https://doi.org/10.1291/hypres.31.931

Yu, J. G., Zhou, R. R., & Cai, G. J. (2011). From hypertension to stroke: mechanisms and potential prevention strategies. *CNS neuroscience & therapeutics*, *17*(5), 577–584. https://doi.org/10.1111/j.1755-5949.2011.00264.x

Zarepour, M., Kaspari, K., Stagge, S., Rethmeier, R., Mendel, R. R., & Bittner, F. (2010). Xanthine dehydrogenase AtXDH1 from Arabidopsis thaliana is a potent producer of superoxide anions via its NADH oxidase activity. *Plant molecular biology*, *72*(3), 301–310. https://doi.org/10.1007/s11103-009-9570-2

Zink, S., Qu, S., Holton, T., Shankar, E., Stanley, P., Eisenberg, D. S., Sawaya, M. R., & Rodriguez, J. A. (2025). Leveraging structure-informed machine learning for fast steric zipper propensity prediction across whole proteomes. *PLoS*

computational biology, 21(8), e1013395. https://doi.org/10.1371/journal.pcbi.1013395

Chapter 6 Appendix

6.1. DLS plots

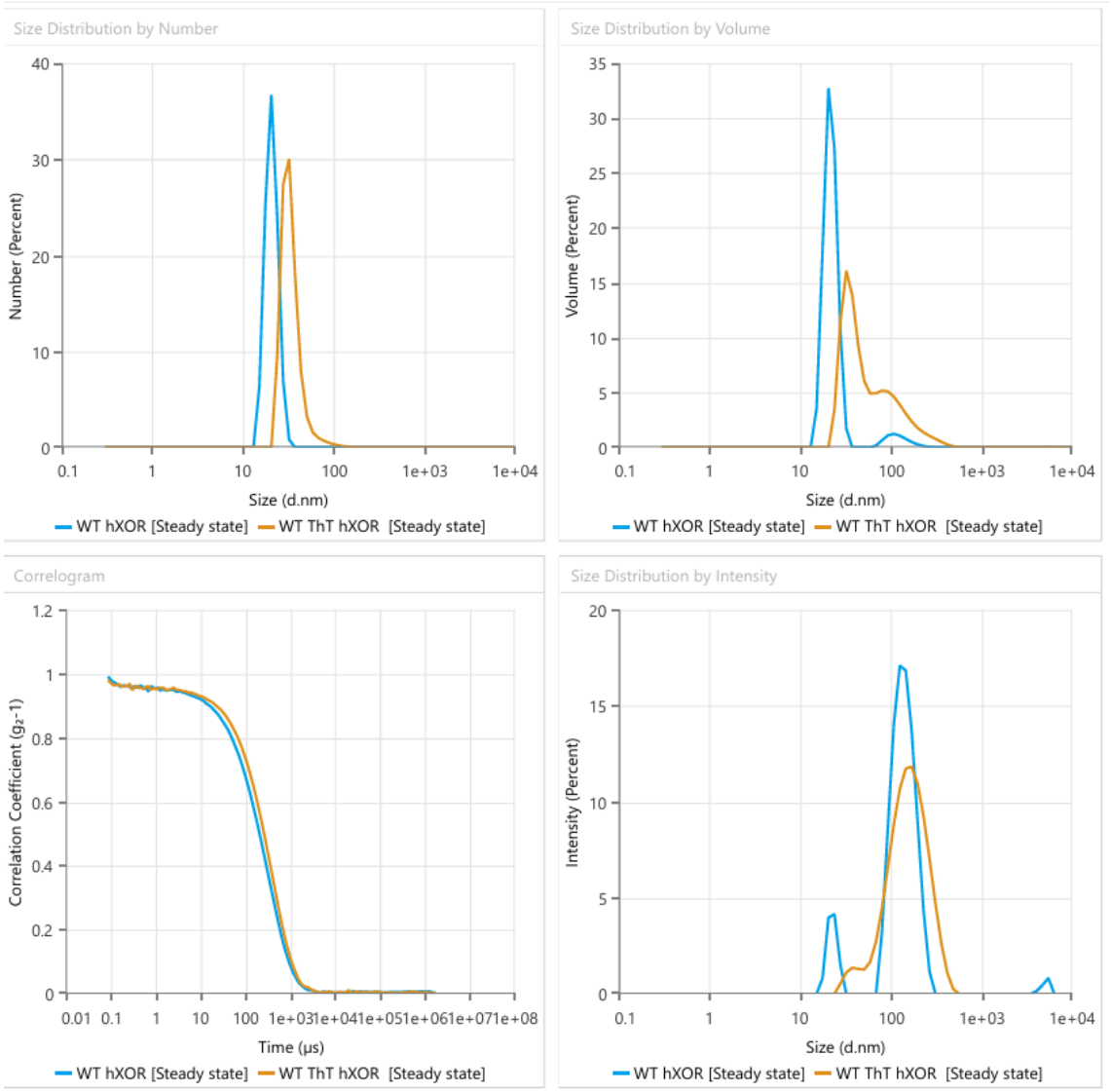

Figure 6.1: DLS plots of WT before and after ThT. Size distributions are shown by number, volume, and intensity with the corresponding correlogram. Blue line represents WT hXOR, and orange line represents WT hXOR with ThT.

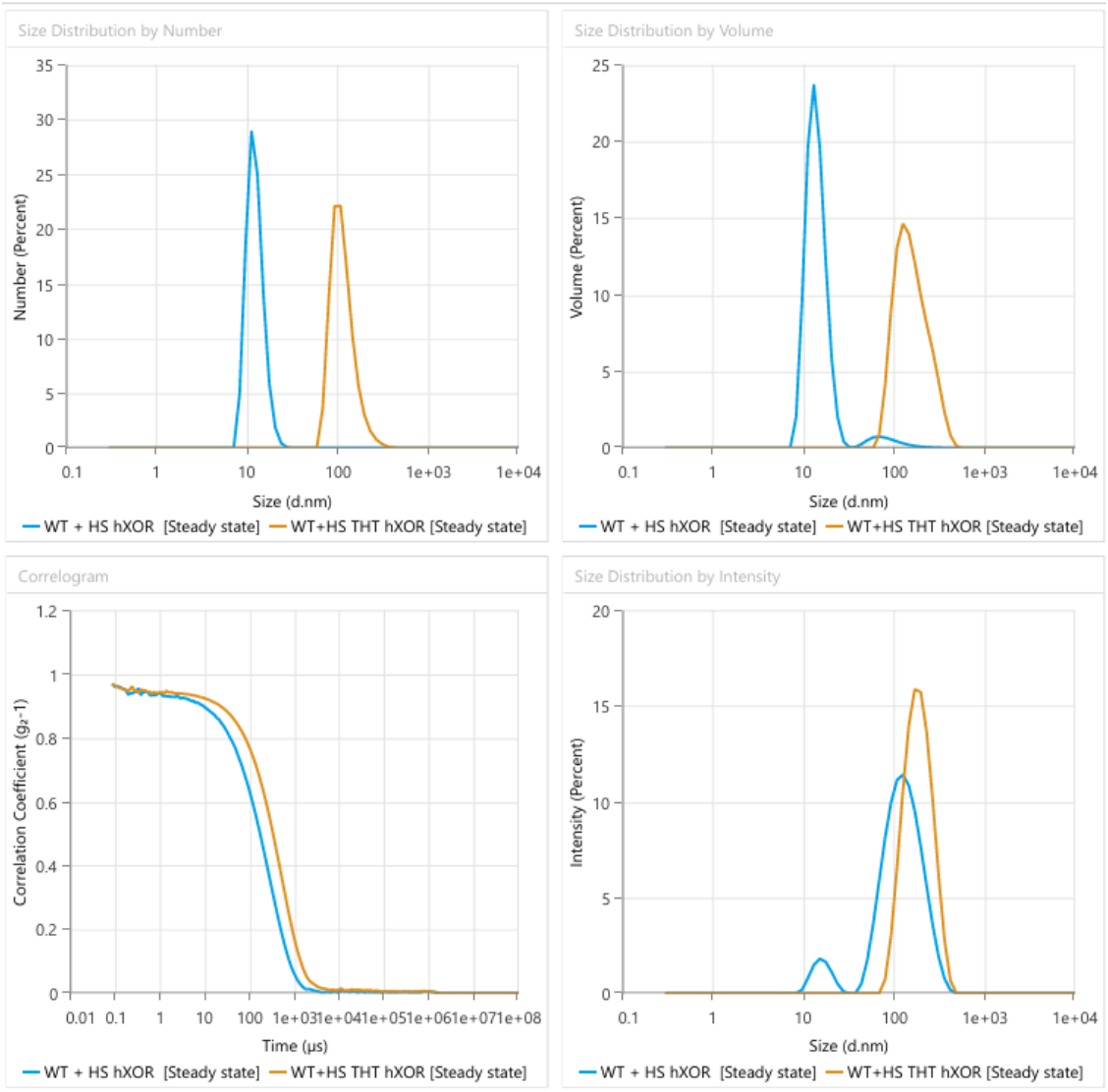

Figure 6.2: DLS plots of WT+HS before and after ThT. Size distributions are shown by number, volume, and intensity with the corresponding correlogram. Blue line represents WT+HS, and orange line represents WT+HS with ThT.

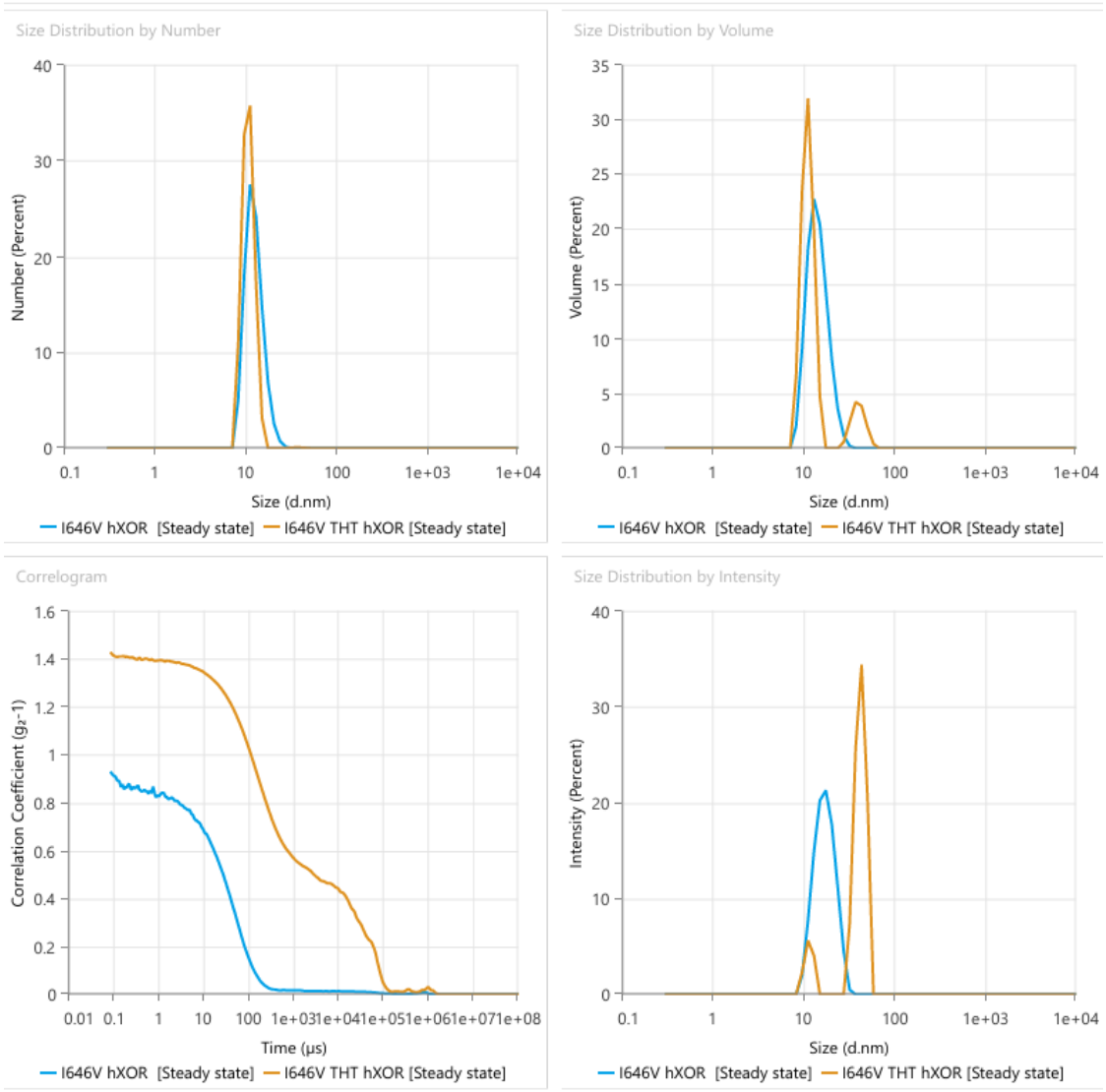

Figure 6.3: DLS plots of I646V before and after ThT. Size distributions are shown by number, volume, and intensity with the corresponding correlogram. Blue line represents I646V variant, whereas the orange line represents I646V with ThT.

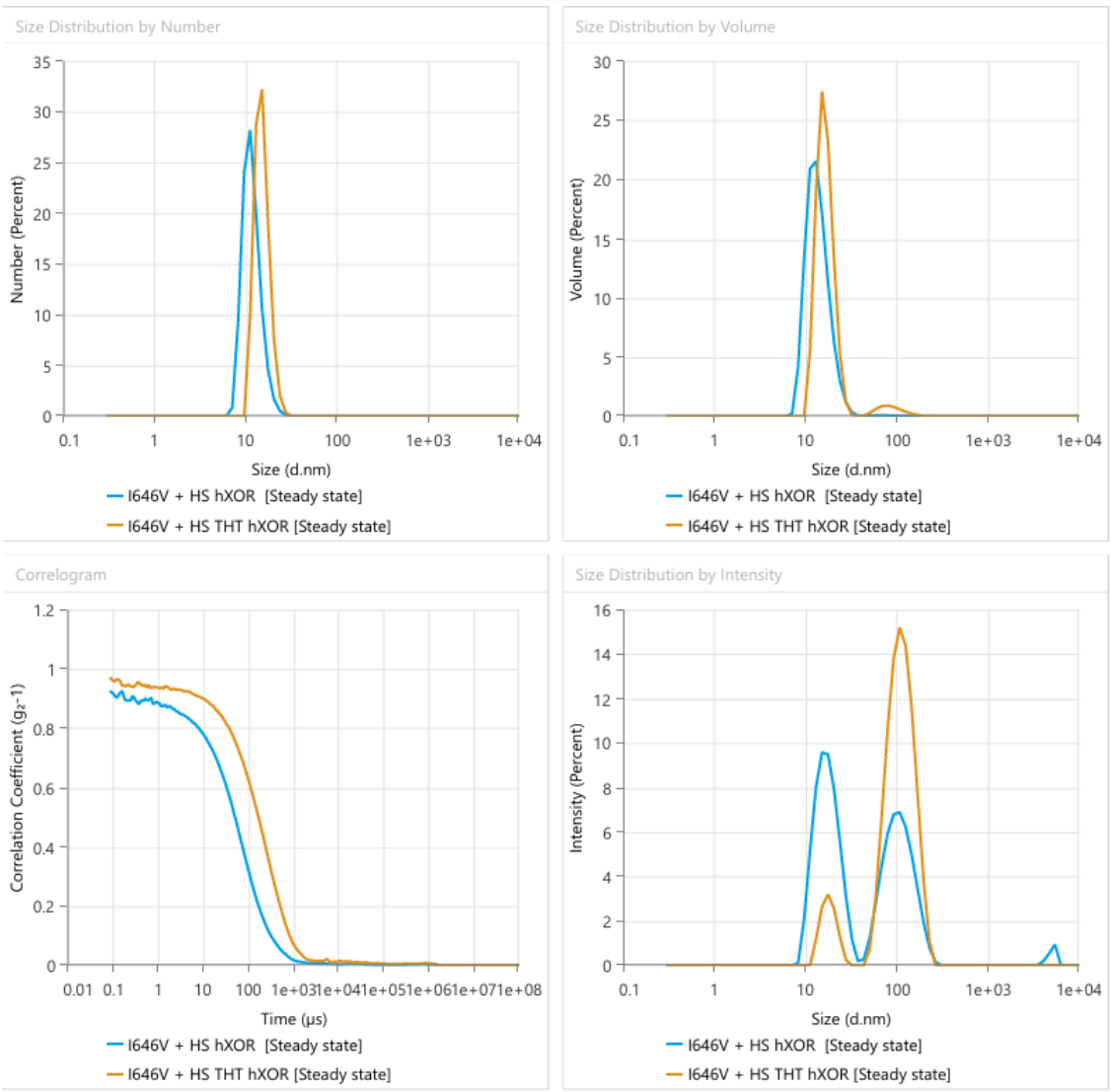

Figure 6.4: DLS plots of I646V+HS before and after ThT. Size distributions are shown by number, volume, and intensity with the corresponding correlogram. Blue line represents I646V+HS, and orange line represents I646V+HS with ThT.

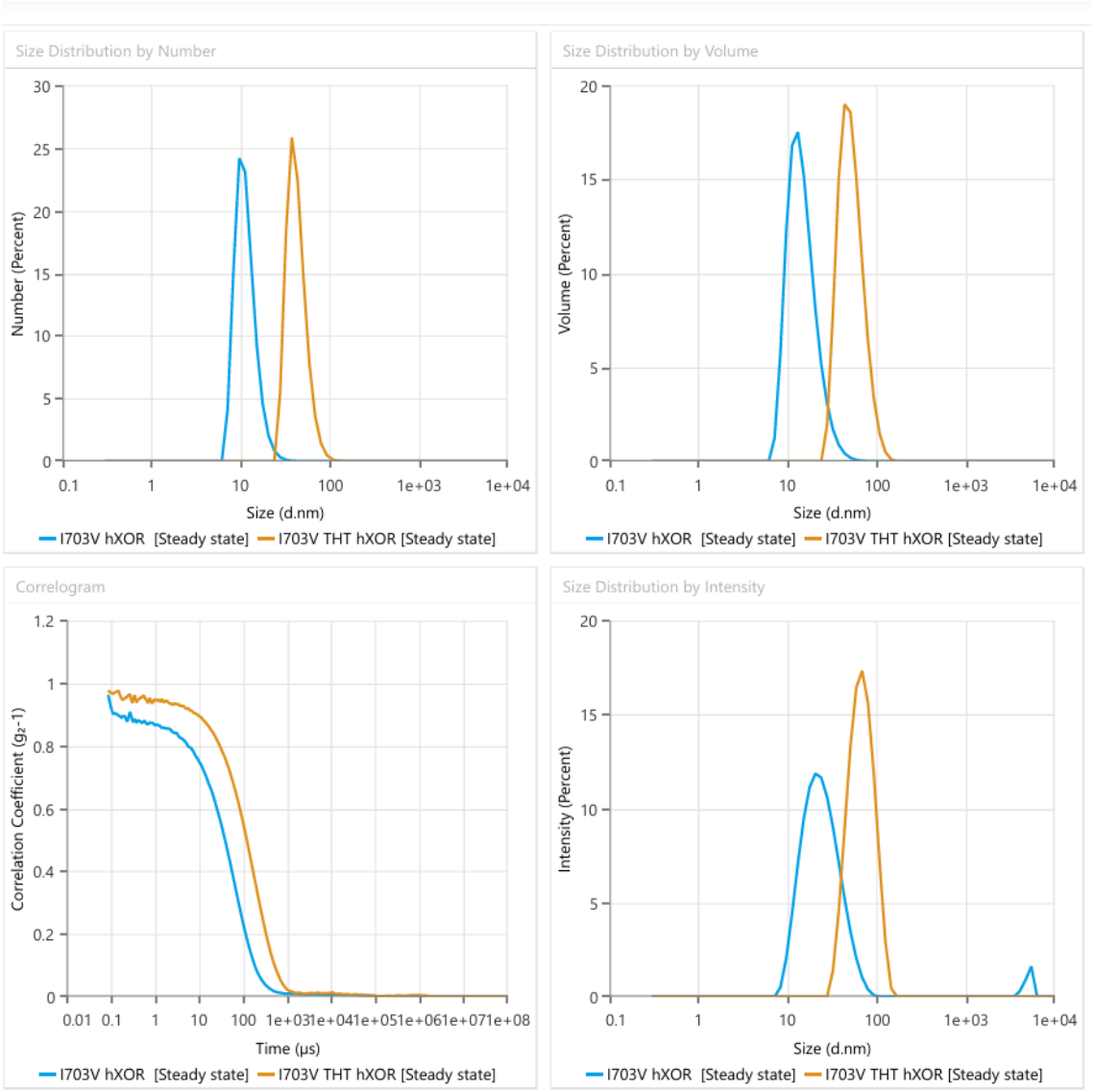

Figure 6.5: DLS plots of I703V before and after ThT. Size distributions are shown by number, volume, and intensity with the corresponding correlogram. Blue line represents I703V, whereas the orange line represents I703V with ThT.

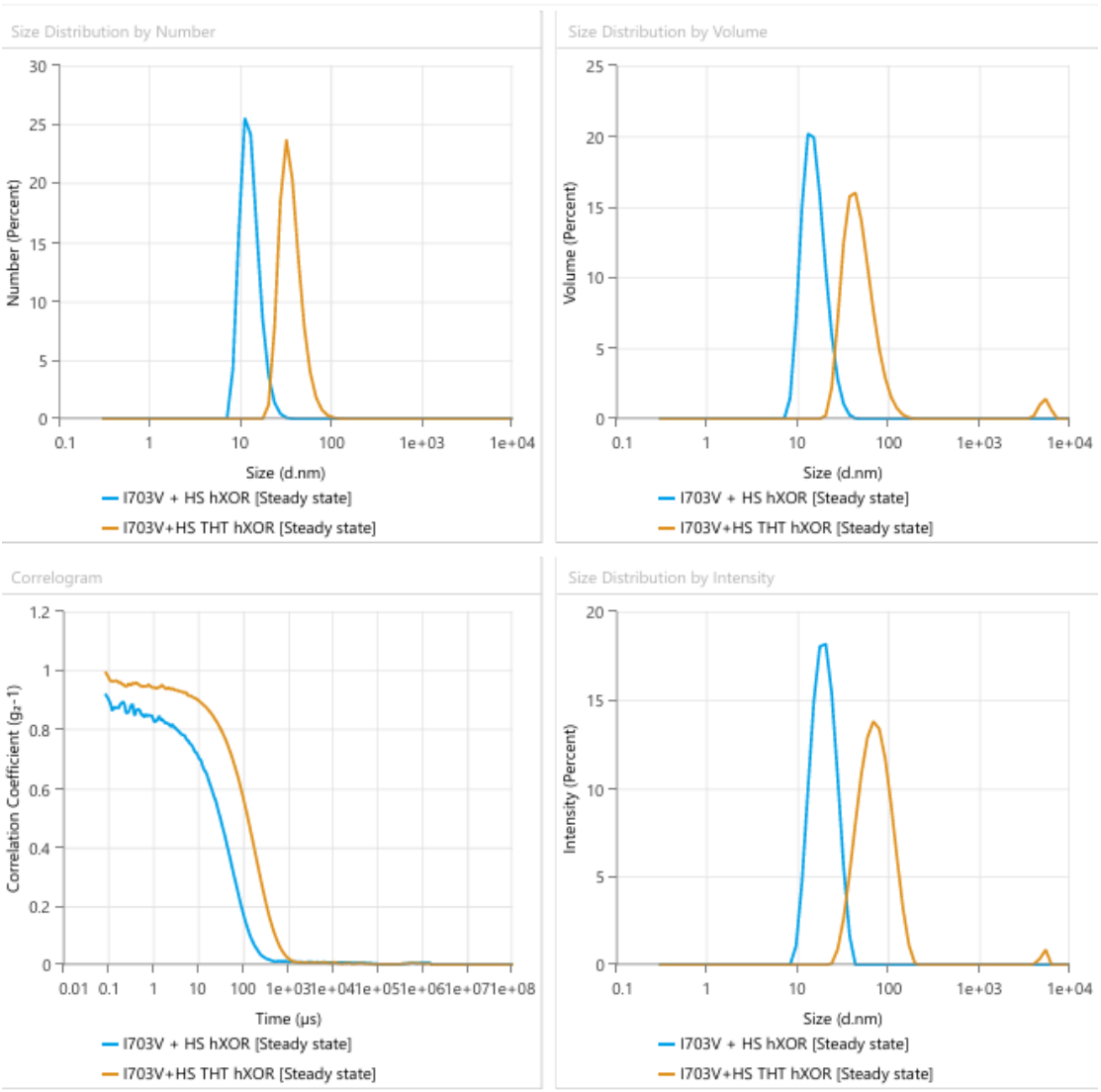

Figure 6.6: DLS plots of I703V+HS before and after ThT. Size distributions are shown by number, volume, and intensity with the corresponding correlogram. Blue line represents WT hXOR, and orange line represents WT hXOR with ThT.

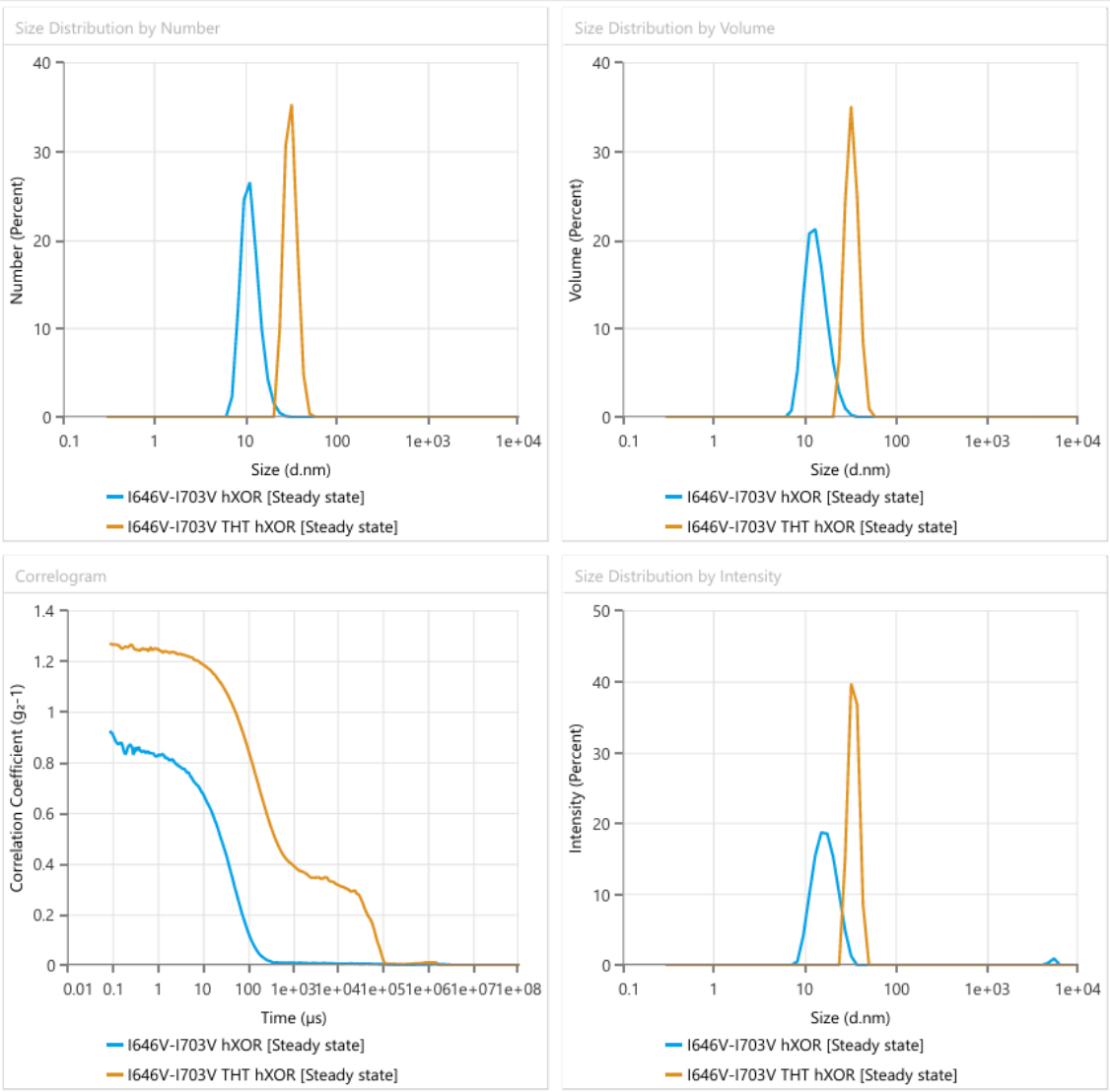

Figure 6.7: DLS plots of I646V-I703V before and after ThT. Size distributions are shown by number, volume, and intensity with the corresponding correlogram. Blue line represents I646V-I703V, and orange line represents I646V-I703V with ThT.

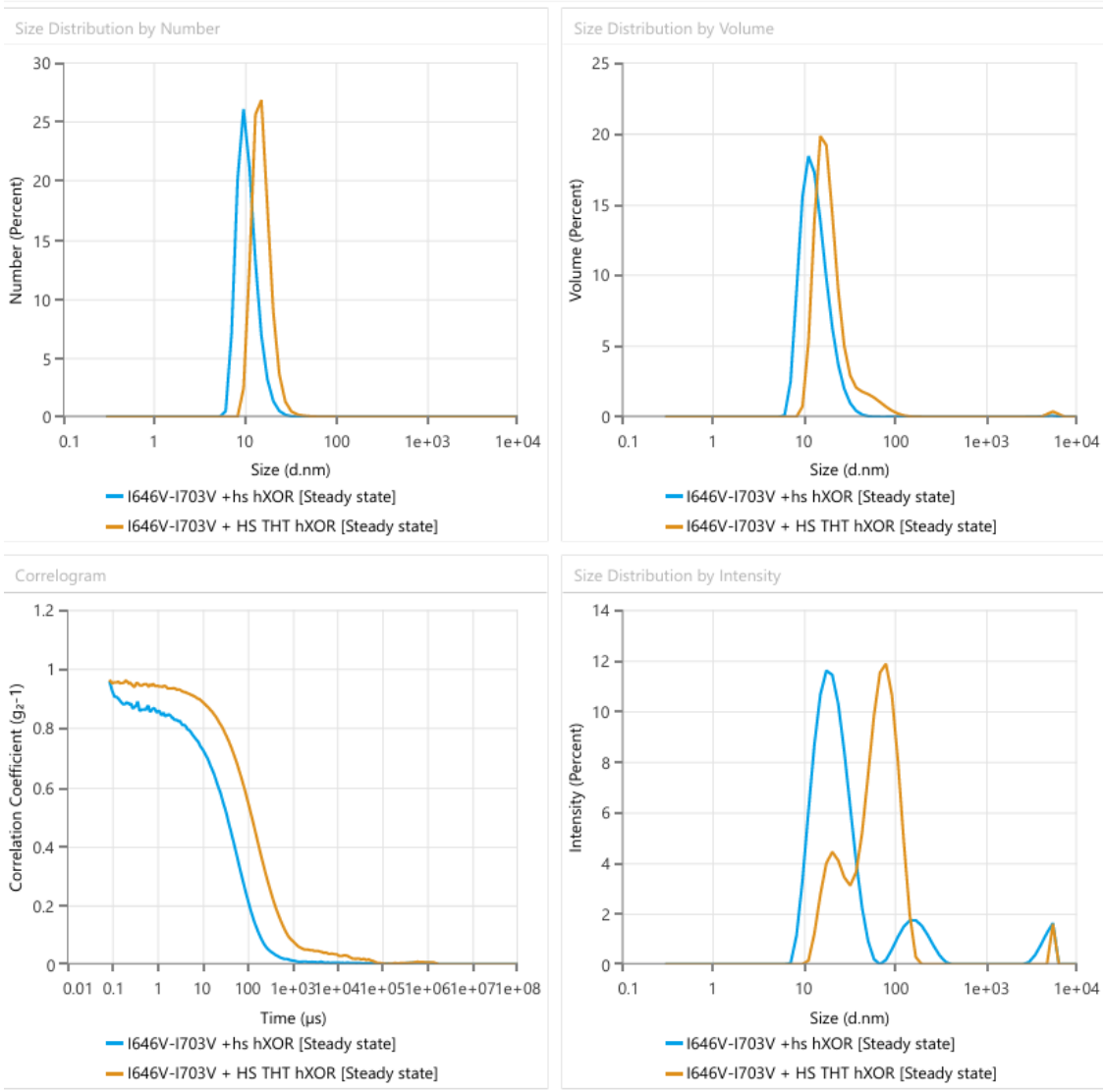

Figure 6.8: DLS plots of I646V-I703V+HS before and after ThT. Size distributions are shown by number, volume, and intensity with the corresponding correlogram. Blue line represents I646V-I703V+HS, and orange line represents I646V-I703V+HS with ThT.

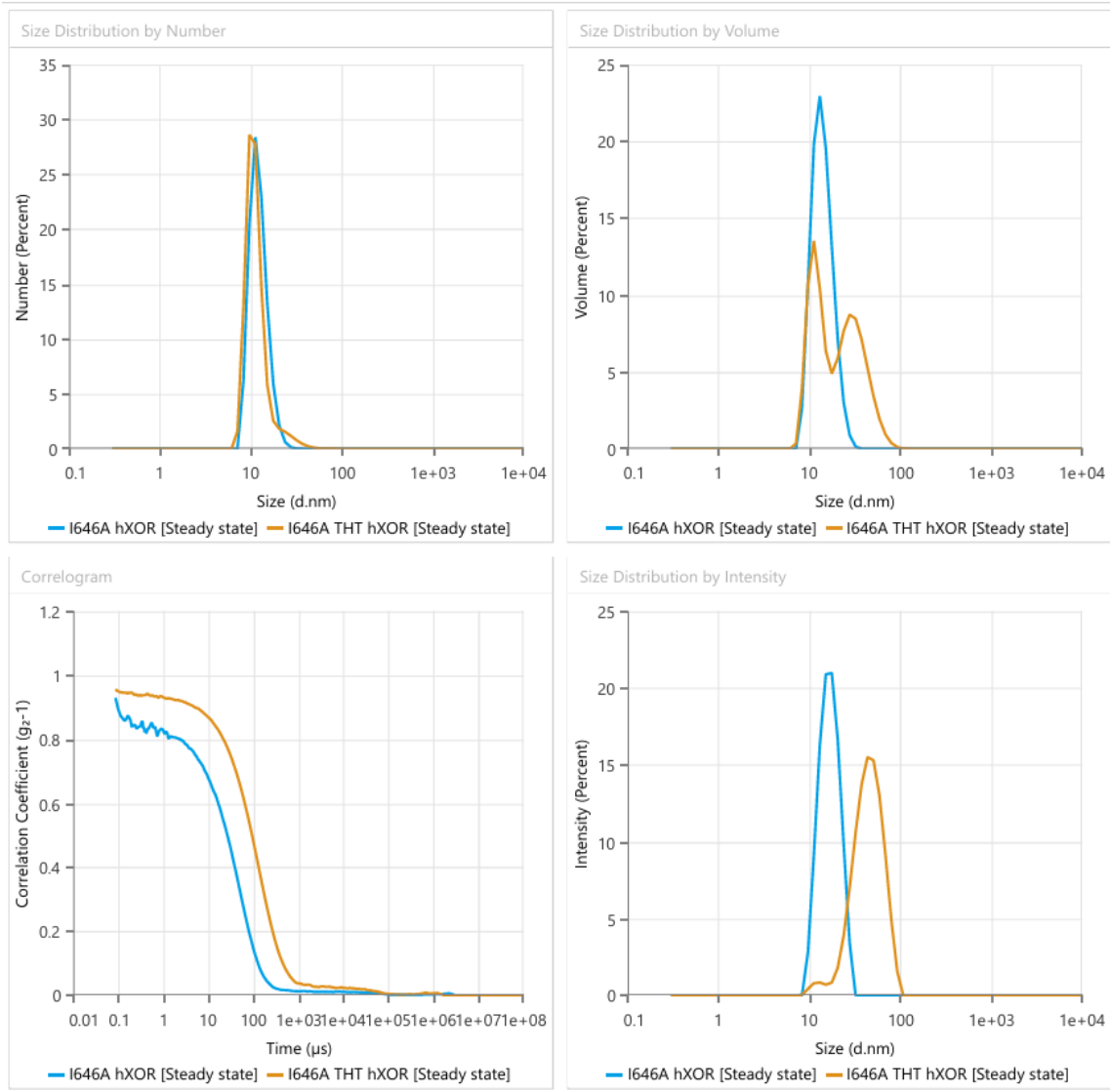

Figure 6.9: DLS plots of I646A before and after ThT. Size distributions are shown by number, volume, and intensity with the corresponding correlogram. Blue line represents I646A, and orange line represents I646A with ThT.

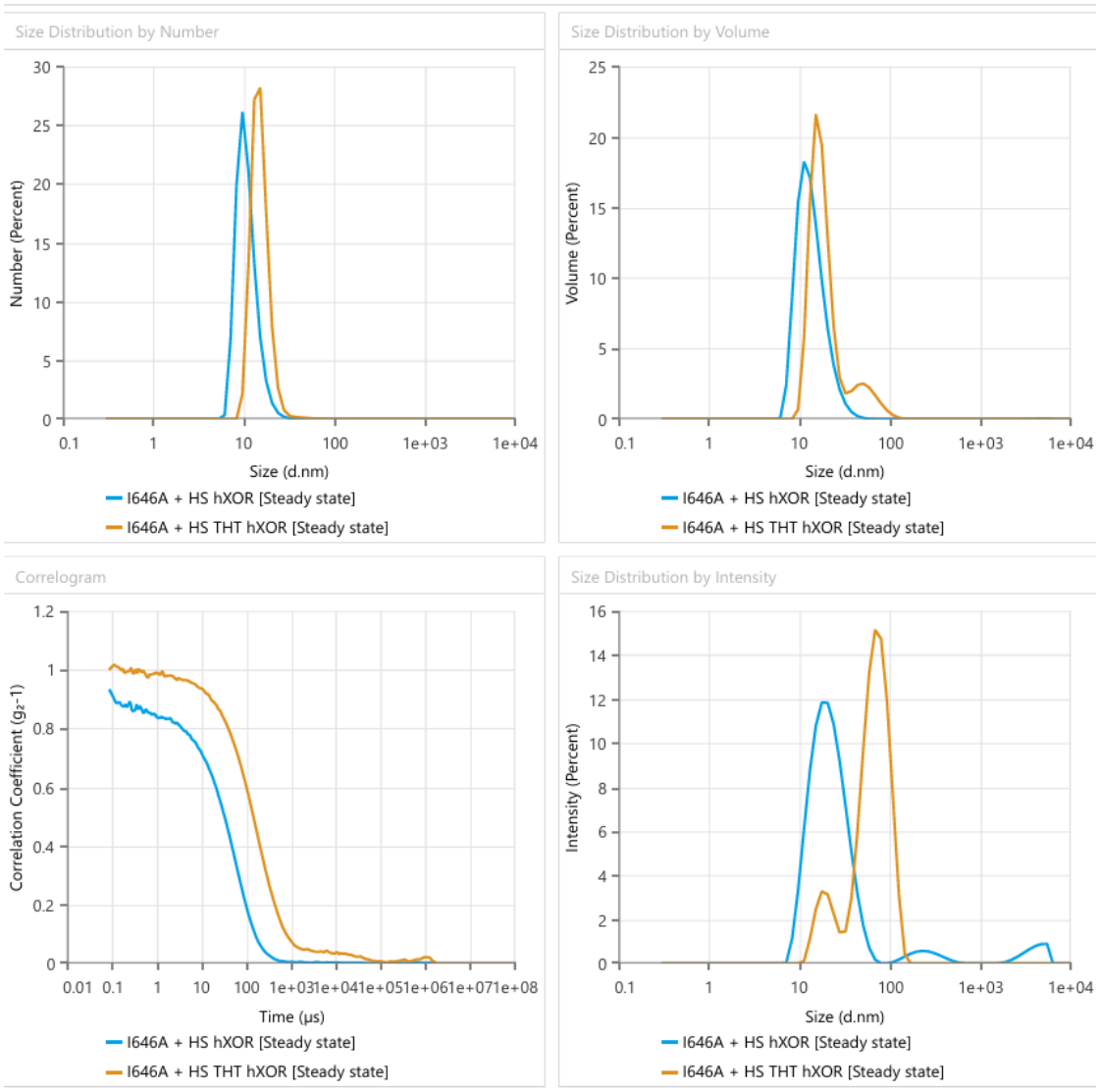

Figure 6.10: DLS plots of I646A+HS before and after ThT. Size distributions are shown by number, volume, and intensity with the corresponding correlogram. Blue line represents I646A+HS, and orange line represents I646A+HS with ThT.